THE FLORIDA STATE UNIVERSITY

COLLEGE OF ARTS AND SCIENCES

SEARCH FOR MULTIPLY CHARGED HEAVY STABLE CHARGED PARTICLES IN DATA COLLECTED WITH THE CMS DETECTOR

By

VENKATESH VEERARAGHAVAN

A Dissertation submitted to the
Department of Physics
in partial fulfillment of the
requirements for the degree of
Doctor of Philosophy

Degree Awarded:
Fall Semester, 2013

Venkatesh Veeraraghavan defended this dissertation on October 30, 2013.

The members of the supervisory committee were:

Todd Adams
Professor Directing Thesis

Oliver Steinbock
University Representative

Harrison Prosper
Committee Member

Laura Reina
Committee Member

Simon Capstick
Committee Member

The Graduate School has verified and approved the above-named committee members, and certifies that the dissertation has been approved in accordance with the university requirements.

ACKNOWLEDGMENTS

I want to thank my advisor Todd Adams for his support, and patience over the course of my Ph.D. work; and seeing me through to the finish. I am grateful to him for all of our discussions that have helped me in better understanding of problems. He has also spent considerable time reading this document carefully several times; it would not have been as polished if he didn't.

It was always joyous conversing with Harrison Prosper, whose enthusiasm for science is infectious. I thank him for his help and patience during the course of my Ph.D. work. I thank Laura Reina, who besides being on my graduate committee, also taught an excellent course on quantum field theory. I also thank Simon Capstick, who helped me in qualifying exam preparations, served on my graduate committee, and gave feedback on this document.

Efforts within the HSCP group of the CMS collaboration were of great help in accomplishing my dissertation research, and I am grateful to them. I thank Jie Chen and Loic Quertenmont for sharing their expertise with me.

I thank fellow experimental graduate students, Brendan Diamond and Jeff Haas, for helping me, even if it meant sacrificing their own work.

It was my good fortune to have met Chris Duston and Ugander Reddy in Tallahassee. Chris was my go-to person in Keen to discuss anything; be it physics, academics, or otherwise, and I always benefited from talking to him. Ugander was a loyal friend and always helpful, even if I called him in middle of the night.

I am grateful to my teachers from my earlier college and University for providing me education. I thank Maya Naik, Pratibha Pai, and CV Venkat Krishnan from SIES College; and Anuradha Misra, Arun Narsale, and MR Press from University of Mumbai.

Lastly, I acknowledge my parents, sister, brother, and numerous relatives for their support and encouragement. I am grateful to my father, who was my teacher for, by far, the lengthiest time. Nothing matters more to my mother than my welfare and I will always be indebted to her for everything she has done for me. Lastly, I remember my aunt for always believing in me and inspiring me.

TABLE OF CONTENTS

List of Tables . . . vii

List of Figures . . . xii

Abstract . . . xviii

1 Introduction **1**

1.1 Standard Model of Particle Physics . . . 1

1.2 Shortcomings of the Standard Model . . . 4

1.3 Beyond Standard Model Theories . . . 6

1.4 Search for Multiply Charged HSCPs in High Energy Colliders . . . 10

1.5 Other Experimental Searches . . . 13

2 Experiment: Collider and Detector **15**

2.1 Large Hadron Collider . . . 15

2.2 Compact Muon Solenoid Detector . . . 20

2.2.1 Coordinate System . . . 21

2.2.2 Layout . . . 22

2.2.3 Inner Tracking System . . . 24

2.2.4 Electromagnetic Calorimeter . . . 27

2.2.5 Hadron Calorimeter . . . 28

2.2.6 Solenoid Magnet . . . 28

2.2.7 Muon System . . . 29

2.2.8 Trigger and Data Acquisition . . . 30

3 Variables Used in the Search **32**

3.1 Ionization Energy Loss . . . 32

3.1.1 Energy Loss Estimators . . . 32

3.1.2 Energy Loss Discriminators . . . 37

3.2 Time-of-Flight . . . 41

3.2.1 Drift Tube Measurements . . . 42

3.2.2 Cathode Strip Chamber Measurements . . . 44

3.2.3 Inverse Beta . . . 44

4 Multiply Charged HSCP Analysis **47**

4.1 Signal Model . . . 47

4.2 Trigger and Data Selection . . . 53

4.2.1 Online Selection 53
4.2.2 Offline Selection 56
4.3 Background Prediction 76

5 Systematic Uncertainties **85**
5.1 Background Prediction 85
5.2 Signal Acceptance 91

6 Results **99**

7 Conclusions **115**
7.1 Summary 115
7.2 Perspectives 116

Appendices **118**

A PYTHIA Parameters **118**

B Theory Cross Section Values **120**

C Offline Selection Efficiency **123**

D Individual Systematic Uncertainties **140**

E Full Results of Optimization **145**

Bibliography 154

Biographical Sketch 159

LIST OF TABLES

1.1 Particle content of the standard model. 2

2.1 Specifications of the silicon strip detector sub systems. 26

4.1 Offline selection variables and their type/values. 60

4.2 Candidate efficiency for various offline selections in data and HSCPs with select charges and masses at $\sqrt{s}$ =7 TeV. The offline selections are listed in the first column and the efficiency values are listed in the remaining columns. The efficiency is for the selection variable listed in the particular row after the selections in the upper rows have been applied. The second row lists the efficiency relative to the number of HSCPs that pass the online selection. The last row lists the overall offline selection efficiency. 74

4.3 Candidate efficiency for various offline selections in data and HSCPs with select charges and masses at $\sqrt{s}$ =8 TeV. The offline selections are listed in the first column and the efficiency values are listed in the remaining columns. The efficiency is for the selection variable listed in the particular row after the selections in the upper rows have been applied. The second row lists the efficiency relative to the number of HSCPs that pass the online selection. The last row lists the overall offline selection efficiency. 75

4.4 Numbers of candidates in A, B, C, and D regions for I_{as}=0.05 and $1/\beta$=1.075 in $\sqrt{s}$ =7 TeV and 8 TeV data. The bottom row lists predicted number of candidates in region D as per the ABCD method. Only statistical uncertainty on the prediction is quoted. 82

5.1 Mean and RMS of timing values recorded in DTs, CSCs, and RPCs. 92

5.2 Summary table of various uncertainties and their respective value/ranges for multiply charged HSCPs for $\sqrt{s} = 7$ and 8 TeV. 96

6.1 Results of optimization for select HSCP charges and masses at $\sqrt{s} = 7$ and 8 TeV showing optimized I_{as} and $1/\beta$ selections, signal acceptance, predicted numbers of background candidates, observed numbers of data candidates, and expected and observed cross section limits. The two quantities in the paranthesis next to signal acceptance are systematic and statistical uncertainties on signal acceptance respectively, expressed as a percentage of the signal acceptance. 102

6.2 Numbers of predicted background candidates for several selections for $\sqrt{s} = 7$ and 8 TeV. 104

6.3 Numbers of predicted background candidates, observed data candidates, and significance for final selection of $(I_{as}, 1/\beta) = (0.5, 1.2)$ for $\sqrt{s} = 7$ and 8 TeV. 106

6.4 Signal acceptance, expected and observed cross section limits for final selection of I_{as}=0.5, and $1/\beta$=1.2 for HSCPs with $Q = 1e$, and $2e$ for $\sqrt{s} = 7$ and 8 TeV. The two quantities in paranthesis are systematic and statistical uncertainty in signal acceptance, expressed as a percentage of the signal acceptance. For the combination of 7 and 8 TeV results, expected and observed limits on signal strength μ are listed. 107

6.5 Signal acceptance, expected and observed cross section limits for final selection of I_{as}=0.5, and $1/\beta$=1.2 for HSCPs with $Q = 3e$, and $4e$ for $\sqrt{s} = 7$ and 8 TeV. The two quantities in paranthesis are systematic and statistical uncertainty in signal acceptance, expressed as a percentage of the signal acceptance. For the combination of 7 and 8 TeV results, expected and observed limits on signal strength μ are listed. 108

6.6 Signal acceptance, expected and observed cross section limits for final selection of I_{as}=0.5, and $1/\beta$=1.2 for HSCPs with $Q = 5e$, and $6e$ for $\sqrt{s} = 7$ and 8 TeV. The two quantities in paranthesis are systematic and statistical uncertainty in signal acceptance, expressed as a percentage of the signal acceptance. For the combination of 7 and 8 TeV results, expected and observed limits on signal strength μ are listed. 109

6.7 Signal acceptance, expected and observed cross section limits for final selection of I_{as}=0.5, and $1/\beta$=1.2 for HSCPs with $Q = 7e$, and $8e$ for $\sqrt{s} = 7$ and 8 TeV. The two quantities in paranthesis are systematic and statistical uncertainty in signal acceptance, expressed as a percentage of the signal acceptance. For the combination of 7 and 8 TeV results, expected and observed limits on signal strength μ are listed. 110

6.8 Mass limits for multiply charged HSCPs with different charges at $\sqrt{s} = 7$ TeV, $\sqrt{s} = 8$ TeV and combination of $\sqrt{s} = 7$ and 8 TeV. 113

B.1 Theory cross section values of multiply charged HSCPs in Drell-Yan-like model for $\sqrt{s} = 7$ TeV. 121

B.2 Theory cross section values of multiply charged HSCPs in Drell-Yan-like model for $\sqrt{s} = 8$ TeV. 122

C.1 Candidate efficiency of HSCPs with $Q = 1e$ and different masses for various offline selections at $\sqrt{s}$ =7 TeV. 124

C.2 Candidate efficiency of HSCPs with $Q = 2e$ and different masses for various

offline selections at $\sqrt{s}$ =7 TeV. 125

C.3 Candidate efficiency of HSCPs with $Q = 3e$ and different masses for various offline selections at $\sqrt{s}$ =7 TeV. 126

C.4 Candidate efficiency of HSCPs with $Q = 4e$ and different masses for various offline selections at $\sqrt{s}$ =7 TeV. 127

C.5 Candidate efficiency of HSCPs with $Q = 5e$ and different masses for various offline selections at $\sqrt{s}$ =7 TeV. 128

C.6 Candidate efficiency of HSCPs with $Q = 6e$ and different masses for various offline selections at $\sqrt{s}$ =7 TeV. 129

C.7 Candidate efficiency of HSCPs with $Q = 7e$ and different masses for various offline selections at $\sqrt{s}$ =7 TeV. 130

C.8 Candidate efficiency of HSCPs with $Q = 8e$ and different masses for various offline selections at $\sqrt{s}$ =7 TeV. 131

C.9 Candidate efficiency of HSCPs with $Q = 1e$ and different masses for various offline selections at $\sqrt{s}$ =8 TeV. 132

C.10 Candidate efficiency of HSCPs with $Q = 2e$ and different masses for various offline selections at $\sqrt{s}$ =8 TeV. 133

C.11 Candidate efficiency of HSCPs with $Q = 3e$ and different masses for various offline selections at $\sqrt{s}$ =8 TeV. 134

C.12 Candidate efficiency of HSCPs with $Q = 4e$ and different masses for various offline selections at $\sqrt{s}$ =8 TeV. 135

C.13 Candidate efficiency of HSCPs with $Q = 5e$ and different masses for various offline selections at $\sqrt{s}$ =8 TeV. 136

C.14 Candidate efficiency of HSCPs with $Q = 6e$ and different masses for various offline selections at $\sqrt{s}$ =8 TeV. 137

C.15 Candidate efficiency of HSCPs with $Q = 7e$ and different masses for various offline selections at $\sqrt{s}$ =8 TeV. 138

C.16 Candidate efficiency of HSCPs with $Q = 8e$ and different masses for various offline selections at $\sqrt{s}$ =8 TeV. 139

E.1 Results of optimization for multiply charged HSCPs with $Q = 1e$, and $2e$ for $\sqrt{s} = 7$ TeV showing optimized I_{as} and $1/\beta$ selections, signal acceptance, predicted numbers of background candidates, observed numbers of data candidates, and expected and observed cross section limits. The two quantities

in the paranthesis next to signal acceptance are systematic and statistical uncertainties on signal acceptance respectively, expressed as a percentage of the signal acceptance. 146

E.2 Results of optimization for multiply charged HSCPs with $Q = 3e$, and $4e$ for $\sqrt{s} = 7$ TeV showing optimized I_{as} and $1/\beta$ selections, signal acceptance, predicted numbers of background candidates, observed numbers of data candidates, and expected and observed cross section limits. The two quantities in the paranthesis next to signal acceptance are systematic and statistical uncertainties on signal acceptance respectively, expressed as a percentage of the signal acceptance. 147

E.3 Results of optimization for multiply charged HSCPs with $Q = 5e$, and $6e$ for $\sqrt{s} = 7$ TeV showing optimized I_{as} and $1/\beta$ selections, signal acceptance, predicted numbers of background candidates, observed numbers of data candidates, and expected and observed cross section limits. The two quantities in the paranthesis next to signal acceptance are systematic and statistical uncertainties on signal acceptance respectively, expressed as a percentage of the signal acceptance. 148

E.4 Results of optimization for multiply charged HSCPs with $Q = 7e$, and $8e$ for $\sqrt{s} = 7$ TeV showing optimized I_{as} and $1/\beta$ selections, signal acceptance, predicted numbers of background candidates, observed numbers of data candidates, and expected and observed cross section limits. The two quantities in the paranthesis next to signal acceptance are systematic and statistical uncertainties on signal acceptance respectively, expressed as a percentage of the signal acceptance. 149

E.5 Results of optimization for multiply charged HSCPs with $Q = 1e$, and $2e$ for $\sqrt{s} = 8$ TeV showing optimized I_{as} and $1/\beta$ selections, signal acceptance, predicted numbers of background candidates, observed numbers of data candidates, and expected and observed cross section limits. The two quantities in the paranthesis next to signal acceptance are systematic and statistical uncertainties on signal acceptance respectively, expressed as a percentage of the signal acceptance. 150

E.6 Results of optimization for multiply charged HSCPs with $Q = 3e$, and $4e$ for $\sqrt{s} = 8$ TeV showing optimized I_{as} and $1/\beta$ selections, signal acceptance, predicted numbers of background candidates, observed numbers of data candidates, and expected and observed cross section limits. The two quantities in the paranthesis next to signal acceptance are systematic and statistical uncertainties on signal acceptance respectively, expressed as a percentage of the signal acceptance. 151

E.7 Results of optimization for multiply charged HSCPs with $Q = 5e$, and $6e$ for $\sqrt{s} = 8$ TeV showing optimized I_{as} and $1/\beta$ selections, signal acceptance,

predicted numbers of background candidates, observed numbers of data candidates, and expected and observed cross section limits. The two quantities in the paranthesis next to signal acceptance are systematic and statistical uncertainties on signal acceptance respectively, expressed as a percentage of the signal acceptance. 152

E.8 Results of optimization for multiply charged HSCPs with $Q = 7e$, and $8e$ for $\sqrt{s} = 8$ TeV showing optimized I_{as} and $1/\beta$ selections, signal acceptance, predicted numbers of background candidates, observed numbers of data candidates, and expected and observed cross section limits. The two quantities in the paranthesis next to signal acceptance are systematic and statistical uncertainties on signal acceptance respectively, expressed as a percentage of the signal acceptance. 153

LIST OF FIGURES

1.1 Distributions of generator-level β ($=v/c$) for HSCPs of various masses at 8 TeV center-of-mass energy in the Drell-Yan-like model (Sec. 4.1). 11

1.2 Bethe-Bloch curve showing the ionization energy loss per pathlength of positive muons in copper medium [35]. 12

2.1 Accelerator complex at CERN [39]. 17

2.2 Schematic layout of the LHC [40]. 18

2.3 Cumulative luminosity as a function of day of the year delivered to CMS during stable beams for proton-proton collisions in 2010, 2011, and 2012 [45]. . . . 21

2.4 Partially assembled CMS detector [46]. 22

2.5 Schematic layout of CMS detector [47]. 23

2.6 Schematic layout of CMS inner tracker [42]. 25

3.1 Distribution of $\frac{dE}{dx}$ for harmonic-2 (left) and truncated-40 (right) estimators in data and simulation [48]. 34

3.2 Distributions of $\frac{dE}{dx}$ as a function of momentum using harmonic-2 (top row) and truncated-40 (bottom row) estimators. Left column shows $\sqrt{s}$ =7 TeV data while right column shows $\sqrt{s}$ =7 TeV simulation [48]. 35

3.3 Distributions of $\frac{dE}{dx}$ as a function of momentum for data and multiply charged HSCP simulations with a mass of 400 GeV and several different charges at $\sqrt{s}$ =8 TeV. 36

3.4 Drawings of expected cluster shapes in the strip detector for singly charged HSCPs (top), backgrounds from jets/nuclear interactions (middle), and multiply charged HSCPs (bottom). Energies deposited by multiply charged HSCPs are expected to be larger than the dynamic measurement range in the strips (253 ADC counts) resulting in saturation. 38

3.5 $\frac{\Delta E}{\Delta x}$ probability distribution function templates used by discriminators. The color scale displays the probability that a minimum ionizing particle traversing a pathlength shown in the X-axis will deposit charge equal to or less than

that shown in the Y-axis. Template for data is shown in left while that for simulation is shown in right [48]. 40

3.6 Distribution of I_{as} as a function of momentum for data (left) and simulation (right) [48]. 41

3.7 Sample drawing illustrating the effect of delayed arrival of slow particles within a DT superlayer. The blue line shows the trajectory of the particle. The initial reconstruction (assuming no delay) results in the reconstructed position (red points) for each hit that is farther from the DT center than its true position. Including the δ_t factor will move the reconstructed position back to align along the blue line. 43

3.8 Distributions of $1/\beta$ in DTs (left) and CSCs (right) for $\sqrt{s}$ =7 TeV data collected in early 2011 [52]. 46

3.9 Distributions of $1/\beta$ for singly charged HSCP simulations of different masses in DTs (left) and CSCs (right) at $\sqrt{s} = 8$ TeV. 46

4.1 Generator-level distributions of p_T (top left), β (top right), and η (bottom) for multiply charged HSCPs of different masses at $\sqrt{s} = 8$ TeV. 49

4.2 2-D generator-level distributions of η and β for multiply charged HSCPs of mass 100 GeV (left) and 400 GeV (right) at $\sqrt{s} = 8$ TeV. 50

4.3 Distributions of I_h (top), energy loss in ECAL (bottom left), and energy loss in HCAL (bottom right) for multiply charged HSCP simulations with mass of 400 GeV and different charges at $\sqrt{s} = 8$ TeV. 51

4.4 Reconstructed p_T as a function of generator-level p_T for multiply charged HSCP simulations with mass of 400 GeV and different charges. Reconstructed p_T is scaled by a factor of $1/Q$ relative to generator-level p_T. 52

4.5 2-D distribution of generator-level β and reconstructed β for 400 GeV multiply charged HSCPs of $Q = 2e$ (left) and $Q = 7e$ (right) at $\sqrt{s} = 8$ TeV. 52

4.6 Distributions of the number of primary vertices in data, SM MC, and multiply charged HSCP simulations before (left) and after reweighting (right) at $\sqrt{s} = 7$ (top) and 8 TeV (bottom). 54

4.7 Muon (top), E_T^{miss} (middle) and total (bottom) trigger efficiency for multiply charged HSCPs of various charges and masses at $\sqrt{s} = 7$ TeV (left) and $\sqrt{s} = 8$ TeV (right). 57

4.8 Generator-level distributions of β of multiply charged HSCPs for generated samples (black), and passing muon trigger (red), E_T^{miss} trigger (green), and combined trigger requirements (blue) at $\sqrt{s} = 7$ TeV. Different masses are shown in the three rows: 200 GeV (top), 500 GeV (middle), and 1000 GeV

(bottom) while various charges are shown in the three columns: $2e$ (left), $5e$ (middle), and $8e$ (right). 58

4.9 Generator-level distributions of β of multiply charged HSCPs for generated samples (black), and passing muon trigger (red), E_T^{miss} trigger (green), and combined trigger requirements (blue) at $\sqrt{s}$ = 8 TeV. Different masses are shown in the three rows: 200 GeV (top), 500 GeV (middle), and 1000 GeV (bottom) while various charges are shown in the three columns: $2e$ (left), $5e$ (middle), and $8e$ (right). 59

4.10 Distributions of number of pixel and strip hits in the inner tracker for data, SM MC, and multiply charged HSCP simulations for $\sqrt{s}$ =7 TeV (left) and $\sqrt{s}$ = 8 TeV (right). 62

4.11 Distributions of number of pixel hits in the inner tracker for data, SM MC, and multiply charged HSCP simulations for $\sqrt{s}$ =7 TeV (left) and $\sqrt{s}$ = 8 TeV (right). 62

4.12 Distributions of fraction of valid hits in inner tracker for data, SM MC, and multiply charged HSCP simulations for $\sqrt{s}$ =7 TeV (left) and $\sqrt{s}$ = 8 TeV (right). 63

4.13 Distributions of number of available $\frac{\Delta E}{\Delta x}$ measurements in the strip detectors for data, SM MC, and multiply charged HSCP simulations for $\sqrt{s}$ =7 TeV (left) and $\sqrt{s}$ = 8 TeV (right). 63

4.14 Distributions of number of $1/\beta$ measurements in the muon system for data, SM MC, and multiply charged HSCP simulations for $\sqrt{s}$ =7 TeV (left) and $\sqrt{s}$ = 8 TeV (right). 64

4.15 Distributions of quality for data, SM MC, and multiply charged HSCP simulations for $\sqrt{s}$ =7 TeV (left) and $\sqrt{s}$ = 8 TeV (right). 64

4.16 Distributions of χ^2 per degree of freedom for data, SM MC, and multiply charged HSCP simulations for $\sqrt{s}$ =7 TeV (left) and $\sqrt{s}$ = 8 TeV (right). . 65

4.17 Distributions of p_T for data, SM MC, and multiply charged HSCP simulations for $\sqrt{s}$ =7 TeV (left) and $\sqrt{s}$ = 8 TeV (right). 66

4.18 Distributions of I_h for data, SM MC, and multiply charged HSCP simulations for $\sqrt{s}$ =7 TeV (left) and $\sqrt{s}$ = 8 TeV (right). 66

4.19 Distributions of I_{as} for data, SM MC, and multiply charged HSCP simulations for $\sqrt{s}$ =7 TeV (left) and $\sqrt{s}$ = 8 TeV (right). 67

4.20 Distributions of $\sigma_{\langle 1/\beta \rangle}$ for data, SM MC, and multiply charged HSCP simulations for $\sqrt{s}$ =7 TeV (left) and $\sqrt{s}$ = 8 TeV (right). 67

4.21 Distributions of relative uncertainty in p_T for data, SM MC, and multiply charged HSCP simulations for $\sqrt{s}$ =7 TeV (left) and $\sqrt{s}$ = 8 TeV (right). . 68

4.22 Distributions of d_{xy} for data, SM MC, and multiply charged HSCP simulations for $\sqrt{s}$ =7 TeV (left) and $\sqrt{s}$ = 8 TeV (right). 69

4.23 Distributions of d_z for data, SM MC, and multiply charged HSCP simulations for $\sqrt{s}$ =7 TeV (left) and $\sqrt{s}$ = 8 TeV (right). 69

4.24 Distributions of calorimeter isolation for data, SM MC, and multiply charged HSCP simulations for $\sqrt{s}$ =7 TeV (left) and $\sqrt{s}$ = 8 TeV (right). SM MC for $\sqrt{s}$ = 8 TeV consists of only Drell-Yan $\rightarrow \mu\mu$ sample, resulting in data-SM MC discrepancy. 70

4.25 Distributions of tracker isolation for data, SM MC, and multiply charged HSCP simulations for $\sqrt{s}$ =7 TeV (left) and $\sqrt{s}$ = 8 TeV (right). SM MC for $\sqrt{s}$ = 8 TeV consists of only Drell-Yan $\rightarrow \mu\mu$ sample, resulting in data-SM MC discrepancy. 71

4.26 Distributions of $1/\beta$ for data, SM MC, and multiply charged HSCP simulations for $\sqrt{s}$ =7 TeV (left) and $\sqrt{s}$ = 8 TeV (right). 71

4.27 Generator-level distributions of β of multiply charged HSCPs for generated samples (black), passing online selection (blue), passing global muon selection (red), and passing offline selections (green). Distributions are shown for multiply charged HSCPs of mass 400 GeV and $Q = 2e$ (left) and $5e$ (right). 73

4.28 Distributions of $1/\beta$ in different I_h ranges for $\sqrt{s}$ =7 TeV (left) and 8 TeV (right) data. 77

4.29 Distributions of $1/\beta$ in different I_{as} ranges for $\sqrt{s}$ =7 TeV (left) and 8 TeV (right) data. 77

4.30 Illustration to explain ABCD background prediction method. 79

4.31 Distributions of candidates in I_h-$1/\beta$ plane for data (top) and multiply charged HSCP simulations with $Q = 2e$ and mass of 400 GeV (bottom). Left column is for $\sqrt{s}$ =7 TeV while right column shows $\sqrt{s}$ =8 TeV scenario. 80

4.32 Distributions of candidates in I_{as}-$1/\beta$ plane for data (top) and multiply charged HSCP simulations with $Q = 2e$ and mass of 400 GeV (bottom). Left column is for $\sqrt{s}$ =7 TeV while right column shows $\sqrt{s}$ =8 TeV scenario. 81

4.33 Number of predicted and observed candidates in region D along with their ratio for $\sqrt{s}$ =7 TeV (left) and 8 TeV (right) data. Uncertainty on the prediction includes both statistical and systematic (20%) contributions. 83

4.34 Number of predicted and observed candidates in region D' along with their ra-

tio for $\sqrt{s}$ =7 TeV (left) and 8 TeV (right) data. Uncertainty on the prediction includes both statistical and systematic (20%) contributions. 84

5.1 Multiple predictions for number of expected background candidates in region D for $\sqrt{s} = 7$ TeV data (top) and $\sqrt{s} = 8$ TeV data (bottom). I_{as} selections are shown in X-axis while $1/\beta$ selections are 1.10 (left) and 1.20 (right). . . 88

5.2 Variance of the multiple predictions (top), statistical uncertainty contribution to the variance (bottom left), and systematic uncertainty contribution to the variance (bottom right) for $\sqrt{s} = 7$ TeV data. 89

5.3 Variance of the multiple predictions (top), statistical uncertainty contribution to the variance (bottom left), and systematic uncertainty contribution to the variance (bottom right) for $\sqrt{s} = 8$ TeV data. 90

5.4 Distributions of I_{as} for protons in momentum range of 0.95–1.0 GeV (left) and 1.20–1.25 GeV (right). Distributions are shown for $\sqrt{s} = 7$ and 8 TeV data as well as simulation. The solid lines represent a Gaussian fit to the respective distributions. 93

5.5 Mean (left) and width (right) of fitted Gaussian for different proton momentum ranges. These are shown for $\sqrt{s} = 7$ and 8 TeV data as well as simulation. . 94

5.6 Signal acceptance ratios of material variated and normal samples after online (top left), offline (top right), and final selection (bottom) at $\sqrt{s} = 8$ TeV. . . 97

5.7 Total relative systematic uncertainty for multiply charged HSCPs at $\sqrt{s} =$ 7 TeV (left) and 8 TeV (right). For $Q = 8e$ and mass of 100 GeV, none of the HSCP candidates pass final selection for $\sqrt{s} = 7$ TeV, and hence the signal is not shown in the figure. 98

6.1 Distributions of I_{as} (left) and $1/\beta$ (right) after offline selections for data and multiply charged HSCP simulations of different charges and mass of 100 GeV (top), 400 GeV (middle), and 700 GeV (bottom) at $\sqrt{s} = 8$ TeV. 101

6.2 Ratios of expected cross section reaches using two sets of I_{as} and $1/\beta$ selections, namely (I_{as}, $1/\beta$)=(0.375, 1.275) and (0.500, 1.200) at $\sqrt{s} = 8$ TeV. Ratios of cross section reaches for 95% CL exclusion is shown in left while that for 5σ discovery is shown in right. 105

6.3 Theory and observed cross section limit curves for $\sqrt{s} = 7$ TeV (top left) and 8 TeV (top right). For combined 7 and 8 TeV results (bottom), observed limits on signal strength μ is shown. 111

6.4 Ratios of cross section reaches for common final selection of (I_{as}, $1/\beta$)=(0.5, 1.2) and optimization selection. Ratios of cross section reaches for 5σ discovery (top) and 95% CL exclusion (bottom) are shown for $\sqrt{s} = 7$ TeV (left) and $\sqrt{s} = 8$ TeV (right). 112

6.5 Summary of mass limits for multiply charged HSCPs from ATLAS [38], and CMS [51, 63] results using data collected during Run I of the LHC. 114

D.1 Individual systematic uncertainties due to various sources and their total for multiply charged HSCPs with $Q = 1e$ for $\sqrt{s}$ =7 TeV (left) and $\sqrt{s} = 8$ TeV (right). Error bar on total uncertainty represents the statistical uncertainty on signal acceptance. 141

D.2 Individual systematic uncertainties due to various sources and their total for multiply charged HSCPs with $Q = 2e$ for $\sqrt{s}$ =7 TeV (left) and $\sqrt{s} = 8$ TeV (right). Error bar on total uncertainty represents the statistical uncertainty on signal acceptance. 141

D.3 Individual systematic uncertainties due to various sources and their total for multiply charged HSCPs with $Q = 3e$ for $\sqrt{s}$ =7 TeV (left) and $\sqrt{s} = 8$ TeV (right). Error bar on total uncertainty represents the statistical uncertainty on signal acceptance. 142

D.4 Individual systematic uncertainties due to various sources and their total for multiply charged HSCPs with $Q = 4e$ for $\sqrt{s}$ =7 TeV (left) and $\sqrt{s} = 8$ TeV (right). Error bar on total uncertainty represents the statistical uncertainty on signal acceptance. 142

D.5 Individual systematic uncertainties due to various sources and their total for multiply charged HSCPs with $Q = 5e$ for $\sqrt{s}$ =7 TeV (left) and $\sqrt{s} = 8$ TeV (right). Error bar on total uncertainty represents the statistical uncertainty on signal acceptance. 143

D.6 Individual systematic uncertainties due to various sources and their total for multiply charged HSCPs with $Q = 6e$ for $\sqrt{s}$ =7 TeV (left) and $\sqrt{s} = 8$ TeV (right). Error bar on total uncertainty represents the statistical uncertainty on signal acceptance. 143

D.7 Individual systematic uncertainties due to various sources and their total for multiply charged HSCPs with $Q = 7e$ for $\sqrt{s}$ =7 TeV (left) and $\sqrt{s} = 8$ TeV (right). Error bar on total uncertainty represents the statistical uncertainty on signal acceptance. 144

D.8 Individual systematic uncertainties due to various sources and their total for multiply charged HSCPs with $Q = 8e$ for $\sqrt{s}$ =7 TeV (left) and $\sqrt{s} = 8$ TeV (right). Error bar on total uncertainty represents the statistical uncertainty on signal acceptance. 144

ABSTRACT

Several models of new physics yield particles that are massive, long-lived, and have an electric charge, Q, greater than that of the electron, e. A search for evidence of such particles was performed using 5.0 fb^{-1} and 18.8 fb^{-1} of proton-proton collision data collected at $\sqrt{s} = 7$ TeV and $\sqrt{s} = 8$ TeV, respectively, with the Compact Muon Solenoid detector at the Large Hadron Collider. The distinctive detector signatures of these particles are that they are slow-moving and highly ionizing. Ionization energy loss and time-of-flight measurements were made using the inner tracker and the muon system, respectively. The search is sensitive to $1e \leq |Q| \leq 8e$. Data were found to be consistent with standard model expectations and upper limits on the production cross section of these particles were computed using a Drell-Yan-like production model. Masses below 517, 687, 752, 791, 798, 778, 753, and 724 GeV are excluded for $|Q| = 1e$, $2e$, $3e$, $4e$, $5e$, $6e$, $7e$, and $8e$, respectively.

CHAPTER 1

INTRODUCTION

Humankind has been curious about the world around us since the earliest of times. The desire to understand the nature of their surroundings has led humans to study the matter around them. The field of particle physics continues this endeavor by framing the following two questions: What fundamental particles make up everything in our Universe? What are the fundamental interactions among these fundamental particles? The process of answering these two questions has advanced our understanding of matter and its interactions at smaller and smaller length scales. The standard model (SM) of particle physics that represents our current understanding of matter and its interactions is summarized in Sec. 1.1. Some of the phenomena not fully described by the SM are discussed in Sec. 1.2. In Sec. 1.3, some SM extensions that yield multiply charged Heavy Stable Charged Particles (the topic of research pursued in this dissertation) are briefly introduced. Section 1.4 describes how to identify multiply charged Heavy Stable Charged Particles in collider experiments. Lastly, Sec. 1.5 summarizes some of the previous searches of multiply charged Heavy Stable Charged Particles.

1.1 Standard Model of Particle Physics

All known fundamental particles have spin values of 0, 1/2, or 1. Particles with half-integer spins are referred to as fermions while those with integer spins are referred to as bosons. There are four kinds of known interactions among particles: strong, electromag-

Table 1.1: Particle content of the standard model.

Fermions					
Leptons			Quarks		
Particle type	Symbol	Electric charge	Particle type	Symbol	Electric charge
electron neutrino	ν_e	0	up	u	2/3
electron	e^-	-1	down	d	-1/3
muon neutrino	ν_μ	0	charm	c	2/3
muon	μ^-	-1	strange	s	-1/3
tau neutrino	ν_τ	0	top	t	2/3
tau	τ^-	-1	bottom	b	-1/3

Bosons		
Particle type	Symbol	Electric charge
gluon	g	0
photon	γ	0
$W^\pm$ boson	$W^\pm$	± 1
Z boson	Z	0
Higgs boson	H	0

netic, weak, and gravitational interactions.

The SM of particle physics encompasses all the known fundamental particles (Tab. 1.1) and three of the four known fundamental interactions: the strong, the electromagnetic, and the weak interactions. These interactions are described by the symmetry group of $SU(3) \times SU(2) \times U(1)$. Gravitational interactions are not described by the SM. The strength of the gravitational interactions is insignificant at the length/energy scales that are currently accessible.

All fermions are classified into three groups, referred to as generations. Each generation has four particles. Two particles in each generation have color charge (a quantum number) and are called quarks (q). The 6 quarks are up and down (u and d, 1st generation), charm and strange (c and s, 2nd generation), and top and bottom (t and b, 3rd generation). The color charge is the quantum number associated with strong interactions. Quarks can carry one of three colors. All quarks have electric charge (a quantum number), and thereby interact electromagnetically. All quarks also interact via the weak force.

The two particles in each generation devoid of color charge are leptons. Among the leptons, one particle in each generation has electric charge and interacts electromagnetically. These are the electron (e^-, 1st generation), the muon (μ^-, 2nd generation), and the tau (τ^-, 3rd generation). The other lepton in each generation is a neutrino, referred to as the electron neutrino (ν_e, 1st generation), the muon neutrino (ν_μ, 2nd generation), and the tau neutrino (ν_τ, 3rd generation). All leptons interact via the weak force.

Every particle has an antiparticle. For quarks and electrically charged leptons, antiparticles have equal and opposite quantum numbers as that of the particles. It is not yet clear whether antiparticles of neutrinos have equal and opposite or equal and same quantum numbers as that of the neutrinos.

Three quarks (each with a different color), three antiquarks (each with a different anticolor), or a quark and an antiquark (with a color and its anticolor) form a bound state resulting in a colorless particle. Isolated colored particles have not been observed. These bound states are referred to as baryons ($qqq/\bar{q}\bar{q}\bar{q}$) and mesons ($q\bar{q}$). Baryons and mesons are collectively called hadrons.

Among the quarks and the electrically charged leptons, particles in the first generation are the lightest and contribute to stable matter while the second and third generations consist of heavier particles that are unstable. The mass of the neutrino in each generation is tiny compared to any of the quarks and the electrically charged leptons. Decay of neutrinos have not been observed, however, neutrinos oscillate from one type to another (ν_e to ν_μ, ν_e to ν_τ, ν_μ to ν_τ, and vice-versa).

Fermions interact with each other via the exchange of spin-1 particles. Strong interactions among colored particles are mediated by the exchange of gluons (g). The gluon is massless and has color charge, but no electric charge. Due to the color charge, the gluon can interact with quarks and other gluons. Electrically charged particles interact electromagnetically via the exchange of a photon (γ). The photon is massless and does not have any electric/color charge. Weak interactions of all fermions are mediated by $W^\pm$ and Z bosons. Both electrically charged $W^\pm$ and electrically neutral Z bosons are massive, contributing

to the feebleness of the weak interactions.

The only spin-0 particle in the SM is the massive Higgs boson with no color/electric charge. The Higgs field disrupts the unified description of the electromagnetic and weak interactions and makes the $W^{\pm}$ and the Z bosons massive, while the photon remains massless [1–6]. As of now, it is the only SM particle yet to be fully confirmed. On 4th July 2012, both the A Toroidal LHC ApparatuS (ATLAS) and Compact Muon Solenoid (CMS) collaborations announced the observation of a new boson with a mass of ~ 126 GeV [7, 8]. The observed particle was consistent with the SM Higgs boson. Detailed studies of its interactions with other particles and its quantum properties are required to establish its true identity.

By March 2013, both collaborations had measured the decay of the boson into five channels: $\gamma\gamma$, ZZ, W^+W^-, $b\bar{b}$ and $\tau^+\tau^-$ [9, 10]. The observed decay rates are consistent with that expected from a SM Higgs boson. Also, a number of possible quantum properties of the boson were studied. Again, they agree with the SM prediction. However, the quantity of available data is not sufficient to study all of the relevant properties in full detail. This will be possible during the next run of the Large Hadron Collider (LHC) in 2015.

Over the past several decades, SM has been tested and confirmed by numerous experiments. The parameters in the SM have been constrained by combining data collected in several experiments [11]. The masses and widths of W and Z bosons, along with the mass of the top quark, agree within one standard deviation of the measurement uncertainty. This exercise helps confirm the SM to a higher degree of accuracy. Deviations from SM predictions can give hints of new phenomena and point to additional questions to be answered.

1.2 Shortcomings of the Standard Model

Despite the remarkable success of the SM, it does not explain several observed phenomena. These include matter-antimatter asymmetry, dark matter, and dark energy. Some of these phenomena are described in this section.

At the Big Bang, it is hypothesized that matter and antimatter were created in equal quantities. As the Universe expanded, matter and antimatter interacted and annihilated. However, the Universe today predominantly consists of matter. Thus, the early Universe, with equal quantities of matter and antimatter, evolved into one dominated by matter. This feature is referred to as matter-antimatter asymmetry. To account for this, the SM must include some difference between the interactions of matter and antimatter that yields the residual excees of matter. The invariance of physics under simultaneous parity inversion and charge conjugation (CP) requires matter and antimatter to be treated equally. While CP violation has been observed experimentally, the size of this violation is insufficient to explain the matter-antimatter assymetry observed in nature.

According to Newtonian dynamics, the angular velocities of stars in spiral galaxies around the galactic center should exhibit a $\frac{1}{\sqrt{r}}$ dependence beyond the core radius of the galaxy, where r is the radial distance from the center of the galaxy. However, the velocities are mesured to remain roughly constant in a region extending well beyond the majority of the visible mass [12]. These observations can be explained by positing the existence of matter with gravitational, but no electromagnetic interactions, hence, dark matter. However, to date, we do not know the nature of dark matter. One solution to the dark matter problem is the presence of a particle that does not interact strongly or electromagnetically but may have weak interactions. Neutrinos are the only SM particles with exclusively weak interactions. However, the number and mass of SM neutrinos is well below that required by the inferred dark matter density and necessitates phenomena beyond the SM.

The spectra of type Ia supernovae were measured as a function of their redshift in 1990s [13]. These measurements show that the expansion rate of the Universe is currently increasing. The source for the accelerating expansion of the Universe is unknown, and is termed dark energy. Presently, it is estimated that SM particles, dark matter, and dark energy constitute approximately 4%, 23%, and 73% of the matter-energy content of the Universe, respectively [14].

The electroweak scale ($\sim$ 100 GeV) and the vacuum expectation value of the Higgs field

($\sim$ 245 GeV) render the typical energy scale in the SM to be of the order of 10^2 GeV. The energy scale at which the strength of the gravitational interaction becomes comparable to the other SM interactions, also known as the Planck scale, is of order 10^{19} GeV. This large difference in the scales of the SM and gravitational forces is referred to as the hierarchy problem. There is no explanation for the hierarchy problem.

Higher-order corrections to the Higgs boson mass squared, m_H^2, involve an ultraviolet cutoff energy scale [15], above which new phenomena are expected to modify the interactions of the SM. If the scale beyond the electroweak scale is the Planck scale, this will yield corrections to m_H^2 of the order of 10^{30}. Stabilizing the Higgs mass to its expected/known value requires precise fine-tuning. In nature, this is usually the result of a symmetry; in this case as yet unexplained.

At the energies studied in the laboratory, the forces of the SM have different strengths. A simpler description of matter and its interactions can be envisioned where all the interactions are unified into one. This can happen at higher energy scales, which are yet to be studied. However, extrapolations of the current SM do not yield this feature [16].

The modern view is that the SM, with these unanswered questions, is a low-energy effective theory. It is expected to breakdown at some energy scale, where newer phenomena will gain promi- nence. At energies beyond this scale, the SM will need to be extended to explain observed phenomena. Numerous theories have been proposed to extend the SM. Some of them are mentioned in Sec. 1.3.

1.3 Beyond Standard Model Theories

Numerous extensions to the SM have been proposed. Supersymmetry (SUSY) is one such theory that invokes a symmetry between particles whose spins differ by 1/2 [15]. In SUSY, SM fields are extended to superfields with each superfield consisting of one fermion and one boson as dynamical degrees of freedom. Thus, for every SM particle, there is a superpartner whose spin differs by 1/2. No superpartners have been observed. Hence, if

SUSY is at all relevant, there must be a mass difference between the particles and their superpartners, implying that SUSY is a broken symmetry.

This symmetry between fermions and bosons helps stabilize the Higgs mass in a natural way [15]. There exists a relative minus sign between the fermionic and bosonic loop contributions that yields a mutual cancellation of the loop corrections to the Higgs mass. SUSY introduces a new quantum number, R-parity, defined as

$$\text{R-parity} = (-1)^{2S+3B+L}, \tag{1.1}$$

where S is the spin, B is the baryon number, and L is the lepton number. R-parity for SM particles is $+1$, and -1 for their superpartners. If R-parity is a conserved quantum number the lightest supersymmetric particle (LSP) will be stable. The LSP is then a dark matter candidate. SUSY also unifies the strong, weak, and electromagnetic forces at very high energies [16].

The Minimal Supersymmetric Standard Model (MSSM) is the simplest supersymmetric extension of the SM. It is constructed using only complementary fields of the existing SM fields [16]. Accomodating all possible SUSY-breaking interactions requires of the order of 100 free parameters. It is not practical to explore this parameter space in its entirety. More practical SUSY models and searches are implemented by collapsing the parameters to a few. For example, Gauge Mediated Supersymmetry Breaking (GMSB) [17] is a sub-model of the MSSM, where SUSY breaking is realized by a gauge interaction through messenger gauge fields. Minimal versions of the GMSB model can be constructed with 5 parameters [18].

Several extensions of the SM yield a massive particle that lives long enough to traverse the entire detector without decaying and undergoing electromagnetic and/or strong interactions with matter [19]. Motivation for such particles can be understood from observed SM phenomena. The decay of electron and proton have not been observed. Stability of the electron can be understood in terms of conservation of electric charge while that of the proton can be understood in terms of conservation of baryon number and lepton number. The

lifetimes of the muon and the neutron are much longer than other unstable SM particles. The muon is long-lived due to the large difference between the masses of the muon and the W-boson. In the case of the neutron, the combination of the weakness of the interaction responsible for its decay and the small difference in the masses of the proton and the neutron result in its long lifetime. Thus, in the SM, conserved quantum numbers yield stable particles and constrained decays result in long-lived particles. Several extensions of the SM give rise to scenarios of a conserved or almost conserved quantum number resulting in stable or long-lived particles. In the CMS collaboration, such massive, long-lived particles with electric charge are referred to as Heavy Stable Charged Particles (HSCPs).

The electric charge, Q, of HSCPs can vary. They can have a fractional electric charge ($|Q| < e$), unit electric charge ($|Q| = 1e$), or multiple electric charge ($|Q| > 1e$), where e is the electric charge of the electron, and are referred to as fractionally charged, singly charged, and multiply charged HSCPs, respectively. Such states could be produced at high energy collider experiments. This dissertation is focused on the search for multiply charged HSCPs. Some of the theories [20–22] yielding such states are discussed in the next few paragraphs.

All SUSY extensions can, in general, yield bound states [23]. These states can be built of supersymmetric quarks, supersymmetric leptons, and the Higgs scalars, resulting in a large variety of baryonic and leptonic balls, referred to as Q-balls [24, 25]. In the early Universe, Q-balls could have been created in abundance in a variety of ways. Production of Q-balls through phase transitions and fusion (similar to Big Bang Nucleosynthesis) have been studied [26–30]. During a phase transition in the early Universe, Q-balls can be created by the aggregation of net charge in a region. Statistical fluctuations can result in large concentrations of charge and is the leading source of charge fluctuations [26]. Cosmic evolution of Q-balls and their relevance to the energy density of the Universe has been studied. Depending on their charge, mass, and the timing of the formation of large Q-ball clusters, they can survive evaporation and remain free particles until today [27]. The smallest Q-balls, consisting of fewer particles, could be observed traversing a suitable detector over

several meters.

Theories involving geometries that are almost-commutative [31] yield the SM of particle physics and additionally two new fermions with electromagnetic charges [32]. These fermions are referred to as AC-fermions/AC-leptons and carry electric charges of $+2e$ and $-2e$, respectively. These new particles have their own lepton flavor number. However, there are no similar extensions to the existing quark families in the SM. The framework allows a new $U(1)$ ($U_{AC}(1)$) interaction among the AC-leptons [21], resulting in an attractive force between them. Dark matter could be a bound state of fundamental and, or, composite charged particles, and AC-leptons fit into this scenario.

One of the possible solutions to the hierarchy problem (Sec. 1.2) centers on the hypothesis that there is only one fundamental scale, the weak scale. This is achieved via the introduction of new spatial dimensions [33]. Here, n additional compact spatial dimensions of radius $\sim R$ are added to the traditional spatial and time dimensions. For distances smaller than R, the strength of the gravitational interaction will be in accordance with $(4+n)$ dimensions, while for distances much larger than R, the inverse square law will hold true. The parameters n and R can be adjusted to match the strength of the gravitational interaction to the strength of the other forces in the SM.

New compact spatial dimensions can result in the production of small black holes in present-day high energy colliders [34]. These black holes can quickly decay into several energetic SM particles or leave behind a remnant [22]. Charged remnants would move through our detector mimicing a multiply charged HSCP.

Rather than following a specific theoretical prediction, one can explore beyond the SM particle physics by studying the expected SM experimental signatures and investigating deviations from it. New phenomena can manifest themselves in numerous ways and we should not be limited to the theoretical guidelines. In addition, most signatures can be interpreted in the context of several extensions to the SM, constraining a wide variety of proposed models. Thus, precision measurements of SM experimental observables are complementary to new phenomena searches based on theoretical intuition.

1.4 Search for Multiply Charged HSCPs in High Energy Colliders

As introduced in Sec. 1.3, a multiply charged HSCP is a massive, long-lived particle that has electric charge. The term massive refers to the fact that these particles must be massive enough not to have been detected in previous high energy collider experiments (typically mass greater than 100 GeV). Constraints from Big Bang Nucleosynthesis and experimental observations require any new multiply charged HSCPs to be unstable. However, they could have a measurable lifetime due to constrained decays, such as small couplings or restricted decay phase space. A lifetime of $\sim$ 5 ns will allow these particles to travel a few tens of meters, the typical size of collider detectors. Thus, from the point of view of searches in collider experiments, multiply charged HSCPs are stable particles. The electric charge results in electromagnetic interactions with other charged particles in the material medium. The magnitude of the electric charge can be equal to or larger than that of the electron. This dissertation searches for multiply charged HSCPs with primarily electromagnetic interactions. Several extensions to the SM predict these particles in the form of Q-balls, AC-leptons, etc. (Sec. 1.3).

Depending on the production cross section, multiply charged HSCPs could be produced at high-energy colliders. For high mass HSCPs, a significant fraction will be produced with non-relativistic kinetic energies as shown in Fig. 1.1. Multiply charged HSCPs will interact electromagnetically and experience enhanced ionization energy loss due to the larger electric charge. The loss of kinetic energy via ionization along their path serves to slow them down.

The quantum mechanical expression for the average electromagnetic energy loss per pathlength of a charged particle traveling in a medium is described by the Bethe-Bloch formula [35],

$$-\left\langle \frac{dE}{dx} \right\rangle = 4\pi N_A r_e^2 m_e c^2 z^2 \frac{Z}{A} \frac{1}{\beta^2} \left[\frac{1}{2} ln \frac{2 m_e c^2 \beta^2 \gamma^2 T_{max}}{I^2} - \beta^2 - \frac{\delta(\beta\gamma)}{2} \right] \times Q^2, \qquad (1.2)$$

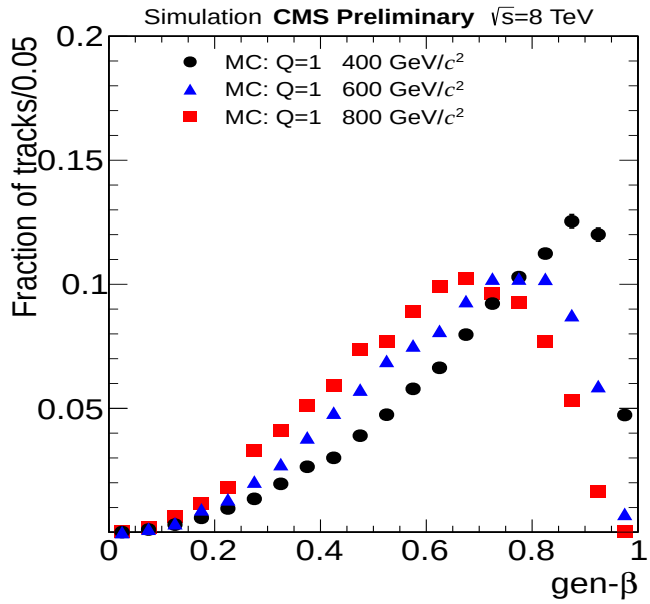

Figure 1.1: Distributions of generator-level β ($=v/c$) for HSCPs of various masses at 8 TeV center-of-mass energy in the Drell-Yan-like model (Sec. 4.1).

where N_A is Avogadro's number, m_e is the mass of the electron, r_e is the classical electron radius, z is the electric charge of the particle in units of e, $\beta = \frac{v}{c}$ where v and c are the speed of the particle in the medium and speed of light in vacuum, respectively, $\gamma = \frac{1}{\sqrt{1-\beta^2}}$, Z and A are the atomic number and atomic mass of the absorber respectively, T_{max} is the maximum kinetic energy that can be imparted to a free electron in a single collision, I is the mean excitation potential, $\delta(\beta\gamma)$ represents the density effect correction to ionization energy loss, and Q is the electric charge of the particle.

As shown in Eq. 1.2, the ionization energy loss of a particle in a given medium depends on its β and charge. The dependency of the energy loss per pathlength on β for a $Q = 1e$ particle (positive muons) in a copper medium is shown in Fig. 1.2 [35]. The qualitative nature of the curve is very general (up to small corrections) for the electromagnetic energy loss of any $Q = 1e$ particle passing through any material. As the particle speed becomes relativistic ($\beta\gamma \sim 2$), the energy loss reaches its minimum value. Beyond this energy loss remains fairly constant, until radiative effects become prominent. In the non-relativistic

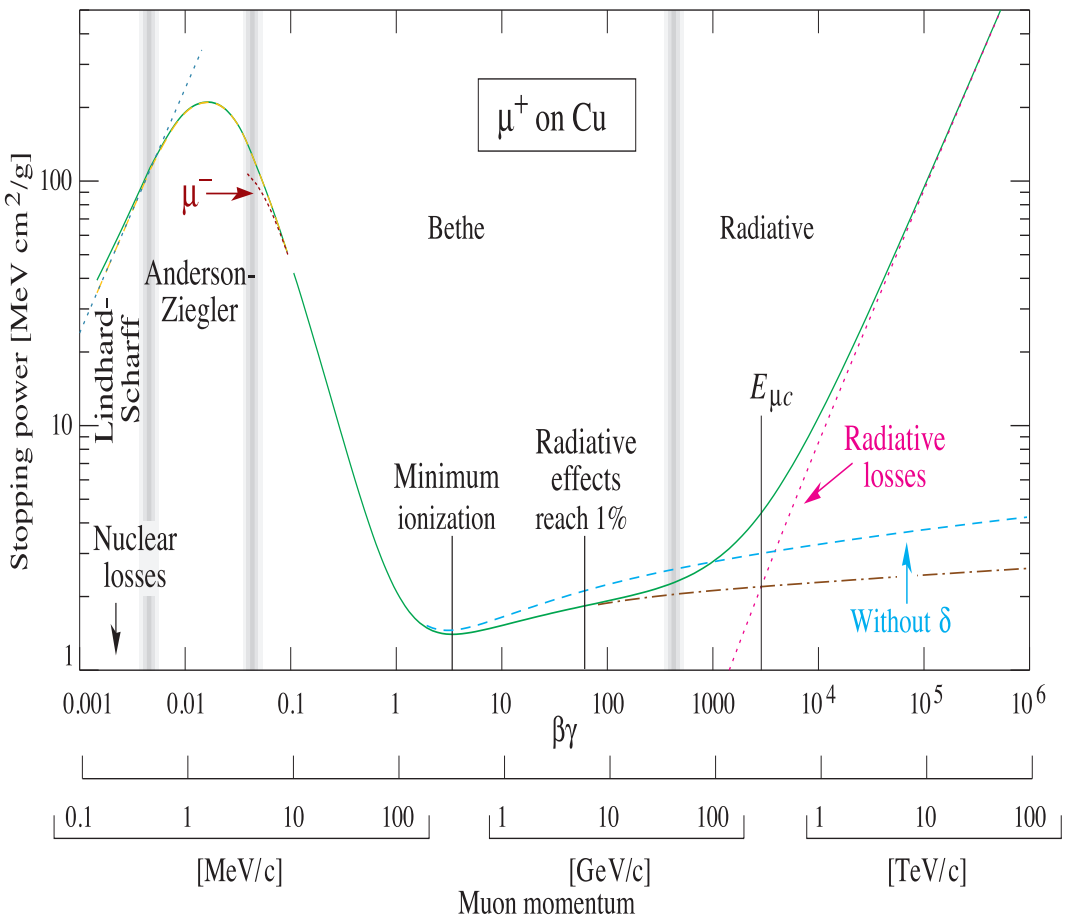

Figure 1.2: Bethe-Bloch curve showing the ionization energy loss per pathlength of positive muons in copper medium [35].

kinematic region, the energy loss of the particle increases for lower speeds with a $\sim \frac{1}{\beta^2}$ dependence. At much lower speeds ($\beta\gamma \sim 0.1$), other effects become prominent. The energy loss also has a Q^2 dependence on the electric charge of the particle.

Ionization energy loss and time-of-flight are the primary signatures used to identify multiply charged HSCPs in high energy collider detectors. The low velocity and higher charge results in large energy loss for these particles traversing a detector. SM particles will be produced with relativistic speeds (except for the lowest momentum particles) while HSCPs will often be non-relativistic. Therefore, HSCPs will tend to have higher ionization energy loss compared to SM particles. Even multiply charged HSCPs produced at relativistic speeds

will have energy loss that is Q^2 times larger than SM particles.

This dissertation describes the search for multiply charged HSCPs in data collected with the CMS detector at the LHC, at the European Organization for Nuclear Research (CERN). The detector is capable of measuring energy deposition at various points along the path of a charged particle as well as the timing for charged particles that reach the outermost parts of the detector. The LHC machine and the CMS detector will be discussed in more detail in Ch. 2. Monte Carlo (MC) samples of multiply charged HSCPs produced via the Drell-Yan-like mechanism are used. Details of the signal model are in Sec. 4.1. Distributions of ionization energy loss and time-of-flight of these particles are shown in Ch. 3.

Collisions in high energy colliders typically occur every few tens of ns. Slow moving particles, such as HSCPs, can continue to travel through the detector for much longer time periods. This can result in the failure to meet trigger timing requirements and the rejection of the event. It is also possible that slow moving particles can trigger during subsequent collisions and fail to be properly reconstructed. Thus, there are restrictions on the lower end of the β-spectrum of slow particles, whereby the events can not be properly recorded.

1.5 Other Experimental Searches

Several searches for multiply charged HSCPs have been performed previously [36–38]. A search for massive, long-lived particles with $Q = 1e$, $4/3e$, and $5/3e$ was done using data collected with the OPAL detector at the Large Electron Positron (LEP) collider [36]. LEP studied electron-positron collisions at several different center-of-mass energies ($\sqrt{s}$). The data analyzed were collected at center-of-mass energies from 130 to 209 GeV with a total integrated luminosity of 693.1 pb^{-1}. The search used energy loss measurements and was sensitive to particle lifetimes longer than 1000 ns. No evidence for the production of such particles was found and model-independent 95% CL upper limits on the production cross sections were placed. The limits range from 0.005–0.028 pb for scalar and spin-1/2 particles with $Q = \pm 1e$. These were interpreted in the context of the Constrained Minimal

Supersymmetric Standard Model as lower limits of 98 (98.5) GeV on the mass of long-lived right (left)- handed scalar muons and scalar taus [36]. For particles with $Q = 4/3e$, and $5/3e$, the cross section limits vary from 0.005–0.020 pb.

The ATLAS collaboration performed a search for multiply charged particles using 3.1 pb^{-1} of proton-proton collision data collected at 7 TeV center-of-mass energy in the early 2010 run of the LHC [37]. Drell-Yan-like production was assumed as a signal model. Distributions of energy loss and lateral shape of the energy loss were used to identify these particles. Trigger and offline selections restricted the range of sensitivity to $Q = 6e$–$17e$, masses of 200–1000 GeV, and lifetimes greater than 100 ns. No evidence of such particles was found and 95% CL upper limits on their production cross sections were set, ranging from 1–12 pb.

The ATLAS collaboration has also performed a search for multiply charged HSCPs with $Q = 2e$–$6e$ using 4.4 fb^{-1} of proton-proton collision data collected at 7 TeV center-of-mass energy [38]. As before, a Drell-Yan-like production of these particles was assumed. Incompatibility of the measured energy losses with that expected from SM particles was used to search for these particles. No evidence of multiply charged HSCPs was found and 95% CL mass limits were placed for the various charges. The lower mass limit was set at 50 GeV for all charges, while the upper mass limits were set at 430, 480, 490, 470, and 420 GeV for $Q = 2e$, $3e$, $4e$, $5e$, and $6e$, respectively.

CHAPTER 2

EXPERIMENT: COLLIDER AND DETECTOR

Experiments in particle physics involve the study of the interaction of two or more particles. In collider experiments, particles are accelerated to high energy and forced to collide, and thereby, interact with each other. The interaction point is surrounded with a suitable detector to capture the aftermath of the collision, specifically, to track the outgoing particles and measure their properties such as energy, and momentum. Information gathered by the detector is then used to infer the nature of the interaction between the colliding particles. This chapter introduces the experimental setup used in the research described in this dissertation.

2.1 Large Hadron Collider

The LHC at CERN is a proton-proton collider designed to operate at a nominal energy of 7 TeV for each proton beam. The design luminosity of the LHC is $\mathcal{L} = 10^{34}$ cm^{-2}s^{-1}, resulting in $\sim 10^9$ proton-proton interactions per second. The LHC is ~ 27 km in circumference and is housed in a tunnel 50 to 175 meters underground on the border of France and Switzerland. The LHC also has a heavy-ion physics program in which the collision of high-energy lead nuclei are studied.

CERN is host to a number of accelerators including the LHC as shown in Fig. 2.1 [39]. Protons are boosted in several smaller accelerators, and then injected into the LHC. An electric field is applied to hydrogen gas to separate the protons and electrons. The protons

are sent to a linear accelerator, Linac 2, which accelerates them to 50 MeV. The protons are further accelerated in several circular accelerators: the Proton Synchrotron Booster (PSB), the Proton Synchotron (PS), and the Super Proton Synchotron (SPS) which accelerate the protons to 1.4 GeV, 25 GeV, and 450 GeV, respectively. During acceleration, the protons are grouped into bunches. Finally, the protons are channelled into the two beam pipes of the LHC where they circulate in opposite directions. The LHC accelerates both proton beams to the desired energy. The nominal energy of each proton beam is 7 TeV and the nominal number of bunches in the LHC is 2808 with each bunch containing $\sim 10^{11}$ protons. The nominal spacing between successive proton bunches is 25 ns.

The schematic layout of the LHC is shown in Fig. 2.2 [40]. The LHC consists of 8 arcs in which the two beam pipes are placed. Detectors are housed at four locations along the LHC where the two beam pipes are made to intersect with one another. The LHC uses superconducting magnets to maneuver the beams. In all, 1232 dipole magnets are used to keep the beams circulating in the beam pipes while 392 quadrupole magnets focus the beam. The magnets are bathed in liquid helium maintained at 1.9 K to preserve their superconductivity. More engineering details of the LHC can be found in [40].

There are 4 detectors placed along the LHC tunnel, namely, ATLAS [41], CMS [42], A Large Ion Collider Experiment (ALICE) [43], and Large Hadron Collider beauty (LHCb) [44]. These detectors are centered on the points where the proton beams cross and interact with each other. ATLAS and CMS are general purpose detectors that study a wide range of physics such as the search for the Higgs boson, the search for new phenomena that might appear at the TeV scale, and the study of strong interactions of heavy nuclei. ALICE and LHCb are specialized detectors focusing on specific phenomena. ALICE is a dedicated heavy-ion detector designed to study the strong interactions of heavy nuclei. LHCb is designed to study the decay of B hadrons (particles containing b and $\bar{b}$) and quantify their differences. Improved precision in the rare decays of B hadrons can reveal new sources of matter-antimatter asymmetry. The ATLAS, ALICE, CMS, and LHCb detectors are placed at Points 1, 2, 5, and 8 of the LHC tunnel respectively (Fig. 2.2). This dissertation re-

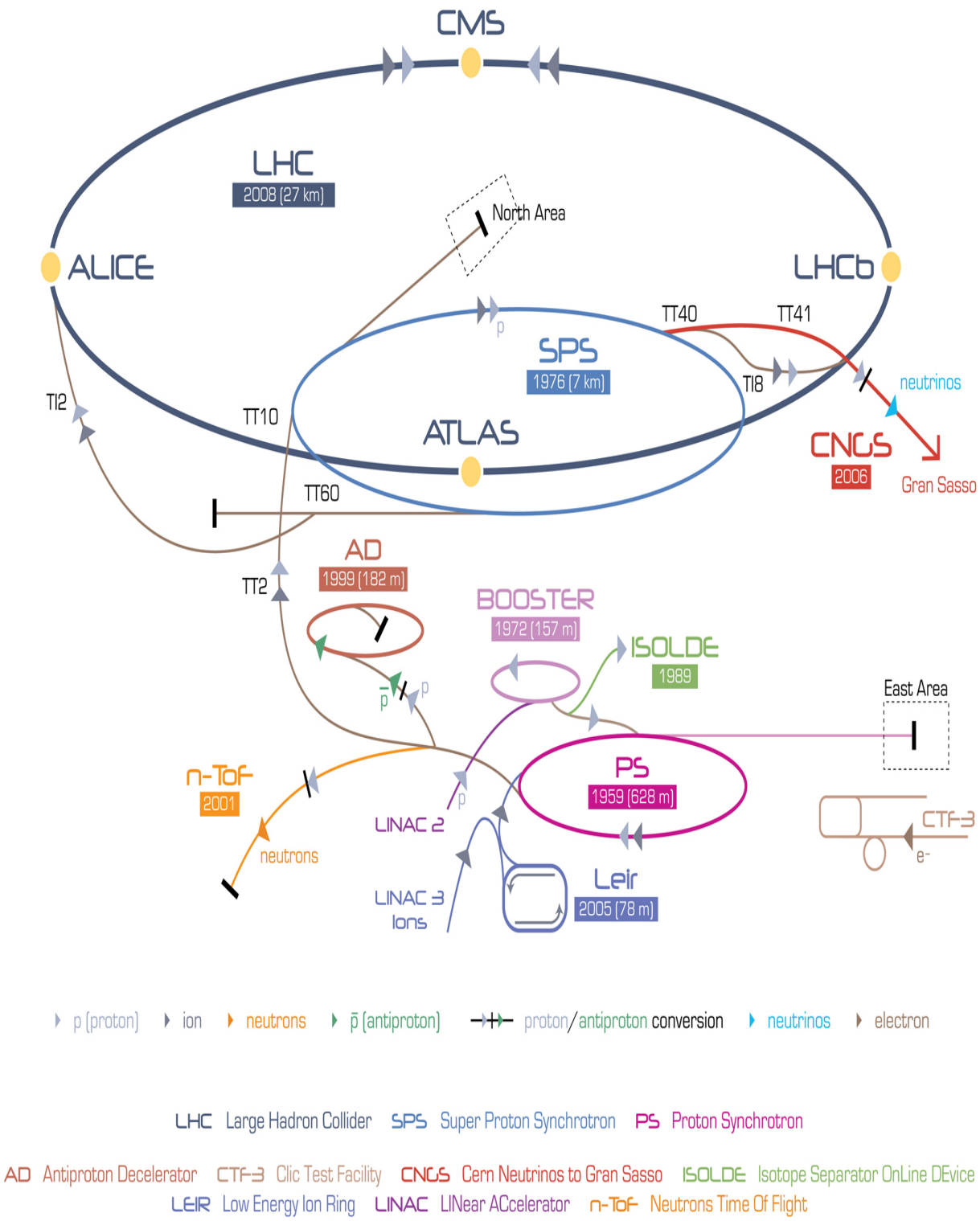

Figure 2.1: Accelerator complex at CERN [39].

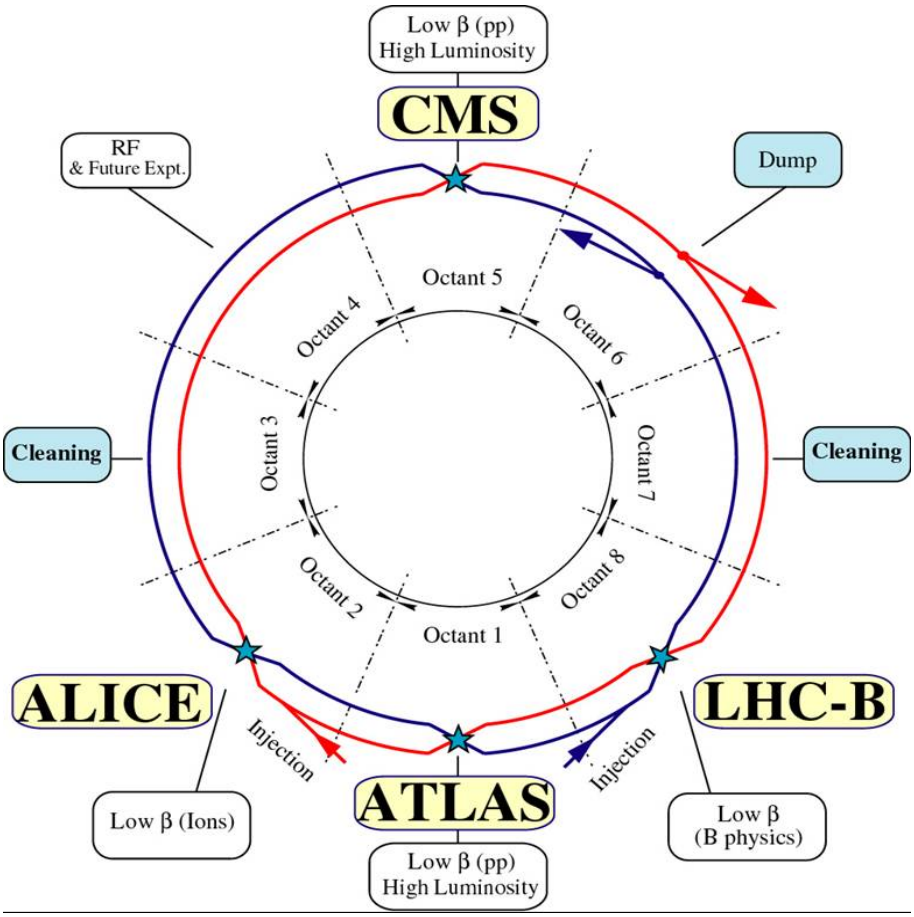

Figure 2.2: Schematic layout of the LHC [40].

ports on the search for multiply charged HSCPs in data collected with the CMS detector in proton-proton collisions during 2011 and 2012. The CMS detector is described in Sec. 2.2.

The LHC began operations on 10th September 2008 by circulating protons in both beam pipes. On 19th September, an electrical failure resulted in the damage of several magnets. This event delayed the operation of the LHC by more than a year. To keep the current in the superconducting magnets within a reliable threshold, it was decided to accelerate the proton beams only to 3.5 TeV, resulting in a center-of-mass energy of 7 TeV. The LHC resumed operations in November 2009. On 23rd November, proton beams were circulating in both beam pipes at the injection energy of 450 GeV and made to collide with one another at the location of the 4 detectors. A week later, on November 30th, the LHC accelerated both proton beams to 1.18 TeV resulting in collisions at a center-of-mass energy of 2.36 TeV. Thus, the LHC became the world's highest energy particle accelerator surpassing the previous highest value of 0.98 TeV per beam, which was achieved by the Tevatron collider.

The LHC resumed its operations in March 2010. On 19th March, both proton beams in the LHC were accelerated to 3.5 TeV. The 3.5 TeV proton beams were brought into collisions at a center-of-mass energy of 7 TeV on 30th March. Proton collisions at the LHC continued until early November. This was followed by the LHC's heavy ion program for one month in which lead ions were brought into collision at a center-of-mass energy of 2.76 TeV per nucleon pair. In March 2011, proton collisions at 7 TeV center-of-mass energy resumed. These were followed by heavy ion collisions at the end of the year. In 2012, the energy of the proton beams was increased resulting in collisions at a center-of-mass energy of 8 TeV. The slight rise in the energy of the beams is within the safety limit of operation and increases the sensitivity of the LHC to new phenomena at the TeV scale. Proton collisions at 8 TeV center-of-mass energy began on 5th April 2012 and continued until the end of the year. A one-month period of heavy ion collisions in early 2013 concluded the Run I era of the LHC operations. The spacing between adjacent proton bunches during the 2011 and 2012 proton-proton collision runs was 50 ns.

The event rate at the LHC is given by

$$N_{event} = \mathcal{L}\sigma_{event}, \tag{2.1}$$

where σ_{event} ($\sim$ 100 mbarn) is the total proton-proton cross-section, and $\mathcal{L}$ is the instantaneous luminosity given by

$$\mathcal{L} = \frac{\gamma f k_B N_P^2}{4\pi\epsilon_n\beta^\star}F, \tag{2.2}$$

where γ is the Lorentz factor, f is the revolution frequency ($\sim$ 11.25 kHz), k_B is the number of bunches, N_P is the number of protons in each bunch, ϵ_n is the normalized transverse emittance (with a design value of 3.75 μm), $\beta^\star$ is the betatron function at the interaction point, and F is the reduction factor due to the crossing angle [40]. The values of the beam parameters evolved during the course of the Run I operations of the LHC. Consequently, the luminosity per time period of collisions increased (Fig. 2.3, [45]). The total integrated luminosity of proton-proton collisions at the interaction point of the CMS detector during 2010, 2011, and 2012 were 44.2 pb^{-1}, 6.1 fb^{-1}, and 23.3 fb^{-1}, respectively.

2.2 Compact Muon Solenoid Detector

The main goals of the LHC program are the search for, and study of, the Higgs boson and to explore particle physics at the TeV scale. To accomplish the physics goals of the LHC program, the CMS detector has been designed with good particle identification, good momentum and energy resolution over a wide range of momenta and angles, and good reconstruction efficiency [42]. The large amount of data corresponding to $\sim 10^9$ inelastic proton-proton collisions occuring every second at the CMS detector can not be stored entirely. During the 2011 and 2012 proton-proton collisions, the CMS trigger and read-out systems recorded $300 - 600$ events every second for subsequent analysis (see Sec. 2.2.8 for a brief outline of the decision-making process of the CMS trigger system). An average of $\sim$ 8 and $\sim$ 15 interactions per bunch crossing (pile-up) were observed at the CMS

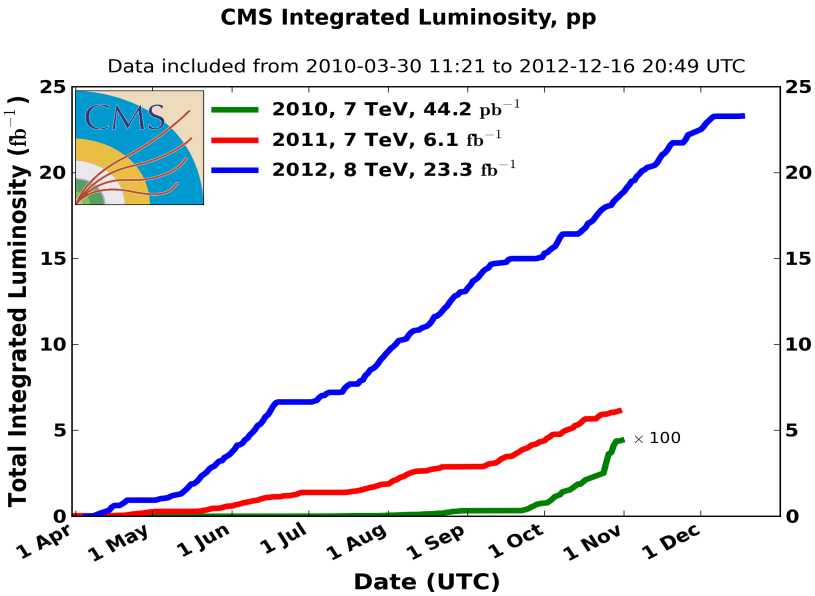

Figure 2.3: Cumulative luminosity as a function of day of the year delivered to CMS during stable beams for proton-proton collisions in 2010, 2011, and 2012 [45].

detector during the 2011 and 2012 proton-proton collisions, respectively. Granularity and time resolution of the CMS detector have been designed to mitigate the effects of pile-up.

Figure 2.4 shows a partially assembled CMS detector [46]. The CMS detector is 21.6 m long, has a diameter of 14.6 m, and weighs 12500 tons. Compared to the ATLAS detector (44 m long, 25 m diameter, and 7000 tons mass), the CMS detector is much smaller but has a larger weight. A 3.8 Tesla superconducting solenoid provides a sufficiently large bending power to measure the momentum of highly energetic muons. Geographically, CMS is located 100 m underground at Point 5 of the LHC tunnel near the French village of Cessy.

2.2.1 Coordinate System

In the CMS coordinate system, the origin is located at the geometric center of the detector (also the nominal collision point). The x-axis points radially inward toward the center of the LHC, the y-axis is vertically upwards, and the z-axis points along the beam direction as per the right-hand rule. The polar angle θ is measured from the z-axis and the

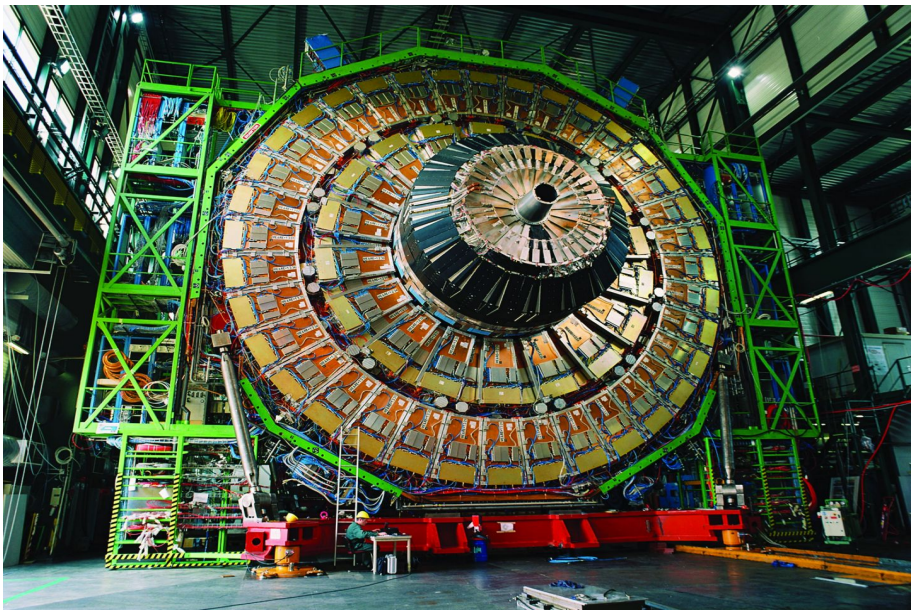

Figure 2.4: Partially assembled CMS detector [46].

azimuthal angle ϕ is measured from the x-axis in the x-y (transverse) plane. Pseudorapidity, defined as $\eta = -\ln \tan(\theta/2)$, is a Lorentz invariant quantity and is therefore preferred for collider experiments. Transverse momentum, p_T, is the component of momentum in the transverse plane. Similarly, transverse energy, E_T, is defined as $E_T = E \sin(\theta)$ where E is the energy deposited by the particle in the calorimeters (see Sec. 2.2.2 for description of the calorimeters). The variables p_T, E_T, η, and ϕ can be used to give the complete kinematical description of particles traversing the CMS detector. The vector momentum imbalance in the transverse plane is calculated as the negative of the vector sum of the transverse momentum of all objects reconstructed within an event. The vector momentum imbalance is referred to as missing transverse momentum, $\vec{E}_T^{miss}$, and its magnitude is referred to as missing transverse energy, E_T^{miss}.

2.2.2 Layout

The CMS detector is made of cylindrical layers of subdetectors, a schematic of which is shown in Fig. 2.5 [47]. From the inside out, the CMS detector is composed of the in-

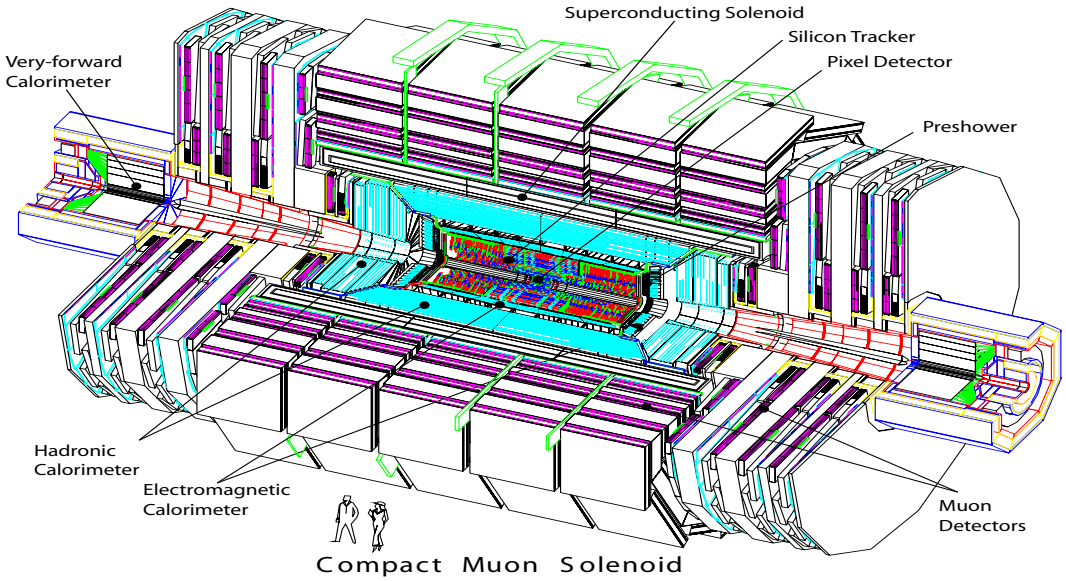

Figure 2.5: Schematic layout of CMS detector [47].

ner tracker, the electromagnetic calorimeter, the hadronic calorimeter, the superconducting solenoid, and the muon detectors. The superconducting solenoid maintains a constant 3.8 Tesla magnetic field within the volume that includes the inner tracker, the electromagnetic calorimeter, and the hadronic calorimeter. The muon detector has layers of iron that shape the magnetic field within the muon detectors. The inner tracker is made of silicon pixel and strip detectors that record the trajectories of charged particles. Charged particles bend in the magnetic field, and the direction of bend reveals the sign of the electric charge of the particle. The radius of curvature can be used to infer p_T/Q of charged particles. Thus, the transverse momentum of charged particles is measured within the ambiguity of the magnitude of the electric charge of the particle. The calorimeters are made of dense material that results in electrons, photons, and hadrons depositing most/all of their energy within the calorimeters. The electromagnetic calorimeter measures the energy of electrons, positrons, and photons while the hadronic calorimeter (in combination with the electromagnetic calorimeter) measures the energy of hadrons. Most muons act as minimum ionizing

particles and can traverse the CMS detector and escape to the outside. The muon system measures the position and momentum of particles that reach the outer layers (primarily muons and possibly HSCPs). Neutrinos have very low interaction cross section with the detector material and go undetected, giving rise to E_T^{miss}.

2.2.3 Inner Tracking System

The inner tracking system lies closest to the nominal interaction point of the CMS detector. To withstand the conditions expected at the LHC such as the large flux of particles, close bunch spacing, and radiation damage, the CMS tracking system is designed with silicon detector technology to have high granularity, fast response, and efficient cooling. Position measurements in the inner tracker are used to reconstruct the trajectories of charged particles and thereby determine their momenta. These position measurements also contribute to the precise reconstruction of primary and secondary vertices. In addition to position measurements, the inner tracker records the energy loss of charged particles within the silicon. The energy loss per pathlength is a key variable in the search for multiply charged HSCPs. The inner tracker is made of pixel and strip detectors, its schematic layout is shown in Fig. 2.6 [42]. The inner tracker region has a length of 5.8 m and a diameter of 2.5 m. The geometric acceptance of the inner tracking system covers $|\eta| < 2.5$.

The pixel detector has three cylindrical layers in the barrel region at radii of 4.4, 7.3, and 10.2 cm and two disks in each of the endcap regions. The pixel detector records the 3-D positions of charged particles passing through each layer/disk. The size of the pixel cells is 100×150 μm^2 resulting in a spatial resolution of $15 - 20$ μm. In all, there are 1440 pixel detector modules containing 66×10^6 pixels.

The strip detector occupies the radial region between 20 cm and 116 cm and is composed of three different subsystems: the Tracker Inner Barrel (TIB) and Disks (TID), the Tracker Outer Barrel (TOB), and the Tracker EndCaps (TEC). Strips are placed parallel to the beam axis in the barrel (forming a cylindrical layer) and radial in the endcaps (in the form of a disk). The strip detector records the 2-D positions of charged particles passing through

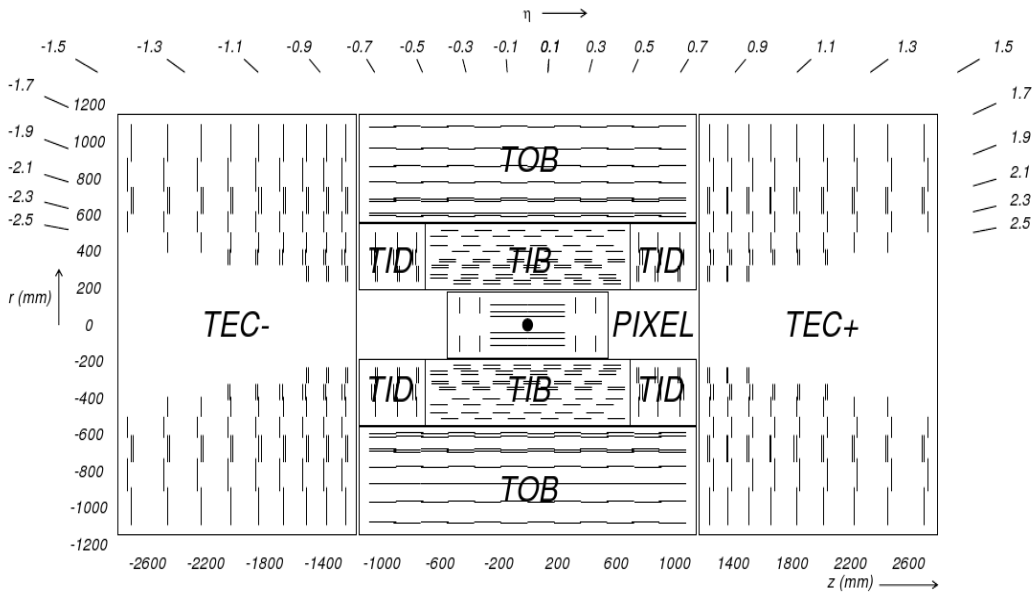

Figure 2.6: Schematic layout of CMS inner tracker [42].

each layer/disk (r-ϕ in the barrel and z-ϕ in the endcaps). Energy loss measurements in the strip detectors is used in the search for multiply charged HSCPs. In total, there are 15148 strip detectors containing 9.3×10^6 strips.

The TIB/TID surrounds the pixel detectors, which in turn is enveloped by the TOB in the barrel and by the TEC in the endcaps. Details of the location of the various subsystems and the number of layers/disks are listed in Tab. 2.1. Strips in each disk of the TEC are arranged in the form of 7 concentric rings. For increasing r and z, the flux of particles traversing the CMS detector decreases. Consequently, a reduced strip granularity is used as one moves outward from the interaction point. The strip pitch in the various layers and disks are listed in Tab. 2.1. Combining information from various layers results in smaller single point resolution. The area covered by the strips increases with r. To limit the number of read-out channels that are required to cover the larger area, an increased strip length is used. The capacitance of the strip sensor contributes to noise and scales with the length of the sensor. In order to have good signal to noise ratio, thicker silicon sensors (corresponding

Table 2.1: Specifications of the silicon strip detector sub systems.

Subsystem	Position in r (cm)	Position in $\|z\|$ (cm)	# of layers/disks	Length (mm)	Thickness (μm)	Pitch (μm)
TIB	$20-55$	<70	4	117	320	$80, 120$
TID	$20-55$	$70-110$	3	85	320	$97-141$
TOB	$60-110$	<109	6	183	500	$122, 183$
TEC	$22-114$	$124-282$	9	$85-202$	$320, 500$	$97-184$

to higher signal) are used in the outer layers. Table 2.1 lists the length and thickness values of the strip sensors in the various layers/disks of all the subsystems.

A charged particle traversing the strip detector will ionize the silicon medium resulting in electron-hole pairs. The charge is collected using an electric field and processed by the read-out electronics into ADC counts. The 8-bit ADC limits the dynamic range of energy loss measurements to $0-255$ ADC counts. The intrinsic noise in the strip detector has an amplitude of $4.5-8.5$ ADC counts depending on the strip thickness, topology, etc. A minimum ionizing particle has an energy loss of 3 MeV/cm along its path, and corresponds to 300 ADC/mm. The bits corresponding to 254 and 255 ADC counts are used to register energy losses in the range of [254, 1024] and greater than 1024 ADC counts, respectively. Therefore, the dynamic measurement range ends at ~ 3 and ~ 2 times the energy loss of a minimum ionizing particle for sensor thickness values of 320 and 500 μm, respectively. This limitation in the measurement range of energy loss of charged particles is referred to as the saturation effect. This is important for the search for multiply charged HSCPs, which can have large energy losses due to slow speed and large electric charge.

A charged particle traversing the strip detector will deposit the majority of its energy in one or two neighboring strips. The latter happens in the case of the charged particle passing through the edge of two sensors. In the offline reconstruction, strip clusters are built starting with a seed strip (signal to noise ratio > 3). Adjacent strips that have signal to noise ratio > 2 are included in the cluster. The energy deposition in the seed strip(s) gets distributed to adjacent strips due to cross-talk effects. The sharing of the signal happens

with a factor of 10^{-n} to the adjacent strips, where n is the number of strips between the strip and the seed (e.g. $n = 1$ refers to the neighboring strip). The total signal size of the cluster must be larger than 5 times the square-root of the sum of the RMS-noise-squared of the individual strips inside it. The centroid of the ADC counts in the various strips is taken as the position of the cluster. The sum of the individual charges in the various strips of the cluster is the cluster charge. The cluster size is the number of strips in the cluster. Energy loss ($\Delta E/\Delta x$) is the charge deposited per pathlength and is obtained by dividing the cluster charge (ΔE) by the geometric pathlength (Δx). The geometric pathlength is $\Delta x = L/\cos\theta$, where L is the thickness of the module, and θ is the angle between the track and the normal to the strip module.

2.2.4 Electromagnetic Calorimeter

The purpose of the electromagnetic calorimeter (ECAL) is to measure the energy of electrons, positrons, and photons. The decay of the Higgs boson into two photons is one of the most important channels in the search for the elusive particle. Around the mass window of $\sim$ 125 GeV, the Higgs boson has a negligible intrinsic width and the measured width is entirely driven by the detector resolution. Hence, having good energy resolution is the main criterion in the design of ECAL in CMS. To operate in the LHC environment, the ECAL has been designed to have good granularity, fast response, and good radiation hardness. The ECAL in CMS is made of lead tungstate ($PbWO_4$) crystals. The high density (8.28 gcm^{-3}), short radiation length (0.89 cm), and the small Molière radius (2.24 cm) of $PbWO_4$ results in a highly granular and compact ECAL. The barrel region of the ECAL has 61200 crystals covering $|\eta| < 1.479$. The endcap region of ECAL covers $1.479 < |\eta| < 3.0$, each of the endcaps have 7324 crystals. Avalanche photodiodes and vacuum phototriodes serve as photodetectors in the barrel and endcap regions respectively. There is a preshower detector in front of both endcap regions covering $1.653 < |\eta| < 2.6$. The preshower is a sampling calorimeter made of two layers of lead followed by silicon strip sensors. The granularity of the preshower improves the position measurement of electrons and photons.

2.2.5 Hadron Calorimeter

The Hadron Calorimeter (HCAL) measures the directions and energies of hadrons. The HCAL is a sampling calorimeter made of successive layers of brass/steel and plastic scintillator. The barrel region covers $|\eta| < 1.3$, the endcap region lies between $1.3 < |\eta| < 3.0$ and the forward hadron calorimeters covers $2.9 < |\eta| < 5.0$. The hermetic coverage of ECAL and HCAL is crucial for the measurement of E_T^{miss}. The interaction length in brass is 16.42 cm. The volume inside the solenoid magnet can accomodate 5.82 interaction lengths at $\eta = 0$. High energy hadrons are not always fully contained within this distance. The solenoid is used as an absorber totalling 1.4 interaction lengths at $\eta = 0$. An array of scintillators outside of the solenoid magnet (the outer hadronic calorimeter) measure the remaining energy of hadrons not completely absorbed in the inner calorimeters or the solenoid material.

2.2.6 Solenoid Magnet

A key part of the CMS detector is the large solenoid magnet. The magnet is 12.5 m long, has a mean diameter of 6.3 m, and weighs 220 tons. Over this volume, a 4 Tesla magnetic field is required to measure the momentum of 1 TeV muons with better than 10% precision. Superconducting magnet technology is used to achieve this high magnetic field. The nominal current in the superconducting solenoid is 19.14 kA and it stores 2.6 GJ of energy in it. The large size of the magnet allows the inner tracker and the calorimeters (except for the outer hadronic calorimeter) to fit inside of it. The feature of the calometers being contained within the solenoid contributes to better energy and E_T^{miss} measurements as the particles produced in the proton-proton collisions do not have to pass through the magnet material before interacting with the calorimeter. The muon system has iron plates that channel and retain the magnetic field. A 3.8 Tesla magnetic field was used during CMS data taking period of the Run I operations of the LHC. The slightly lower than design value was chosen to provide an additional safety factor for operations of the solenoid.

2.2.7 Muon System

Muons are minimum ionizing particles that can reach the outermost parts of the detector and escape to the outside. HSCPs may also reach and traverse the muon system. The momenta of muons can be measured both within the solenoid magnetic field and within the muon system. The muon system in CMS records the arrival time and position of particles. The arrival times of slow-moving HSCPs will be delayed compared to muons ($v \sim c$) and timing information can be used to search for these exotic particles.

Based on the varying radiation environments and the large volume to be covered, three types of gaseous detectors are used in the muon system. Drift tube (DT) chambers are used in the barrel region where the neutron-induced background is small, the muon rate is low, and the return magnetic field is uniform. The DT chambers cover $|\eta| < 1.2$ and are segmented along the z-direction into 5 wheels. In each of the wheels, the DT chambers are arranged into 4 concentric stations with layers of iron in between. Each wheel is segmented along the ϕ direction forming 12 sectors. There are 4 DT chambers in each sector (one DT chamber in each station). DT chambers in stations 1, 2, and 3 contain of 3 superlayers (SL) while that in 4th station has 2 SL. In each of the chambers, two SL measure the coordinate in r-ϕ plane and one SL measures the coordinate along the z direction (the fourth station does not measure the z-position). Each SL is made of 4 DT cells that are $2-3$ meters long and 42 mm wide. Consecutive layers of DTs cells are staggered by half of their size to avoid edge effects and to overcome the two-fold ambiguity of the path of the particle relative to the central wire. Signal produced in the various DT cells can be used to determine the timing of particles.

Cathode strip chambers (CSCs) are used in the endcap regions where the neutron-induced background is high, the muon rate is high, and the return magnetic field is non-uniform. The CSCs cover $0.9 < |\eta| < 2.4$ and have good granularity, fast response time, and good radiation hardness. In each of the endcaps, there are 4 CSC stations with layers of iron between the chambers to channel the return magnetic field. In each chamber, the cathode strips are projected radially outwards and yield a precise measurement in the r-ϕ plane.

The anode wires are approximately perpendicular to the strips and provide η measurement. Signal produced in both the strips and the wires can be used to determine the timing of particles.

Resistive plate chambers (RPCs) are gaseous double-plate chambers that supplement the DTs and CSCs in the barrel and endcap regions respectively. RPCs provide a fast response with good time resolution, but have a coarser position resolution than the DTs and the CSCs.

2.2.8 Trigger and Data Acquisition

The LHC operating at the design luminosity will result in $\sim 10^9$ inelastic collision events every second within the CMS detector. Because the size of the data related to each event is $\sim$ 1.5 MB, it is impossible to store all events and a massive reduction in their rate is required. Fortunately, most events are low-energy collisions that can be discarded. The task of selecting the interesting high-energy collisions is accomplished by the trigger system that is implemented in two steps: Level-1 (L1) Trigger and High-Level Trigger (HLT). The trigger system must reduce the number of events recorded per second to $\sim 300 - 600$ for storage and analysis.

The L1 trigger consists of custom-designed hardware processors. The L1 trigger looks for simple signatures of interesting events such as large energy depositions arising from the decay of a massive particle, or the track patterns of a high p_T particle in the muon system arising from the passage of an HSCP. The L1 trigger decision is made in several stages: local, regional, and global. The local triggers are based on energy deposits in the calorimeter or hit patterns in the muon system in coarsely segmented regions. Regional triggers combine the information of local triggers to form trigger objects such as electron or muon candidates. Trigger objects are ranked based on energy, momentum, and quality. The highest-ranked calorimeter and muon objects are passed to the global L1 trigger to accept/reject the event. In the case of former, the event is sent to the HLT. While the L1 trigger makes a decision, event information is kept in temporary buffers. The L1 trigger

reduces the event rate to 100 kHz.

The HLT consists of thousands of software processors. After the L1 trigger accepts the event, the HLT looks at more refined event information to decide whether to keep the event or not. The HLT reconstructs the relevant objects and regions of the detector and compares event characteristics such as p_T, E_T^{miss}, etc. with threshold values. Based on an affirmative decision of the HLT, the event is stored and used in subsequent analysis.

CHAPTER 3

VARIABLES USED IN THE SEARCH

The multiply charged HSCP analysis uses ionization energy loss and time-of-flight measurements in the CMS detector. This chapter describes the measurement of these variables as used in the analysis.

3.1 Ionization Energy Loss

Both pixel and strip detectors record the ionization energy loss of charged particles. However, the tools for using energy loss measurements in the pixel detector were not fully developed and the saturation effect in the pixel detector occurs at $\sim$ 1.5 times the energy loss of a minimum ionizing particle as compared to $\sim$ $2-3$ times in the strip detector. There are only 3 layers in the pixel detector and using them does not yield significant improvement compared to the energy loss per pathlength determined using a larger number of measurements in the strip detector. Therefore, the search for multiply charged HSCPs is performed using only ionization energy loss measurements in the strip detector.

3.1.1 Energy Loss Estimators

Energy loss of a charged particle in a material medium is a stochastic process. Hence, $\frac{\Delta E}{\Delta x}$ measurements in the various layers of the strip detector are combined to obtain a reliable estimate of the energy loss per pathlength of a charged particle traversing the strip detectors. Fluctuations in the energy loss of a charged particle in a thin medium is

given by the Landau distribution [35]. Consequently, $\frac{\Delta E}{\Delta x}$ suffers large fluctuations and, therefore, the mean energy loss is not a useful quantity for estimation of the energy loss. A better quantity is the most probable energy loss, $\frac{dE}{dx}$, and can be estimated in a variety of ways. These include the median, truncated-40, and harmonic-2 estimators. In all three estimators, the individual $\frac{\Delta E}{\Delta x}$ measurements, totalling to N, are arranged in increasing order. The median estimator picks the median value among all measurements and can be unreliable in the case of a small number of measurements. The truncated-40 estimator ignores 40% of the highest energy depositions, and calculates the average of the remaining ones. Ignoring 40% of the higher energy depositions reduces the bias of the truncated-40 estimator to multiply charged HSCP signatures. However, ignoring 40% of the higher $\frac{\Delta E}{\Delta x}$ values is not desirable in the case of a small number of measurements. The harmonic-2 estimator uses all measurements with a power factor of -2 as

$$I_h = \left(\frac{1}{N} \sum_{i=1}^{N} \left(\frac{\Delta E}{\Delta x} \right)_i^k \right)^{(1/k)}, \tag{3.1}$$

where $k = -2$. By suppressing higher values of $\frac{\Delta E}{\Delta x}$, the harmonic-2 estimator can distinguish SM particles that have a few fluctuations to higher values of $\frac{\Delta E}{\Delta x}$ from multiply charged HSCPs that will have several high values of $\frac{\Delta E}{\Delta x}$. Hence, the harmonic-2 estimator is used for $\frac{dE}{dx}$ computation.

Figure 3.1 shows the most probable $\frac{dE}{dx}$ distribution for both harmonic-2 and truncated-40 estimators in $\sqrt{s}$ =7 TeV data and simulation [48]. Tracks are selected with momentum greater than 5 GeV, a vertex compatible with the proton-proton interaction region, and at least 13 hits in the strip detectors. Good agreement between data and simulation is noted. The slight discrepancy is due to differences in calibration between data and simulation. The harmonic-2 estimator has a larger trend toward lower values of $\frac{dE}{dx}$ than the truncated-40 estimator.

The 2-D distribution of I_h and momentum for particles (as in the Bethe-Bloch curve) in $\sqrt{s}$ =7 TeV data and simulation is shown in Fig. 3.2 [48]. A sample of low momentum

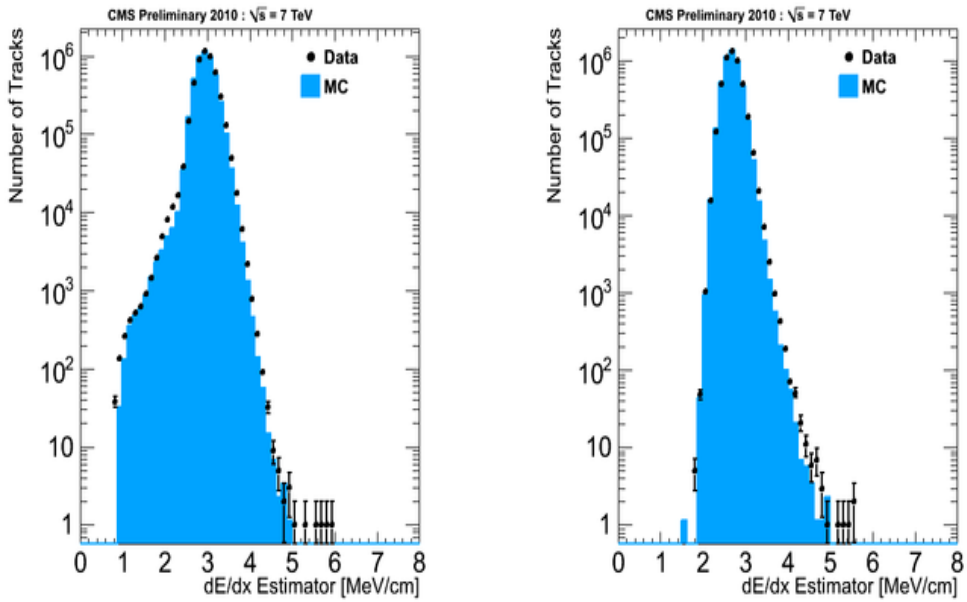

Figure 3.1: Distribution of $\frac{dE}{dx}$ for harmonic-2 (left) and truncated-40 (right) estimators in data and simulation [48].

tracks with a vertex compatible with the proton-proton interaction region, and at least 13 hits in the strip detectors are used. The increase in $\frac{dE}{dx}$ at lower momentum is clearly seen. Separate bands, corresponding to particles with different masses are also visible. Kaon and proton bands are visible in both data and simulation. The deuteron band is observed in data, however, since it is not generated in PYTHIA [49], it is not seen in simulation.

The 2-D distributions of $\frac{dE}{dx}$ and momentum for $\sqrt{s}$ =8 TeV data and that expected for multiply charged HSCPs of $|Q| = 1e$, $2e$, and $3e$ are shown in Fig. 3.3. A common mass of 400 GeV is used for all three charges. Tracks reconstructed as global muons (a track reconstructed in the inner tracker and matched to one reconstructed in the muon detector) and with a vertex compatible with the proton-proton interaction region, $p_T > 45$ GeV, and $I_h > 3$ MeV/cm are used. For multiply charged HSCPs, the increase in $\frac{dE}{dx}$ at lower momentum along with the formation of separate bands, corresponding to different charges is clearly seen. I_h values for $|Q| = 2e$ and $3e$ are less than a factor of Q^2 times larger than the I_h values for $|Q| = 1e$ due to the saturation effect.

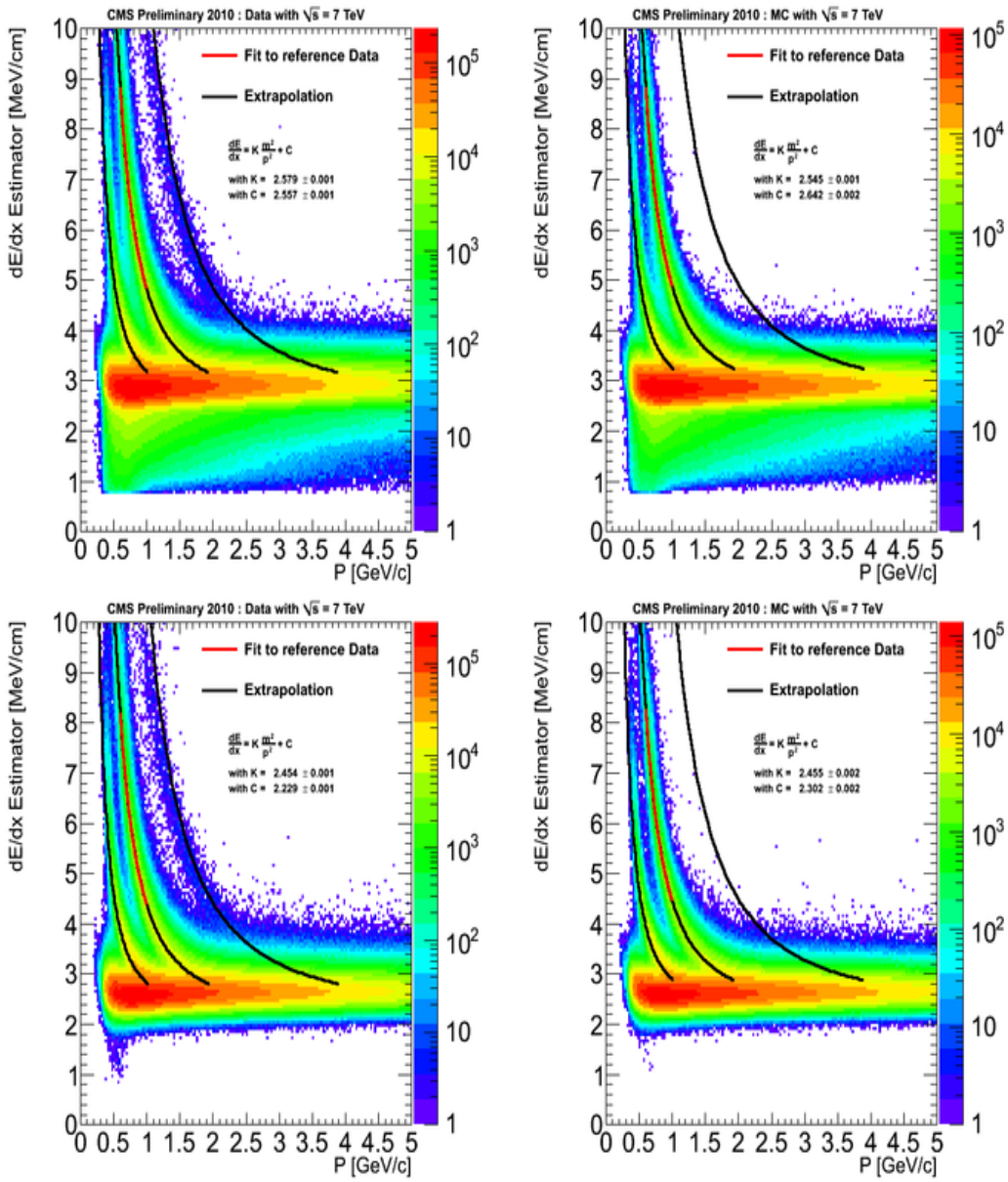

Figure 3.2: Distributions of $\frac{dE}{dx}$ as a function of momentum using harmonic-2 (top row) and truncated-40 (bottom row) estimators. Left column shows $\sqrt{s}$ =7 TeV data while right column shows $\sqrt{s}$ =7 TeV simulation [48].

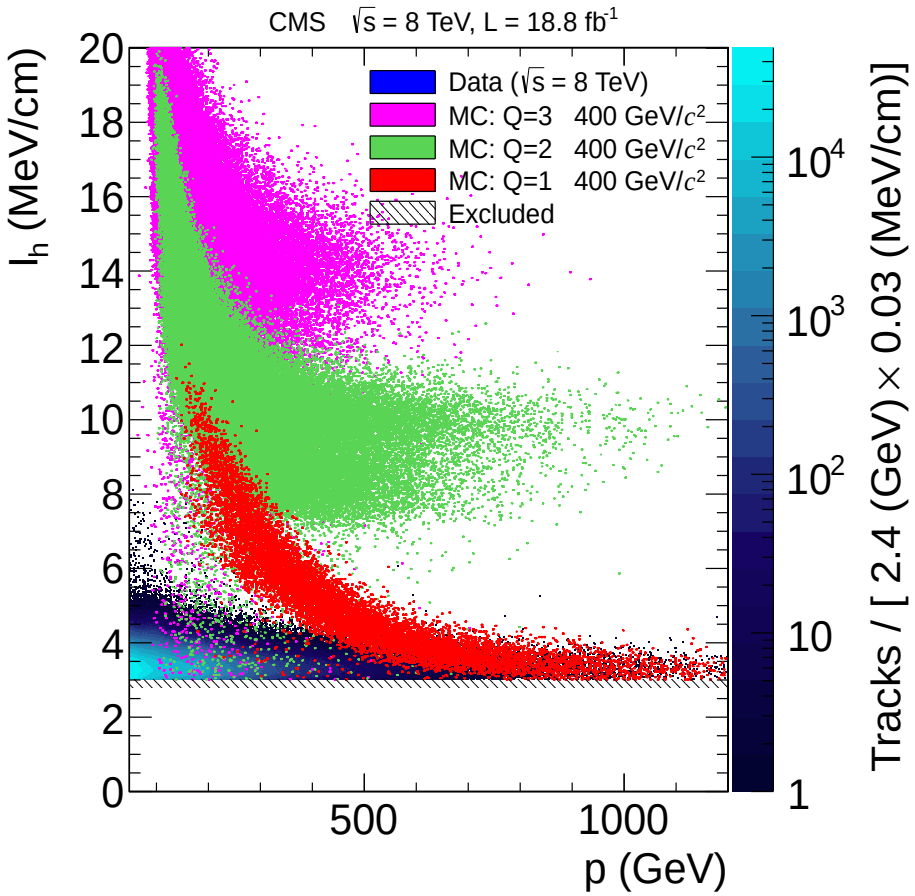

Figure 3.3: Distributions of $\frac{dE}{dx}$ as a function of momentum for data and multiply charged HSCP simulations with a mass of 400 GeV and several different charges at $\sqrt{s}$ =8 TeV.

Particles with unit electric charge passing through the silicon strip detector will tend to deposit energy in one or two strips with cross-talk producing a signal of $\sim 10\%$ in the neighboring strips and $\sim 1\%$ in the next-to-neighboring strips (Fig. 3.4 (top)). Clusters are formed by summing the energy in all adjacent strips. For a typical SM particle that is minimum ionizing, a fairly narrow cluster is formed. An important background for searches for particles that have large $\frac{dE}{dx}$ occurs when two or more particles pass through a silicon detector close enough that they are merged into a single cluster with high $\frac{dE}{dx}$ (Fig. 3.4, (middle)). Jets and/or nuclear interactions in the silicon can produce such signals. In other searches for HSCPs in the CMS collaboration, this background is reduced by applying a cluster cleaning procedure that removes wide clusters and clusters containing multiple strips saturated [50, 51].

The multiply charged HSCP analysis does not use the cluster cleaning procedure. The exceptionally large energy deposition that is expected for $|Q| > 1e$ signal particles produces wider clusters with one or more strip readouts above the saturation level (Fig. 3.4 (bottom)). This results in an undesirable signal efficiency loss when the cluster cleaning is applied to multiply charged signals. The large $\frac{dE}{dx}$ also results in a larger energy deposition in the calorimeters which results in the multiply charged HSCP search using a different isolation than the $|Q| \leq 1e$ HSCP searches (Sec. 4.2.2).

3.1.2 Energy Loss Discriminators

The individual $\frac{\Delta E}{\Delta x}$ measurements can also be combined into a discriminator for improved separation between signal and background. The discriminator compares the individual $\frac{\Delta E}{\Delta x}$ values to that expected from a minimum ionizing particle and assigns a probability, P_h, that a minimum ionizing particle will have the same or lesser $\frac{\Delta E}{\Delta x}$.

The most probable $\frac{dE}{dx}$ has a small non-linear dependence on the pathlength, x, as $\Delta\rho/x \sim a \ln x + b$, where a and b are constants [35]. The CMS detector uses strip detectors with two different thickness: 320 μm in the inner four layers of the barrel, all the disks of the TID, and the first four rings of the TEC disks; and 500 μm in the outer six layers of the

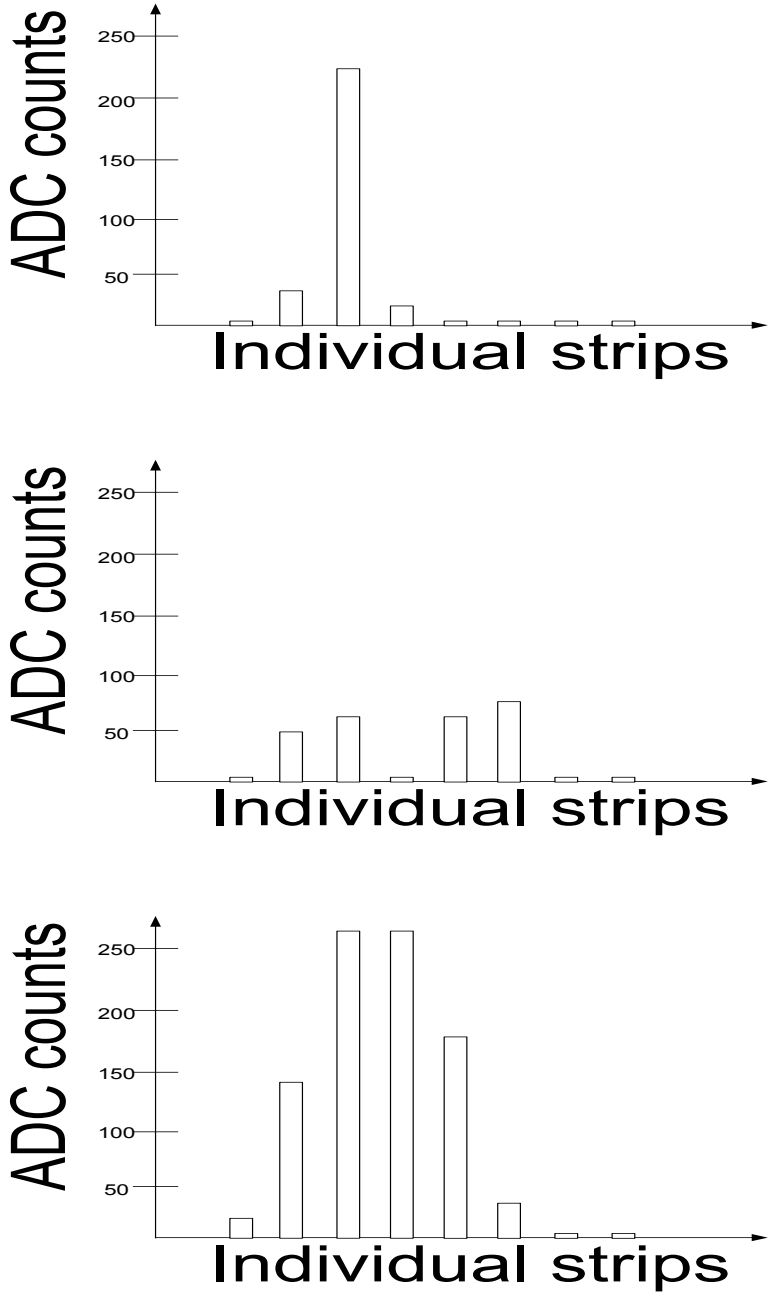

Figure 3.4: Drawings of expected cluster shapes in the strip detector for singly charged HSCPs (top), backgrounds from jets/nuclear interactions (middle), and multiply charged HSCPs (bottom). Energies deposited by multiply charged HSCPs are expected to be larger than the dynamic measurement range in the strips (253 ADC counts) resulting in saturation.

barrel and the last three rings of the TEC disks. Also, the effective length traversed by a charged particle in the strip varies with the direction of the particle. The $\frac{dE}{dx}$ discriminator uses probability distribution function templates dependent on the pathlength traversed in the strips and is therefore preferred over the $\frac{dE}{dx}$ estimator. The $\frac{dE}{dx}$ discriminators also account for the saturation effect.

Several $\frac{dE}{dx}$ discriminators can be constructed. These include the Product discriminator, the Smirnov-Cramer-von Mises discriminator, and the Asymmetric Smirnov-Cramer-von Mises discriminator. In all three discriminators, the P_h values are arranged in increasing order and N is the number of $\frac{\Delta E}{\Delta x}$ measurements. The discriminators have a value between 0 and 1. The product discriminator, I_P, is

$$I_P = \left(\prod_{h=1}^{N} P_h \right)^{\frac{1}{N}}, \tag{3.2}$$

and yields a value of ~ 0.5 for a minimum ionizing particle. Values close to 0 and 1 correspond to low and high ionization, respectively, indicating incompatibility with the case of a minimum ionizing particle. The Smirnov-Cramer-von Mises discriminator, I_d, is constructed similar to the Kolmogorov-Smirnov test and measures the distance between the observed set of $\frac{\Delta E}{\Delta x}$ measurements and the expected distribution from a minimum ionizing particle as in

$$I_d = \frac{3}{N} \times \left(\frac{1}{12N} + \sum_{h=1}^{N} \left[P_h - \frac{2h-1}{2N} \right]^2 \right). \tag{3.3}$$

Minimum ionizing particles have I_d values close to 0 while particles with ionization lower/higher than minimum ionizing particles have I_d values close to 1. The Asymmetric Smirnov-Cramer-von Mises discriminator, I_{as}, is similar to I_d, but uses the probability value as a weighting factor as in

$$I_{as} = \frac{3}{N} \times \left(\frac{1}{12N} + \sum_{h=1}^{N} \left[P_h \times \left(P_h - \frac{2h-1}{2N} \right)^2 \right] \right). \tag{3.4}$$

The additional factor results in large values of I_{as} discriminator only for higher ionization

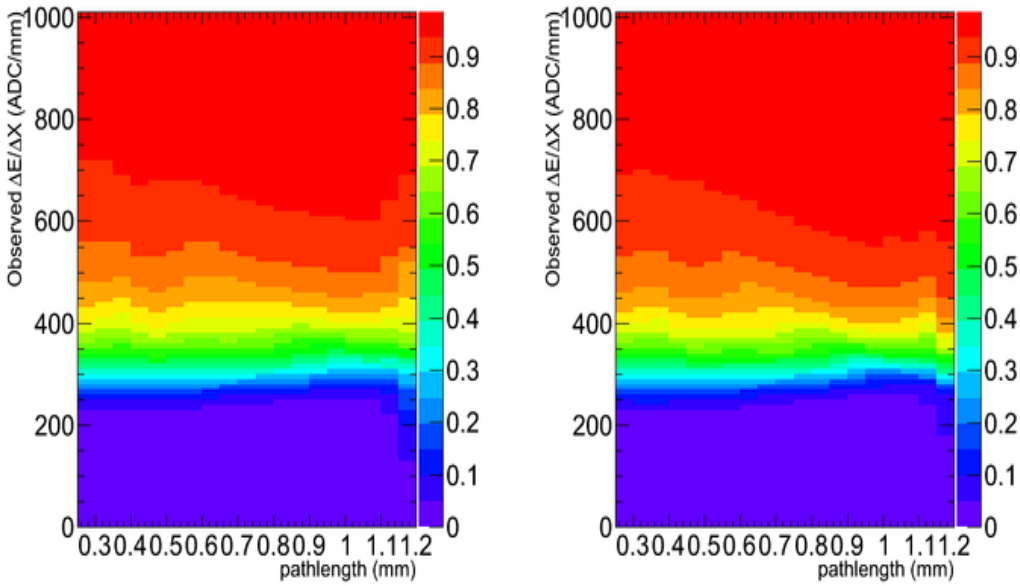

Figure 3.5: $\frac{\Delta E}{\Delta x}$ probability distribution function templates used by discriminators. The color scale displays the probability that a minimum ionizing particle traversing a pathlength shown in the X-axis will deposit charge equal to or less than that shown in the Y-axis. Template for data is shown in left while that for simulation is shown in right [48].

values than the minimum ionizing particle. Minimum ionizing particles and particles with ionization lower than minimum ionizing particles will have I_{as} values close to 0. The I_{as} discriminator is sensitive to incompatibility with the case of a minimum ionizing particle only for larger ionization. For this reason, the I_{as} discriminator is used in the search for multiply charged HSCPs.

The template probability distribution functions for the charge deposited by a minimum ionizing particle to be equal to or less than a certain value over a pathlength are shown in Fig. 3.5 [48]. The distributions cover pathlengths of $200 - 1600$ μm with 50 μm intervals. These distributions are obtained using tracks with momentum greater than 5 GeV and at least 5 hits in the strip detectors.

The 2-D distribution of I_{as} and momentum for $\sqrt{s}$ =7 TeV data and simulation is shown in Fig. 3.6 [48]. As in Fig. 3.2, a sample of low momentum tracks with a vertex compatible with the proton-proton interaction region, and at least 13 hits in the strip detectors are

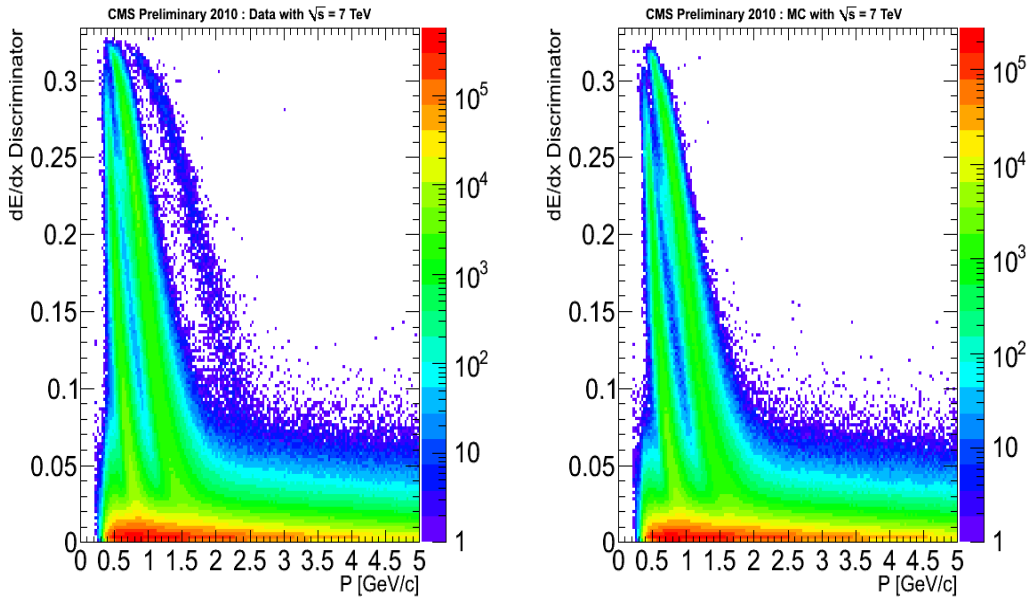

Figure 3.6: Distribution of I_{as} as a function of momentum for data (left) and simulation (right) [48].

used. The increase in I_{as} at lower momentum along with formation of separate bands (corresponding to particles with different masses) is clearly seen. Kaon and proton bands are visible in both data and simulation. The deuteron band is observed in data, but is not simulated.

3.2 Time-of-Flight

Time-of-flight measurements can identify slow moving particles from those with $\beta \sim 1$. The pathlength between the interaction point in CMS and the muon system is ~ 4 m and can separate slow moving multiply charged HSCPs from relativistic SM particles. Good spatial and time resolution of DTs and CSCs in the muon system is important in the search for multiply charged HSCPs in data collected with the CMS detector.

3.2.1 Drift Tube Measurements

Charged particles traversing DTs in the muon system will ionize the gaseous medium. The electrons are collected by the central anode wire and the signal amplitude and time are recorded by the read-out electronics. The DT timing for a long-lived charged particle that is produced in proton-proton collisions in the CMS detector and traverses through the DTs, depends on the time-of-flight of the particle from the interaction point to the DT cell, the drift time of the ionization electrons to the central wire, and the delay due to the signal propagation along the wire. Measurements in the various layers of the DT chambers are used to constrain the trajectory of the particle in the muon system and to determine the time-of-flight of the particle from the interaction point in CMS to the muon system.

The drift time of the ionization electrons in the various DT cells are calculated using drift time values obtained from a sample of prompt muons selected for calibration. Hits in the ϕ and z-directions are grouped to form a track segment. Further refinements of the track segment are factored into three sources of time corrections: time-of-flight from the interaction point to the DT cell (t_c), propagation time of the signal along the central wire (t_w), and an off-time correction (δ_t) necessary only for non-prompt/delayed particles and similar for all hits of the track segment.

Timing corrections due to t_c and t_w are used to coarsely determine the trajectory of the charged particle. The trajectory of the track is further refined by iterating over δ_t values. An illustration of how the δ_t correction is determined for a slow moving particle is shown in Fig. 3.7, which shows the cross-sectional view of DT cells in various layers of a DT SL. DT cells that record a signal are shown in white. The staggered arrangement helps identify the path of the particle relative to the central wire. The particle trajectory is shown as a straight line. Once t_c and t_w corrections are implemented, the trajectory of the particle is iterated using different values of δ_t to match the measured timing in DT cells. Starting with $\delta_t \sim 0$ (corresponding to $\beta \sim 1$ particle), the delayed arrival of the signal results in shifting the position of the particle toward the edge of the cell (shown in red boxes). Positive values of δ_t will shift the position of the particle closer to the central wire. Eventually, for the

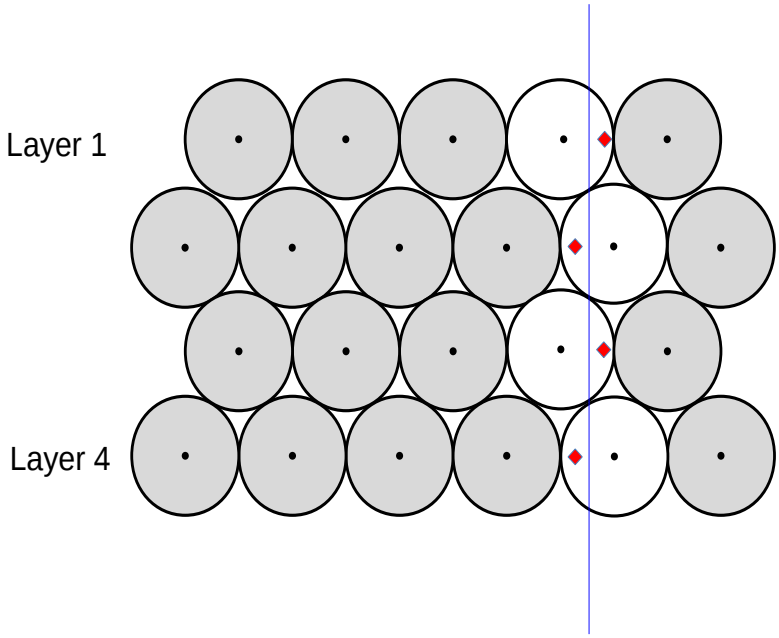

Figure 3.7: Sample drawing illustrating the effect of delayed arrival of slow particles within a DT superlayer. The blue line shows the trajectory of the particle. The initial reconstruction (assuming no delay) results in the reconstructed position (red points) for each hit that is farther from the DT center than its true position. Including the δ_t factor will move the reconstructed position back to align along the blue line.

proper time delay, the position of the particle within the various DT cells will be aligned (shown in blue line).

Each DT chamber is independently used to constrain the path of the charged particle and to determine δ_t. Each DT chamber has eight layers of DT cells that measure along the ϕ direction and four layers that measure along the z direction (fourth DT chamber does not measure the z coordinate). The straight line fit constraining the δ_t value uses 2 degrees of freedom and therefore, at least 3 measurements in a DT chamber are required to utilize the δ_t value. For these reasons, the δ_t measurement is done using only the ϕ-coordinate.

3.2.2 Cathode Strip Chamber Measurements

A charged particle traversing the CSCs will ionize the gaseous medium. Electrons and positive ions will be collected by the anode wire and the cathode strips, respectively. Strips and wires are nearly perpendicular to each other and yield a 2-D position measurement (r-ϕ). Signal recorded in the various layers of the strips and the wires can be used to determine the timing of particles traversing the CSCs. The determination of timing is the same as for the DTs (Sec. 3.2.1).

3.2.3 Inverse Beta

The β of a particle is related to δ_t as

$$\delta_t = t_{\beta c} - t_c = \frac{L}{\beta c} - \frac{L}{c}, \tag{3.5}$$

where L is the flight distance. Rearranging Eq. 3.5 yields $1/\beta$ of the particle

$$\frac{1}{\beta} = 1 + \frac{c\delta_t}{L}. \tag{3.6}$$

The average $1/\beta$ value of the particle, $\langle 1/\beta \rangle$, is calculated as a weighted average of the $1/\beta$ measurements in the various layers of the muon system. The weight for the ith DT measurement is given by

$$w_i = \frac{(n-2)}{n} \frac{L_i^2}{\sigma_{DT}^2}, \tag{3.7}$$

where n is the number of ϕ-direction measurements in the DT chamber used to constrain δ_t and $\sigma_{DT} = 3$ ns is the time resolution of the DT measurements. The factor $(n-2)/n$ accounts for the fact that the δ_t values are computed using two parameters of a straight line determined from the same n measurements. The weight for the ith CSC measurement is given by

$$w_i = \frac{L_i^2}{\sigma_i^2}, \tag{3.8}$$

where σ_i, the measured time resolution, is 7.0 ns for strips and 8.6 ns for wires.

The uncertainty in the $1/\beta$ measurement, $\sigma_{1/\beta}$, is given by

$$\sigma_{1/\beta} = \sqrt{\sum_{i=1}^{N} \frac{(1/\beta_i - \langle 1/\beta \rangle)^2 \times w_i}{N-1}}, \tag{3.9}$$

where N is the number of δ_t measurements of the particle.

In the DTs, the spatial resolution is ~ 100 μm in the r-ϕ plane, and is slightly degraded in the z-direction. The timing resolution in the DTs is a few ns. An overall timing resolution of better than 3 ns was achieved during the Run I proton-proton collision runs. The spatial resolution in the CSCs is better than 150 μm. The timing resolution in the strips and the wires were 7.0 ns and 8.6 ns, respectively, during the Run I proton-proton collision runs.

Distributions of $1/\beta$ in the DTs and the CSCs for $\sqrt{s}$ =7 TeV proton-proton collision data collected during early 2011 operations is shown in Fig. 3.8. A sample of tracks reconstructed as global muons, and with a vertex compatible with the proton-proton interaction region, $p_T > 35$ GeV, and $I_h > 3$ MeV/cm are used. The resolution of $1/\beta$ in both the DTs and the CSCs is ~ 0.06.

Figure 3.9 shows the expected $1/\beta$ distribution for singly charged HSCPs of different masses in DTs and CSCs. Tracks reconstructed as global muons, and with a vertex compatible with the proton-proton interaction region, $p_T > 45$ GeV, and $I_h > 3$ MeV/cm are used. The $1/\beta$ distribution extends to larger values for higher masses.

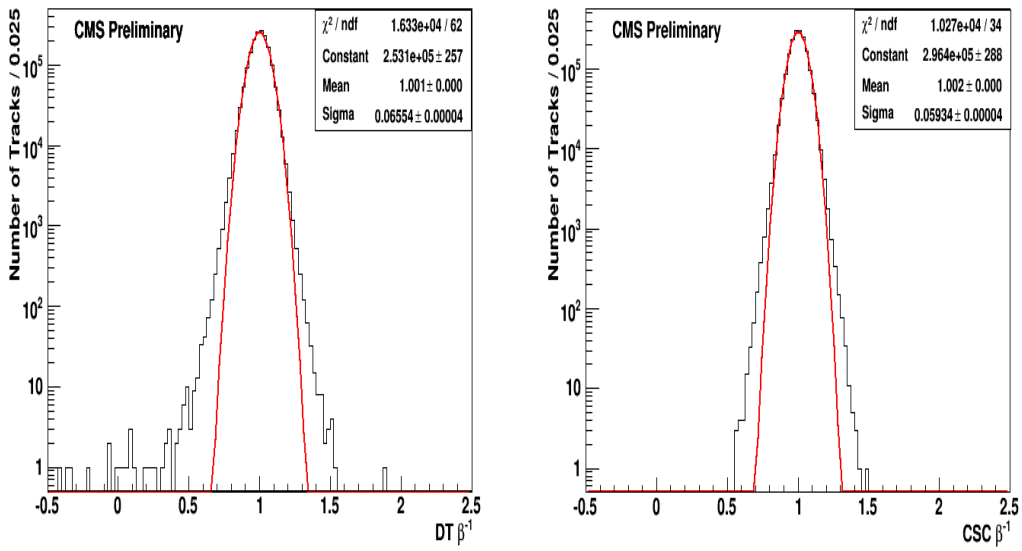

Figure 3.8: Distributions of $1/\beta$ in DTs (left) and CSCs (right) for $\sqrt{s}$ =7 TeV data collected in early 2011 [52].

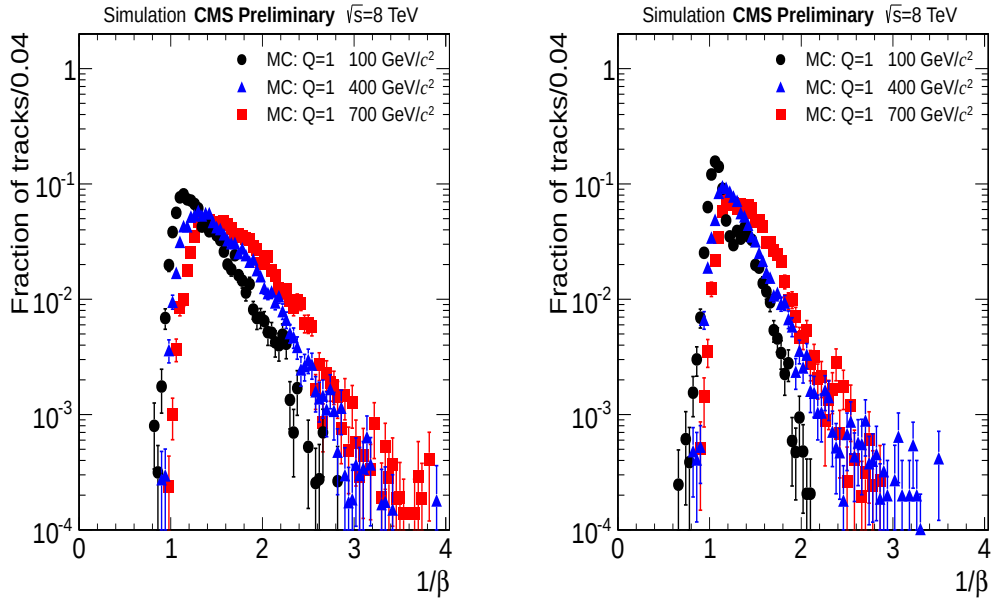

Figure 3.9: Distributions of $1/\beta$ for singly charged HSCP simulations of different masses in DTs (left) and CSCs (right) at $\sqrt{s} = 8$ TeV.

CHAPTER 4

MULTIPLY CHARGED HSCP ANALYSIS

A broad search program covering various HSCP scenarios has been pursued by the CMS collaboration. Dedicated searches are performed for fractionally, singly, and multiply charged HSCPs with three search strategies using either the inner tracker only, the muon system only, or the two systems combined [51].

This analysis searches for multiply charged HSCPs that can be observed in both the inner tracker and the muon system. Ionization energy loss measurements in the inner tracker and time-of-flight measurements in the muon system are used to identify highly ionizing and slow moving particles that are compatible with multiply charged HSCPs.

4.1 Signal Model

MC samples of multiply charged HSCPs are generated using the model considered in Ref. [53]. In this model, multiply charged HSCPs are new spin-1/2 particles with an arbitrary electric charge and are charged under $U(1)$, but neutral under $SU(3)_C$ and $SU(2)_L$. This model serves as a simple generic benchmark for multiply charged HSCPs that have primarily electromagnetic interactions. The multiply charged HSCPs couple only to the photon and the Z and are pair-produced via a modified Drell-Yan mechanism. With no $SU(2)$ interactions, coupling of multiply charged HSCPs to the Z is modified. The weak isospin $t_{3L} = 0$ results in the axial coupling $g_A = 0$ and the vector coupling $g_V = -2Q\sin^2(\theta_W)$ (Eqs. 10.5 (a) and 10.5 (b) in Ref. [35]).

Signal samples are generated as a 4th generation lepton (τ') pair-produced via a modified Drell-Yan process using PYTHIA v6.422 (v6.426) [49] for $\sqrt{s} = 7$ (8) TeV production. The lepton is set to be stable to resemble its long-lived nature. PYTHIA parameters used in the signal sample generation are listed in App. A. CTEQ6L1 parton distribution functions [54] are used. Samples were generated for $|Q| = 1e$ to $8e$ in integer steps of e and masses of 100-1000 GeV in steps of 100 GeV. Cross section values for the signal samples were calculated at leading order with three contributions from γ-only, Z-only, and interference terms. All three terms have a Q^2 dependence. The interference term is negative and almost equal to (and cancels) the Z-only contribution. This results in the total cross section being approximately equal to the γ-only process. Total cross sections for all signal samples are listed in App. B.

The generator-level distributions of p_T, β, and η for multiply charged HSCPs with different masses at $\sqrt{s} = 8$ TeV are shown in Fig. 4.1. With increasing mass, the p_T distribution becomes harder, the β distribution is shifted towards lower values, and the η distribution is shifted toward the central region. Figure 4.2 shows the generator-level 2-D distribution of β and η for multiply charged HSCPs with two different masses (100 and 400 GeV). These kinematic distributions do not depend on charge. Signal MC is generated for all charges assuming $Q = 1e$. Prior to detector simulation, the charge of the HSCP is changed to the desired value. Detector response of the signal samples is modelled using GEANT4 framework [55].

Validation plots for the simulation of multiply charged HSCPs are shown in Figs. 4.3 and 4.4. Energy loss of multiply charged HSCPs in the inner tracker, ECAL, and HCAL increases for higher charges as Q^2 (Fig. 4.3). Due to saturation effect in the inner tracker, energy loss measurements for higher charge signals reach a plateau. Standard reconstruction assumes all charged particles have unit charge ($Q = 1e$). The reconstructed p_T is consequently scaled by a factor of $1/Q$ (Fig. 4.4).

The 2-D distributions of reconstructed-β versus generator-level β for multiply charged HSCPs of mass 400 GeV and two different charges ($2e$ and $7e$) at $\sqrt{s} = 8$ TeV are shown in

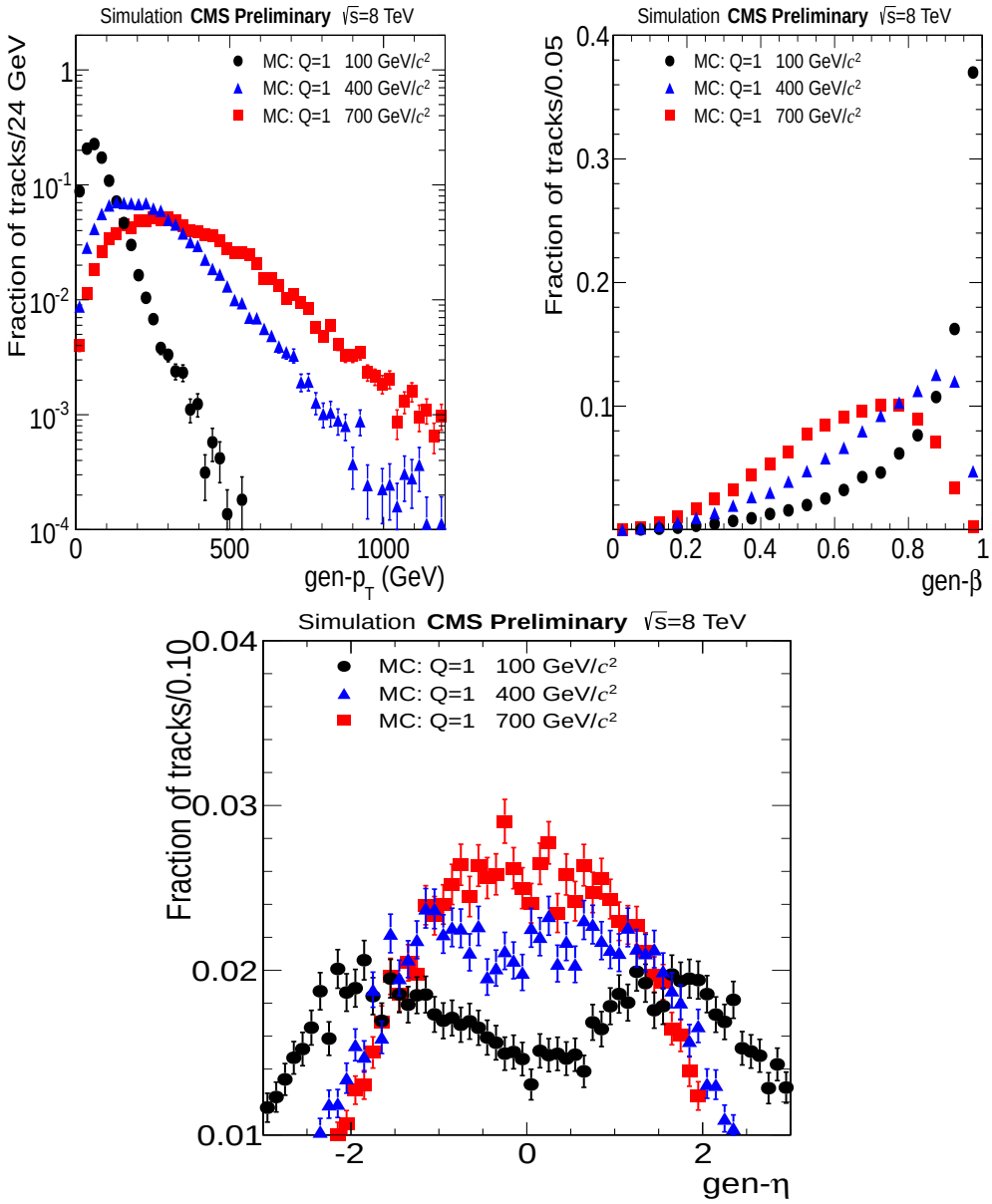

Figure 4.1: Generator-level distributions of p_T (top left), β (top right), and η (bottom) for multiply charged HSCPs of different masses at $\sqrt{s} = 8$ TeV.

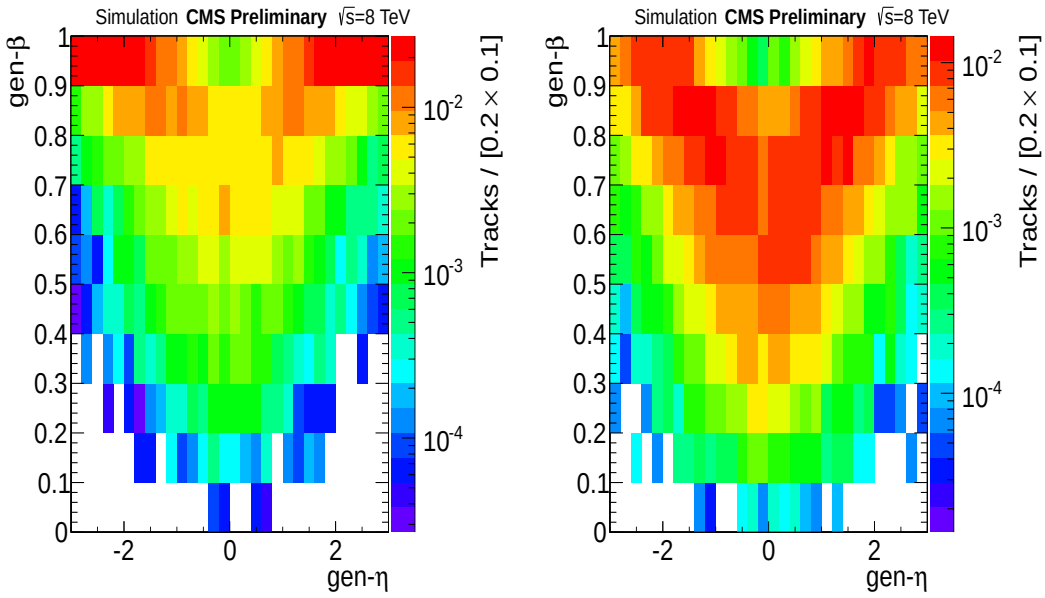

Figure 4.2: 2-D generator-level distributions of η and β for multiply charged HSCPs of mass 100 GeV (left) and 400 GeV (right) at $\sqrt{s} = 8$ TeV.

Figure 4.5. These distributions are shown for signal tracks that pass the online (Sec. 4.2.1) and global muon requirements (Sec. 4.2.2). With increasing charge, under-measurement of p_T (Fig. 4.4) and enhancement in energy-loss (Fig. 4.3) result in a larger fraction of HSCPs that fail the online and global muon requirements. This feature is more pronounced in the case of slower particles resulting in a higher cut-off at the low-end of the generator-level β distribution for higher charges. Energy loss serves to slow down HSCPs, yielding a lower value of reconstructed β with respect to the generator-level value. A fraction of HSCPs have reconstructed β larger than 1.0 due to timing resolution.

SM MC samples have been used for comparison with data. Samples for 7 TeV consist of events from strong interactions, $W^{\pm}$, Drell-Yan, $t\bar{t}$, and di-boson production. For 8 TeV, only Drell-Yan$\rightarrow$ $\mu\mu$ sample is used. The background prediction in the multiply charged HSCP analysis is entirely data-driven (Sec. 4.3) and is unaffected by the unavailability of all SM MC samples.

For all MC samples, minimum bias collision events are overlaid to the primary collision

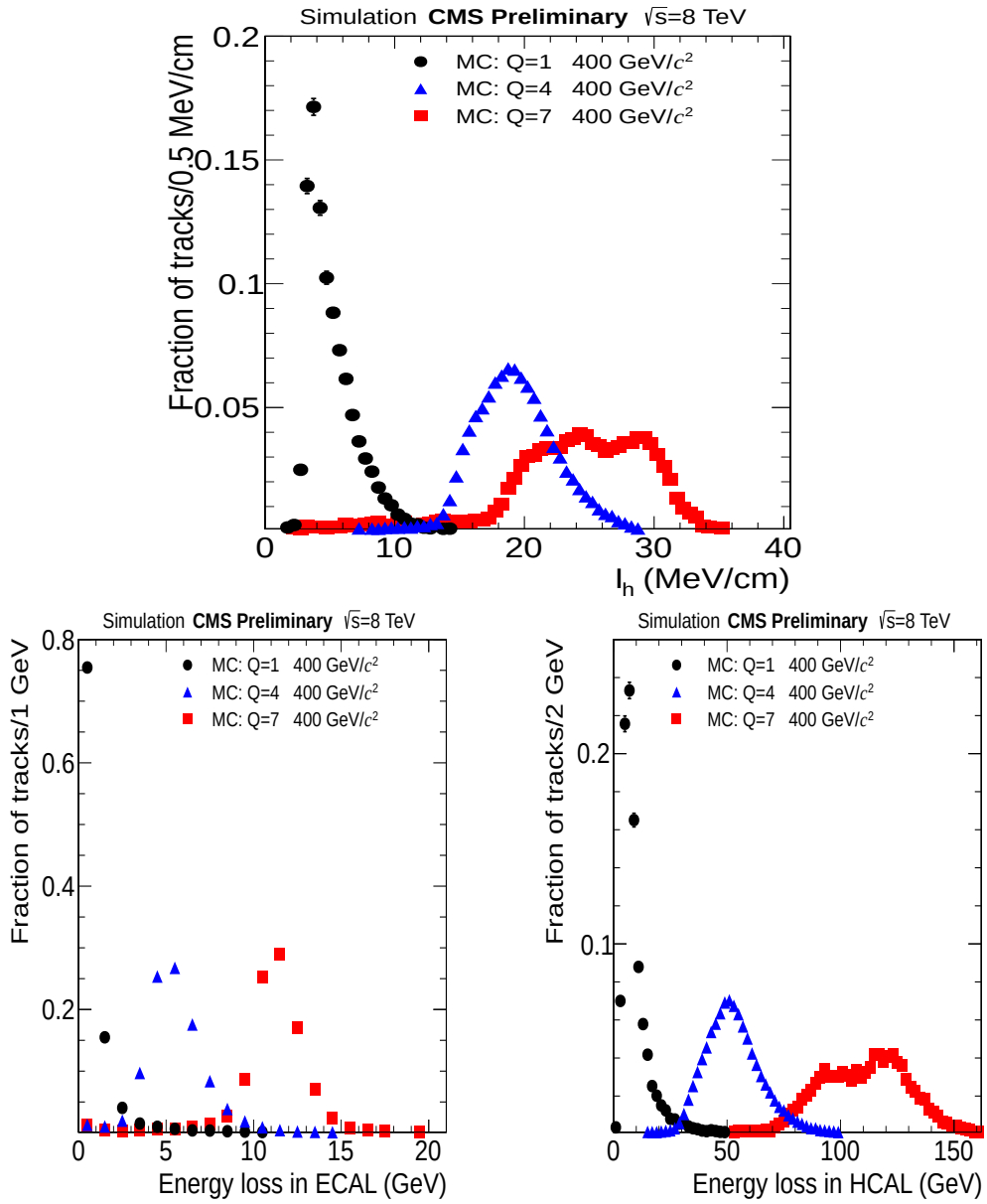

Figure 4.3: Distributions of I_h (top), energy loss in ECAL (bottom left), and energy loss in HCAL (bottom right) for multiply charged HSCP simulations with mass of 400 GeV and different charges at $\sqrt{s} = 8$ TeV.

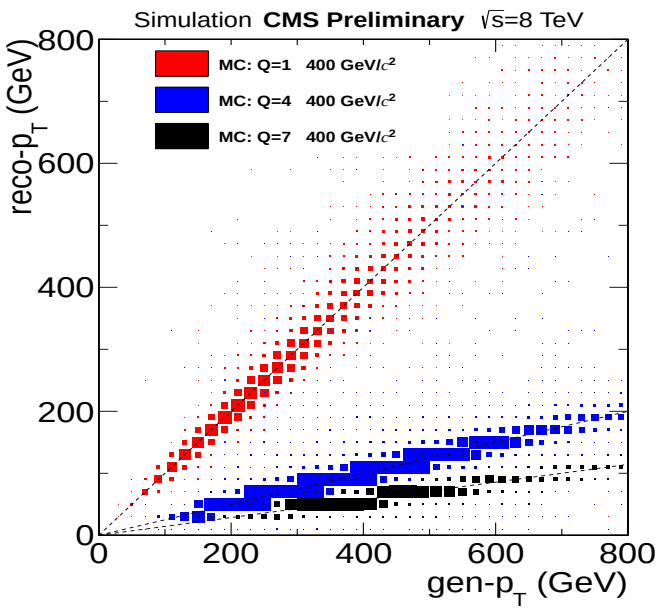

Figure 4.4: Reconstructed p_T as a function of generator-level p_T for multiply charged HSCP simulations with mass of 400 GeV and different charges. Reconstructed p_T is scaled by a factor of $1/Q$ relative to generator-level p_T.

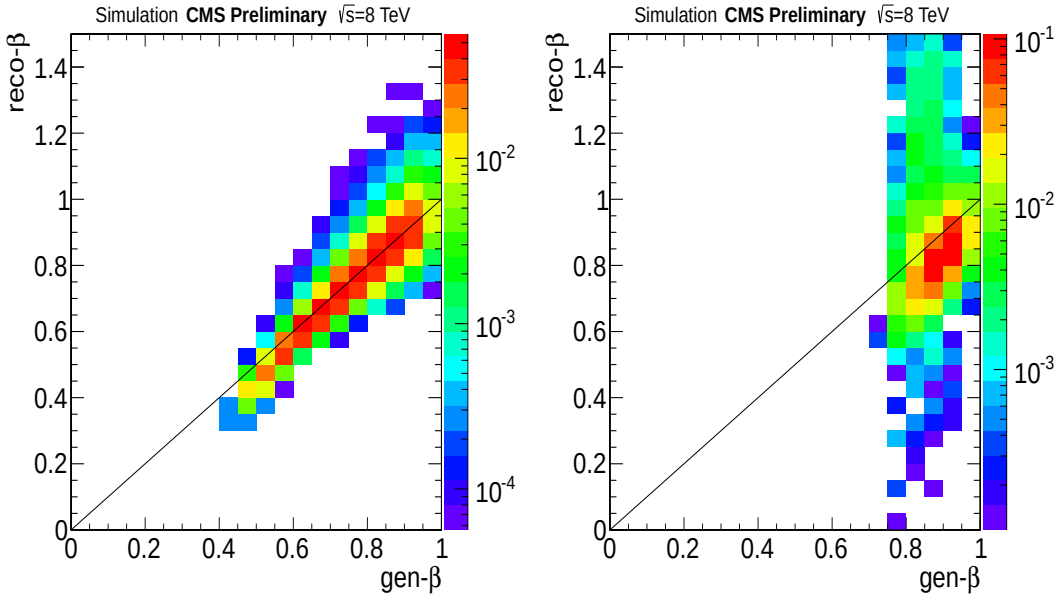

Figure 4.5: 2-D distribution of generator-level β and reconstructed β for 400 GeV multiply charged HSCPs of $Q = 2e$ (left) and $Q = 7e$ (right) at $\sqrt{s} = 8$ TeV.

event to simulate pile-up. Events are then reweighted to match the pile-up observed in data. Figure 4.6 shows the distribution of the number of primary vertices for MC samples before and after reweighting. These distributions are shown after online (Sec. 4.2.1), global muon, η, primary vertex, and track quality selections (Sec. 4.2.2) have been implemented. After reweighting, reasonable agreement with data is noted.

4.2 Trigger and Data Selection

The multiply charged HSCP analysis uses data from the 2011 and the 2012 proton-proton collision runs of the LHC, corresponding to 7 TeV and 8 TeV center-of-mass energies, respectively. High p_T muon and large E_T^{miss} triggers are used to collect the data sample used in the search. Data collected when parts of the detector were not fully functional were discarded. The CMS Data Certification group analyzes and identifies usable data (most/all detector systems operating well) collected with the CMS detector. Lists of good data are maintained in their respective JSON files. JSON files used for 7 TeV and 8 TeV center-of-mass energies were Cert_160404-180252_7TeV_ReRecoNov08_Collisions11_JSON_v2.txt and Cert_190456-208686_8TeV_PromptReco_Collisions12_JSON.txt, respectively. Triggers related to the multiply charged HSCP search were not operational for a tiny fraction of certified data (Sec. 4.2.1) and the corresponding data were excluded. Total dataset used in the multiply charged HSCP search contains an integrated luminosity of 5.0 fb^{-1} of $\sqrt{s} = 7$ TeV data and 18.8 fb^{-1} of $\sqrt{s} = 8$ TeV data.

4.2.1 Online Selection

The muon trigger requires a track segment in the muon system to be matched to a track reconstructed in the inner tracker and the fitted global track to have $p_T > 40$ GeV and $|\eta| < 2.1$. The specific CMS trigger name used in both 2011 and 2012 was HLT_Mu40_eta2p1. A lower p_T threshold of 30 GeV was used during the initial part of the 2011 run. To compensate for increased event rates due to higher instantaneous luminosity in the later

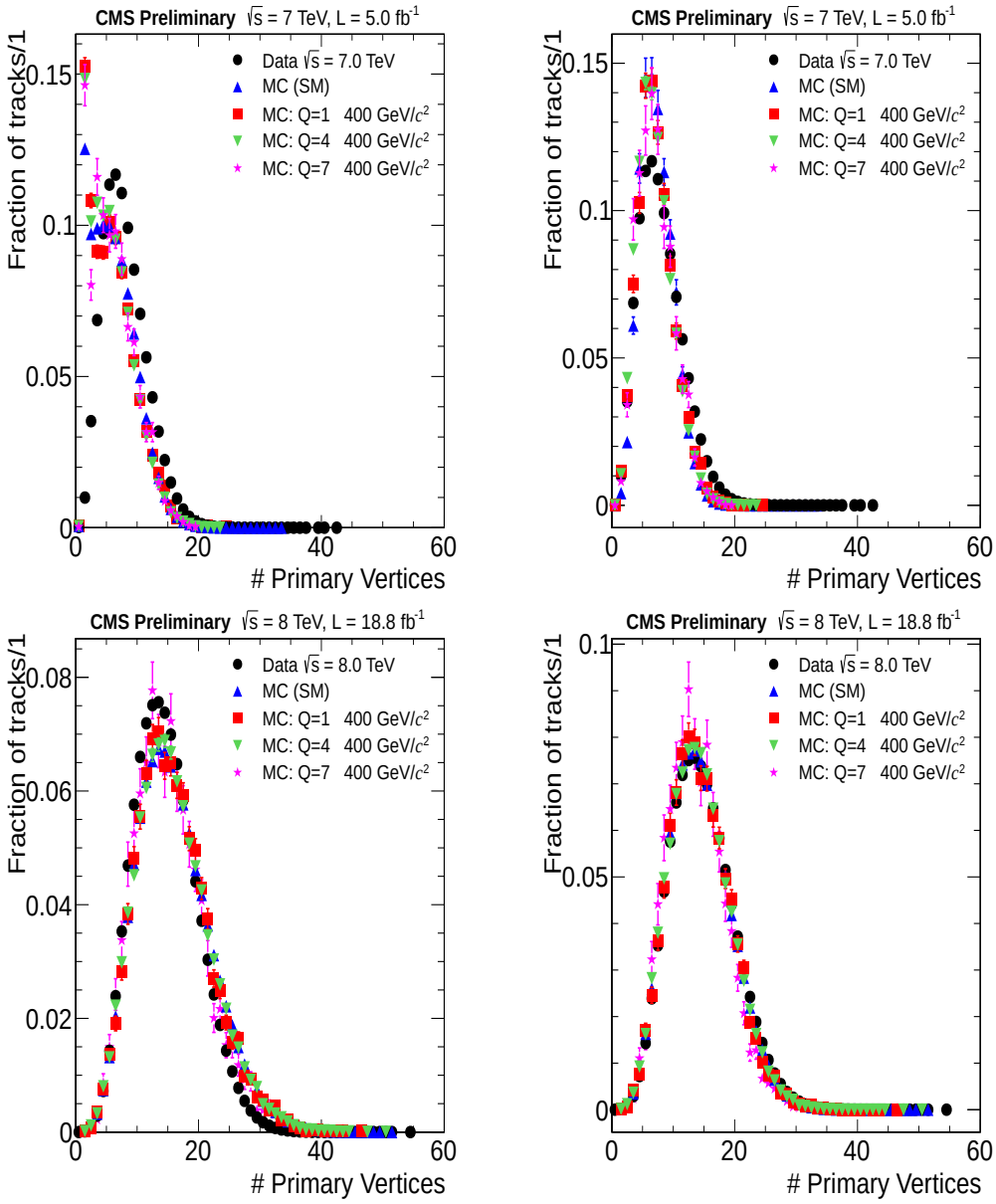

Figure 4.6: Distributions of the number of primary vertices in data, SM MC, and multiply charged HSCP simulations before (left) and after reweighting (right) at $\sqrt{s} = 7$ (top) and 8 TeV (bottom).

part of the run, the threshold was raised to 40 GeV. Data collected with lower thresholds were reprocessed requiring a 40 GeV track. This trigger is sensitive to multiply charged HSCPs that are long-lived and energetic enough to reach the muon system.

All muon triggers used with the CMS detector include a L1-based RPC trigger. It operates during the -12.5 ns to $+12.5$ ns time window, when collisions occur, as well as during the $+12.5$ ns to $+37.5$ ns time window, when there are no collisions. Tracks selected by the RPC trigger are passed to the muon trigger at HLT and are recorded on passing the corresponding HLT requirements. This feature adds sensitivity to particles that arrive late to the muon system. The trigger was not available during the early part of the 2011 data taking period, covering 0.41 fb^{-1} ($\sim 8\%$ of 2011 data). Alternate signal MC samples with and without the RPC trigger were processed and appropriate weighting is used. Due to a misconfiguration, half of the RPC trigger system was not properly operational during part of the 2012 data taking period. The CMS detector recorded 0.16 fb^{-1} ($< 1\%$ of 2012 data) during the corresponding time period. Given that it represents a tiny fraction of all 2012 data, the corresponding data were excluded from the analysis.

The E_T^{miss} trigger requires missing transverse energy in the event to be 150 GeV or larger. The missing energy is computed using the particle flow reconstruction [56]. A cleaning procedure within the reconstruction rejects tracks reconstructed in the inner tracker that do not have a matching track reconstructed in the muon system and have mis-matched energy deposition in the calorimeter. Only the energy deposited in calorimeter is used in E_T^{miss} calculation. The specific CMS trigger name used in both 2011 and 2012 was HLT_PFMHT150. Slow particles will not be reconstructed by the muon trigger if they fail the timing requirements. However, a fraction of these events can be recorded using the E_T^{miss} trigger and reconstructed offline.

Muon, E_T^{miss}, and total trigger efficiencies for multiply charged HSCP signals of various masses and charges are shown in Fig. 4.7. Trends in the various trigger efficiencies with respect to charge and mass of the multiply charged HSCP can be understood in terms of their generator-level kinematics (Figs. 4.1 and 4.2). The generator-level β distributions of

HSCP candidates along with those that pass the muon, E_T^{miss}, and either of the two online selection requirements are shown in Figs. 4.8 and 4.9 for $\sqrt{s}$ = 7 TeV and $\sqrt{s}$ = 8 TeV respectively.

Muon trigger efficiency for multiply charged HSCPs increases with increasing mass, reaching a maximum value and then decreasing. The most energetic low mass HSCPs are produced in the forward direction. As the mass increases, the HSCPs become non-relativistic with a harder p_T spectrum. The latter contributes to the increase in efficiency with increase in mass. For higher masses, the β distribution is shifted towards lower values (Fig. 4.1). Timing requirements of the muon trigger result in the drop in efficiency for low-β particles resulting in lower trigger efficiencies with increasing mass. The E_T^{miss} trigger has a small contribution in the case of slow multiply charged HSCPs, as seen for large mass and large charge. E_T^{miss} trigger efficiency increases with increase in mass.

Muon trigger efficiency of a multiply charged HSCP with a given mass decreases as charge increases. This is primarily due to the reconstructed p_T being scaled by a factor of $1/Q$. Greater energy loss and eventual mismatch between the tracks reconstructed in the inner tracker and the muon system also contribute to the lowering in efficiency. E_T^{miss} trigger efficiency increases with increase in charge.

Total trigger efficiency for multiply charged HSCPs is dominated by the muon trigger and consequently has a similar trend in mass and charge as that of the muon trigger. Overlap between muon and E_T^{miss} trigger efficiencies results in the total being less than the sum of the individual efficiencies. For low charge, E_T^{miss} trigger efficiency largely overlaps with the muon trigger efficiency. With increase in charge, E_T^{miss} trigger contribution increases and are complementary to the muon trigger efficiency. The trigger efficiency is slightly enhanced going from 7 TeV to 8 TeV center-of-mass energy.

4.2.2 Offline Selection

The data sample collected online is further refined using offline selections. Energy loss measurements in the inner tracker yield $\frac{dE}{dx}$ while timing measurements in the muon system

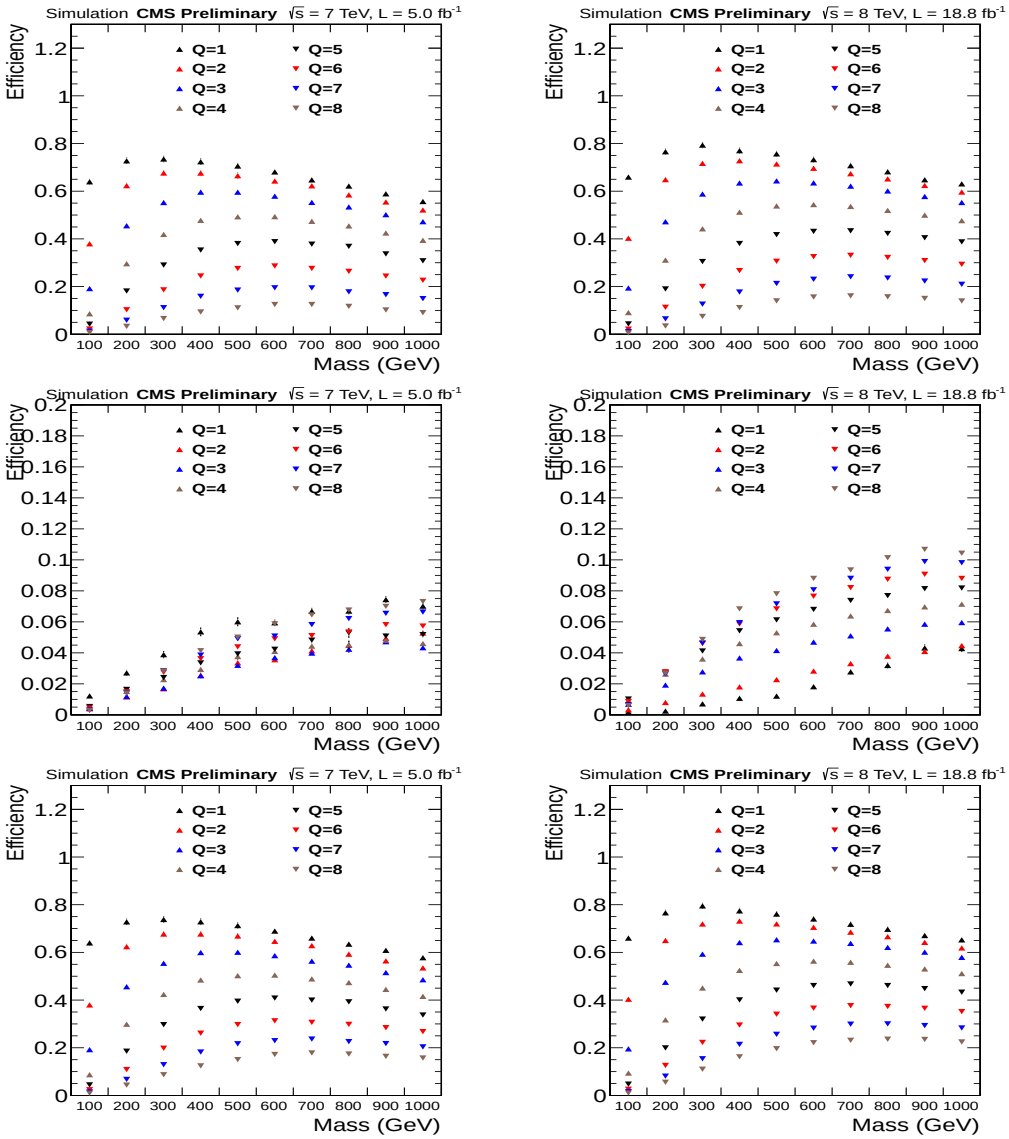

Figure 4.7: Muon (top), E_T^{miss} (middle) and total (bottom) trigger efficiency for multiply charged HSCPs of various charges and masses at $\sqrt{s} = 7$ TeV (left) and $\sqrt{s} = 8$ TeV (right).

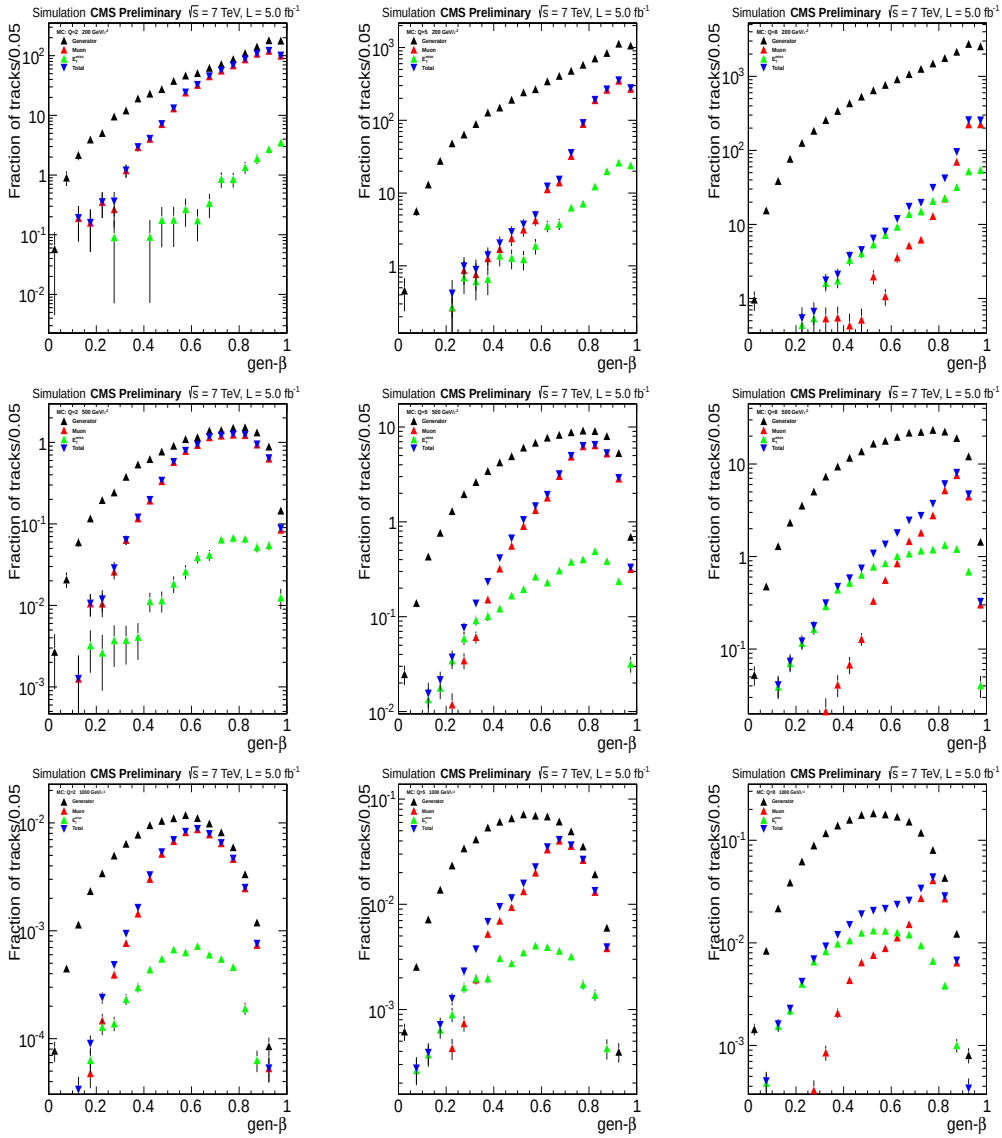

Figure 4.8: Generator-level distributions of β of multiply charged HSCPs for generated samples (black), and passing muon trigger (red), E_T^{miss} trigger (green), and combined trigger requirements (blue) at $\sqrt{s} = 7$ TeV. Different masses are shown in the three rows: 200 GeV (top), 500 GeV (middle), and 1000 GeV (bottom) while various charges are shown in the three columns: $2e$ (left), $5e$ (middle), and $8e$ (right).

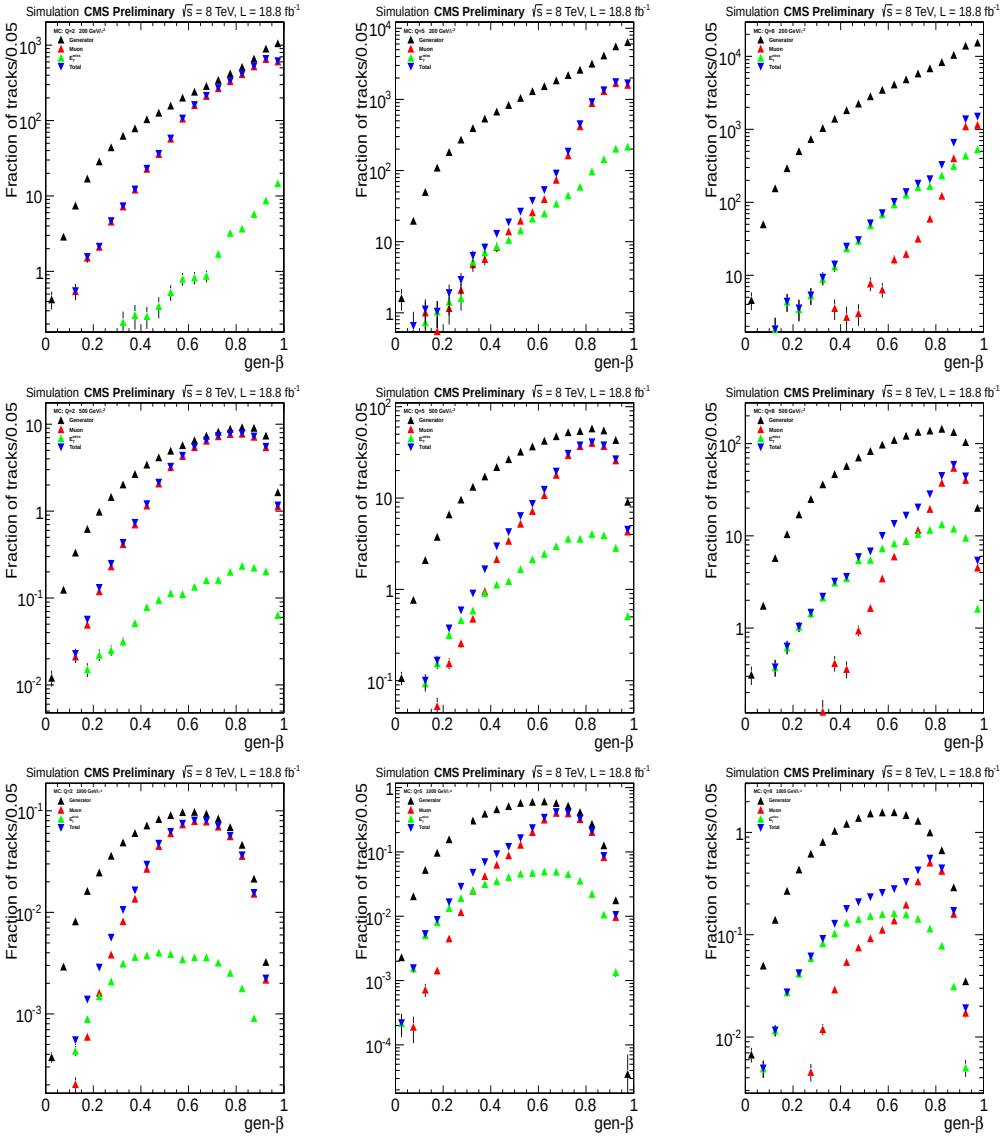

Figure 4.9: Generator-level distributions of β of multiply charged HSCPs for generated samples (black), and passing muon trigger (red), E_T^{miss} trigger (green), and combined trigger requirements (blue) at $\sqrt{s} = 8$ TeV. Different masses are shown in the three rows: 200 GeV (top), 500 GeV (middle), and 1000 GeV (bottom) while various charges are shown in the three columns: $2e$ (left), $5e$ (middle), and $8e$ (right).

Table 4.1: Offline selection variables and their type/values.

Variable	**Type or threshold value**
Reconstructed track	Global muon
$\|\eta\|$	< 2.1
Primary vertex: $\|z\|$	< 15 cm
Primary vertex: $\sqrt{x^2 + y^2}$	< 2 cm
Primary vertex: degrees of freedom	> 3
# Tracker hits (strips and pixels)	> 7
# Pixel hits	> 1
Fraction of valid hits	> 0.80
# $\frac{\Delta E}{\Delta x}$ measurements	> 5
# $1/\beta$ measurements	> 7
# DT- $1/\beta$ OR # CSC- $1/\beta$ measurements	> 5
Global muon track purity	> 1
Global muon track χ^2/dof	< 5.0
p_T	> 45 GeV
I_h	> 3.0 MeV/cm
$\sigma_{\langle 1/\beta \rangle}$	< 0.07
d_{xy}	< 0.5 cm
$\sum\limits_{\Delta R<0.3} p_T$	< 50 GeV
σ_{p_T}/p_T	< 0.25
d_z	< 0.5 cm
$\langle 1/\beta \rangle$	> 1.0

yield time-of-flight. Hence, tracks reconstructed in the inner tracker are matched to those in the muon system and required to form a global muon [57]. Further, the global muon track is required to have certain quality criteria. Offline kinematic variables of p_T, I_h, and $1/\beta$ are required to be above threshold values.

Table 4.1 lists all the offline selection variables and their types or threshold values. The selection variables are listed in Tab. 4.1 in the order in which they are applied. Distributions of the selection variables (Figs. 4.10 to 4.26) contain candidate tracks that meet all the previous selections other than the particular one being considered. Each of the selection variables are discussed ahead.

The effective geometric boundary of the muon trigger is $|\eta| = 2.1$. Hence, candidate

global muon tracks are required to be within $|\eta| < 2.1$. This search is insensitive to multiply charged HSCPs that are produced in the forward direction.

The reconstructed event is required have at least one good primary vertex. The quality of the primary vertex is ensured by requiring it to be within 2 cm and 15 cm with respect to the nominal interaction point along the radial and longitudinal directions, respectively. Also, the primary vertex is required to have at least 4 degrees of freedom.

The reconstructed global muon track is required to consist of at least 8 recorded (valid) hits in the inner tracker. Hits in both strip and pixel detectors are counted, the latter to add sensitivity for signals with fewer number of hits along its path. At least two of these hits must be in the pixel detector. It is required that 80% of the intermediate layers between the first and last silicon layers that record the reconstructed track should contain measurements related to the track. Figures 4.10, 4.11, and 4.12 show the distributions of the number of strip and pixel hits in the inner tracker, the number of pixel hits in the inner tracker, and the valid fraction of hits in the inner tracker, respectively. The distributions are shown for data, SM MC, and select multiply charged HSCP signal samples. The disagreement between data and SM MC arises from only including Drell-Yan $\rightarrow \mu\mu$ sample production in the $\sqrt{s}$ =8 TeV SM MC. I_h and I_{as} are computed using only hits in the strip detector and for tracks with at least six $\frac{\Delta E}{\Delta x}$ measurements to ensure a reliable evaluation. Figure 4.13 shows the distribution of the number of available measurements in the strip detectors.

Timing measurements in the various muon system layers are used to compute $\langle 1/\beta \rangle$. At least eight measurements are required to have a reliable estimate of $\langle 1/\beta \rangle$. Six of the measurements must be exclusively in either the DTs or the CSCs. Figure 4.14 shows the distribution of the number of available $1/\beta$ measurements in the muon system.

The reconstructed global muon track should be of high purity (quality > 1). Also, the χ^2 per degree of freedom of the fitted global muon track is required to be less than 5. Figures 4.15 and 4.16 show the quality and χ^2 per degree of freedom distributions for the global muon track.

The p_T of the global muon track, derived from the inner tracker, is required to be larger

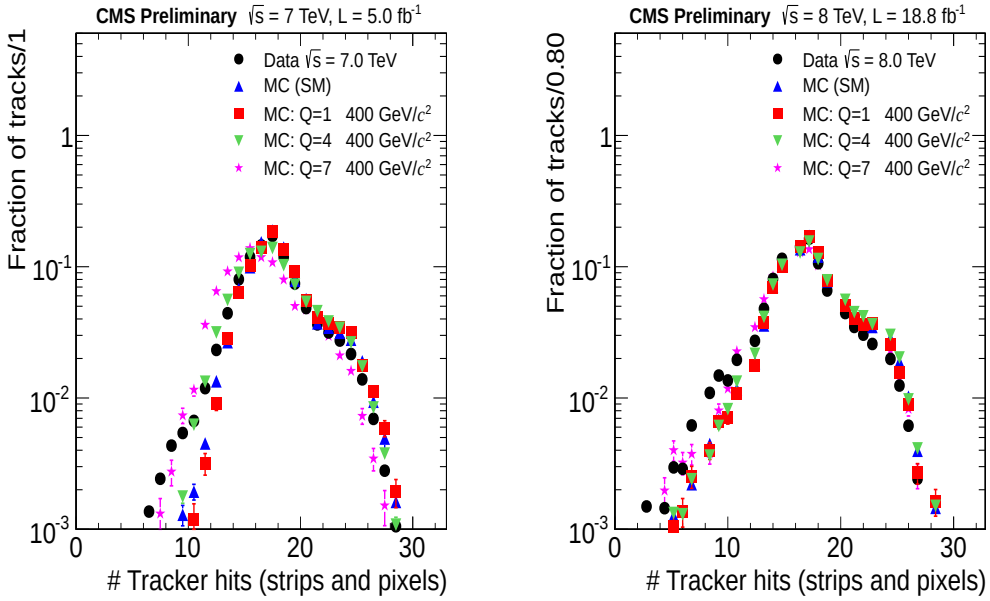

Figure 4.10: Distributions of number of pixel and strip hits in the inner tracker for data, SM MC, and multiply charged HSCP simulations for $\sqrt{s}$ =7 TeV (left) and $\sqrt{s}$ = 8 TeV (right).

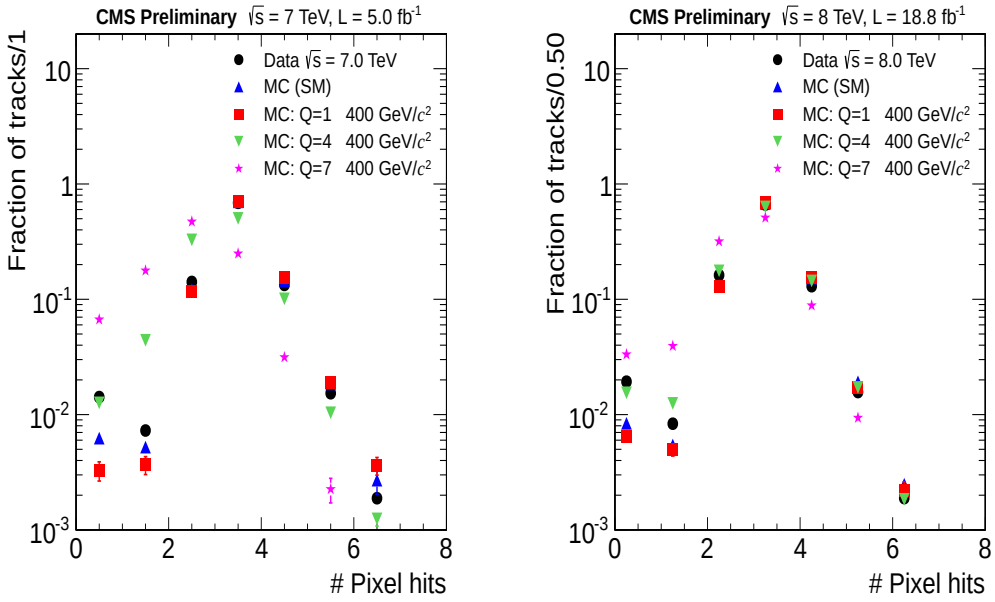

Figure 4.11: Distributions of number of pixel hits in the inner tracker for data, SM MC, and multiply charged HSCP simulations for $\sqrt{s}$ =7 TeV (left) and $\sqrt{s}$ = 8 TeV (right).

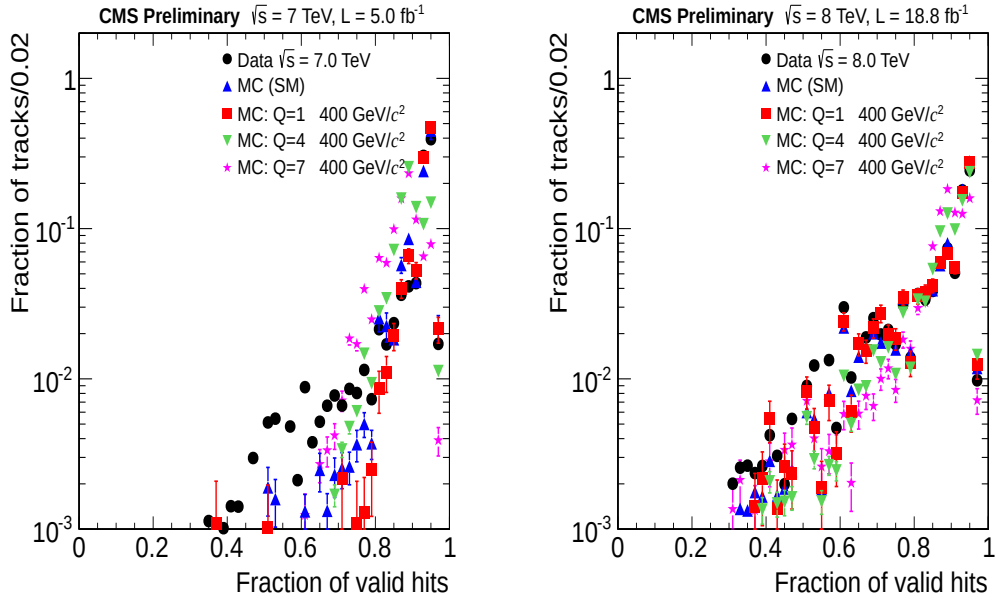

Figure 4.12: Distributions of fraction of valid hits in inner tracker for data, SM MC, and multiply charged HSCP simulations for $\sqrt{s}$ =7 TeV (left) and $\sqrt{s} = 8$ TeV (right).

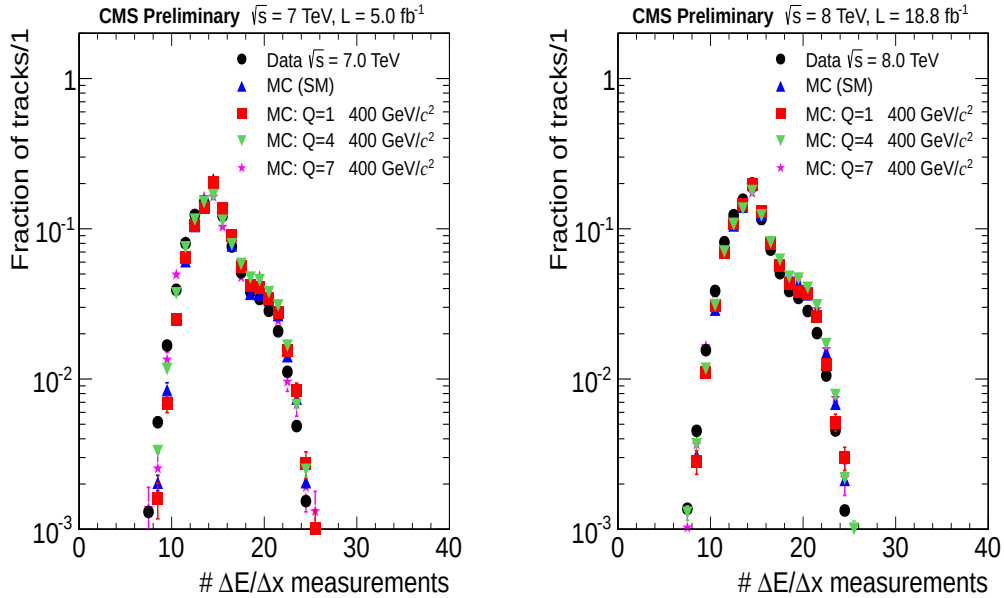

Figure 4.13: Distributions of number of available $\frac{\Delta E}{\Delta x}$ measurements in the strip detectors for data, SM MC, and multiply charged HSCP simulations for $\sqrt{s}$ =7 TeV (left) and $\sqrt{s} = 8$ TeV (right).

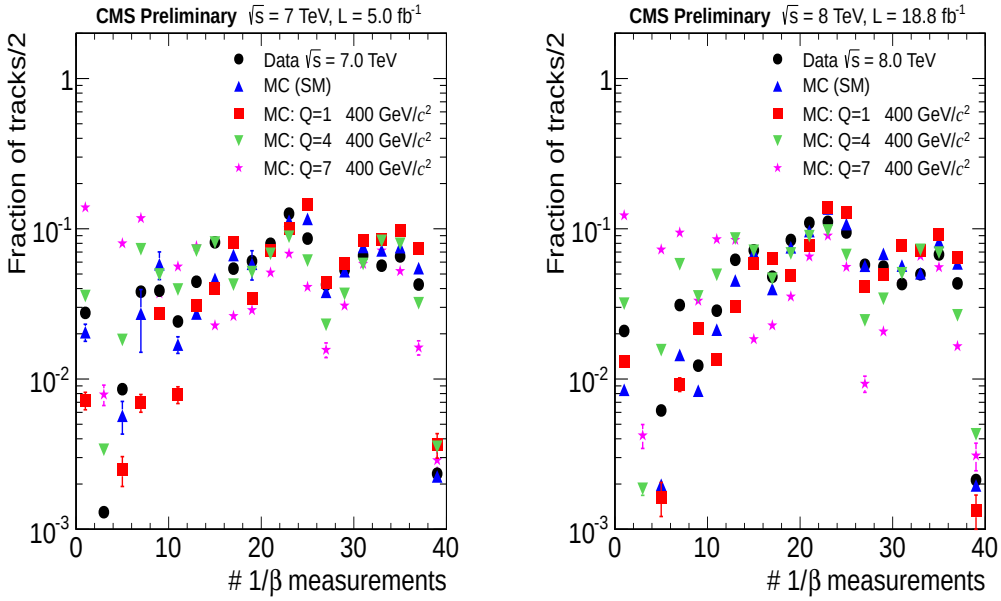

Figure 4.14: Distributions of number of $1/\beta$ measurements in the muon system for data, SM MC, and multiply charged HSCP simulations for $\sqrt{s}$ =7 TeV (left) and $\sqrt{s}$ = 8 TeV (right).

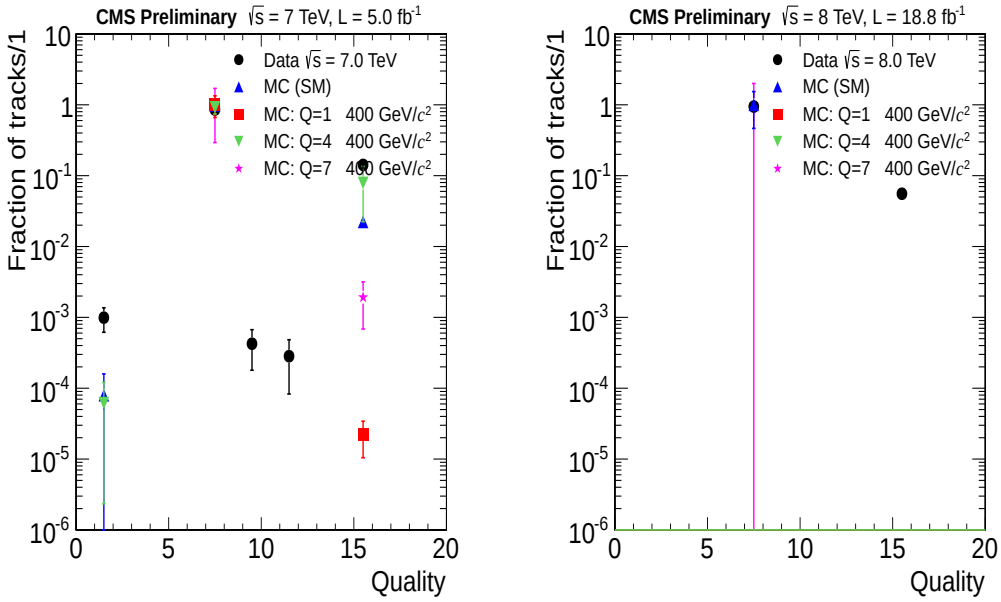

Figure 4.15: Distributions of quality for data, SM MC, and multiply charged HSCP simulations for $\sqrt{s}$ =7 TeV (left) and $\sqrt{s}$ = 8 TeV (right).

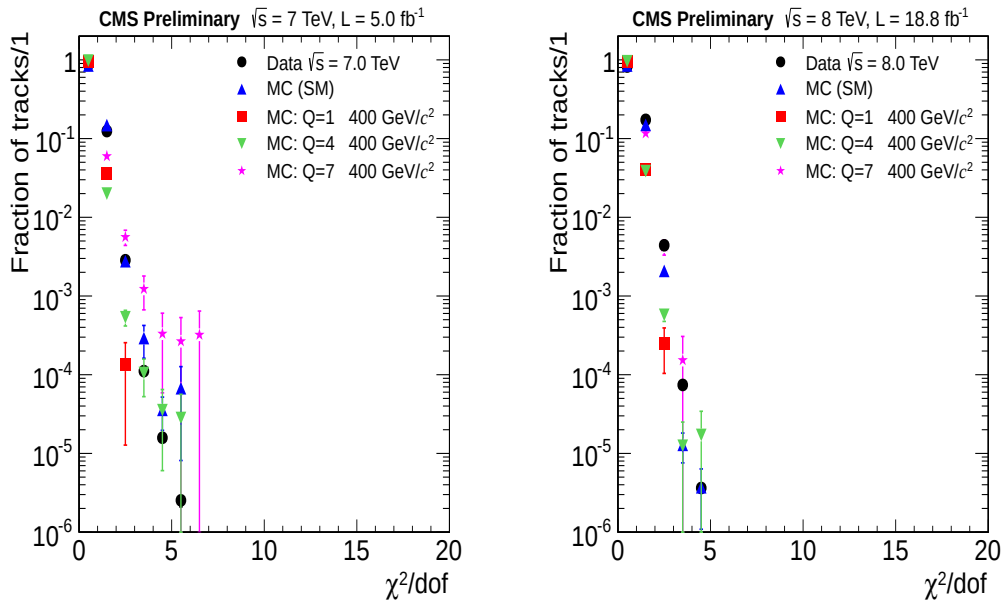

Figure 4.16: Distributions of χ^2 per degree of freedom for data, SM MC, and multiply charged HSCP simulations for $\sqrt{s}$ =7 TeV (left) and $\sqrt{s} = 8$ TeV (right).

than 45 GeV (Fig. 4.17). This threshold choice is guided by the muon trigger p_T threshold of 40 GeV. In the case of multiply charged HSCPs, the scaling of the reconstructed p_T by a factor of $1/Q$ results in reduced signal efficiency with increasing charge.

The I_h value associated with the track reconstructed in the inner tracker is required to be larger than 3 MeV/cm, which is approximately the average $\frac{dE}{dx}$ for a speed of light SM particle. This is motivated to reduce the number of stored minimum ionizing particle tracks in the data sample to a reasonable size. Multiply charged HSCPs, with large $\frac{dE}{dx}$, are unaffected by this choice. Figures 4.18 and 4.19 show the I_h and I_{as} distributions.

The uncertainty on the computed $\langle 1/\beta \rangle$ value, $\sigma_{\langle 1/\beta \rangle}$, is required to be less than 0.07. The relative uncertainty on the p_T measurement, σ_{p_T}/p_T, is required to be less than 25%. Figures 4.20 and 4.21 show the distributions of the uncertainty in $\langle 1/\beta \rangle$ and p_T measurements.

The reconstructed global muon track is required to be compatible with a good offline reconstructed primary vertex. The radial and longitudinal impact parameters, d_{xy} and d_z,

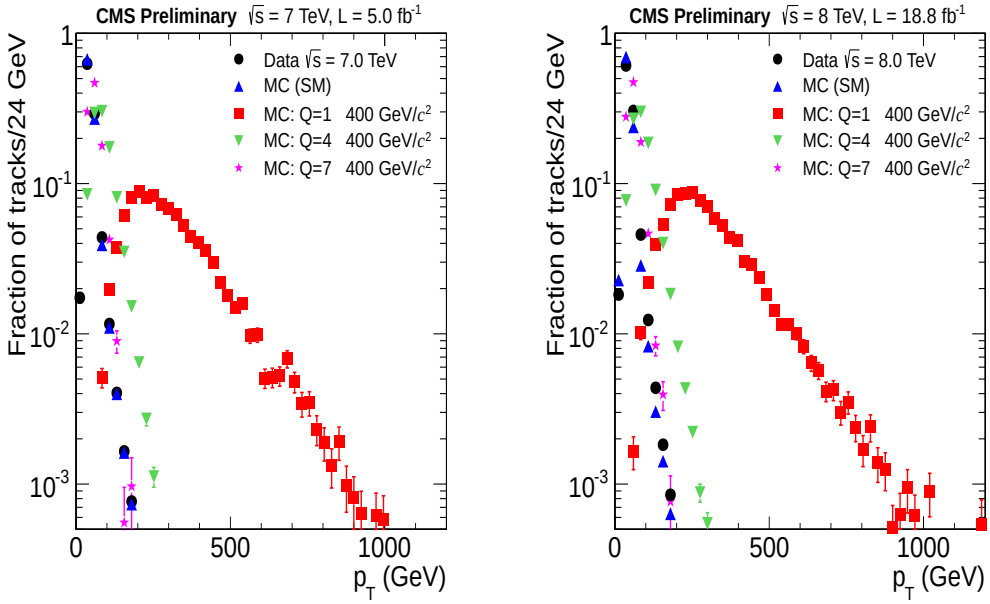

Figure 4.17: Distributions of p_T for data, SM MC, and multiply charged HSCP simulations for $\sqrt{s}$ =7 TeV (left) and $\sqrt{s}$ = 8 TeV (right).

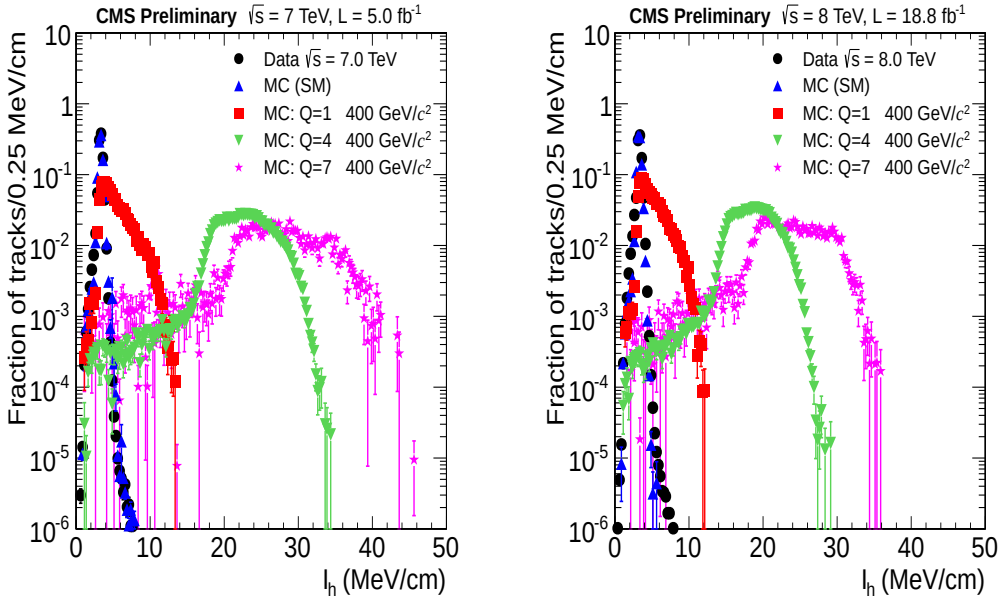

Figure 4.18: Distributions of I_h for data, SM MC, and multiply charged HSCP simulations for $\sqrt{s}$ =7 TeV (left) and $\sqrt{s}$ = 8 TeV (right).

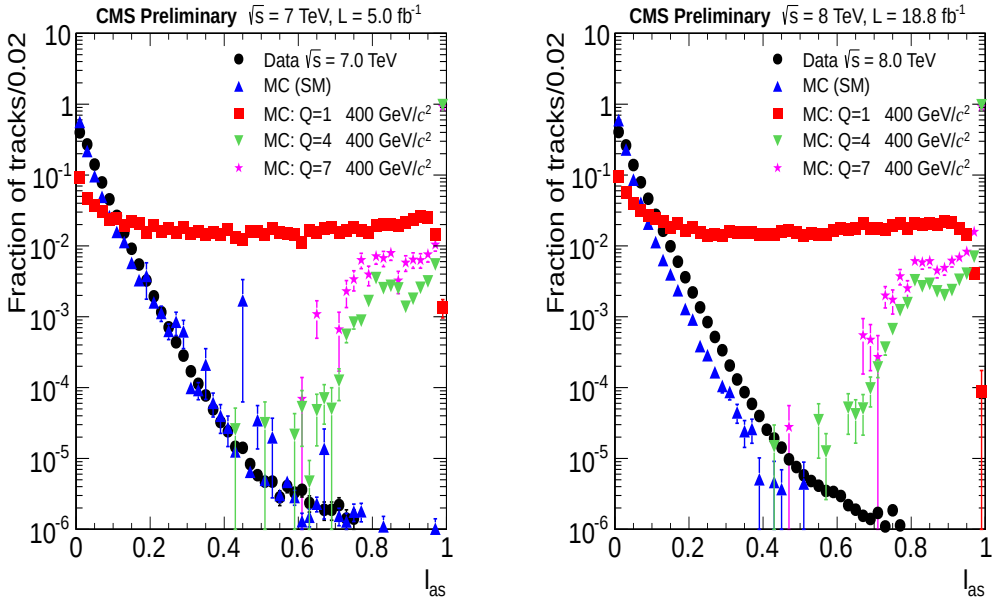

Figure 4.19: Distributions of I_{as} for data, SM MC, and multiply charged HSCP simulations for $\sqrt{s}$ =7 TeV (left) and $\sqrt{s} = 8$ TeV (right).

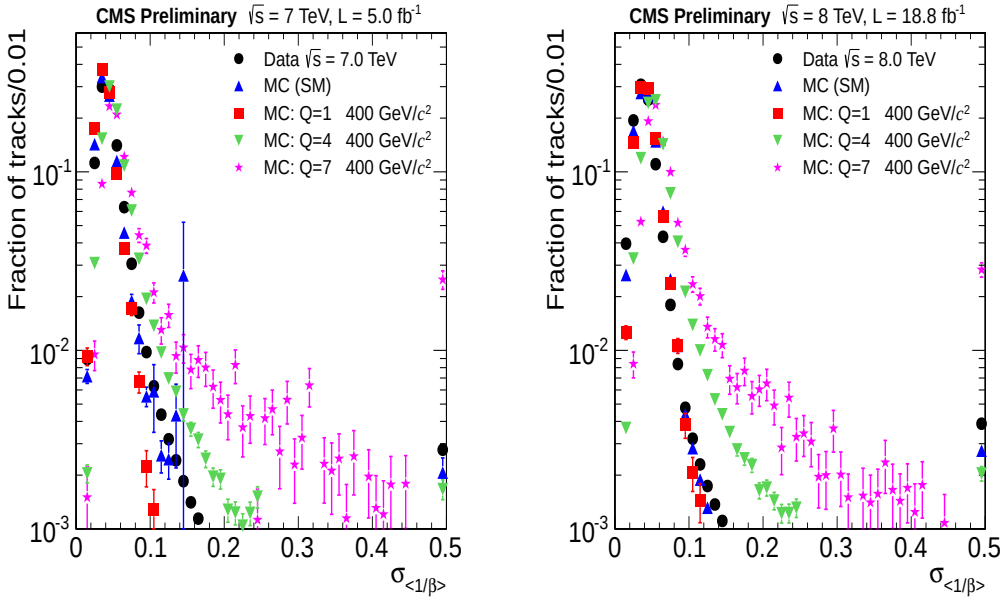

Figure 4.20: Distributions of $\sigma_{\langle 1/\beta \rangle}$ for data, SM MC, and multiply charged HSCP simulations for $\sqrt{s}$ =7 TeV (left) and $\sqrt{s} = 8$ TeV (right).

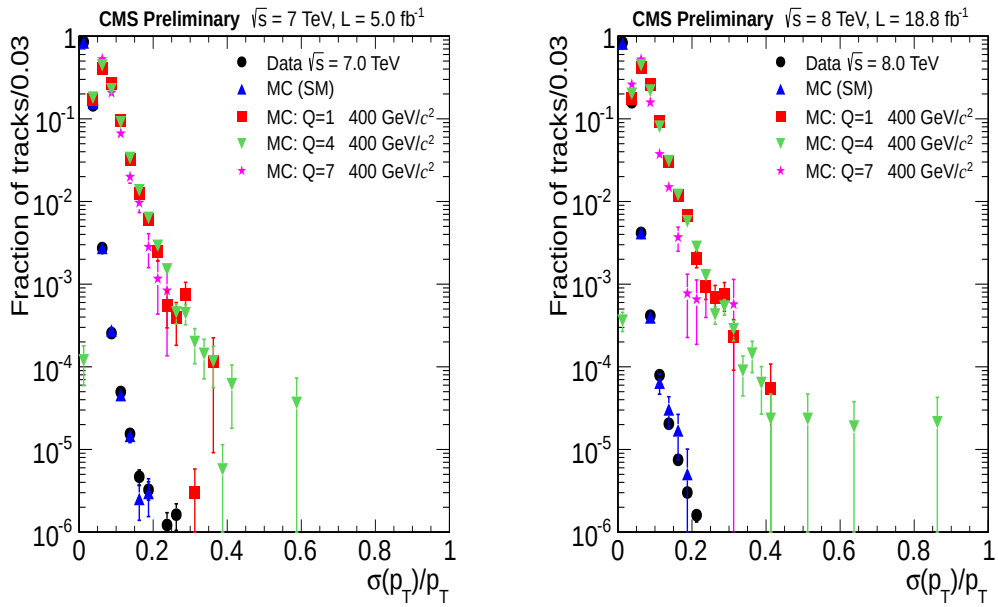

Figure 4.21: Distributions of relative uncertainty in p_T for data, SM MC, and multiply charged HSCP simulations for $\sqrt{s}$ =7 TeV (left) and $\sqrt{s} = 8$ TeV (right).

of the track reconstructed in the inner tracker with respect to the good primary vertex that minimizes d_z are both required to be less than 0.5 cm. Figures 4.22 and 4.23 show the d_{xy} and d_z distributions.

Large numbers of overlapping or adjacent hits, as arising in the case of jets, can bias the measured $\frac{dE}{dx}$ value of a track reconstructed in the inner tracker to higher values. Similarly, multiple adjacent hits can significantly degrade the hit resolution and bias the measured p_T to larger values. To reject such signal-like behaviours arising from the backgrounds, all HSCP searches in the CMS collaboration that employ the inner tracker apply isolation requirements on the track reconstructed in the inner tracker.

Two types of isolation requirements are considered: tracker-based and calorimeter-based. Tracker isolation, defined as the sum of the p_T of all tracks (apart from the candidate track) within a cone of $\Delta R = \sqrt{(\delta\phi)^2 + (\delta\eta)^2} = 0.3$ along the candidate track direction, is required to be less than 50 GeV. Calorimeter isolation, E/p, is defined as the ratio of the energy deposited in the electromagnetic and hadronic calorimeters along the candidate

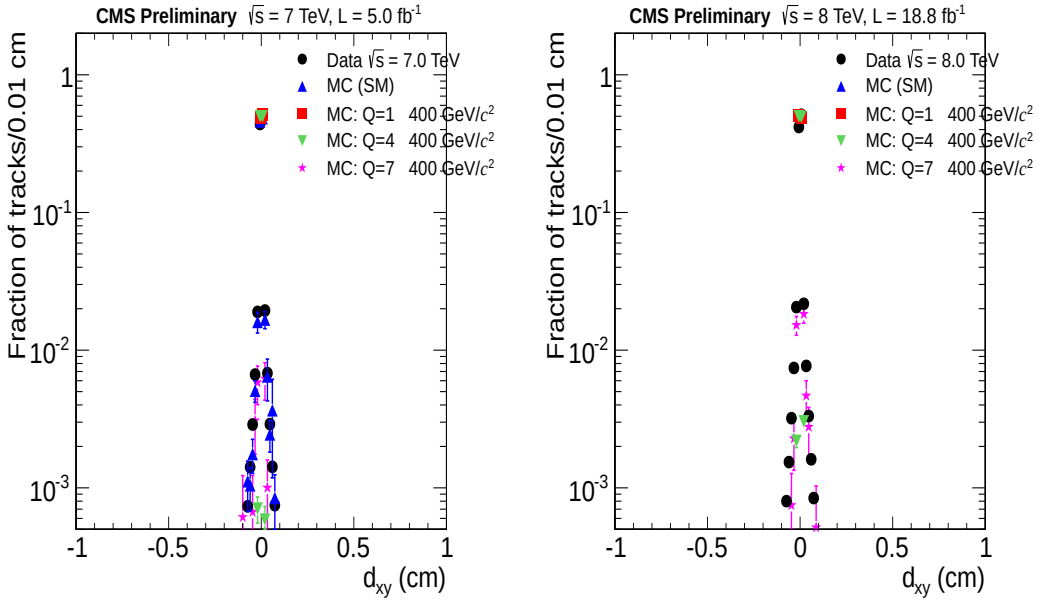

Figure 4.22: Distributions of d_{xy} for data, SM MC, and multiply charged HSCP simulations for $\sqrt{s}$ =7 TeV (left) and $\sqrt{s} = 8$ TeV (right).

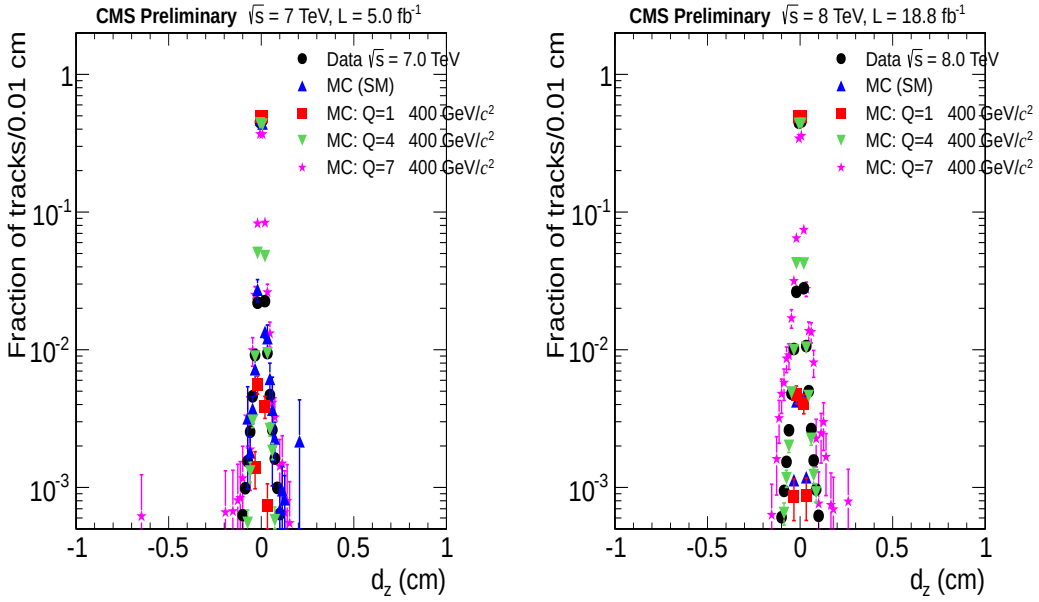

Figure 4.23: Distributions of d_z for data, SM MC, and multiply charged HSCP simulations for $\sqrt{s}$ =7 TeV (left) and $\sqrt{s} = 8$ TeV (right).

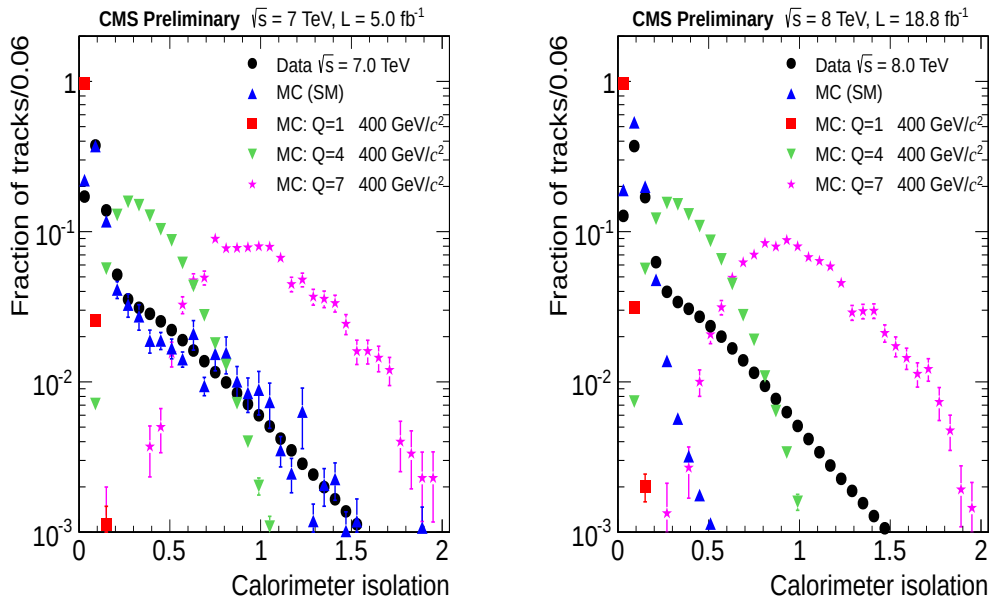

Figure 4.24: Distributions of calorimeter isolation for data, SM MC, and multiply charged HSCP simulations for $\sqrt{s}$ =7 TeV (left) and $\sqrt{s} = 8$ TeV (right). SM MC for $\sqrt{s} = 8$ TeV consists of only Drell-Yan $\rightarrow \mu\mu$ sample, resulting in data-SM MC discrepancy.

track direction within a cone of $\Delta R = 0.3$ to the candidate track momentum. Calorimeter isolation is required to be less than 0.3. The tracker-based isolation samples only the tracks near the candidate, whereas the calorimeter-based isolation samples the energy deposited by both the candidate and its nearby particles.

Figures 4.24 and 4.25 show the calorimeter and tracker isolation distributions. Relative to a $|Q| = 1e$ HSCP, a multiply charged HSCP will lose Q^2 times more energy along its path, while its track momentum will be scaled by a $1/Q$ factor. Requiring $E/p < 0.3$ significantly lowers the signal efficiency for multiply charged HSCP signals. Hence, the multiply charged HSCP search only requires the tracker isolation to be less than 50 GeV and does not use the calorimeter isolation for candidate selection.

Figure 4.26 shows the $1/\beta$ distributions. The global muon track is required to have a reconstructed $1/\beta$ value greater than 1.0.

The candidate efficiency at various stages of offline selections for multiply charged HSCP

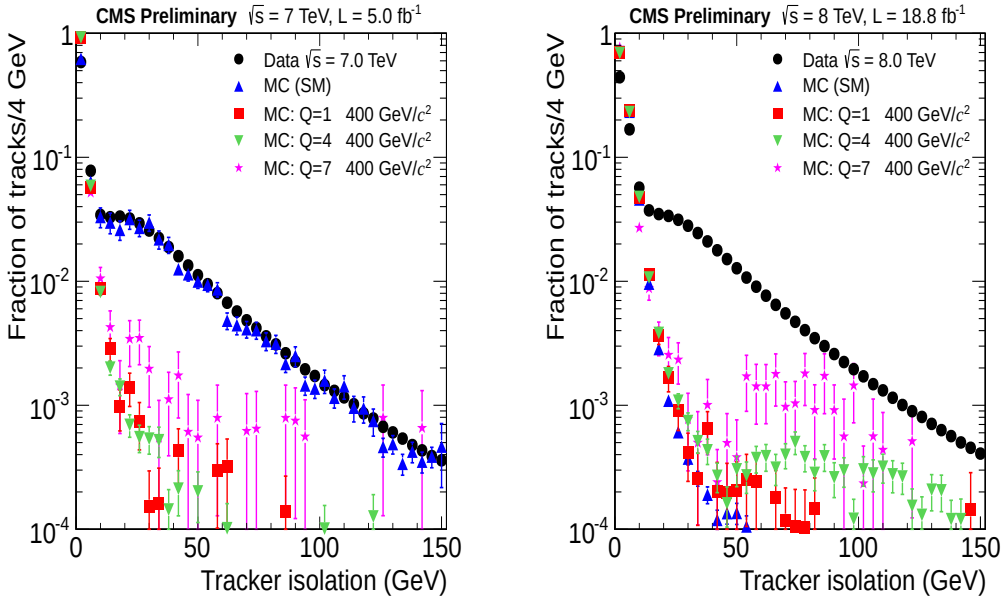

Figure 4.25: Distributions of tracker isolation for data, SM MC, and multiply charged HSCP simulations for $\sqrt{s}$ =7 TeV (left) and $\sqrt{s}$ = 8 TeV (right). SM MC for $\sqrt{s}$ = 8 TeV consists of only Drell-Yan $\rightarrow \mu\mu$ sample, resulting in data-SM MC discrepancy.

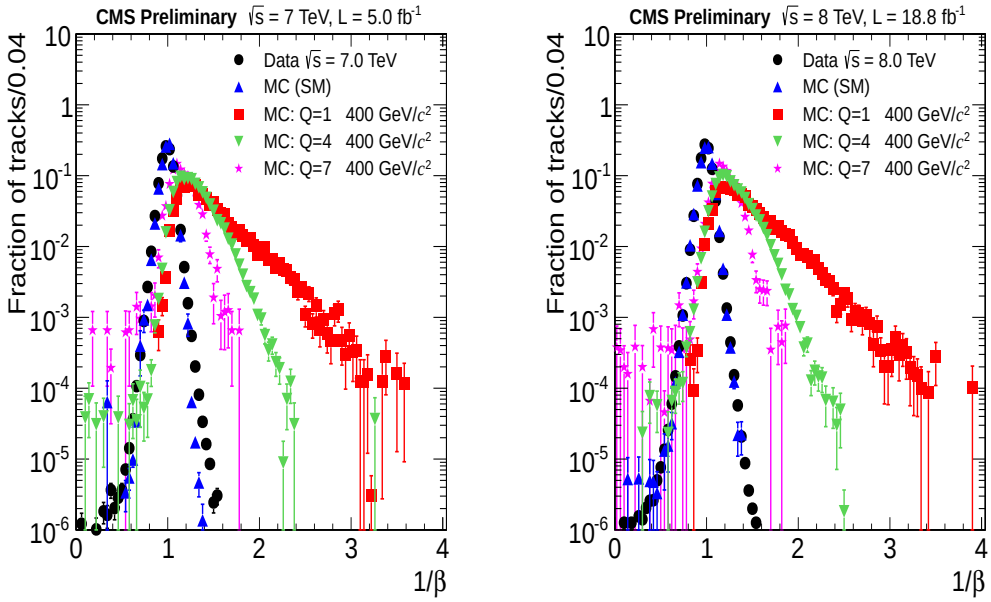

Figure 4.26: Distributions of $1/\beta$ for data, SM MC, and multiply charged HSCP simulations for $\sqrt{s}$ =7 TeV (left) and $\sqrt{s}$ = 8 TeV (right).

signals (with $Q = 1e, 4e$, and $7e$ and mass of 100, 400, and 700 GeV) as well as data for $\sqrt{s} = 7$ TeV and $\sqrt{s} = 8$ TeV are listed in Tabs. 4.2 and 4.3, respectively. Appendix C lists candidate efficiency of all considered multiply charged HSCP signals for the various offline selections. The various selections are applied in the order listed and the efficiency values are for the selection after the previous selections have been applied. The overall selection efficiency is also listed.

The efficiency of multiply charged HSCPs for the various offline selections vary with charge and mass. These variations can be understood in terms of differences in the generator-level p_T and β distributions which vary with the mass of the HSCP (Fig. 4.1) along with the scaling of the reconstructed p_T by a factor of $1/Q$ and the Q^2 enhancement of the energy loss:

- Larger energy loss with increasing charge results in a smaller fraction of HSCPs being tagged as global muons. The additional energy loss due to lower β for higher mass HSCPs further reduces the fraction of HSCPs that meet the requirements of a global muon.

- Larger bending with increase in charge of the HSCP results in lower efficiency for the number of $1/\beta$ measurements selection.

- The efficiency for the p_T selection decreases with increase in charge of the HSCP and increases with increase in mass of the HSCP. The decrease in efficiency for the p_T selection with increasing charge is reduced for larger HSCP masses.

- The p_T requirement ($p_T > 45 \times Q$) also means that only particles with large kinetic energies are selected. These surviving particles are highly boosted in the case of highly charged HSCPs and radiate δ-rays[1], yielding a large uncertainty in their measured $1/\beta$ values. Consequently, a large fraction of highly charged HSCPs fail the $\sigma_{\langle 1/\beta \rangle}$ selection requirement. The decrease in efficiency for the $\sigma_{\langle 1/\beta \rangle}$ selection with increase in charge is reduced for higher masses.

[1] δ-rays are highly energetic secondary electrons that produce further ionization.

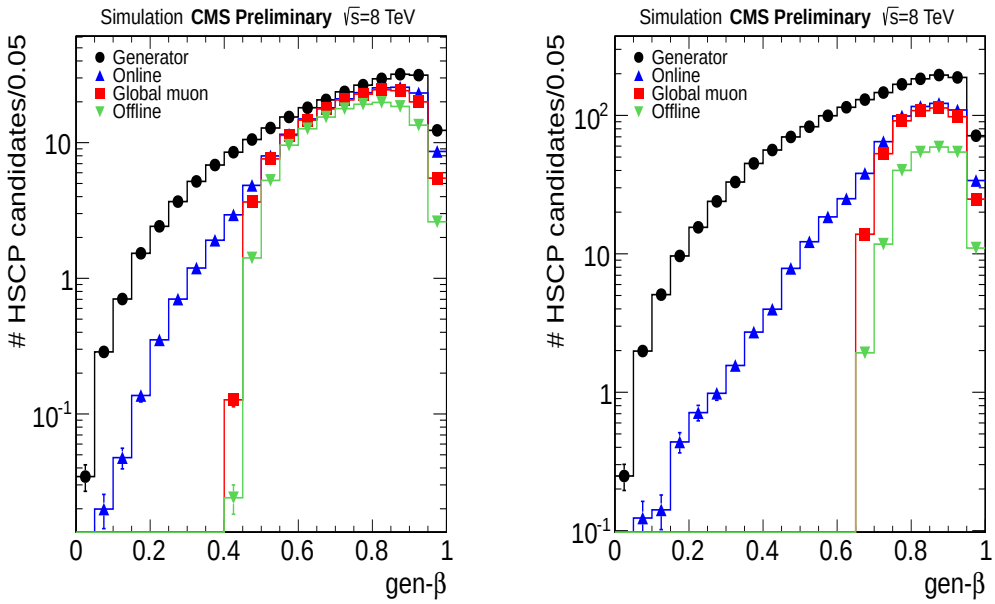

Figure 4.27: Generator-level distributions of β of multiply charged HSCPs for generated samples (black), passing online selection (blue), passing global muon selection (red), and passing offline selections (green). Distributions are shown for multiply charged HSCPs of mass 400 GeV and $Q = 2e$ (left) and $5e$ (right).

- Timing resolution in the muon system yields $1/\beta < 1.0$ for a larger fraction of the low mass and high charge HSCPs that meet all of the previous selection requirements resulting in their additional inefficiency.

The overall selection efficiency decreases with increasing HSCP charge (for all masses). With increasing mass, the p_T spectrum becomes harder and the β spectrum becomes softer. The overall selection efficiency increases with increase in mass of the HSCP. Above a certain mass, contributions of p_T and β spectrum to the offline selection efficiency counter-balance each other and the overall selection efficiency has a constant value.

The β distributions of multiply charged HSCP of mass 400 GeV and $Q = 2e$ and $5e$ at generator-level and after online and offline selections are shown in Fig. 4.27. The lower values of the β spectrum are suppressed with increasing charge of the HSCP.

Table 4.2: Candidate efficiency for various offline selections in data and HSCPs with select charges and masses at $\sqrt{s}$ =7 TeV. The offline selections are listed in the first column and the efficiency values are listed in the remaining columns. The efficiency is for the selection variable listed in the particular row after the selections in the upper rows have been applied. The second row lists the efficiency relative to the number of HSCPs that pass the online selection. The last row lists the overall offline selection efficiency.

Offline Selection	Data	$Q = 1e$			$Q = 4e$			$Q = 7e$		
		Mass (GeV)			Mass (GeV)			Mass (GeV)		
		100	400	700	100	400	700	100	400	700
Global muon	0.88	0.89	0.95	0.96	0.86	0.81	0.80	0.59	0.53	0.46
$\lvert\eta\rvert$	0.99	0.93	0.96	0.98	0.96	0.97	0.99	0.98	0.98	0.99
Primary vertex	1.00	1.00	1.00	1.00	1.00	1.00	1.00	1.00	1.00	1.00
# Tracker hits (strips and pixels)	1.00	1.00	1.00	1.00	1.00	1.00	1.00	1.00	1.00	1.00
# Pixel hits	0.98	0.99	0.99	0.99	0.93	0.94	0.95	0.72	0.76	0.78
Valid fraction	0.98	1.00	1.00	1.00	0.99	0.99	0.99	0.96	0.96	0.97
# $\frac{\Delta E}{\Delta x}$ measurements	1.00	1.00	1.00	1.00	1.00	1.00	1.00	1.00	1.00	1.00
# $1/\beta$ measurements	0.93	0.99	0.98	0.98	0.85	0.88	0.87	0.58	0.67	0.66
Quality	1.00	1.00	1.00	1.00	1.00	1.00	1.00	1.00	1.00	1.00
χ^2/dof	1.00	1.00	1.00	1.00	1.00	1.00	1.00	1.00	1.00	1.00
p_T	0.49	0.96	1.00	1.00	0.59	0.95	1.00	0.32	0.77	0.92
I_h	0.91	0.90	0.98	0.99	1.00	1.00	1.00	0.99	1.00	1.00
$\sigma_{\langle 1/\beta \rangle}$	0.91	0.98	0.97	0.96	0.74	0.82	0.80	0.44	0.64	0.69
d_{xy}	1.00	1.00	1.00	1.00	1.00	1.00	1.00	1.00	1.00	1.00
$\sum_{\Delta R<0.3} p_T$	0.93	1.00	1.00	1.00	1.00	1.00	1.00	0.97	0.99	1.00
σ_{p_T}/p_T	1.00	1.00	1.00	0.98	1.00	1.00	0.99	1.00	1.00	1.00
d_z	1.00	1.00	1.00	1.00	1.00	1.00	1.00	1.00	1.00	1.00
$\langle 1/\beta \rangle$	0.45	0.96	0.99	1.00	0.72	0.98	1.00	0.49	0.92	0.98
Overall	0.13	0.66	0.84	0.87	0.20	0.49	0.50	0.02	0.12	0.14

Table 4.3: Candidate efficiency for various offline selections in data and HSCPs with select charges and masses at $\sqrt{s}$ =8 TeV. The offline selections are listed in the first column and the efficiency values are listed in the remaining columns. The efficiency is for the selection variable listed in the particular row after the selections in the upper rows have been applied. The second row lists the efficiency relative to the number of HSCPs that pass the online selection. The last row lists the overall offline selection efficiency.

Offline Selection	Data	$Q = 1e$			$Q = 4e$			$Q = 7e$		
		Mass (GeV)			Mass (GeV)			Mass (GeV)		
		100	400	700	100	400	700	100	400	700
Global muon	0.79	0.86	0.92	0.94	0.83	0.81	0.80	0.65	0.61	0.57
$\lvert\eta\rvert$	0.99	0.89	0.94	0.97	0.96	0.95	0.96	0.96	0.98	0.98
Primary vertex	1.00	1.00	1.00	1.00	1.00	1.00	1.00	1.00	1.00	1.00
# Tracker hits (strips and pixels)	0.99	0.99	0.99	0.99	0.99	0.99	0.99	0.98	0.99	0.99
# Pixel hits	0.97	0.99	0.99	0.99	0.97	0.97	0.97	0.91	0.93	0.93
Valid fraction	0.94	0.97	0.96	0.97	0.96	0.97	0.97	0.95	0.96	0.97
# $\frac{\Delta E}{\Delta x}$ measurements	1.00	1.00	1.00	1.00	1.00	1.00	1.00	1.00	1.00	1.00
# $1/\beta$ measurements	0.95	0.99	0.98	0.96	0.87	0.90	0.89	0.64	0.72	0.72
Quality	1.00	1.00	1.00	1.00	1.00	1.00	1.00	1.00	1.00	1.00
χ^2/dof	1.00	1.00	1.00	1.00	1.00	1.00	1.00	1.00	1.00	1.00
p_T	0.51	0.96	1.00	1.00	0.63	0.95	1.00	0.30	0.80	0.93
I_h	0.90	0.91	0.98	0.99	1.00	1.00	1.00	1.00	1.00	1.00
$\sigma_{\langle 1/\beta \rangle}$	0.95	0.98	0.96	0.94	0.73	0.79	0.77	0.48	0.62	0.66
d_{xy}	1.00	1.00	1.00	1.00	1.00	1.00	1.00	1.00	1.00	1.00
$\sum_{\Delta R<0.3} p_T$	0.92	1.00	0.97	0.89	0.99	0.99	0.99	0.97	0.98	0.98
σ_{p_T}/p_T	1.00	1.00	1.00	0.98	1.00	1.00	0.99	1.00	1.00	1.00
d_z	1.00	1.00	1.00	1.00	1.00	1.00	1.00	1.00	1.00	1.00
$\langle 1/\beta \rangle$	0.43	0.93	0.99	1.00	0.74	0.97	0.99	0.68	0.96	0.98
Overall	0.11	0.57	0.72	0.67	0.22	0.47	0.48	0.03	0.18	0.21

4.3 Background Prediction

The multiply charged HSCP analysis employs a data-driven method to predict the expected SM background. The essence of data-driven prediction is that data candidates from one region of phase space (background region) are used to predict the number of expected SM candidates in another region of phase space (signal region). Distributions of data candidates in the background region need to be studied and understood to ensure the applicability of data-driven method. Data-driven methods avoid uncertainties in simulation that can be large or unknown.

Data distributions of $1/\beta$ in different I_h (Fig. 4.28) and I_{as} (Fig. 4.29) ranges are similar. The various I_h and I_{as} ranges considered in Figs. 4.28 and 4.29 correspond to low values of $\frac{dE}{dx}$, as expected for SM particles that satisfy all online and offline selections. Multiply charged HSCPs have large $\frac{dE}{dx}$ values and should have a minimal presence, if any, in the low-$\frac{dE}{dx}$ phase space. Similarity of $1/\beta$ curves in different $\frac{dE}{dx}$ ranges highlights the lack of evidence of correlation among these variables for SM particles. Non-correlation of $\frac{dE}{dx}$ and $1/\beta$ variables among SM particles that satisfy all online and offline selection requirements is expected. SM particles are highly boosted and reside in the flat region of the Bethe-Bloch curve (Figs. 1.2 and 3.3) where fluctuations in $\frac{dE}{dx}$ are random irrespective of the measured $1/\beta$ value.

The data-driven background prediction method used in the multiply charged HSCP analysis exploits the lack of correlation of I_{as} and $1/\beta$ variables among SM particles. The number of SM particles with large $\frac{dE}{dx}$ and large $1/\beta$ values can be obtained by scaling the number of SM particles in the region with small $\frac{dE}{dx}$ and large $1/\beta$ or vice-versa. Using I_{as} and $1/\beta$ selections, data candidates in the I_{as}-$1/\beta$ phase space (Fig. 4.30) are divided into four regions: A, B, C, and D. Region A consists of candidates with I_{as} and $1/\beta$ values lower than the selection threshold. Candidates in region B have I_{as} values lower than the selection value and $1/\beta$ values higher than the chosen threshold. Region C contains candidates with I_{as} and $1/\beta$ values larger and lower than selection threshold, respectively.

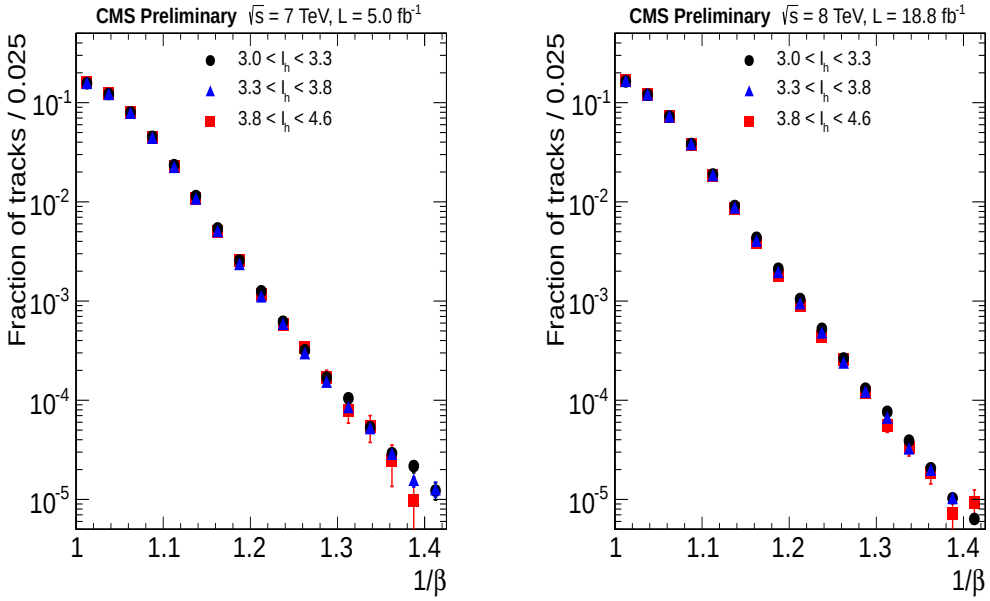

Figure 4.28: Distributions of $1/\beta$ in different I_h ranges for $\sqrt{s}$ =7 TeV (left) and 8 TeV (right) data.

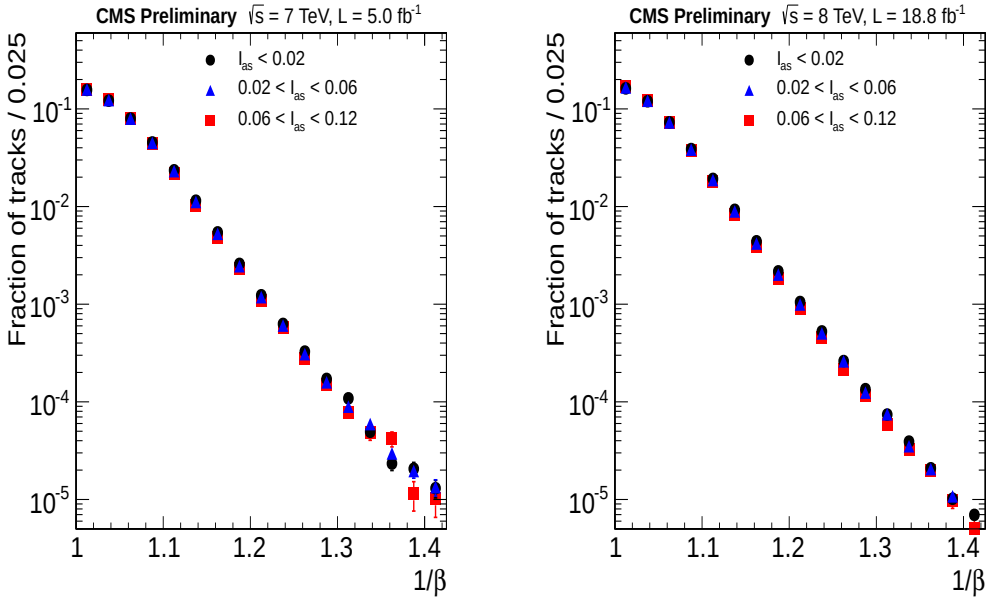

Figure 4.29: Distributions of $1/\beta$ in different I_{as} ranges for $\sqrt{s}$ =7 TeV (left) and 8 TeV (right) data.

Candidates in region D have I_{as} and $1/\beta$ values larger than the selection threshold. Given that SM particles are non-correlated in the variables of I_{as} and $1/\beta$, the number of SM candidates in the four regions (N_A, N_B, N_C, and N_D) are related via

$$\frac{N_A}{N_B} = \frac{N_C}{N_D}, \tag{4.1}$$

or,

$$N_D = \frac{N_B N_C}{N_A}. \tag{4.2}$$

This data-based prediction for the number of expected SM candidates with large I_{as} and $1/\beta$ values (Eq. 4.2) is referred to as the ABCD method. Statistical uncertainty in the number of predicted candidates in region D is given by

$$\sigma(N_D) = \sqrt{\left(\frac{N_B}{N_A}\right)^2 N_C + \left(\frac{N_C}{N_A}\right)^2 N_B + \left(\frac{N_B N_C}{N_A^2}\right)^2 N_A}. \tag{4.3}$$

The predicted and observed numbers of candidates in region D are compared to infer the agreement/disagreement with the SM case. Further, it is interpreted in terms of the presence or absence of multiply charged HSCPs in data collected with the CMS detector.

By using both $\frac{dE}{dx}$ and $1/\beta$ information, the background prediction method increases the separation between SM particles and multiply charged HSCPs. The 2-D distributions of I_h-$1/\beta$ and I_{as}-$1/\beta$ for data as well as select multiply charged HSCP signal are shown in Figs. 4.31 and 4.32, respectively.

Table 4.4 lists the numbers of data candidates in the A, B, C, and D regions for I_{as} selection of 0.05 and $1/\beta$ selection of 1.075. I_{as} and $1/\beta$ selections are such that SM candidates have an overwhelming presence in all four regions. For both $\sqrt{s}$ =7 and 8 TeV data, N_A/N_B and N_C/N_D along with N_A/N_C and N_B/N_D agree within $\sim$ 7% of each other. Numbers of predicted candidates in region D (Eq. 4.2) along with their statistical uncertainty (Eq. 4.3) are also listed. The ABCD method makes a slight underprediction of $\sim$ 7% relative to the observation. Systematic uncertainty on the background prediction

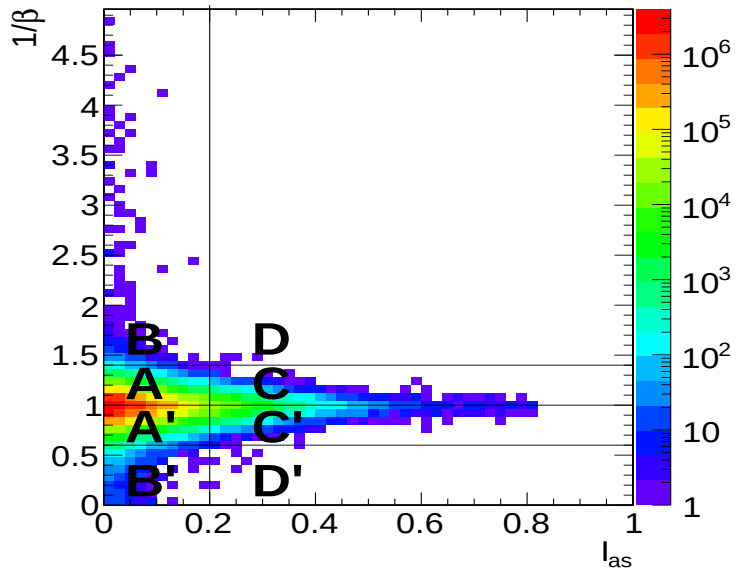

Figure 4.30: Illustration to explain ABCD background prediction method.

(Sec. 5.1) accounts for the underestimation.

Cosmic events are an important consideration for fractionally charged and muon-only HSCP searches [51]. The former is a dedicated search for HSCPs with $Q < 1e$ while the latter identifes HSCPs using only the muon system. The energy deposition of an out-of-time cosmic ray particle will not be completely profiled, resembling a fractionally charged particle behaviour. Muon-only HSCP search uses minimal inner tracker requirements and relaxed vertex conditions allowing an energetic cosmic ray particle to be identified as an HSCP. Cosmic background prediction in both fractionally charged and muon-only HSCP analyses have been evaluated to at most a few candidates. The multiply charged HSCP analysis has quality requirements on the track reconstructed in the inner tracker and the primary vertex offset relative to the nominal interaction point (Sec. 4.2.2), along with tight I_{as} selections (Ch. 6). These additional quality requirements render the cosmic background to be negligible for the multiply charged HSCP search.

There are two implicit assumptions in the background prediction method. First, the

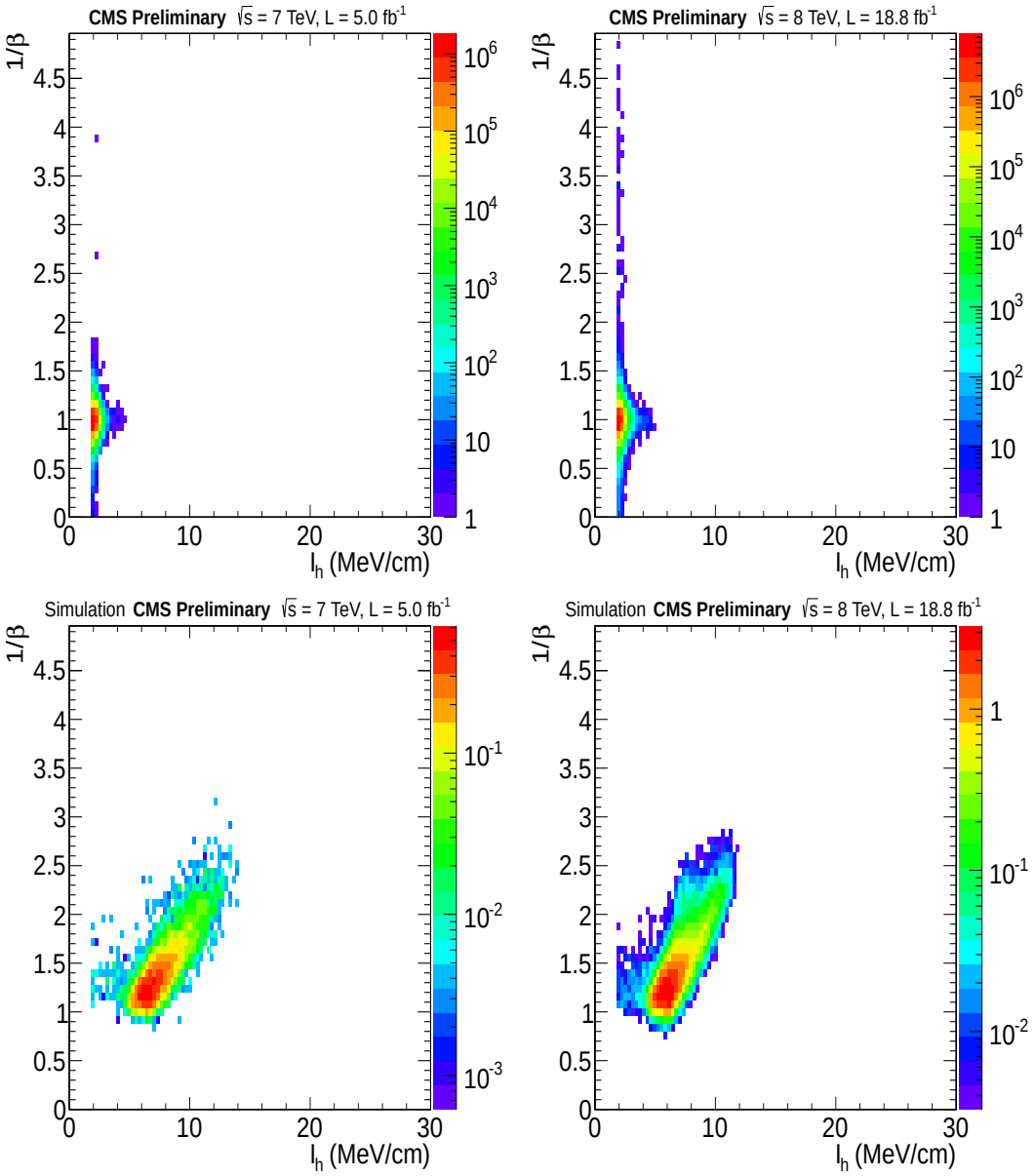

Figure 4.31: Distributions of candidates in I_h-$1/\beta$ plane for data (top) and multiply charged HSCP simulations with $Q = 2e$ and mass of 400 GeV (bottom). Left column is for $\sqrt{s}$ =7 TeV while right column shows $\sqrt{s}$ =8 TeV scenario.

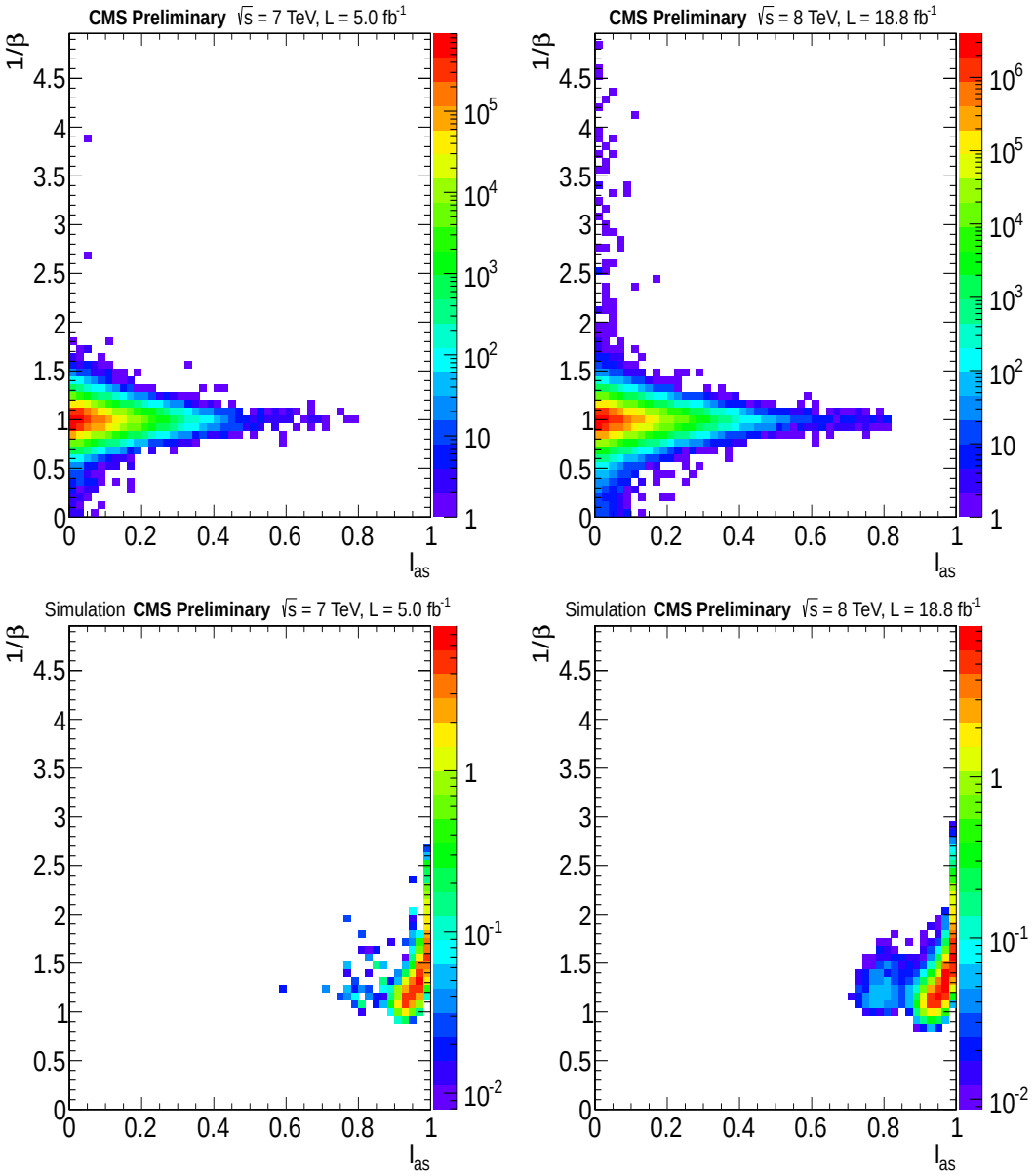

Figure 4.32: Distributions of candidates in I_{as}-$1/\beta$ plane for data (top) and multiply charged HSCP simulations with $Q = 2e$ and mass of 400 GeV (bottom). Left column is for $\sqrt{s}$ =7 TeV while right column shows $\sqrt{s}$ =8 TeV scenario.

Table 4.4: Numbers of candidates in A, B, C, and D regions for I_{as}=0.05 and $1/\beta$=1.075 in $\sqrt{s}$ =7 TeV and 8 TeV data. The bottom row lists predicted number of candidates in region D as per the ABCD method. Only statistical uncertainty on the prediction is quoted.

Region	I_{as}	$1/\beta$	Number of candidates	
			$\sqrt{s} = 7$ TeV	$\sqrt{s} = 8$ TeV
A	< 0.05	< 1.075	1300690	5356750
B	< 0.05	> 1.075	326717	1127750
C	> 0.05	< 1.075	469946	2025470
D	> 0.05	> 1.075	110957	397969
N_D prediction (ABCD method)			118044 ± 288	426421 ± 533

method assumes an absence of correlations in the variables of I_{as} and $1/\beta$ for SM particles. Small correlations among the two variables might not be visible in Figs. 4.28 and 4.29. It is important to quantify the effect of these correlations on the analysis in the case of selections where a small signal is expected over the predicted background. Also, the lack of correlations have been observed only for small values of $\frac{dE}{dx}$, the situation can change in the signal region of large $\frac{dE}{dx}$. Second, the presence of signal candidates in background regions can reduce the sensitivity of the search.

To explore the above mentioned issues with the validity of the background prediction method, we performed two types of cross-checks using data regions that are dominated by SM particles. The first test uses data candidates that pass all offline selections. A loose I_{as} and $1/\beta$ threshold defines A, B, C, and D regions (Fig. 4.30). Predicted and observed number of candidates in region D are compared. This cross-check is repeated for several I_{as} and $1/\beta$ selections. Small values of I_{as} and $1/\beta$ ensure that any signal from new physics in region D is overwhelmed by the SM contribution. Predicted and observed numbers of candidates along with their ratio for several loose I_{as} and $1/\beta$ selections are shown in Fig. 4.33. Uncertainty on the prediction includes both statistical and systematic (20%) contributions. There is reasonable agreement between prediction and observation.

A second cross-check of the background prediction method is done using data candidates passing all offline selections but with inverted $1/\beta$ selection ($1/\beta < 1.0$). An I_{as} and $1/\beta$

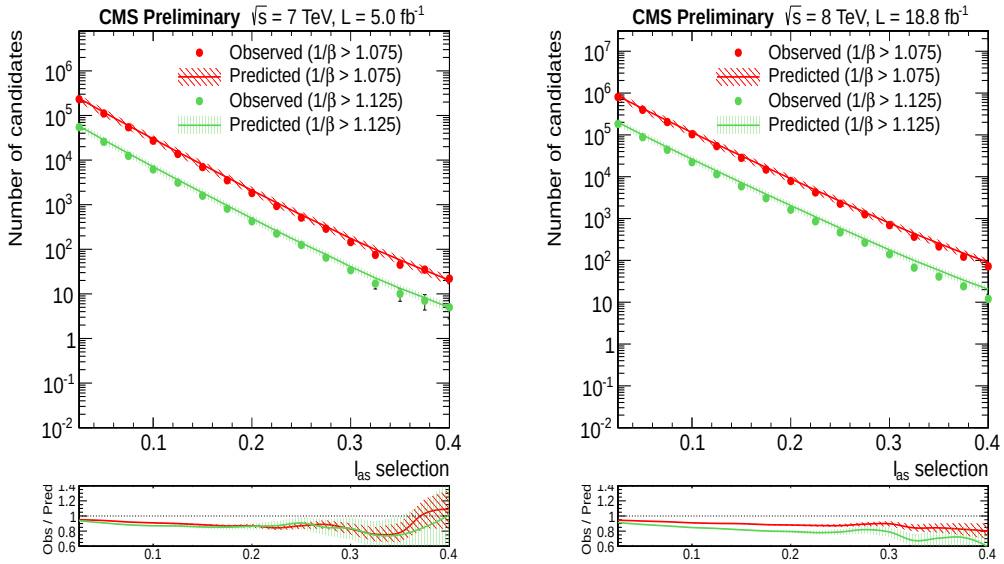

Figure 4.33: Number of predicted and observed candidates in region D along with their ratio for $\sqrt{s}$ =7 TeV (left) and 8 TeV (right) data. Uncertainty on the prediction includes both statistical and systematic (20%) contributions.

threshold defines the four regions: A', B', C', and D' (Fig. 4.30). Using ABCD method in $1/\beta < 1.0$ phase space, numbers of predicted and observed candidates in D' region are compared for several I_{as} and $1/\beta$ selections. Predicted and observed numbers of candidates in D' region, and their ratios are shown in Fig. 4.34. Uncertainty on the prediction includes both statistical and systematic (20%) contributions. A smaller $1/\beta$ selection decreases the likelihood of HSCP signals in the D' region. Hence, this cross-check for the validity of the ABCD method is extended to tight I_{as} and $1/\beta$ selections. Once again, there is decent agreement between prediction and observation.

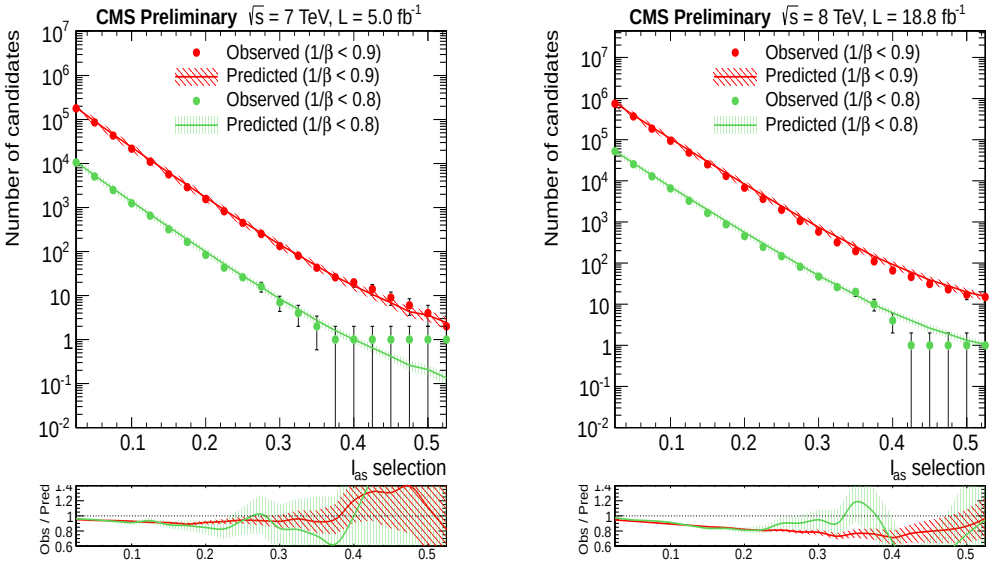

Figure 4.34: Number of predicted and observed candidates in region D' along with their ratio for $\sqrt{s}$ =7 TeV (left) and 8 TeV (right) data. Uncertainty on the prediction includes both statistical and systematic (20%) contributions.

CHAPTER 5

SYSTEMATIC UNCERTAINTIES

The multiply charged HSCP analysis considers systematic uncertainties on the background prediction method (Sec. 5.1) and signal simulation (Sec. 5.2). In addition, the uncertainty on the measured luminosity is taken as 2.2% for $\sqrt{s} = 7$ TeV data [58] and 4.4% for $\sqrt{s} = 8$ TeV data [59].

5.1 Background Prediction

Reasonable agreement between prediction and observation (Figs. 4.33 and 4.34) demonstrates the usability of the background prediction method. Assumptions of ABCD method (absence of correlations in I_{as} and $1/\beta$ variables among SM particles, and absence of signal in background regions) are further tested using alternate predictions from orthogonal data regions that are much farther from the signal region of large $1/\beta$ values. The spread in the various predictions is used to quantify the systematic uncertainty in background prediction.

The ABCD method (Sec. 4.3) can be used to predict the expected number of SM candidates in the signal (D) region using candidates in $1/\beta < 1.0$ region (A', B', C', and D' regions, see Fig. 4.30). These are given by P_2 and P_3 as

$$P_2 = \frac{N_B N'_C}{N'_A}, \tag{5.1}$$

$$P_3 = \frac{N_B N'_D}{N'_B}, \tag{5.2}$$

where I_{as} selection is common in both $1/\beta > 1.0$ and $1/\beta < 1.0$ regions while $1/\beta$ selection in the two regions, are in principle, unrelated. In the multiply charged HSCP analysis, we used $1/\beta$ selection in the $1/\beta > 1.0$ region to define the $1/\beta$ selection in the $1/\beta < 1.0$ region. If X is the $1/\beta$ selection in $1/\beta > 1.0$ region, $2 - X$ is the $1/\beta$ selection used in $1/\beta < 1.0$ region. P_2 is calculated using the core of background distribution that has a larger number of background candidates than P_3 which is calculated using the lower tail of background distribution. Original prediction of the ABCD method (Eq. 4.2) is referred to as P_1. Region B is common among all predictions and its relative contribution to statistical uncertainty in all predictions is the same. Hence, the term due to region B in Eq. 4.3 is ignored. Statistical uncertainty on P_1, $\sigma(P_1)$, is

$$\sigma(P_1) = \sqrt{\left(\frac{N_B}{N_A}\right)^2 N_C + \left(\frac{N_B N_C}{(N_A)^2}\right)^2 N_A}. \tag{5.3}$$

Similarly, statistical uncertainty on P_2 and P_3 are computed. The systematic uncertainty on the background prediction is quantified using the three predictions (P_1, P_2, and P_3) and their respective statistical uncertainty ($\sigma(P_1)$, $\sigma(P_2)$, and $\sigma(P_3)$).

The mean of all predictions is

$$\text{Mean} = \frac{1}{\sum\limits_{i=1}^{N} \frac{1}{(\sigma(P_i))^2}} \left[\sum_{i=1}^{N} \frac{P_i}{(\sigma(P_i))^2}\right], \tag{5.4}$$

where P_i are the individual predictions, $\sigma(P_i)$ are their respective statistical uncertainty values, and $N = 3$ is the number of predictions. The variance of the multiple predictions is

$$V_{\text{STAT+SYST}} = \sqrt{\frac{1}{N-1} \sum_{i=1}^{N} (\text{Mean} - P_i)^2}. \tag{5.5}$$

The size of the variance depends on both systematic and statistical uncertainties. Statistical

uncertainty in the variance is

$$V_{\mathrm{STAT}} = \sqrt{\frac{1}{N}\sum_{i=1}^{N}(\sigma(P_i))^2}. \tag{5.6}$$

Assuming that statistical and systematic uncertainties are added in quadrature to yield the variance, systematic uncertainty on the background prediction is computed as

$$V_{\mathrm{SYST}} = \sqrt{(V_{\mathrm{STAT+SYST}})^2 - (V_{\mathrm{STAT}})^2} \qquad (\text{if } V_{\mathrm{STAT+SYST}} > V_{\mathrm{STAT}}). \tag{5.7}$$

The three predictions for several I_{as} and $1/\beta$ selections are shown in Fig. 5.1 for both $\sqrt{s} = 7$ and 8 TeV data. With increasing I_{as} and $1/\beta$ thresholds, fewer candidates survive in C, C', and D' regions resulting in larger statistical uncertainties in the three predictions. Among the three predictions, P_3 is computed using the smallest numbers of data candidates and has the largest statistical uncertainty. This is more pronounced for $\sqrt{s} = 7$ TeV where approximately four times fewer data were collected than that at $\sqrt{s} = 8$ TeV. The various predictions have reasonable agreement amongst themselves.

Variance of the three predictions relative to their mean along with statistical and systematic uncertainty contributions to the variance relative to the mean are shown in Figs. 5.2 and 5.3 for $\sqrt{s} = 7$ TeV and $\sqrt{s} = 8$ TeV data, respectively. With increasing I_{as} and $1/\beta$ selections, the variance of the three predictions, and the statistical and systematic uncertainty contributions to the variance increase. For very high I_{as} and $1/\beta$ selections, the statistical uncertainty is comparable to (or even larger than) the variance and extraction of systematic uncertainty contribution breaks down. With four times more data, all three quantities have lower values at $\sqrt{s}$ =8 TeV than at $\sqrt{s}$ =7 TeV. Systematic uncertainty is less than 10% for most selections and increases beyond 20% for few selections. Final I_{as} and $1/\beta$ selections for the multiply charged HSCP analysis are 0.50 and 1.20, respectively (Ch. 6) for both $\sqrt{s} = 7$ TeV data and $\sqrt{s} = 8$ TeV data. Systematic uncertainty on the background prediction is quantified as 20%.

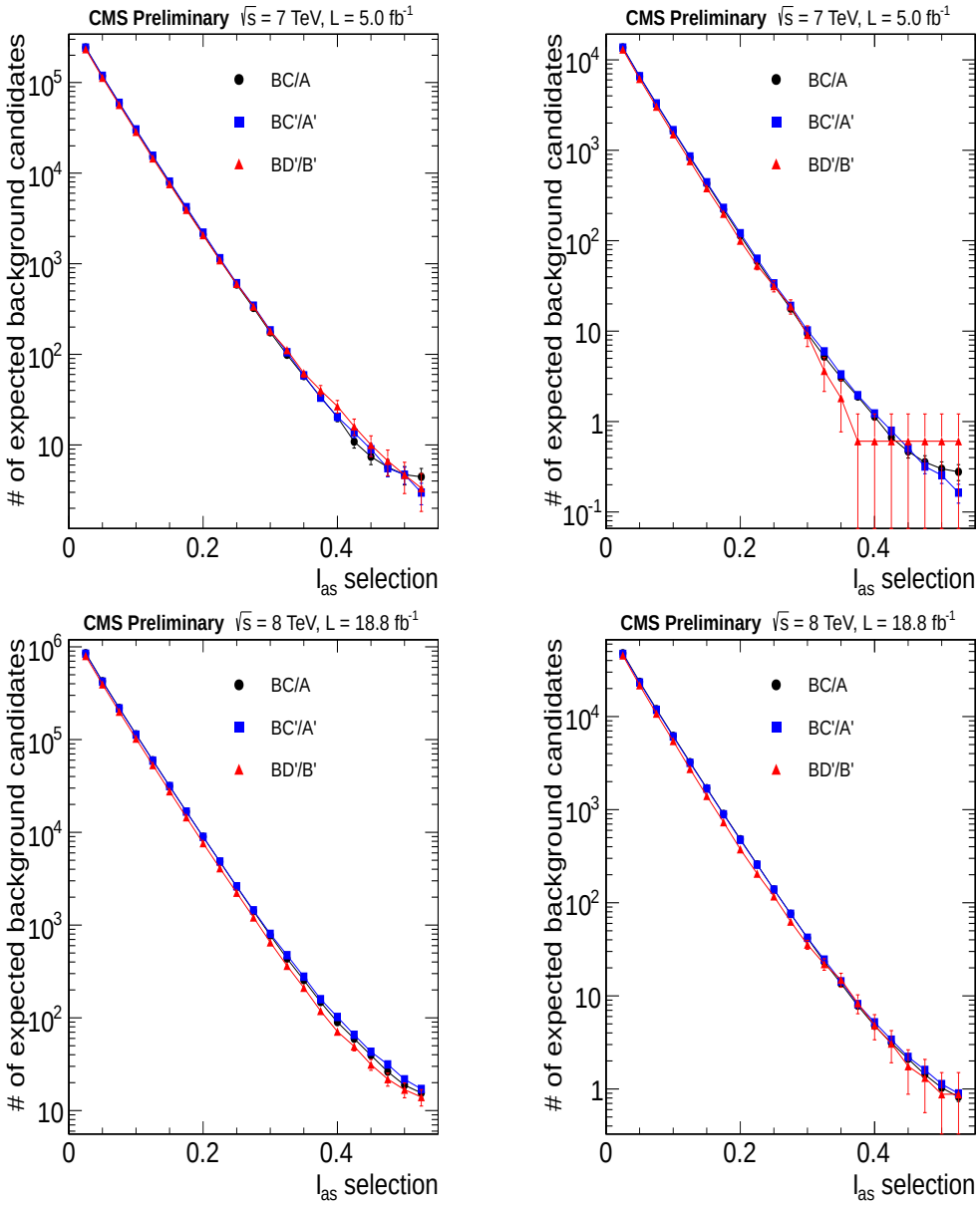

Figure 5.1: Multiple predictions for number of expected background candidates in region D for $\sqrt{s} = 7$ TeV data (top) and $\sqrt{s} = 8$ TeV data (bottom). I_{as} selections are shown in X-axis while $1/\beta$ selections are 1.10 (left) and 1.20 (right).

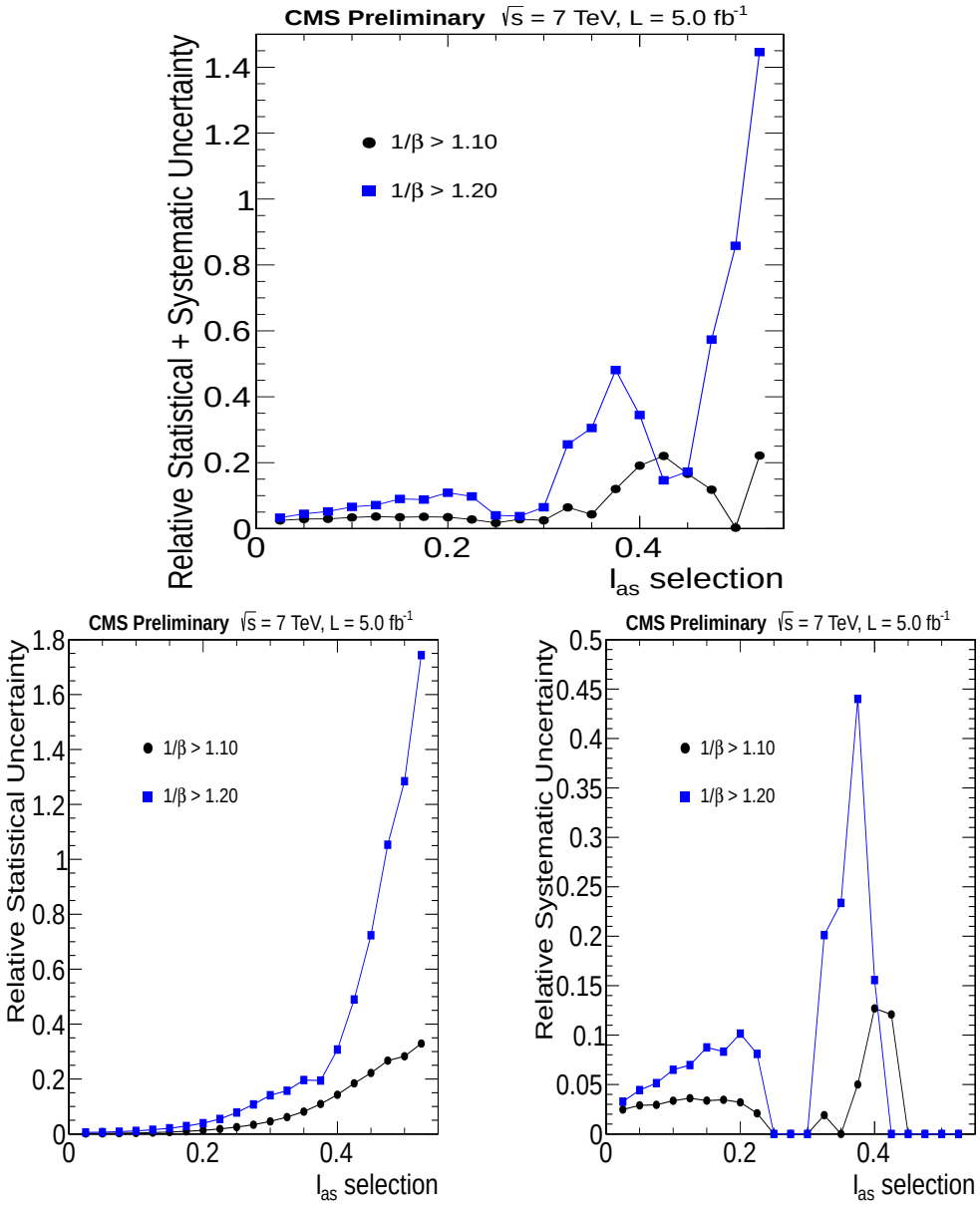

Figure 5.2: Variance of the multiple predictions (top), statistical uncertainty contribution to the variance (bottom left), and systematic uncertainty contribution to the variance (bottom right) for $\sqrt{s} = 7$ TeV data.

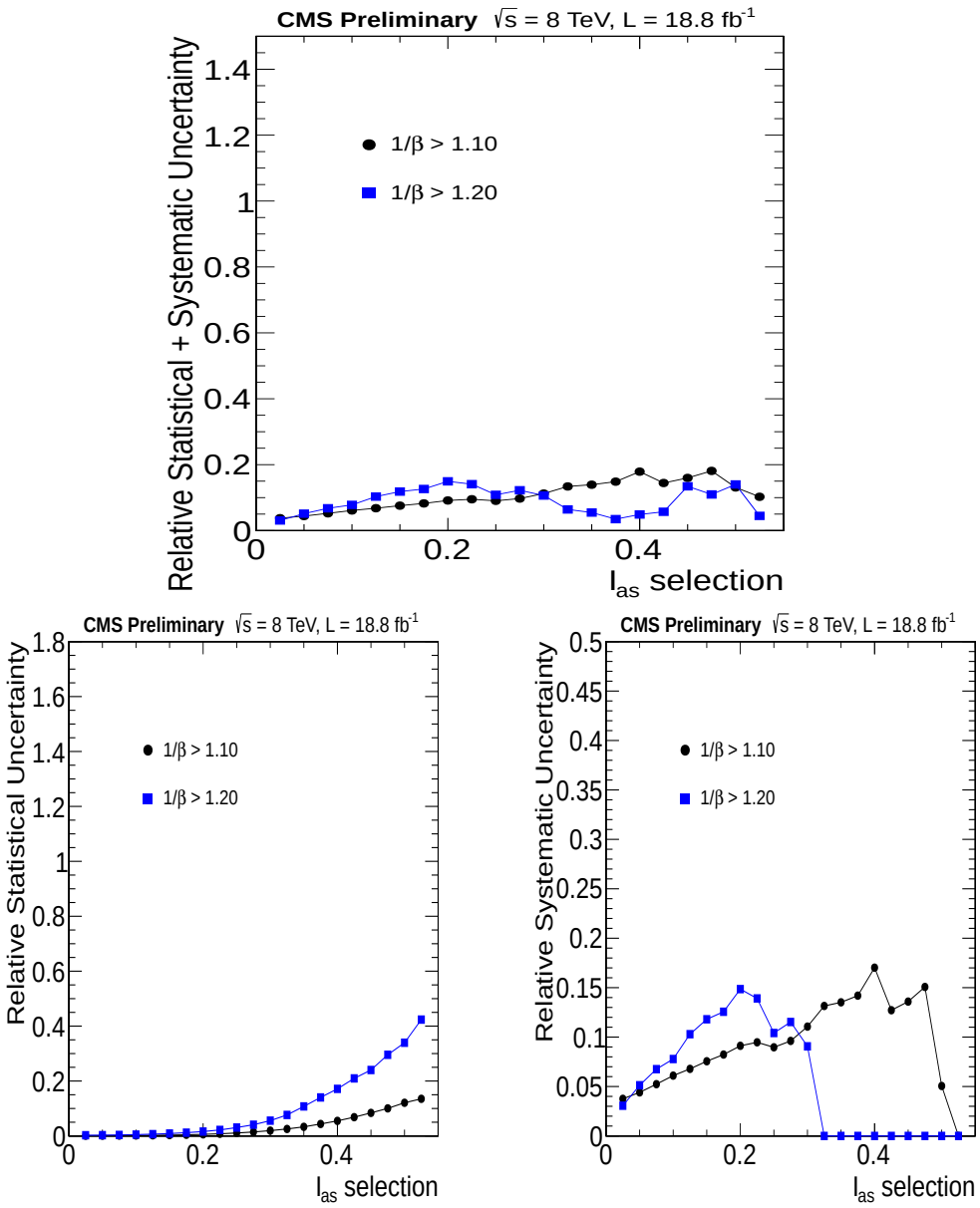

Figure 5.3: Variance of the multiple predictions (top), statistical uncertainty contribution to the variance (bottom left), and systematic uncertainty contribution to the variance (bottom right) for $\sqrt{s} = 8$ TeV data.

5.2 Signal Acceptance

Signal acceptance in the multiply charged HSCP analysis is determined using MC simulation. Several features of data and simulation were compared to quantify how well the latter models data collected with the CMS detector. Differences were taken as an uncertainty on the final signal acceptance.

Uncertainties are evaluated in either of two methods. First, data and SM-based simulation samples with known behaviour are compared. Second, for cases where no known SM sample exists for comparison of data and simulation, alternate signal samples were made using newer conservative values for variables whose effect were under study. These alternate samples were recreated using the full simulation chain, but had fewer statistics than the base samples. Change in signal acceptance for the final selection (Ch. 6) between these two samples is taken as a systematic uncertainty. Several of the uncertainties and the prescription to compute them are taken from Physics Object Group efforts within the CMS collaboration.

Uncertainties are considered on both the muon and E_T^{miss} triggers with each evaluated separately. Muon trigger efficiency differs in data and simulation by less than 5% over all energies. This is taken from muon reconstruction studies that used 2010 data [60].

A slow particle can be recorded in the subsequent bunch crossing due to non-synchronization of muon system timing electronics. This effect was studied in MC by shifting the timing of simulated hits by the non-synchronization of the muon system observed in data. Mean and RMS of timing values recorded in DTs, CSCs, and RPCs for data collected at $\sqrt{s}$ =7 and 8 TeV are listed in Tab. 5.1. Each subpart of DTs, CSCs, and RPCs that record timing are assigned a random timing offset value from a Gaussian distribution of mean and RMS. Alternate high mass gluino samples were reprocessed with recorded timing in the muon system offset by the values assigned to the various subparts using the procedure described above. Among all signal samples considered for various HSCP analyses, gluino samples have the most non-relativistic β spectrum and results obtained using them correspond to a

Table 5.1: Mean and RMS of timing values recorded in DTs, CSCs, and RPCs.

Muon subsystem	$\sqrt{s}$ =7 TeV		$\sqrt{s}$ =8 TeV	
	Mean	RMS	Mean	RMS
DT	0.5	1.0	0.5	1.0
CSC	0.0	1.5	2.3	1.0
RPC	0.06	5.14	0.06	5.14

conservative estimate for multiply charged HSCP signals produced via the modified Drell-Yan process. Signal efficiency for the final selection changed by 2% for $\sqrt{s}$ =7 TeV and by 4% for $\sqrt{s}$ =8 TeV. These uncertainties are used for multiply charged HSCP signals of all charges and masses.

Uncertainty on the jet energy scale (JES) is considered as a source of bias for the E_T^{miss} trigger. High mass gluino samples were reprocessed with the energy of simulated jets varied by the maximal JES uncertainty at HLT level. As compared to multiply charged HSCPs, gluino samples have a larger efficiency for E_T^{miss} trigger and provide a better estimate of the effect of JES uncertainty. Change in signal acceptance for final selection was 2% for $\sqrt{s}$ = 7 TeV and 1% for $\sqrt{s}$ = 8 TeV. These uncertainties are used for multiply charged HSCP signals of all charges and masses. Total uncertainty in trigger acceptance due to various sources is taken as the square root of the individual uncertainties added in quadrature.

The energy loss of minimum ionizing particles is under-estimated in simulation compared to data for both $\sqrt{s}$ =7 TeV and $\sqrt{s}$ =8 TeV. To neutralize the mismatch, hit-level $\frac{\Delta E}{\Delta x}$ in MC samples was scaled up so as to match the most probable $\frac{\Delta E}{\Delta x}$ in data. The scaling factors were 14% and 5% for $\sqrt{s}$ =7 TeV and $\sqrt{s}$ =8 TeV samples respectively. After rescaling, I_{as} distributions of minimum ionizing particles in data and simulation had a decent agreement.

Low-momentum protons have large $\frac{dE}{dx}$ and resemble HSCP-like behaviour. Uncertainties related to $\frac{dE}{dx}$ in the inner tracker are evaluated by comparing low-momentum protons in data and simulation. Hit-level $\frac{\Delta E}{\Delta x}$ of low-momentum protons in simulation were scaled up by the same factors mentioned above. Following the rescaling, I_{as} distribution of protons in different momentum ranges were fitted to a Gaussian (Fig. 5.4). Differences in mean and

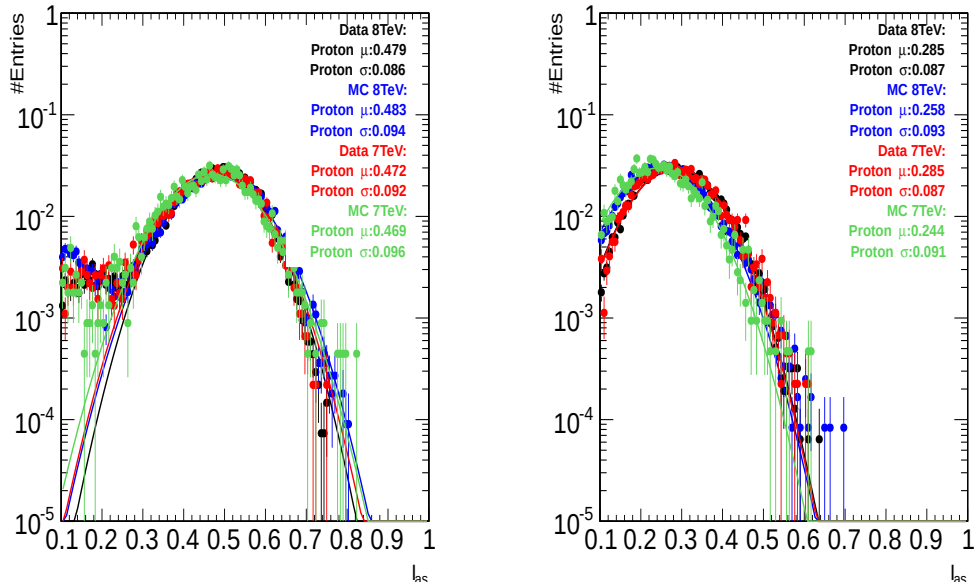

Figure 5.4: Distributions of I_{as} for protons in momentum range of 0.95–1.0 GeV (left) and 1.20–1.25 GeV (right). Distributions are shown for $\sqrt{s}$ = 7 and 8 TeV data as well as simulation. The solid lines represent a Gaussian fit to the respective distributions.

width of the fitted Gaussian between data and simulation (Fig. 5.5) are used to determine the uncertainty on I_{as} scale and resolution. Decent match of parameters in data and simulation is noted. Uncertainty on I_{as} scale is taken as the maximal difference between data and simulation, as 0.05 for both $\sqrt{s}$ =7 and 8 TeV. Widths in simulation are larger than in data and consequently, no uncertainty is considered on I_{as} resolution.

I_{as} values of signal samples were shifted up by 0.05 and the change in signal acceptance for the final selection was taken as the systematic uncertainty due to I_{as} scale. Final I_{as} selection in the multiply charged HSCP analysis is chosen as 0.5 (Ch. 6). Since I_{as} is underestimated in simulation, signal acceptance increases. For $Q = 1e$ samples, change in signal acceptance of up to 12% is seen for low masses and reduces to 4% for higher masses. Values of I_{as} of $Q \geq 2e$ samples are much farther from the final I_{as} selection and change in signal acceptance is zero.

Di-muon events yielding an invariant mass within a Z-boson mass window of 80-100 GeV

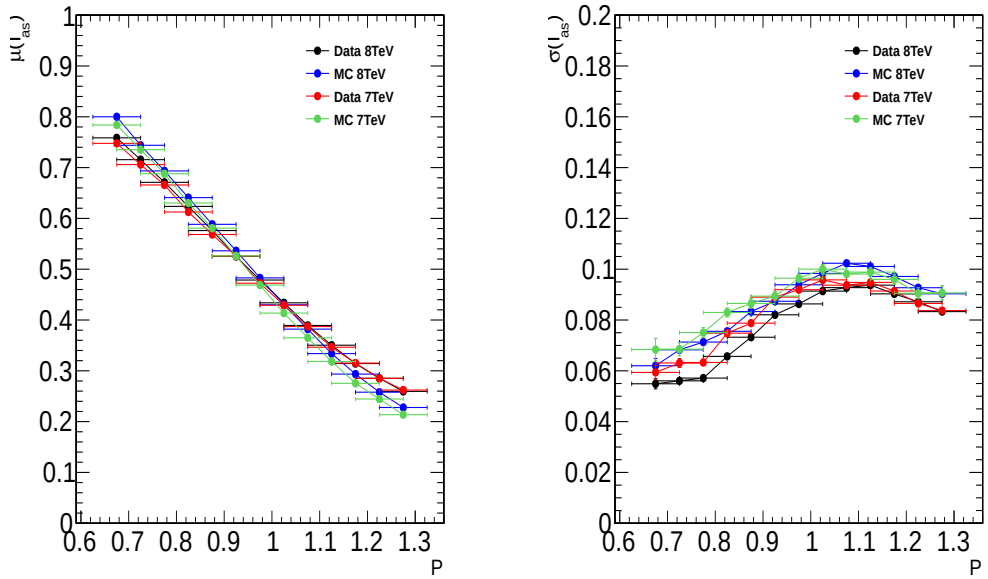

Figure 5.5: Mean (left) and width (right) of fitted Gaussian for different proton momentum ranges. These are shown for $\sqrt{s} = 7$ and 8 TeV data as well as simulation.

were used to estimate the uncertainty on the $1/\beta$ scale. $1/\beta$ scales in data and simulation were found to be offset by 0.003 in DTs and 0.02 in CSCs for $\sqrt{s}$ =7 TeV, and by 0.005 in both the DTs and CSCs for $\sqrt{s}$ =8 TeV. There was reasonable agreement between $1/\beta$ resolutions in data and simulation. The $1/\beta$ value of candidates is negatively offset by the above mentioned scale values and the change in signal acceptance for the final selection is taken as the uncertainty due to the $1/\beta$ scale. No change in signal acceptance is seen for $Q = 1e$. Final $1/\beta$ selection in the multiply charged HSCP analysis is chosen as 1.2 (Ch. 6). With increasing charge, higher end of $1/\beta$ distribution is increasingly cut-off and final $1/\beta$ selection is in the far-tail region resulting in larger changes in signal acceptance. With increasing mass, the $1/\beta$ distribution extends to larger values resulting in smaller changes in signal acceptance. Largest observed changes in signal acceptance for $\sqrt{s} = 7$ and 8 TeV signals are 55% and 16% respectively. For high mass signals, change in signal acceptance is reduced to less than 3% and 1% for $\sqrt{s} = 7$ and 8 TeV signals, respectively.

Uncertainty on candidate momentum measured in the inner tracker is evaluated accord-

ing to the prescription of the CMS tracker performace group [60]. The momentum value is re-estimated as

$$\frac{1}{p'_T} = \frac{1}{p_T} + \delta_{K_T}(q', \phi, \eta), \tag{5.8}$$

where

$$\delta_{K_T}(q', \phi, \eta) = A + B\eta^2 + q'C\sin(\phi - \phi_0), \tag{5.9}$$

and $A = 0.236$ TeV^{-1}, $B = -0.135$ TeV^{-1}, $C = 0.282$ TeV^{-1}, $\phi_0 = 1.337$, and q' is $+1$ for positively charged particles and -1 for negatively charged particles. Using the new momentum value, the signal acceptance changes by at most 9% and 12% for $\sqrt{s} = 7$ and 8 TeV signal samples respectively. Change in signal acceptance due to p_T rescaling is largest for low mass signals that have the softest p_T distribution.

Uncertainty in the number of pile-up events in data was estimated by using new pile-up weights for signal events. The minimum bias cross section was varied by 5–6% to derive the new pile-up weights. Following this prescription, signal acceptance for the final selection changed by less than 1% for all signal samples for both $\sqrt{s} = 7$ and 8 TeV.

Knowledge of amount of material in the CMS detector is important in the search for multiply charged HSCPs that have Q^2-enhanced $\frac{dE}{dx}$ along their path. Increased material budget can result in slowing down HSCPs and their failing the trigger timing requirements and/or global muon requirements. The CMS material budget is known within 1% [61]. This feature is conservatively replicated by increasing the density of brass used in the HCAL by 5%. Alternate signal samples for a grid of HSCP charges and masses were simulated with this prescription. Signal acceptance after online (Sec. 4.2.1), offline (Sec. 4.2.2), and final selection (Ch. 6) for the regular and material variated samples were compared. Ratio of the respective acceptances for each of the signal samples is shown in Fig. 5.6. Decrease in acceptance for material variated samples is not more than 3% after online and offline selections. For the final selection, change in acceptance is negligible for most considered signals other than high-Q, low mass samples. For 100 GeV samples, acceptance increases by 20% for $Q = 4e$ and decreases by 55% for $Q = 5e$, although with large statistical

Table 5.2: Summary table of various uncertainties and their respective value/ranges for multiply charged HSCPs for $\sqrt{s} = 7$ and 8 TeV.

Source of Systematic Uncertainty	Relative uncertainty (%)	
Signal acceptance	$\sqrt{s} = 7$ TeV	$\sqrt{s} = 8$ TeV
— Trigger acceptance	5.7	6.5
— Ionization energy loss	0–12	0–12
— Time-of-flight	0–54	0–16
— Track momentum scale	0–9	0–12
— Pile-up	< 1	< 1
— Detector material	3	3
— Track reconstruction efficiency	2	2
— Muon reconstruction efficiency	2	2
Total signal acceptance	7–55	8–21
Collision background prediction	20	20
Integrated luminosity	2.2	4.4

uncertainties. Considering that the acceptances are essentially unchanged after the online and offline selections where larger number of candidates survive, these differences are of statistical nature. A 3% uncertainty is assigned for imperfect knowledge of the CMS material budget.

Uncertainties in track and muon reconstruction are taken as 2% each. These are obtained from Tracker Detector Performance Group [62] and Muon Physics Object Group [60] studies within the CMS collaboration.

All individual systematic uncertainties for multiply charged HSCPs are shown in Figs. D.1 to D.8 (App. D). Total systematic uncertainty on signal acceptance is taken as the square root of the individual uncertainties added in quadrature. It ranges from 7–54% and 8–21% for $\sqrt{s} = 7$ and 8 TeV samples respectively (Fig. 5.7). The systematic uncertainty is large for high-Q, low mass samples as the chosen final selection (Ch. 6) lies in the very-far tail of their $1/\beta$ distribution. Summary of all systematic uncertainties and their respective value/ranges in the multiply charged HSCP analysis are listed in Tab. 5.2.

Apart from systematic uncertainties, statistical uncertainty on the final signal acceptance is also considered. These are most relevant for high-Q, low mass samples where the

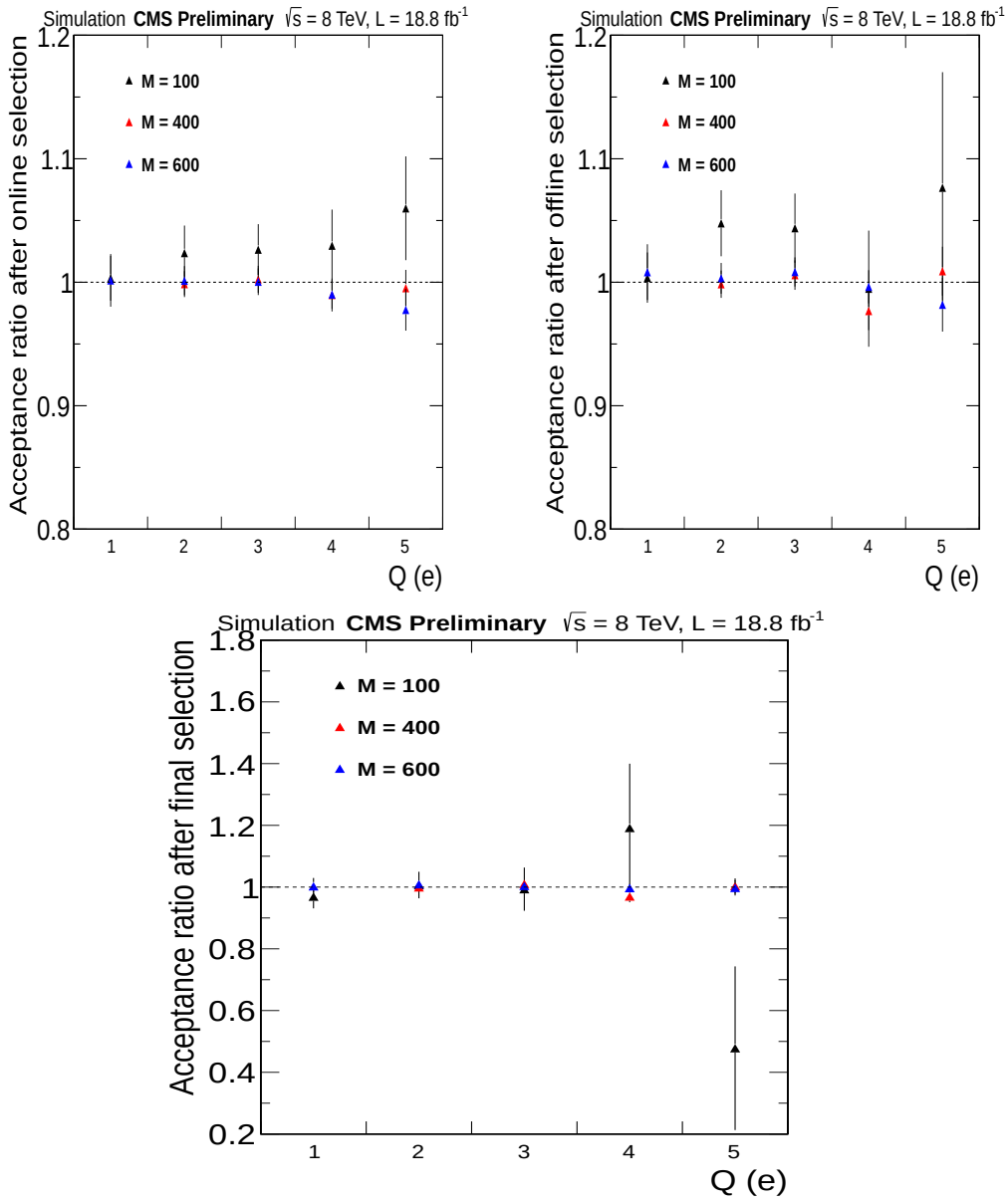

Figure 5.6: Signal acceptance ratios of material variated and normal samples after online (top left), offline (top right), and final selection (bottom) at $\sqrt{s} = 8$ TeV.

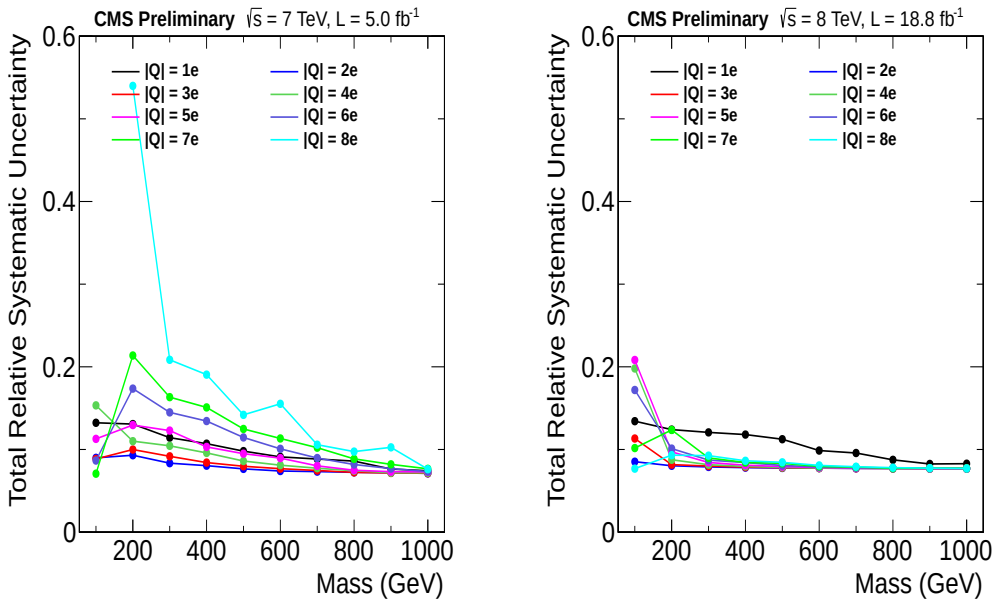

Figure 5.7: Total relative systematic uncertainty for multiply charged HSCPs at $\sqrt{s} = 7$ TeV (left) and 8 TeV (right). For $Q = 8e$ and mass of 100 GeV, none of the HSCP candidates pass final selection for $\sqrt{s} = 7$ TeV, and hence the signal is not shown in the figure.

chosen final selection (Ch. 6) resides in the very far tail of their $1/\beta$ distribution. Statistical uncertainty on the final signal acceptance are 30%, 55%, and 100% for mass of 100 GeV and $Q = 5e, 6e$, and $7e$ signal samples respectively at $\sqrt{s} = 7$ TeV and exceed their corresponding systematic uncertainty values. None of the candidates for $Q = 8e$ and mass of 100 GeV sample for $\sqrt{s} = 7$ TeV pass the final selection. For $\sqrt{s} = 8$ TeV samples, statistical uncertainty on the final signal acceptance are 26%, 60%, and 73% for mass of 100 GeV and $Q = 6e, 7e$, and $8e$ respectively and surpass their corresponding systematic uncertainty values.

CHAPTER 6

RESULTS

The final selection is determined by iterating over all possible combinations of I_{as} and $1/\beta$ selections within the range $0 < I_{as} < 0.55$ and $1.0 < 1/\beta < 1.45$. The scan is done in steps of 0.025. The final selection can be optimized for best discovery potential or best cross section limit. Given the aims of the LHC program and the CMS collaboration, the former is chosen. The discovery scenario requires the expected mean significance of the observed excess to be equal to five standard deviations with at least five observed candidates. The expected cross section values attained by aiming for discovery are at most 10% worse than those obtained for best limit and thereby cross section exclusions are not compromised significantly.

The optimization algorithm uses, for each of the selections, the number of predicted background candidates along with its uncertainty and the signal acceptance. Event-level acceptances are obtained from MC simulations. Given the signal is pair-produced in the considered model, signal acceptance is the same irrespective of whether one/both candidates within an event pass the final selection. It is required that there be at least 25 candidates in each of the background regions (A, B, and C) to ensure a reliable background prediction in the signal region. Final I_{as} and $1/\beta$ selections were optimized for multiply charged HSCPs with varying charges and masses in the first public result of the CMS collaboration that was based only on $\sqrt{s} = 7$ TeV data [63].

In Ref. [51], where a joint result of all HSCP analyses within the CMS collaboration

for both $\sqrt{s} = 7$ and 8 TeV was published, online and offline selections within the various analyses were made as uniform as possible. Relative to Ref. [63], the multiply charged HSCP analysis in Ref. [51] added the E_T^{miss} trigger, changed the relative tracker isolation requirement ($\sum_{\Delta R<0.3} p_T/p_T < 0.1$) to an absolute tracker isolation requirement ($\sum_{\Delta R<0.3} p_T <$ 50 GeV), removed cluster cleaning requirement, reevaluated systematic uncertainties, and used a single final selection irrespective of the HSCP charge and mass.

The majority of the I_{as} distribution for HSCPs with $Q \geq 2e$ lie near 1.0 (Fig. 6.1). The reconstructed $1/\beta$ distribution for HSCPs with $Q \geq 2e$ vary (Fig. 6.1) due to two primary factors that depend on the HSCP mass and/or charge: (1) the generator-level β distribution (Fig. 4.1) and (2) the online and offline selection efficiency (Sec. 4.2). Results of optimization are presented for multiply charged HSCPs of select charges and masses in Tab. 6.1 (full results of optimization are listed in App. E). No statistically significant excess over the predicted number of background candidates is seen in data for any of the optimized selections. No excess is seen in any of the optimized selections for $\sqrt{s} = 7$ TeV. Some of the optimized selections for $\sqrt{s} = 8$ TeV have a slight excess over prediction; maximal observed significance is 1.1 for the selection of (I_{as}, $1/\beta$)=(0.525, 1.175).

Values of I_{as} for HSCPs with $Q \geq 2e$ are well separated from the background region resulting in similar optimized I_{as} selections for various charges and masses. On the other hand, $1/\beta$ distributions vary widely with HSCP charge and mass yielding a broader range of optimized $1/\beta$ selections for various charges and masses. Different final selections have varying background predictions. Optimized final selections for HSCPs of same charge and mass differ slightly between $\sqrt{s}$ =7 and 8 TeV as during the latter running period four times more data were collected resulting in a slightly more extended background region.

Multitude of optimized final selections for HSCPs with different charges, masses and center-of-mass energies were simplified in Ref. [51] by using a single final selection for all signal samples and center-of-mass energies. A reasonably tight final selection should be able to identify or have hints of a multiply charged HSCP signal and thereby not compromise the discovery potential. This approach simplifies the description and ease of interpretation

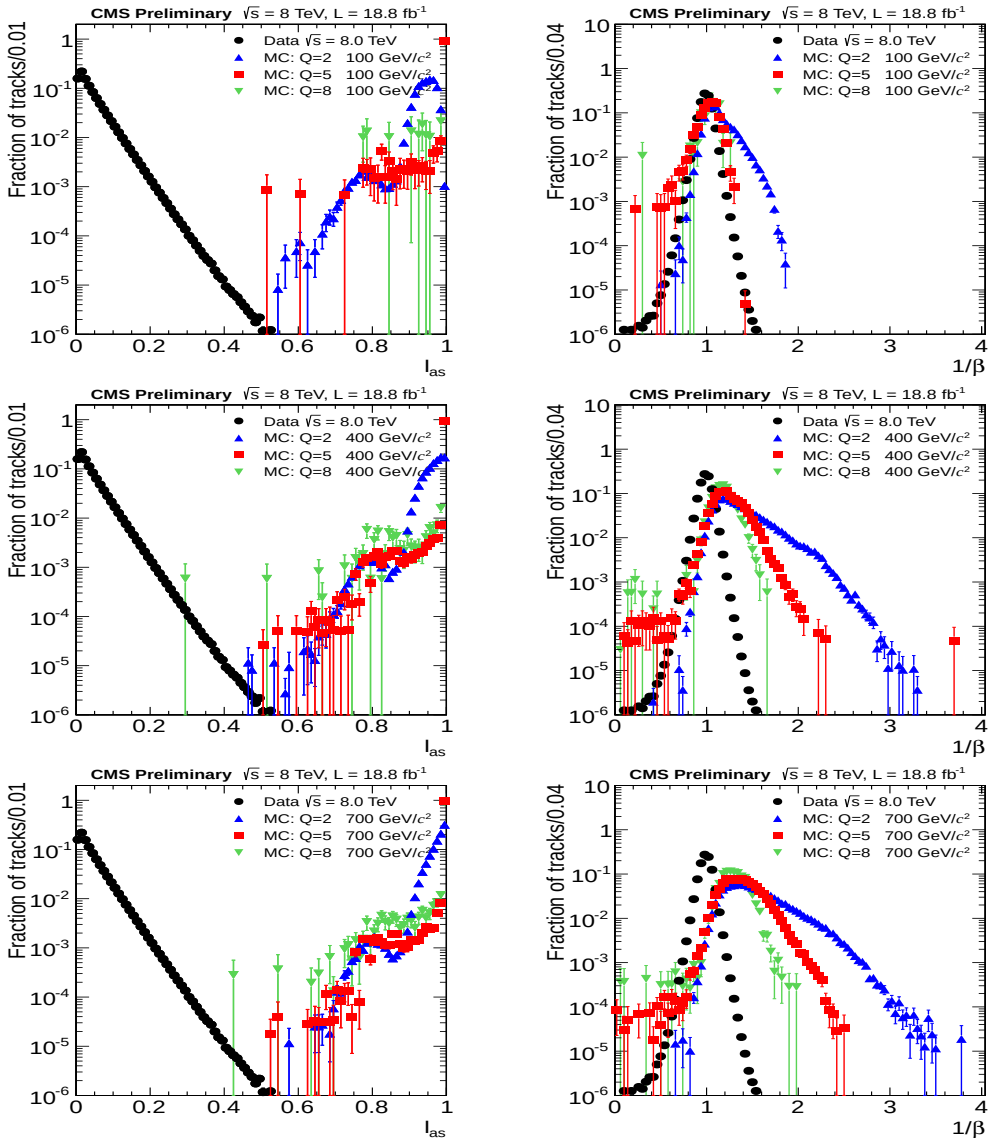

Figure 6.1: Distributions of I_{as} (left) and $1/\beta$ (right) after offline selections for data and multiply charged HSCP simulations of different charges and mass of 100 GeV (top), 400 GeV (middle), and 700 GeV (bottom) at $\sqrt{s} = 8$ TeV.

Table 6.1: Results of optimization for select HSCP charges and masses at $\sqrt{s} = 7$ and 8 TeV showing optimized I_{as} and $1/\beta$ selections, signal acceptance, predicted numbers of background candidates, observed numbers of data candidates, and expected and observed cross section limits. The two quantities in the paranthesis next to signal acceptance are systematic and statistical uncertainties on signal acceptance respectively, expressed as a percentage of the signal acceptance.

$\sqrt{s} = 7$ TeV								
Q (e)	Mass (GeV)	I_{as}	$1/\beta$	Acceptance	Prediction	Observation	σ (pb)	
							Exp.	Obs.
2	100	0.525	1.200	0.1048 (9%, 3.3%)	0.139 ± 0.039	0	0.0055	0.0057
	400	0.475	1.375	0.3753 (7.9%, 1.7%)	0.004 ± 0.001	0	0.0015	0.0017
	600	0.500	1.425	0.4139 (8%, 1.1%)	0.0013 ± 0.0004	0	0.0014	0.0015
4	100	0.500	1.100	0.0104 (18%, 4%)	2.730 ± 0.772	2	0.095	0.092
	400	0.525	1.275	0.192 (10%, 0.88%)	0.022 ± 0.006	0	0.003	0.0033
	600	0.525	1.275	0.2845 (8.4%, 0.9%)	0.022 ± 0.006	0	0.002	0.0022
6	100	0.500	1.100	3.84×10^{-4} (24%, 13%)	2.730 ± 0.772	2	2.6	2.6
	400	0.525	1.250	0.03235 (16%, 2.8%)	0.039 ± 0.011	0	0.017	0.019
	600	0.525	1.250	0.07648 (12%, 1.8%)	0.039 ± 0.011	0	0.0074	0.0079
$\sqrt{s} = 8$ TeV								
Q (e)	Mass (GeV)	I_{as}	$1/\beta$	Acceptance	Prediction	Observation	σ (pb)	
							Exp.	Obs.
2	100	0.525	1.275	0.06808 (8.9%, 1.2%)	0.058 ± 0.013	0	0.0022	0.0023
	400	0.500	1.350	0.3791 (7.8%, 0.5%)	0.013 ± 0.003	0	4.1×10^{-4}	4.2×10^{-4}
	600	0.500	1.375	0.4364 (7.8%, 0.45%)	0.008 ± 0.002	0	3.5×10^{-4}	3.7×10^{-4}
4	100	0.525	1.125	0.009946 (12%, 3.4%)	3.540 ± 0.805	3	0.029	0.029
	400	0.525	1.300	0.1822 (8%, 0.76%)	0.032 ± 0.007	0	8.5×10^{-4}	8.8×10^{-4}
	600	0.525	1.325	0.2638 (7.8%, 0.62%)	0.018 ± 0.004	0	5.8×10^{-4}	5.9×10^{-4}
6	100	0.525	1.125	7.48×10^{-4} (13%, 12%)	3.540 ± 0.805	3	0.38	0.39
	400	0.525	1.250	0.04918 (8.6%, 1.5%)	0.110 ± 0.025	0	0.003	0.0033
	600	0.525	1.300	0.08965 (8%, 1.1%)	0.032 ± 0.007	0	0.0017	0.0018

by the outside community. Determining a final selection for different charges, masses, and center-of-mass energies is referred to as 2nd optimization. It was checked that HSCP discovery scenario or cross section limits were not compromised.

With the large separation between I_{as} values of multiply charged HSCPs and background region, a high I_{as} value can be easily chosen as the common final selection for all charges and masses. However, with widely varying $1/\beta$ distributions among the different charges and masses, it is a delicate exercise to arrive at a common final $1/\beta$ selection. For a fixed I_{as} selection, an increment (decrement) in $1/\beta$ selection decreases (increases) both signal efficiency and background estimates. Change in discovery potential due to relative changes in signal efficiency and background estimates differ depending on whether the change in selection occurs in the bulk or tail of signal and background $1/\beta$ distributions. In the bulk of the signal and background distributions, there exists a range of $1/\beta$ selection values that have compensating background estimates and signal efficiencies and thereby yield similar discovery potential. For lower and higher $1/\beta$ selections, we have observed that the discovery potential is degraded due to relatively larger background estimates and relatively lower signal efficiencies.

With widely varying $1/\beta$ distributions for various charges and masses, a simple method was used to perform a 2nd optimization in the multiply charged analysis. In this approach, discovery potential for a number of selections with similar background estimates were examined. Numbers of predicted background candidates for several I_{as} and $1/\beta$ selections are listed in Tab. 6.2. Discovery potential for several selections with ~ 0.55 (~ 0.15) predicted background candidates for $\sqrt{s} = 8$ (7) TeV were examined. These selections are (I_{as}, $1/\beta$) $= (0.375, 1.275)$, $(0.425, 1.250)$, $(0.450, 1.225)$, $(0.500, 1.200)$, and $(0.525, 1.175)$.

Discovery potential for each of these selections were compared relative to (I_{as}, $1/\beta$) $= (0.375,\ 1.275)$ that has the largest $1/\beta$ threshold. For all selections, the discovery potential was better than for the comparison selection. For (I_{as}, $1/\beta$) $= (0.500,\ 1.200)$, the discovery prospect was improved for $Q \geq 2e$ and for all masses compared to (I_{as}, $1/\beta$) $= (0.425,\ 1.250)$, and $(0.450, 1.225)$. Further lowering $1/\beta$ selection to 1.175 gives mixed

Table 6.2: Numbers of predicted background candidates for several selections for $\sqrt{s} = 7$ and 8 TeV.

$\sqrt{s} = 7$ TeV							
$1/\beta$ \ I_{as}	0.375	0.400	0.425	0.450	0. 475	0.500	0.525
1.175	1.89	1.13	0.67	0.47	0.36	0.30	0.28
1.200	0.94	0.57	0.33	0.23	0.18	0.15	0.14
1.225	0.49	0.30	0.17	0.12	0.09	0.08	0.07
1.250	0.26	0.16	0.09	0.07	0.05	0.04	0.04
1.275	0.15	0.09	0.05	0.04	0.03	0.02	0.02
$\sqrt{s} = 8$ TeV							
$1/\beta$ \ I_{as}	0.375	0.400	0.425	0.450	0. 475	0.500	0.525
1.175	7.84	4.77	3.13	2.11	1.43	1.03	0.82
1.200	3.92	2.38	1.56	1.05	0.71	0.52	0.41
1.225	2.00	1.21	0.80	0.54	0.37	0.27	0.21
1.250	1.04	0.63	0.41	0.28	0.19	0.14	0.11
1.275	0.55	0.33	0.22	0.15	0.10	0.07	0.06

results for low and high mass multiply charged HSCPs. For $(I_{as},\ 1/\beta) = (0.525,\ 1.175)$, the low mass cross section reaches are enhanced while the high mass ones are degraded. Given that low mass HSCPs are already excluded with $1/\beta$ selection of 1.200 and that lower cross section reach for high mass HSCPs would yield a higher mass reach, it was decided use the final selection of $(I_{as},\ 1/\beta) = (0.500,\ 1.200)$.

Ratios of expected cross section reaches for 95% CL exclusion as well as 5σ discovery for two selections of $(I_{as},\ 1/\beta) = (0.375,\ 1.275)$, and $(0.500,\ 1.200)$ are shown in Fig. 6.2 for $\sqrt{s} = 8$ TeV. For $Q \geq 2e$, cross section reaches are essentially unchanged for high masses while several-fold increase is seen for low masses. The reach in expected cross section limits is slightly degraded for low mass, singly charged HSCPs. Given other dedicated analyses for singly charged HSCPs, this is not a problem. Expected reaches for some high-Q, low-mass HSCPs could not be evaluated for the higher $1/\beta$ selection due to limited available signal MC resulting in them being absent in Fig. 6.2.

A feature of using a common final selection for all charges and masses is that it resides

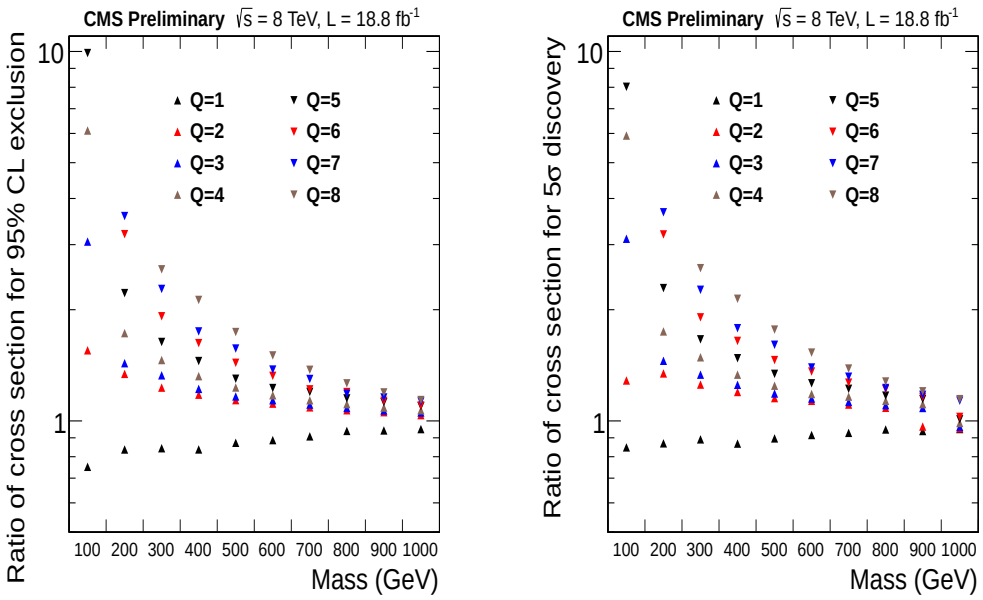

Figure 6.2: Ratios of expected cross section reaches using two sets of I_{as} and $1/\beta$ selections, namely (I_{as}, $1/\beta$)=(0.375, 1.275) and (0.500, 1.200) at $\sqrt{s} = 8$ TeV. Ratios of cross section reaches for 95% CL exclusion is shown in left while that for 5σ discovery is shown in right.

in the far-tail of the $1/\beta$ distribution for high-Q, low mass HSCPs. These signals have relatively small online and offline selection efficiencies and using a final $1/\beta$ selection in their tail region further contributes to their low overall acceptance. For HSCP with $Q = 8e$ and mass of 100 GeV, none of the HSCP candidates within the available $\sqrt{s} = 7$ TeV MC sample pass the final selection (meaning signal acceptance $< 5.2 \times 10^{-6}$).

Numbers of predicted background candidates and observed data candidates for (I_{as}, $1/\beta$) = (0.5, 1.2) are listed in Tab. 6.3 for $\sqrt{s} = 7$ and 8 TeV. No statistically relevant excess over prediction is observed in data.

Devoid of any statistically significant excess over prediction, 95% CL upper limits on HSCP signal cross sections were computed for both $\sqrt{s} = 7$ and 8 TeV. As is common practice within the CMS collaboration, we used a CLs approach [64–66] that uses lognormal pdfs [67, 68] to integrate over the nuisance parameters. The latter are the integrated luminosity, the signal acceptance and the expected background in the signal region. Results

Table 6.3: Numbers of predicted background candidates, observed data candidates, and significance for final selection of $(I_{as}, 1/\beta) = (0.5, 1.2)$ for $\sqrt{s} = 7$ and 8 TeV.

$\sqrt{s}$	7 TeV	8 TeV
Number of predicted background candidates	0.15 ± 0.04	0.52 ± 0.12
Number of observed data candidates	0	1
Significance	0.0	0.6

of $\sqrt{s} = 7$ and 8 TeV limits are combined to set limits on the signal strength μ $(= \sigma/\sigma_{th})$. With limited available MC, statistical uncertainty on the number of events that pass the final selection is also taken into account in the limits computation.

The expected and observed cross section limit values for all multiply charged HSCP signals are listed in Tabs. 6.4-6.7, as well as the signal acceptances with their respective systematic and statistical uncertainties. Observed cross section limits vary from 0.001 to 140 pb for $\sqrt{s} = 7$ TeV and from 4.1×10^{-4} to 20 pb for $\sqrt{s} = 8$ TeV. Lower and higher ends of this range are obtained from low and high charge HSCPs respectively. Theory and observed cross section limits for muliply charged HSCPs with $Q = 1$ to $8e$ are shown in Fig. 6.3 as a function of their mass.

We compared cross section reaches obtained by using a common final selection with those of optimization. Ratios of cross section reaches in the two approaches are shown in Fig. 6.4 for 5σ discovery as well as 95% CL exclusion. For most signals, cross section reach for 5σ discovery scenario with a common final selection is within a factor of two of that obtained with optimization. Contrary to the expectation that optimization should yield the selection with the lowest cross section reach, it is observed that the reach improves for few signals (ratio < 1.0). This happens because the optimization algorithm uses an approximation, in that it computes the cross section that can yield close to, but not exactly a 5σ excess. Optimized selection for most of the signals have predicted background of $\sim 10^{-3}$ as compared to $\sim 10^{-1}$ in the case of the chosen common final selection. This results in slightly lower cross section for 95% CL exclusion using the chosen common final selection than through optimization.

Table 6.4: Signal acceptance, expected and observed cross section limits for final selection of I_{as}=0.5, and $1/\beta$=1.2 for HSCPs with $Q = 1e$, and $2e$ for $\sqrt{s} = 7$ and 8 TeV. The two quantities in paranthesis are systematic and statistical uncertainty in signal acceptance, expressed as a percentage of the signal acceptance. For the combination of 7 and 8 TeV results, expected and observed limits on signal strength μ are listed.

Signal		$\sqrt{s} = 7$ TeV			$\sqrt{s} = 8$ TeV			7+8 TeV combined	
Q (e)	Mass (GeV)	Acceptance	σ (pb)		Acceptance	σ (pb)		σ/σ_{th}	
			Exp.	Obs.		Exp.	Obs.	Exp.	Obs.
1	100	0.159 (13%, 2.8%)	0.0036	0.0041	0.1447 (13%, 2.6%)	0.0011	0.0017	0.002	0.0027
	200	0.285 (13%, 2%)	0.002	0.0021	0.2556 (12%, 1.9%)	6.4×10^{-4}	9.1×10^{-4}	0.015	0.021
	300	0.3714 (11%, 1.8%)	0.0015	0.0016	0.3397 (12%, 1.7%)	4.9×10^{-4}	6.9×10^{-4}	0.059	0.086
	400	0.404 (11%, 1.7%)	0.0014	0.0015	0.3904 (12%, 1.5%)	4.3×10^{-4}	6.2×10^{-4}	0.2	0.28
	500	0.4654 (9.8%, 1.5%)	0.0012	0.0013	0.4386 (11%, 1.4%)	3.8×10^{-4}	5.6×10^{-4}	0.56	0.77
	600	0.498 (9.1%, 1%)	0.0012	0.0012	0.4663 (9.9%, 1.4%)	3.6×10^{-4}	5.1×10^{-4}	1.5	2.1
	700	0.5106 (8.8%, 0.99%)	0.0011	0.0012	0.4726 (9.6%, 1.4%)	3.5×10^{-4}	5.0×10^{-4}	3.7	5.3
	800	0.5206 (8.6%, 0.94%)	0.0011	0.0012	0.4662 (8.7%, 1.4%)	3.5×10^{-4}	5.2×10^{-4}	9.2	13
	900	0.5069 (7.6%, 0.92%)	0.0011	0.0012	0.4423 (8.2%, 1.4%)	3.6×10^{-4}	5.5×10^{-4}	22	30
	1000	0.4891 (7.4%, 0.94%)	0.0012	0.0012	0.4224 (8.3%, 1.5%)	3.8×10^{-4}	5.8×10^{-4}	50	72
2	100	0.1048 (9%, 3.3%)	0.0054	0.0061	0.1055 (8.5%, 0.98%)	0.0016	0.0023	6.7×10^{-4}	7.7×10^{-4}
	200	0.3632 (9.3%, 1.7%)	0.0016	0.0017	0.3291 (8%, 0.53%)	4.9×10^{-4}	7.3×10^{-4}	0.0029	0.0041
	300	0.4991 (8.3%, 1.4%)	0.0011	0.0012	0.4662 (7.9%, 0.44%)	3.5×10^{-4}	5.1×10^{-4}	0.011	0.015
	400	0.5517 (8%, 1.3%)	0.001	0.0011	0.5375 (7.8%, 0.4%)	3.0×10^{-4}	4.4×10^{-4}	0.036	0.051
	500	0.5857 (7.6%, 1.3%)	0.00098	0.001	0.5645 (7.8%, 0.38%)	2.9×10^{-4}	4.2×10^{-4}	0.11	0.15
	600	0.5853 (7.4%, 0.89%)	0.00098	0.001	0.5767 (7.7%, 0.38%)	2.8×10^{-4}	4.1×10^{-4}	0.3	0.43
	700	0.5774 (7.3%, 0.91%)	0.00099	0.001	0.5728 (7.7%, 0.38%)	2.8×10^{-4}	4.1×10^{-4}	0.76	1.1
	800	0.549 (7.2%, 1.3%)	0.001	0.0011	0.5593 (7.7%, 0.39%)	2.9×10^{-4}	4.2×10^{-4}	1.9	2.7
	900	0.5146 (7.2%, 0.9%)	0.0011	0.0011	0.5336 (7.7%, 0.39%)	3.0×10^{-4}	4.4×10^{-4}	4.7	6.4
	1000	0.4768 (7.1%, 0.94%)	0.0012	0.0012	0.5025 (7.7%, 0.4%)	3.2×10^{-4}	4.7×10^{-4}	11	15

Table 6.5: Signal acceptance, expected and observed cross section limits for final selection of I_{as}=0.5, and $1/\beta$=1.2 for HSCPs with $Q = 3e$, and $4e$ for $\sqrt{s} = 7$ and 8 TeV. The two quantities in paranthesis are systematic and statistical uncertainty in signal acceptance, expressed as a percentage of the signal acceptance. For the combination of 7 and 8 TeV results, expected and observed limits on signal strength μ are listed.

Signal		$\sqrt{s} = 7$ TeV			$\sqrt{s} = 8$ TeV			7+8 TeV combined	
Q (e)	Mass (GeV)	Acceptance	σ (pb)		Acceptance	σ (pb)		σ/σ_{th}	
			Exp.	Obs.		Exp.	Obs.	Exp.	Obs.
3	100	0.02196 (8.8%, 8%)	0.026	0.028	0.01659 (11%, 2.6%)	0.0099	0.014	0.0018	0.0025
	200	0.1827 (10%, 1.7%)	0.0031	0.0033	0.1808 (8.2%, 0.74%)	9.1×10^{-4}	0.0013	0.0023	0.0031
	300	0.3309 (9.2%, 1.4%)	0.0017	0.0018	0.319 (8%, 0.54%)	5.1×10^{-4}	7.3×10^{-4}	0.0071	0.0097
	400	0.4287 (8.4%, 0.78%)	0.0013	0.0014	0.4132 (7.9%, 0.47%)	4.0×10^{-4}	5.7×10^{-4}	0.021	0.029
	500	0.4715 (8%, 0.83%)	0.0012	0.0013	0.4638 (7.8%, 0.44%)	3.5×10^{-4}	5.0×10^{-4}	0.06	0.085
	600	0.4823 (7.7%, 0.77%)	0.0012	0.0012	0.4844 (7.7%, 0.43%)	3.3×10^{-4}	4.8×10^{-4}	0.16	0.22
	700	0.4765 (7.4%, 1%)	0.0012	0.0012	0.4947 (7.7%, 0.42%)	3.3×10^{-4}	4.7×10^{-4}	0.4	0.56
	800	0.4697 (7.2%, 1.3%)	0.0012	0.0013	0.4867 (7.7%, 0.42%)	3.3×10^{-4}	4.8×10^{-4}	1	1.4
	900	0.444 (7.1%, 1%)	0.0013	0.0013	0.4745 (7.7%, 0.42%)	3.4×10^{-4}	4.9×10^{-4}	2.4	3.3
	1000	0.4178 (7.1%, 1%)	0.0014	0.0014	0.458 (7.7%, 0.43%)	3.5×10^{-4}	5.1×10^{-4}	5.7	8
4	100	0.001665 (15%, 9.8%)	0.34	0.37	0.002271 (20%, 7.2%)	0.075	0.11	0.0085	0.011
	200	0.06921 (11%, 1.6%)	0.0082	0.0086	0.07792 (8.7%, 1.2%)	0.0021	0.0031	0.0031	0.0043
	300	0.1692 (10%, 1.1%)	0.0033	0.0036	0.1831 (8.1%, 0.74%)	8.9×10^{-4}	0.0013	0.0072	0.01
	400	0.2544 (9.6%, 0.75%)	0.0022	0.0023	0.2668 (7.9%, 0.61%)	6.1×10^{-4}	8.8×10^{-4}	0.019	0.026
	500	0.3105 (8.6%, 0.81%)	0.0019	0.002	0.3209 (7.8%, 0.55%)	5.1×10^{-4}	7.3×10^{-4}	0.048	0.067
	600	0.3356 (8.1%, 0.82%)	0.0017	0.0018	0.3527 (7.7%, 0.52%)	4.6×10^{-4}	6.7×10^{-4}	0.12	0.17
	700	0.3362 (7.7%, 1.4%)	0.0017	0.0018	0.3654 (7.7%, 0.51%)	4.4×10^{-4}	6.5×10^{-4}	0.31	0.43
	800	0.3359 (7.4%, 1.9%)	0.0017	0.0018	0.3655 (7.7%, 0.5%)	4.4×10^{-4}	6.5×10^{-4}	0.75	1.1
	900	0.3242 (7.2%, 1.2%)	0.0018	0.0018	0.3606 (7.7%, 0.51%)	4.5×10^{-4}	6.5×10^{-4}	1.8	2.5
	1000	0.3038 (7.2%, 1.3%)	0.0019	0.002	0.3475 (7.7%, 0.52%)	4.7×10^{-4}	6.8×10^{-4}	4.2	5.9

Table 6.6: Signal acceptance, expected and observed cross section limits for final selection of I_{as}=0.5, and $1/\beta$=1.2 for HSCPs with $Q = 5e$, and $6e$ for $\sqrt{s} = 7$ and 8 TeV. The two quantities in paranthesis are systematic and statistical uncertainty in signal acceptance, expressed as a percentage of the signal acceptance. For the combination of 7 and 8 TeV results, expected and observed limits on signal strength μ are listed.

Signal		$\sqrt{s} = 7$ TeV			$\sqrt{s} = 8$ TeV			7+8 TeV combined	
Q (e)	Mass (GeV)	Acceptance	σ (pb)		Acceptance	σ (pb)		σ/σ_{th}	
			Exp.	Obs.		Exp.	Obs.	Exp.	Obs.
5	100	1.82×10^{-4} (11%, 29%)	3.2	3.6	4.47×10^{-4} (21%, 16%)	0.4	0.55	0.03	0.042
	200	0.01875 (13%, 4.2%)	0.03	0.033	0.02485 (9.7%, 2.1%)	0.0067	0.0096	0.0064	0.009
	300	0.06712 (12%, 2.1%)	0.0083	0.0091	0.08275 (8.4%, 1.1%)	0.002	0.0029	0.01	0.015
	400	0.119 (10%, 1.1%)	0.0048	0.005	0.1447 (8.1%, 0.95%)	0.0011	0.0016	0.022	0.032
	500	0.1626 (9.5%, 1.3%)	0.0035	0.0037	0.1918 (7.9%, 0.73%)	8.6×10^{-4}	0.0012	0.052	0.074
	600	0.1919 (8.9%, 1.8%)	0.003	0.0031	0.2215 (7.8%, 0.68%)	7.4×10^{-4}	0.001	0.13	0.18
	700	0.2057 (8%, 1.7%)	0.0028	0.003	0.2432 (7.7%, 0.65%)	6.6×10^{-4}	0.00096	0.3	0.42
	800	0.2178 (7.5%, 2.8%)	0.0026	0.0028	0.2446 (7.7%, 0.64%)	6.6×10^{-4}	0.00096	0.71	1
	900	0.2007 (7.3%, 1.7%)	0.0029	0.003	0.2431 (7.7%, 0.65%)	6.6×10^{-4}	0.00097	1.7	2.3
	1000	0.1886 (7.3%, 1.7%)	0.003	0.0032	0.2348 (7.7%, 0.65%)	6.9×10^{-4}	0.001	4.1	5.6
6	100	2.0×10^{-5} (7.4%, 55%)	33	36	1.56×10^{-4} (17%, 26%)	1.2	1.7	0.064	0.088
	200	0.003238 (17%, 5%)	0.18	0.19	0.0064 (10%, 4.3%)	0.026	0.037	0.018	0.026
	300	0.02024 (14%, 2.5%)	0.028	0.03	0.03423 (8.7%, 1.8%)	0.0048	0.007	0.018	0.026
	400	0.0449 (13%, 2.4%)	0.013	0.013	0.0681 (8.4%, 1.3%)	0.0024	0.0036	0.034	0.048
	500	0.07156 (11%, 1.9%)	0.008	0.0084	0.1037 (8.1%, 1%)	0.0016	0.0023	0.069	0.096
	600	0.09238 (10%, 1.6%)	0.0062	0.0065	0.1316 (7.9%, 0.91%)	0.0012	0.0018	0.15	0.21
	700	0.1011 (9%, 1.5%)	0.0057	0.006	0.1489 (7.8%, 0.84%)	0.0011	0.0016	0.34	0.48
	800	0.1074 (8.2%, 1.5%)	0.0053	0.0056	0.1537 (7.7%, 0.84%)	0.001	0.0015	0.81	1.1
	900	0.1051 (7.7%, 1.5%)	0.0054	0.0058	0.1533 (7.7%, 0.85%)	0.0011	0.0015	1.9	2.6
	1000	0.09907 (7.3%, 1.6%)	0.0058	0.006	0.1498 (7.7%, 0.86%)	0.0011	0.0016	4.4	6

Table 6.7: Signal acceptance, expected and observed cross section limits for final selection of I_{as}=0.5, and $1/\beta$=1.2 for HSCPs with $Q = 7e$, and $8e$ for $\sqrt{s} = 7$ and 8 TeV. The two quantities in paranthesis are systematic and statistical uncertainty in signal acceptance, expressed as a percentage of the signal acceptance. For the combination of 7 and 8 TeV results, expected and observed limits on signal strength μ are listed.

Signal		$\sqrt{s} = 7$ TeV			$\sqrt{s} = 8$ TeV			7+8 TeV combined	
Q (e)	Mass (GeV)	Acceptance	σ (pb)		Acceptance	σ (pb)		σ/σ_{th}	
			Exp.	Obs.		Exp.	Obs.	Exp.	Obs.
7	100	6×10^{-6} (7.1%, 1e+02%)	1.3e+02	1.4e+02	1.5×10^{-5} (7.9%, 60%)	15	20	0.55	0.72
	200	5.28×10^{-4} (21%, 12%)	1.1	1.2	0.001917 (12%, 6.9%)	0.087	0.13	0.047	0.065
	300	0.005347 (16%, 4.8%)	0.11	0.12	0.01336 (9%, 3.1%)	0.012	0.018	0.036	0.05
	400	0.01567 (15%, 4%)	0.037	0.039	0.03306 (8.4%, 2.9%)	0.0049	0.0072	0.053	0.072
	500	0.02606 (12%, 3.1%)	0.022	0.023	0.05715 (8.3%, 2.1%)	0.0028	0.0042	0.096	0.13
	600	0.03781 (11%, 2.5%)	0.015	0.016	0.07841 (7.9%, 1.8%)	0.0021	0.0031	0.19	0.28
	700	0.04634 (10%, 2.3%)	0.012	0.013	0.0915 (7.9%, 1.6%)	0.0018	0.0026	0.43	0.6
	800	0.04907 (8.9%, 2.2%)	0.012	0.012	0.0985 (7.7%, 1.6%)	0.0017	0.0025	0.95	1.3
	900	0.05044 (8.2%, 2.2%)	0.011	0.012	0.09834 (7.7%, 1.6%)	0.0017	0.0025	2.2	3.1
	1000	0.04609 (7.6%, 2.3%)	0.012	0.013	0.09449 (7.7%, 1.7%)	0.0017	0.0025	5.3	7.3
8	100	$< 5.2 \times 10^{-6}$	-	-	1.1×10^{-5} (7.7%, 73%)	22	29	0.69	0.99
	200	7.1×10^{-5} (54%, 38%)	9.7	11	6.37×10^{-4} (9.3%, 11%)	0.26	0.38	0.11	0.16
	300	0.001289 (21%, 10%)	0.44	0.48	0.005095 (9.2%, 5.4%)	0.032	0.047	0.073	0.1
	400	0.004482 (19%, 7.6%)	0.13	0.14	0.01564 (8.6%, 3.8%)	0.01	0.015	0.089	0.13
	500	0.008374 (14%, 5.6%)	0.068	0.073	0.0319 (8.4%, 2.6%)	0.0051	0.0074	0.14	0.19
	600	0.01265 (16%, 4.5%)	0.045	0.048	0.04587 (8.1%, 2.2%)	0.0035	0.0052	0.26	0.37
	700	0.01748 (11%, 4%)	0.033	0.035	0.05403 (7.9%, 2%)	0.003	0.0044	0.56	0.79
	800	0.02031 (9.7%, 3.6%)	0.028	0.03	0.06176 (7.8%, 2%)	0.0026	0.0038	1.2	1.7
	900	0.01986 (10%, 3.6%)	0.028	0.031	0.06155 (7.7%, 1.9%)	0.0026	0.0039	2.7	3.9
	1000	0.01862 (7.6%, 3.8%)	0.031	0.032	0.06008 (7.7%, 1.9%)	0.0027	0.004	6.4	9

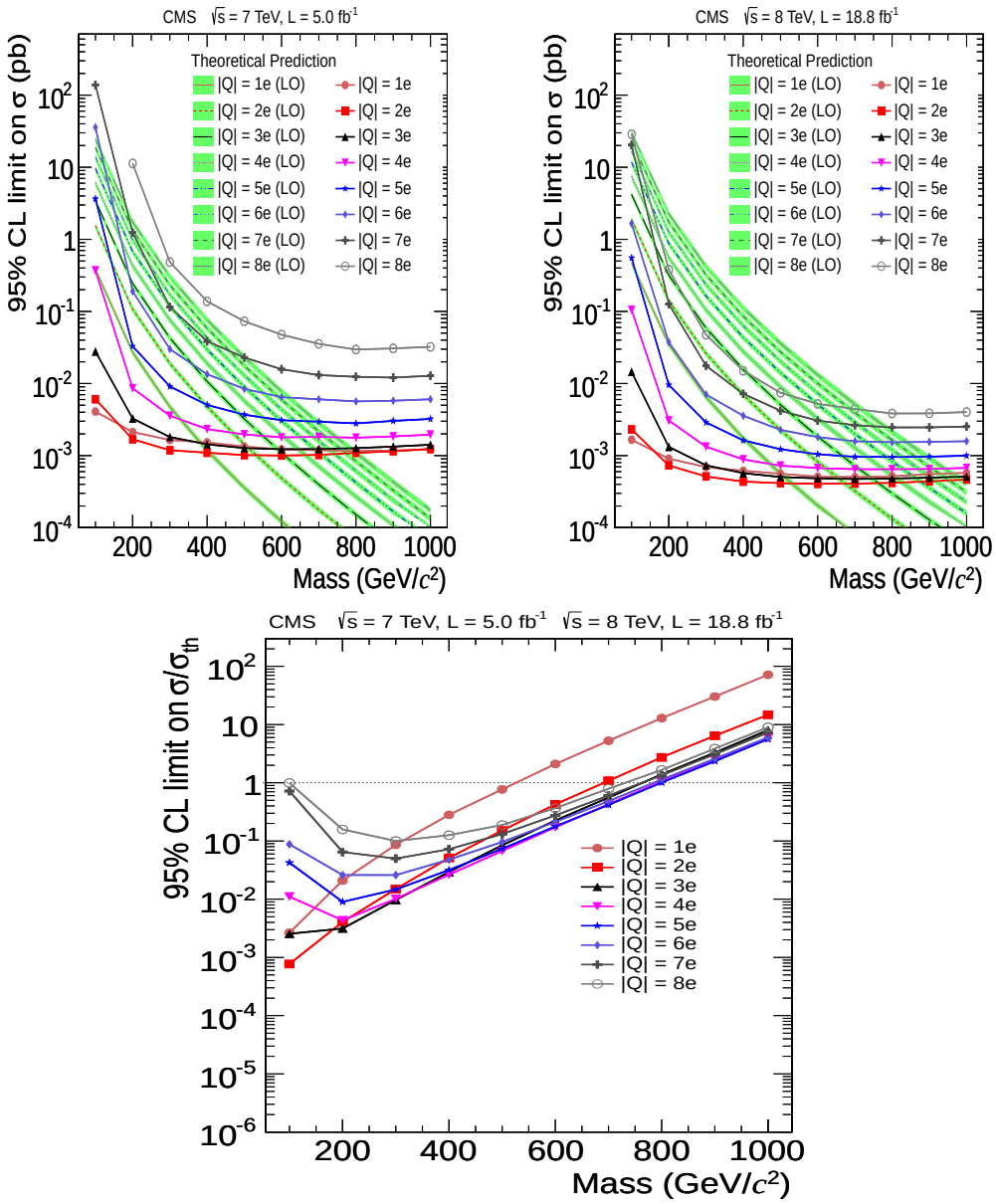

Figure 6.3: Theory and observed cross section limit curves for $\sqrt{s} = 7$ TeV (top left) and 8 TeV (top right). For combined 7 and 8 TeV results (bottom), observed limits on signal strength μ is shown.

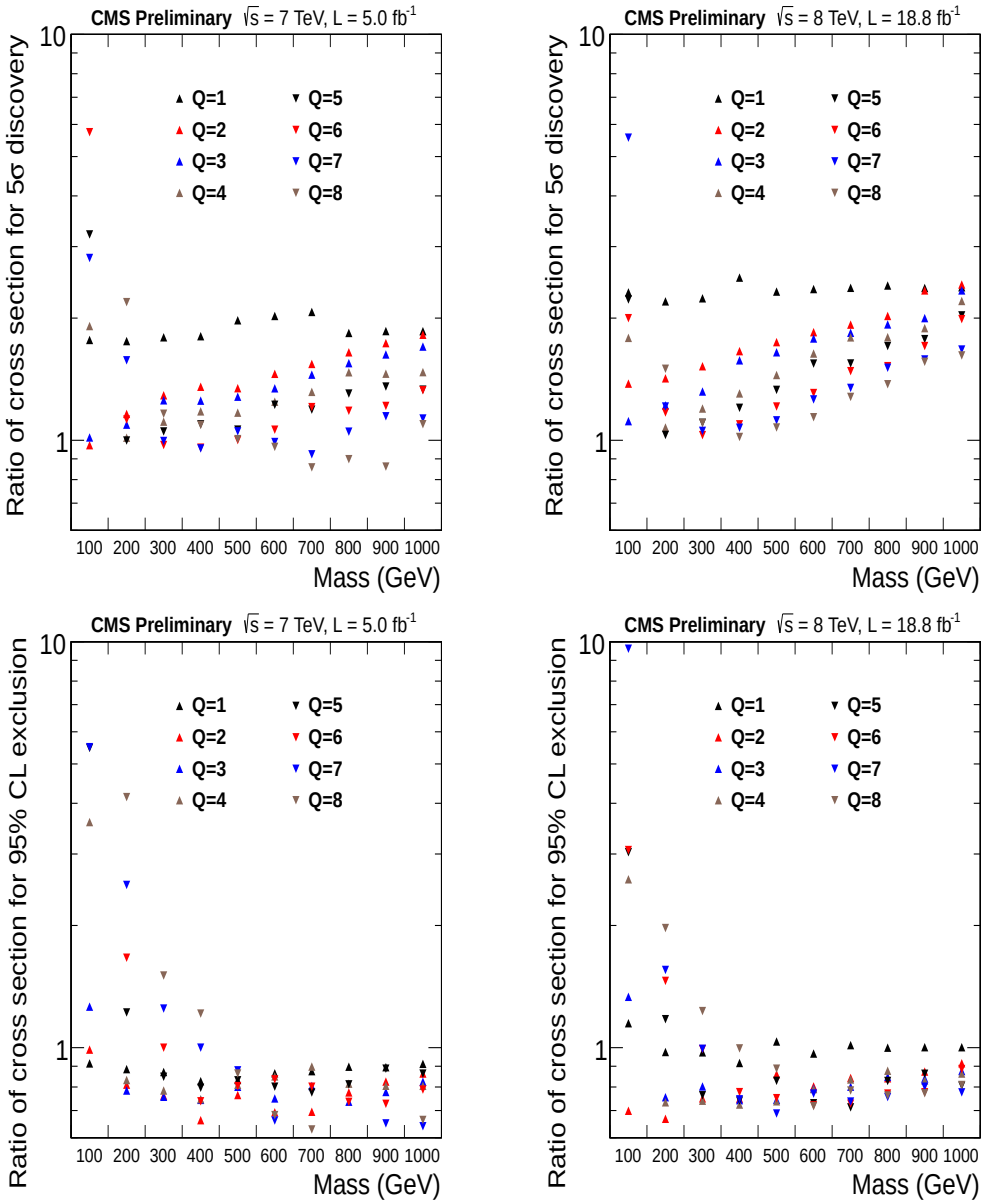

Figure 6.4: Ratios of cross section reaches for common final selection of (I_{as}, $1/\beta$)=(0.5, 1.2) and optimization selection. Ratios of cross section reaches for 5σ discovery (top) and 95% CL exclusion (bottom) are shown for $\sqrt{s} = 7$ TeV (left) and $\sqrt{s} = 8$ TeV (right).

Table 6.8: Mass limits for multiply charged HSCPs with different charges at $\sqrt{s} = 7$ TeV, $\sqrt{s} = 8$ TeV and combination of $\sqrt{s} = 7$ and 8 TeV.

$\|Q\|$ (e)	$\sqrt{s} = 7$ TeV	$\sqrt{s} = 8$ TeV	7 and 8 TeV combined
1	> 390	> 500	> 517
2	> 544	> 682	> 687
3	> 593	> 757	> 752
4	> 612	> 784	> 791
5	> 598	> 789	> 798
6	$< 197, > 568$	> 780	> 778
7	$< 200, > 479$	> 761	> 753
8	-	> 730	> 724

The point of intersection between the theory and observed curves in Fig. 6.3 yields a mass limit. For combined 7 TeV and 8 TeV results, all masses with $\mu < 1$ are excluded. All mass limit values are listed in Tab. 6.8. With the chosen final selection, the observed cross section limit values are higher than theory cross section values for HSCPs with $Q = 6e$, $7e$ and mass of 100 GeV and for all masses of HSCPs with $Q = 8e$ at $\sqrt{s} = 7$ TeV. However, all high-Q, low mass HSCPs can be excluded at $\sqrt{s} = 8$ TeV. Overall, multiply charged HSCPs with $Q = 1, 2, 3, 4, 5, 6, 7, 8e$ are excluded below masses of 517, 687, 752, 791, 798, 778, 753, and 724 GeV, respectively, in the considered Drell-Yan-like model. Mass limits for $Q = 1e$ can be compared with dedicated singly charged HSCP analysis. The *Tracker+TOF* analysis places a mass limit of 574 GeV for $Q = 1e$ HSCPs in the considered Drell-Yan-like model (Ref. [51]). Summary of mass limits for multiply charged HSCPs with different electric charges from various ATLAS [38], and CMS [51, 63] results performed using data collected during Run I of the LHC is shown in Fig. 6.5.

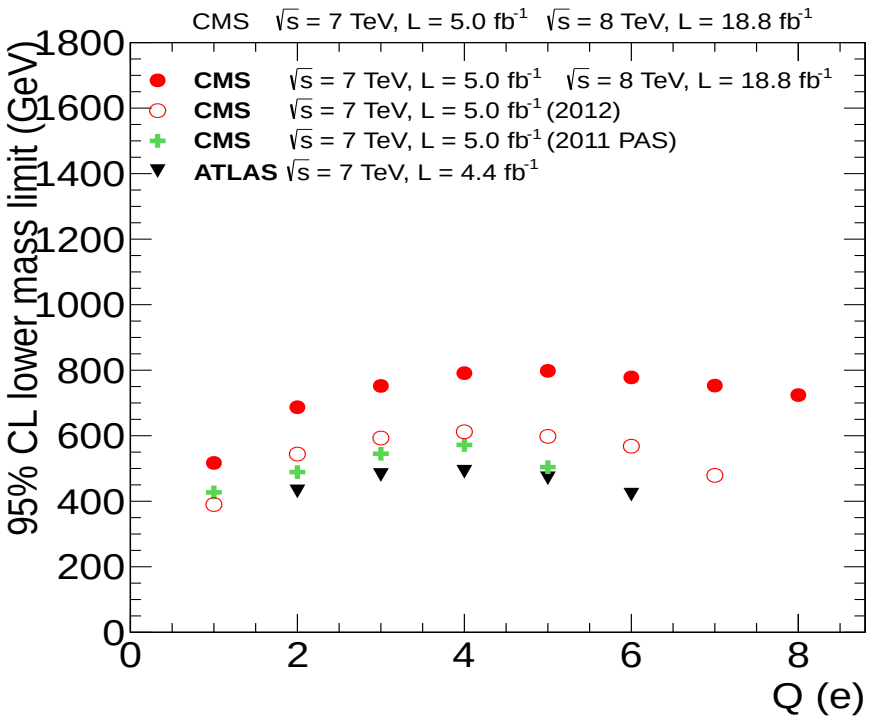

Figure 6.5: Summary of mass limits for multiply charged HSCPs from ATLAS [38], and CMS [51, 63] results using data collected during Run I of the LHC.

CHAPTER 7

CONCLUSIONS

7.1 Summary

The LHC delivered 5 fb^{-1} and 24 fb^{-1} of proton-proton collision data at 7 TeV and 8 TeV center of mass energies, respectively, to the CMS detector in 2011 and 2012. We have searched for multiply charged HSCPs in data recorded with the CMS detector. Energy loss measurements in the inner tracker and timing measurements in the muon system were used to identify highly ionizing and slow moving particles, respectively.

Several aspects of multiply charged HSCPs make this analysis unique compared to others carried out within the CMS collaboration. Ionization energy loss of multiply charged HSCPs is often larger than the dynamic measurement range resulting in saturation effect. SM particles can radiate δ-rays and mimic signal-like behaviour. Larger bending in the magnetic field results in under-measurement of p_T and search sensitivity for multiply charged HSCPs is degraded with increasing charge. For this reason, p_T is not be used as a search variable. Slow, multiply charged HSCPs can fail the timing requirements of the online selection. Large $\frac{dE}{dx}$ along their path slows them down even more. This work describes how each of these challenges were studied and met.

Data recorded with the CMS detector have been determined to be consistent with SM expectations. Upper limits on the production cross section of multiply charged HSCPs in the Drell-Yan-like model have been computed for various scenarios of electric charge and

mass. The cross section limits have been translated into limits on the mass of multiply charged HSCPs with various charges. These results constitute the most stringent limits for multiply charged HSCPs to date. This multiply charged HSCP search is a new component to the various HSCP searches that have been pursued by the CMS collaboration [51].

7.2 Perspectives

The LHC is expected to commence Run II operations in 2015 at a higher center-of-mass energy and increased instantaneous luminosity. Both these features will allow the current multiply charged HSCP analysis to explore lower production cross sections. Bunch spacing between successive proton bunches in Run II operations will be reduced to 25 ns which will require narrower timing requirements and reduce the sensitivity of the analysis to slow particles as compared to Run I operations.

The current search strategy can possibly be improved in multitude of ways. Online selections based on large $\frac{dE}{dx}$ in the silicon tracker can be used to directly trigger on multiply charged HSCPs. Cluster shape studies of singly charged particles can be expanded to multiply charged ones, thereby providing a better $\frac{dE}{dx}$ and mass measurement. Timing measurements using ECAL can also be used to identify multiply charged HSCPs.

With large energy loss and bending in the magnetic field, search sensitivity for multiply charged HSCPs that might not reach the muon system can be improved by using only the inner sections of the CMS detector. Online selections can be done using $\frac{dE}{dx}$ triggers. The numbers of highly ionizing hits can be used to separate multiply charged HSCPs from SM particles. With more than 20 inner tracker measurements, CMS has good resolution for the high-end tail of minimum ionizing particles, which can help identify multiply charged HSCPs. In the future, data collected with the CMS detector will be able to improve on the results presented here through a combination of higher center-of-mass energy, larger luminosity, and additional improved analysis techniques.

The Monopole and Exotics Detector at the LHC (MoEDAL) project plans a future

search for exotic particles. The MoEDAL detector consists of an array of plastic Nuclear Track Detectors (NTDs) and is to be placed around the interaction point of the LHCb detector (Sec. 2.1). The large energy loss of a highly charged particle will cause permanent damage to the NTDs, while the motion of SM particles will not result in any visible degradation. With this clean signature, highly ionizing particles can be uniquely identified. Only a few such events are enough to confirm their passage. Also, being a passive signature, there are no constraints on the trigger and reconstruction requirements. The MoEDAL detector is well placed to search for exotic particles such as magnetic monopoles and multiply charged HSCPs.

APPENDIX A

PYTHIA PARAMETERS

Pythia settings used in the generation of signal samples are given below. These settings are also used to calculate theory cross section of signal samples (App. B). Meaning of the various settings are mentioned in paranthesis next to them. In the modified Drell-Yan process, coupling of the Z to multiply charged HSCPs is changed. To differentiate the new Z from the regular one, it is denoted as Z'.

MSEL = 0 (user defined processes)

MSUB (141) = 1 (turn on coupling of fermions to $\gamma^\star/Z/Z'$)

MSTP (44) = 5 (only $\gamma^\star$, Z', and their interference included)

PMAS (32,1) = 91.187 (mass of Z' (GeV))

PMAS (32,2) = 2.4952 (width of Z' (GeV))

CKIN (1) = 100.0 (minimum $\sqrt{s}$ (GeV), same as mass of τ')

CKIN (2) = -1 (no maximum $\sqrt{s}$)

MSTP (1) = 4 (4th generation process)

KCHG (17,1) = -24 (Q of τ' in units of $e/3$, sign is important in order to get the coupling correct)

PMAS (17,1) = 100.0 (mass of τ' (GeV))

MDCY (17,1) = 0 (set τ' to be stable)

MWID (17) = 0 (set τ' width to be 0)

MDME (289,1) = 0 (forbid Z' decay into $d\bar{d}$)

MDME (290,1) = 0 (forbid Z' decay into $u\bar{u}$)

MDME (291,1) = 0 (forbid Z' decay into $s\bar{s}$)

MDME (292,1) = 0 (forbid Z' decay into $c\bar{c}$)

MDME (293,1) = 0 (forbid Z' decay into $b\bar{b}$)

MDME (294,1) = 0 (forbid Z' decay into $t\bar{t}$)

MDME (297,1) = 0 (forbid Z' decay into e^-e^+)

MDME (298,1) = 0 (forbid Z' decay into $\nu_e\ \bar{\nu_e}$)

MDME (299,1) = 0 (forbid Z' decay into $\mu^-\mu^+$)

MDME (300,1) = 0 (forbid Z' decay into $\nu_\mu\ \bar{\nu_\mu}$)

MDME (301,1) = 0 (forbid Z' decay into $\tau^-\tau^+$)

MDME (302,1) = 0 (forbid Z' decay into $\nu_\tau\ \bar{\nu_\tau}$)

MDME (303,1) = 1 (force Z' decay into $\tau'^-\tau'^+$)

PARJ (192) = (24/3)*0.92 (vector coupling with no $SU(2)$ interactions)

PARJ (193) = 0.0 (axial coupling with no $SU(2)$ interactions)

APPENDIX B

THEORY CROSS SECTION VALUES

Cross section values of multiply charged HSCPs in the Drell-Yan-like model (Sec. 4.1) are listed here.

Table B.1: Theory cross section values of multiply charged HSCPs in Drell-Yan-like model for $\sqrt{s} = 7$ TeV.

Mass (GeV)	Q (e)							
	1	2	3	4	5	6	7	8
100	0.3841	1.537	3.429	6.089	9.58	13.81	18.76	24.44
200	0.02714	0.1076	0.2441	0.4324	0.6789	0.9753	1.326	1.74
300	0.004753	0.01901	0.04277	0.0762	0.1186	0.1711	0.2326	0.3032
400	0.001181	0.00478	0.01069	0.01906	0.02964	0.04269	0.05851	0.07615
500	0.0003588	0.001433	0.003221	0.005779	0.008984	0.01294	0.01765	0.02314
600	0.0001216	0.0004857	0.001092	0.001943	0.00304	0.004378	0.005994	0.007773
700	0.00004423	0.0001781	0.0003978	0.0007113	0.001107	0.001596	0.002167	0.002833
800	0.00001701	0.00006802	0.0001524	0.0002714	0.000424	0.0006142	0.00080358	0.00109
900	0.000006736	0.00002687	0.00006064	0.0001074	0.0001679	0.0002416	0.0003305	0.0004318
1000	0.000002718	0.00001091	0.00002449	0.0000434	0.00006841	0.00009884	0.0001338	0.0001751

Table B.2: Theory cross section values of multiply charged HSCPs in Drell-Yan-like model for $\sqrt{s} = 8$ TeV.

Mass (GeV)	Q (e)							
	1	2	3	4	5	6	7	8
100	0.468	1.88	4.193	7.478	11.67	16.8	22.88	29.87
200	0.03509	0.1402	0.3164	0.5595	0.8763	1.264	1.731	2.249
300	0.006512	0.02622	0.05892	0.105	0.1642	0.2353	0.3211	0.4203
400	0.001754	0.006968	0.01574	0.02789	0.04358	0.06327	0.08576	0.112
500	0.0005631	0.002257	0.005078	0.009025	0.01417	0.02039	0.0275	0.03613
600	0.000204	0.0008183	0.001839	0.00327	0.005143	0.00736	0.01003	0.01317
700	0.00007977	0.0003228	0.0007211	0.00128	0.002004	0.00291	0.003934	0.005169
800	0.00003324	0.0001333	0.0003003	0.0005334	0.0008316	0.001202	0.001638	0.002133
900	0.00001434	0.00005764	0.0001294	0.0002295	0.0003584	0.0005163	0.0007001	0.0009207
1000	0.00000631	0.0000254	0.00005687	0.0001014	0.0001585	0.0002276	0.0003113	0.0004097

APPENDIX C

OFFLINE SELECTION EFFICIENCY

Candidate efficiency of multiply charged HSCPs with $Q = 1$–$8e$ and mass of 100–1000 GeV for various offline selections (Sec. 4.2.2) at $\sqrt{s}$ =7 and 8 TeV are listed here. Offline selections are listed in the order in which they are applied. Efficiency for global muon selection is relative to the number of HSCP candidates that pass the online selection. For all other offline selections, the efficiency is relative to the number of HSCP candidates that pass all previous offline selections. Overall offline selection efficiency is also listed.

Table C.1: Candidate efficiency of HSCPs with $Q = 1e$ and different masses for various offline selections at $\sqrt{s}$ =7 TeV.

Offline Selection	Mass (GeV)									
	100	200	300	400	500	600	700	800	900	1000
Global muon	0.89	0.91	0.94	0.95	0.95	0.96	0.96	0.97	0.97	0.97
$\|\eta\|$	0.93	0.94	0.96	0.96	0.97	0.98	0.98	0.99	0.99	0.99
Primary vertex	1.00	1.00	1.00	1.00	1.00	1.00	1.00	1.00	1.00	1.00
# Tracker hits (strips and pixels)	1.00	1.00	1.00	1.00	1.00	1.00	1.00	1.00	1.00	1.00
# Pixel hits	0.99	0.99	0.99	0.99	0.99	0.99	0.99	0.99	0.99	0.99
Valid fraction	1.00	1.00	1.00	1.00	1.00	1.00	1.00	1.00	1.00	1.00
# $\frac{\Delta E}{\Delta x}$ measurements	1.00	1.00	1.00	1.00	1.00	1.00	1.00	1.00	1.00	1.00
# $1/\beta$ measurements	0.99	0.99	0.99	0.98	0.98	0.98	0.98	0.98	0.97	0.97
Quality	1.00	1.00	1.00	1.00	1.00	1.00	1.00	1.00	1.00	1.00
χ^2/dof	1.00	1.00	1.00	1.00	1.00	1.00	1.00	1.00	1.00	1.00
p_T	0.96	1.00	1.00	1.00	1.00	1.00	1.00	1.00	1.00	1.00
I_h	0.90	0.94	0.97	0.98	0.99	0.99	0.99	0.99	0.99	0.99
$\sigma_{\langle 1/\beta \rangle}$	0.98	0.98	0.97	0.97	0.97	0.96	0.96	0.96	0.96	0.96
d_{xy}	1.00	1.00	1.00	1.00	1.00	1.00	1.00	1.00	1.00	1.00
$\sum_{\Delta R<0.3} p_T$	1.00	1.00	1.00	1.00	1.00	1.00	1.00	1.00	1.00	1.00
σ_{p_T}/p_T	1.00	1.00	1.00	1.00	1.00	0.99	0.98	0.96	0.93	0.89
d_z	1.00	1.00	1.00	1.00	1.00	1.00	1.00	1.00	1.00	1.00
$\langle 1/\beta \rangle$	0.96	0.98	0.99	0.99	1.00	1.00	1.00	1.00	1.00	1.00
Overall	0.66	0.76	0.82	0.84	0.85	0.86	0.87	0.85	0.82	0.78

Table C.2: Candidate efficiency of HSCPs with $Q = 2e$ and different masses for various offline selections at $\sqrt{s}$ =7 TeV.

Offline Selection	Mass (GeV)									
	100	200	300	400	500	600	700	800	900	1000
Global muon	0.89	0.89	0.91	0.92	0.93	0.94	0.94	0.94	0.94	0.94
$\lvert\eta\rvert$	0.94	0.95	0.96	0.97	0.97	0.98	0.99	0.99	0.99	0.99
Primary vertex	1.00	1.00	1.00	1.00	1.00	1.00	1.00	1.00	1.00	1.00
# Tracker hits (strips and pixels)	1.00	1.00	1.00	1.00	1.00	1.00	1.00	1.00	1.00	1.00
# Pixel hits	0.99	0.99	0.99	0.99	0.99	0.99	0.99	0.99	0.99	0.99
Valid fraction	1.00	1.00	1.00	1.00	1.00	1.00	1.00	1.00	1.00	1.00
# $\frac{\Delta E}{\Delta x}$ measurements	1.00	1.00	1.00	1.00	1.00	1.00	1.00	1.00	1.00	1.00
# $1/\beta$ measurements	0.98	0.98	0.97	0.97	0.97	0.97	0.97	0.96	0.96	0.95
Quality	1.00	1.00	1.00	1.00	1.00	1.00	1.00	1.00	1.00	1.00
χ^2/dof	1.00	1.00	1.00	1.00	1.00	1.00	1.00	1.00	1.00	1.00
p_T	0.80	0.96	0.99	1.00	1.00	1.00	1.00	1.00	1.00	1.00
I_h	1.00	1.00	1.00	1.00	1.00	1.00	1.00	1.00	1.00	1.00
$\sigma_{\langle 1/\beta \rangle}$	0.96	0.95	0.95	0.95	0.94	0.94	0.94	0.93	0.93	0.93
d_{xy}	1.00	1.00	1.00	1.00	1.00	1.00	1.00	1.00	1.00	1.00
$\sum_{\Delta R<0.3} p_T$	1.00	1.00	1.00	1.00	1.00	1.00	1.00	1.00	1.00	1.00
σ_{p_T}/p_T	1.00	1.00	1.00	0.99	0.98	0.97	0.96	0.93	0.90	0.85
d_z	1.00	1.00	1.00	1.00	1.00	1.00	1.00	1.00	1.00	1.00
$\langle 1/\beta \rangle$	0.89	0.96	0.98	0.99	1.00	1.00	1.00	1.00	1.00	1.00
Overall	0.54	0.71	0.75	0.79	0.80	0.79	0.79	0.76	0.74	0.70

Table C.3: Candidate efficiency of HSCPs with $Q = 3e$ and different masses for various offline selections at $\sqrt{s}$ =7 TeV.

Offline Selection	Mass (GeV)									
	100	200	300	400	500	600	700	800	900	1000
Global muon	0.89	0.88	0.87	0.87	0.88	0.88	0.88	0.88	0.88	0.88
$\lvert\eta\rvert$	0.96	0.95	0.96	0.97	0.98	0.98	0.99	0.99	0.99	1.00
Primary vertex	1.00	1.00	1.00	1.00	1.00	1.00	1.00	1.00	1.00	1.00
# Tracker hits (strips and pixels)	1.00	1.00	1.00	1.00	1.00	1.00	1.00	1.00	1.00	1.00
# Pixel hits	0.96	0.97	0.97	0.97	0.97	0.97	0.97	0.98	0.97	0.98
Valid fraction	0.99	1.00	0.99	0.99	1.00	1.00	0.99	1.00	1.00	1.00
# $\frac{\Delta E}{\Delta x}$ measurements	1.00	1.00	1.00	1.00	1.00	1.00	1.00	1.00	1.00	1.00
# $1/\beta$ measurements	0.94	0.94	0.94	0.94	0.94	0.93	0.93	0.93	0.92	0.92
Quality	1.00	1.00	1.00	1.00	1.00	1.00	1.00	1.00	1.00	1.00
χ^2/dof	1.00	1.00	1.00	1.00	1.00	1.00	1.00	1.00	1.00	1.00
p_T	0.71	0.89	0.95	0.98	0.99	1.00	1.00	1.00	1.00	1.00
I_h	1.00	1.00	1.00	1.00	1.00	1.00	1.00	1.00	1.00	1.00
$\sigma_{\langle 1/\beta \rangle}$	0.89	0.89	0.90	0.89	0.89	0.88	0.88	0.87	0.87	0.86
d_{xy}	1.00	1.00	1.00	1.00	1.00	1.00	1.00	1.00	1.00	1.00
$\sum_{\Delta R<0.3} p_T$	1.00	1.00	1.00	1.00	1.00	1.00	1.00	1.00	1.00	1.00
σ_{p_T}/p_T	1.00	1.00	1.00	1.00	0.99	0.99	0.98	0.97	0.96	0.94
d_z	1.00	1.00	1.00	1.00	1.00	1.00	1.00	1.00	1.00	1.00
$\langle 1/\beta \rangle$	0.82	0.94	0.97	0.98	0.99	1.00	1.00	1.00	1.00	1.00
Overall	0.39	0.56	0.63	0.65	0.67	0.67	0.67	0.66	0.64	0.63

Table C.4: Candidate efficiency of HSCPs with $Q = 4e$ and different masses for various offline selections at $\sqrt{s}$ =7 TeV.

Offline Selection	Mass (GeV)									
	100	200	300	400	500	600	700	800	900	1000
Global muon	0.86	0.84	0.82	0.81	0.80	0.80	0.80	0.80	0.79	0.79
$\lvert\eta\rvert$	0.96	0.96	0.97	0.97	0.98	0.99	0.99	0.99	0.99	1.00
Primary vertex	1.00	1.00	1.00	1.00	1.00	1.00	1.00	1.00	1.00	1.00
# Tracker hits (strips and pixels)	1.00	1.00	1.00	1.00	1.00	1.00	1.00	1.00	1.00	1.00
# Pixel hits	0.93	0.94	0.94	0.94	0.95	0.95	0.95	0.95	0.95	0.95
Valid fraction	0.99	0.99	0.99	0.99	0.99	0.99	0.99	0.99	0.99	0.99
# $\frac{\Delta E}{\Delta x}$ measurements	1.00	1.00	1.00	1.00	1.00	1.00	1.00	1.00	1.00	1.00
# $1/\beta$ measurements	0.85	0.86	0.87	0.88	0.88	0.87	0.87	0.85	0.86	0.85
Quality	1.00	1.00	1.00	1.00	1.00	1.00	1.00	1.00	1.00	1.00
χ^2/dof	1.00	1.00	1.00	1.00	1.00	1.00	1.00	1.00	1.00	1.00
p_T	0.59	0.82	0.90	0.95	0.97	0.99	1.00	1.00	1.00	1.00
I_h	1.00	1.00	1.00	1.00	1.00	1.00	1.00	1.00	1.00	1.00
$\sigma_{\langle 1/\beta \rangle}$	0.74	0.79	0.81	0.82	0.82	0.81	0.80	0.79	0.79	0.78
d_{xy}	1.00	1.00	1.00	1.00	1.00	1.00	1.00	1.00	1.00	1.00
$\sum_{\Delta R<0.3} p_T$	1.00	1.00	1.00	1.00	1.00	1.00	1.00	1.00	1.00	1.00
σ_{p_T}/p_T	1.00	1.00	1.00	1.00	1.00	0.99	0.99	0.99	0.98	0.98
d_z	1.00	1.00	1.00	1.00	1.00	1.00	1.00	1.00	1.00	1.00
$\langle 1/\beta \rangle$	0.72	0.90	0.95	0.98	0.99	0.99	1.00	1.00	1.00	1.00
Overall	0.20	0.38	0.45	0.49	0.51	0.51	0.50	0.49	0.49	0.48

Table C.5: Candidate efficiency of HSCPs with $Q = 5e$ and different masses for various offline selections at $\sqrt{s}$ =7 TeV.

Offline Selection	Mass (GeV)									
	100	200	300	400	500	600	700	800	900	1000
Global muon	0.79	0.80	0.76	0.74	0.72	0.71	0.70	0.70	0.69	0.67
$\lvert\eta\rvert$	0.97	0.97	0.98	0.98	0.98	0.98	0.99	0.99	0.99	0.99
Primary vertex	1.00	1.00	1.00	1.00	1.00	1.00	1.00	1.00	1.00	1.00
# Tracker hits (strips and pixels)	1.00	1.00	1.00	1.00	1.00	1.00	1.00	1.00	1.00	1.00
# Pixel hits	0.88	0.89	0.90	0.90	0.91	0.91	0.91	0.93	0.92	0.92
Valid fraction	0.98	0.98	0.98	0.98	0.98	0.98	0.99	0.98	0.99	0.99
# $\frac{\Delta E}{\Delta x}$ measurements	1.00	1.00	1.00	1.00	1.00	1.00	1.00	1.00	1.00	1.00
# $1/\beta$ measurements	0.74	0.77	0.80	0.81	0.81	0.80	0.81	0.79	0.79	0.78
Quality	1.00	1.00	1.00	1.00	1.00	1.00	1.00	1.00	1.00	1.00
χ^2/dof	1.00	1.00	1.00	1.00	1.00	1.00	1.00	1.00	1.00	1.00
p_T	0.50	0.73	0.84	0.90	0.93	0.96	0.98	0.99	1.00	1.00
I_h	1.00	1.00	1.00	1.00	1.00	1.00	1.00	1.00	1.00	1.00
$\sigma_{\langle 1/\beta \rangle}$	0.61	0.67	0.73	0.74	0.75	0.74	0.73	0.73	0.72	0.71
d_{xy}	1.00	1.00	1.00	1.00	1.00	1.00	1.00	1.00	1.00	1.00
$\sum_{\Delta R<0.3} p_T$	1.00	1.00	1.00	1.00	1.00	1.00	1.00	1.00	1.00	1.00
σ_{p_T}/p_T	1.00	1.00	1.00	1.00	1.00	1.00	0.99	0.99	0.99	0.99
d_z	1.00	1.00	1.00	1.00	1.00	1.00	1.00	1.00	1.00	1.00
$\langle 1/\beta \rangle$	0.59	0.86	0.93	0.96	0.98	0.99	0.99	1.00	1.00	1.00
Overall	0.09	0.22	0.30	0.33	0.35	0.35	0.35	0.36	0.35	0.33

Table C.6: Candidate efficiency of HSCPs with $Q = 6e$ and different masses for various offline selections at $\sqrt{s}$ =7 TeV.

Offline Selection	Mass (GeV)									
	100	200	300	400	500	600	700	800	900	1000
Global muon	0.70	0.72	0.67	0.64	0.62	0.60	0.59	0.58	0.56	0.55
$\lvert\eta\rvert$	0.97	0.98	0.98	0.98	0.99	0.99	0.99	0.99	0.99	1.00
Primary vertex	1.00	1.00	1.00	1.00	1.00	1.00	1.00	1.00	1.00	1.00
# Tracker hits (strips and pixels)	1.00	1.00	1.00	1.00	1.00	1.00	1.00	1.00	1.00	1.00
# Pixel hits	0.81	0.82	0.83	0.84	0.84	0.85	0.85	0.86	0.87	0.87
Valid fraction	0.97	0.97	0.98	0.98	0.98	0.98	0.98	0.98	0.98	0.98
# $\frac{\Delta E}{\Delta x}$ measurements	1.00	1.00	1.00	1.00	1.00	1.00	1.00	1.00	1.00	1.00
# $1/\beta$ measurements	0.63	0.68	0.71	0.74	0.74	0.74	0.73	0.72	0.71	0.70
Quality	1.00	1.00	1.00	1.00	1.00	1.00	1.00	1.00	1.00	1.00
χ^2/dof	1.00	1.00	1.00	1.00	1.00	1.00	1.00	1.00	1.00	1.00
p_T	0.42	0.64	0.78	0.83	0.89	0.93	0.96	0.98	0.99	1.00
I_h	1.00	1.00	1.00	1.00	1.00	1.00	1.00	1.00	1.00	1.00
$\sigma_{\langle 1/\beta \rangle}$	0.54	0.59	0.64	0.67	0.71	0.69	0.69	0.68	0.68	0.66
d_{xy}	1.00	1.00	1.00	1.00	1.00	1.00	1.00	1.00	1.00	1.00
$\sum_{\Delta R<0.3} p_T$	0.99	1.00	1.00	1.00	1.00	1.00	1.00	1.00	1.00	1.00
σ_{p_T}/p_T	1.00	1.00	1.00	1.00	1.00	1.00	1.00	1.00	0.99	0.99
d_z	1.00	1.00	1.00	1.00	1.00	1.00	1.00	1.00	1.00	1.00
$\langle 1/\beta \rangle$	0.54	0.79	0.90	0.95	0.97	0.98	0.99	0.99	1.00	0.99
Overall	0.04	0.11	0.17	0.20	0.22	0.23	0.23	0.23	0.22	0.21

Table C.7: Candidate efficiency of HSCPs with $Q = 7e$ and different masses for various offline selections at $\sqrt{s}$ =7 TeV.

Offline Selection	Mass (GeV)									
	100	200	300	400	500	600	700	800	900	1000
Global muon	0.59	0.60	0.56	0.53	0.50	0.49	0.46	0.44	0.43	0.42
$\lvert\eta\rvert$	0.98	0.98	0.98	0.98	0.99	0.99	0.99	0.99	0.99	1.00
Primary vertex	1.00	1.00	1.00	1.00	1.00	1.00	1.00	1.00	1.00	1.00
# Tracker hits (strips and pixels)	1.00	1.00	1.00	1.00	1.00	1.00	1.00	1.00	1.00	1.00
# Pixel hits	0.72	0.74	0.75	0.76	0.75	0.76	0.78	0.78	0.79	0.80
Valid fraction	0.96	0.96	0.96	0.96	0.97	0.97	0.97	0.97	0.97	0.97
# $\frac{\Delta E}{\Delta x}$ measurements	1.00	1.00	1.00	1.00	1.00	1.00	1.00	1.00	1.00	1.00
# $1/\beta$ measurements	0.58	0.60	0.64	0.67	0.68	0.68	0.66	0.65	0.65	0.63
Quality	1.00	1.00	1.00	1.00	1.00	1.00	1.00	1.00	1.00	1.00
χ^2/dof	1.00	1.00	1.00	1.00	1.00	1.00	1.00	1.00	1.00	1.00
p_T	0.32	0.52	0.69	0.77	0.82	0.88	0.92	0.95	0.98	0.99
I_h	0.99	1.00	1.00	1.00	1.00	1.00	1.00	1.00	1.00	1.00
$\sigma_{\langle 1/\beta \rangle}$	0.44	0.53	0.60	0.64	0.68	0.68	0.69	0.69	0.68	0.67
d_{xy}	1.00	1.00	1.00	1.00	1.00	1.00	1.00	1.00	1.00	1.00
$\sum_{\Delta R<0.3} p_T$	0.97	0.98	0.99	0.99	0.99	1.00	1.00	1.00	1.00	1.00
σ_{p_T}/p_T	1.00	1.00	1.00	1.00	1.00	1.00	1.00	1.00	1.00	1.00
d_z	1.00	1.00	1.00	1.00	1.00	1.00	1.00	1.00	1.00	1.00
$\langle 1/\beta \rangle$	0.49	0.74	0.88	0.92	0.96	0.98	0.98	0.99	0.99	0.99
Overall	0.02	0.05	0.09	0.12	0.13	0.14	0.14	0.14	0.14	0.13

Table C.8: Candidate efficiency of HSCPs with $Q = 8e$ and different masses for various offline selections at $\sqrt{s}$ =7 TeV.

Offline Selection	Mass (GeV)									
	100	200	300	400	500	600	700	800	900	1000
Global muon	0.48	0.47	0.44	0.41	0.38	0.36	0.34	0.32	0.30	0.28
$\lvert\eta\rvert$	0.97	0.98	0.98	0.99	0.99	0.99	0.99	0.99	0.99	0.99
Primary vertex	1.00	1.00	1.00	1.00	1.00	1.00	1.00	1.00	1.00	1.00
# Tracker hits (strips and pixels)	1.00	1.00	1.00	1.00	1.00	1.00	1.00	1.00	1.00	1.00
# Pixel hits	0.61	0.61	0.61	0.63	0.64	0.65	0.65	0.68	0.68	0.70
Valid fraction	0.96	0.95	0.95	0.96	0.96	0.96	0.95	0.96	0.97	0.97
# $\frac{\Delta E}{\Delta x}$ measurements	1.00	1.00	1.00	1.00	1.00	1.00	1.00	1.00	1.00	1.00
# $1/\beta$ measurements	0.51	0.54	0.57	0.62	0.64	0.63	0.63	0.62	0.60	0.58
Quality	1.00	1.00	1.00	1.00	1.00	1.00	1.00	1.00	1.00	1.00
χ^2/dof	1.00	1.00	1.00	1.00	1.00	1.00	1.00	1.00	1.00	1.00
p_T	0.29	0.42	0.59	0.67	0.74	0.81	0.86	0.92	0.96	0.98
I_h	1.00	1.00	0.99	1.00	1.00	1.00	1.00	1.00	1.00	1.00
$\sigma_{\langle 1/\beta \rangle}$	0.42	0.50	0.59	0.65	0.68	0.68	0.68	0.70	0.68	0.69
d_{xy}	1.00	1.00	1.00	1.00	1.00	1.00	1.00	1.00	1.00	1.00
$\sum_{\Delta R<0.3} p_T$	0.95	0.97	0.99	0.98	0.98	0.99	0.99	0.99	0.99	0.99
σ_{p_T}/p_T	1.00	1.00	1.00	1.00	1.00	1.00	1.00	1.00	0.99	0.99
d_z	1.00	1.00	1.00	1.00	1.00	1.00	1.00	1.00	1.00	1.00
$\langle 1/\beta \rangle$	0.56	0.70	0.86	0.92	0.96	0.97	0.99	0.99	0.99	0.99
Overall	0.01	0.02	0.04	0.06	0.07	0.07	0.08	0.08	0.08	0.07

Table C.9: Candidate efficiency of HSCPs with $Q = 1e$ and different masses for various offline selections at $\sqrt{s}$ =8 TeV.

Offline Selection	Mass (GeV)									
	100	200	300	400	500	600	700	800	900	1000
Global muon	0.86	0.89	0.91	0.92	0.93	0.93	0.94	0.93	0.92	0.92
$\lvert\eta\rvert$	0.89	0.91	0.93	0.94	0.95	0.96	0.97	0.97	0.98	0.99
Primary vertex	1.00	1.00	1.00	1.00	1.00	1.00	1.00	1.00	1.00	1.00
# Tracker hits (strips and pixels)	0.99	0.99	1.00	0.99	0.99	0.99	0.99	0.99	1.00	1.00
# Pixel hits	0.99	0.99	0.99	0.99	0.99	0.99	0.99	0.99	0.99	0.99
Valid fraction	0.97	0.97	0.97	0.96	0.97	0.97	0.97	0.96	0.97	0.96
# $\frac{\Delta E}{\Delta x}$ measurements	1.00	1.00	1.00	1.00	1.00	1.00	1.00	1.00	1.00	1.00
# $1/\beta$ measurements	0.99	0.98	0.98	0.98	0.97	0.97	0.96	0.96	0.95	0.94
Quality	1.00	1.00	1.00	1.00	1.00	1.00	1.00	1.00	1.00	1.00
χ^2/dof	1.00	1.00	1.00	1.00	1.00	1.00	1.00	1.00	1.00	1.00
p_T	0.96	1.00	1.00	1.00	1.00	1.00	1.00	1.00	1.00	1.00
I_h	0.91	0.94	0.96	0.98	0.98	0.99	0.99	0.99	0.99	0.99
$\sigma_{\langle 1/\beta \rangle}$	0.98	0.97	0.96	0.96	0.95	0.94	0.94	0.93	0.93	0.93
d_{xy}	1.00	1.00	1.00	1.00	1.00	1.00	1.00	1.00	1.00	1.00
$\sum_{\Delta R<0.3} p_T$	1.00	0.99	0.98	0.97	0.95	0.92	0.89	0.86	0.82	0.78
σ_{p_T}/p_T	1.00	1.00	1.00	1.00	1.00	0.99	0.98	0.96	0.94	0.90
d_z	1.00	1.00	1.00	1.00	1.00	1.00	1.00	1.00	1.00	1.00
$\langle 1/\beta \rangle$	0.93	0.96	0.98	0.99	0.99	1.00	1.00	1.00	1.00	1.00
Overall	0.57	0.66	0.70	0.72	0.72	0.70	0.67	0.63	0.58	0.53

Table C.10: Candidate efficiency of HSCPs with $Q = 2e$ and different masses for various offline selections at $\sqrt{s}$ =8 TeV.

Offline Selection	Mass (GeV)									
	100	200	300	400	500	600	700	800	900	1000
Global muon	0.87	0.87	0.89	0.90	0.91	0.91	0.92	0.92	0.92	0.92
$\lvert\eta\rvert$	0.91	0.92	0.93	0.94	0.95	0.96	0.97	0.97	0.98	0.98
Primary vertex	1.00	1.00	1.00	1.00	1.00	1.00	1.00	1.00	1.00	1.00
# Tracker hits (strips and pixels)	1.00	1.00	1.00	1.00	1.00	1.00	0.99	1.00	1.00	1.00
# Pixel hits	0.99	0.98	0.99	0.99	0.99	0.99	0.99	0.99	0.99	0.99
Valid fraction	0.97	0.97	0.97	0.97	0.97	0.97	0.97	0.97	0.97	0.97
# $\frac{\Delta E}{\Delta x}$ measurements	1.00	1.00	1.00	1.00	1.00	1.00	1.00	1.00	1.00	1.00
# $1/\beta$ measurements	0.97	0.97	0.97	0.97	0.96	0.96	0.96	0.95	0.95	0.94
Quality	1.00	1.00	1.00	1.00	1.00	1.00	1.00	1.00	1.00	1.00
χ^2/dof	1.00	1.00	1.00	1.00	1.00	1.00	1.00	1.00	1.00	1.00
p_T	0.81	0.96	0.99	1.00	1.00	1.00	1.00	1.00	1.00	1.00
I_h	1.00	1.00	1.00	1.00	1.00	1.00	1.00	1.00	1.00	1.00
$\sigma_{\langle 1/\beta \rangle}$	0.95	0.94	0.94	0.93	0.92	0.92	0.92	0.91	0.91	0.90
d_{xy}	1.00	1.00	1.00	1.00	1.00	1.00	1.00	1.00	1.00	1.00
$\sum_{\Delta R<0.3} p_T$	1.00	1.00	1.00	0.99	0.99	0.99	0.99	0.99	0.98	0.98
σ_{p_T}/p_T	1.00	1.00	1.00	0.99	0.98	0.97	0.95	0.92	0.89	0.85
d_z	1.00	1.00	1.00	1.00	1.00	1.00	1.00	1.00	1.00	1.00
$\langle 1/\beta \rangle$	0.87	0.95	0.97	0.98	0.99	0.99	1.00	1.00	1.00	1.00
Overall	0.49	0.63	0.67	0.69	0.70	0.70	0.69	0.67	0.64	0.60

Table C.11: Candidate efficiency of HSCPs with $Q = 3e$ and different masses for various offline selections at $\sqrt{s}$ =8 TeV.

Offline Selection	Mass (GeV)									
	100	200	300	400	500	600	700	800	900	1000
Global muon	0.86	0.86	0.86	0.86	0.86	0.86	0.87	0.87	0.86	0.86
$\lvert\eta\rvert$	0.94	0.93	0.94	0.94	0.95	0.96	0.96	0.97	0.98	0.98
Primary vertex	1.00	1.00	1.00	1.00	1.00	1.00	1.00	1.00	1.00	1.00
# Tracker hits (strips and pixels)	0.99	0.99	0.99	0.99	0.99	1.00	0.99	1.00	1.00	1.00
# Pixel hits	0.98	0.98	0.98	0.98	0.98	0.98	0.98	0.98	0.98	0.98
Valid fraction	0.97	0.97	0.97	0.97	0.97	0.97	0.97	0.97	0.97	0.97
# $\frac{\Delta E}{\Delta x}$ measurements	1.00	1.00	1.00	1.00	1.00	1.00	1.00	1.00	1.00	1.00
# $1/\beta$ measurements	0.94	0.94	0.94	0.94	0.94	0.94	0.93	0.93	0.93	0.92
Quality	1.00	1.00	1.00	1.00	1.00	1.00	1.00	1.00	1.00	1.00
χ^2/dof	1.00	1.00	1.00	1.00	1.00	1.00	1.00	1.00	1.00	1.00
p_T	0.69	0.90	0.96	0.98	0.99	1.00	1.00	1.00	1.00	1.00
I_h	1.00	1.00	1.00	1.00	1.00	1.00	1.00	1.00	1.00	1.00
$\sigma_{\langle 1/\beta \rangle}$	0.88	0.88	0.88	0.87	0.87	0.86	0.86	0.85	0.85	0.85
d_{xy}	1.00	1.00	1.00	1.00	1.00	1.00	1.00	1.00	1.00	1.00
$\sum_{\Delta R<0.3} p_T$	1.00	1.00	0.99	0.99	0.99	0.99	0.99	0.99	0.99	0.99
σ_{p_T}/p_T	1.00	1.00	1.00	1.00	0.99	0.98	0.98	0.96	0.95	0.94
d_z	1.00	1.00	1.00	1.00	1.00	1.00	1.00	1.00	1.00	1.00
$\langle 1/\beta \rangle$	0.82	0.93	0.96	0.98	0.99	0.99	0.99	1.00	1.00	1.00
Overall	0.35	0.52	0.57	0.60	0.61	0.61	0.61	0.60	0.59	0.57

Table C.12: Candidate efficiency of HSCPs with $Q = 4e$ and different masses for various offline selections at $\sqrt{s}$ =8 TeV.

Offline Selection	Mass (GeV)									
	100	200	300	400	500	600	700	800	900	1000
Global muon	0.83	0.84	0.83	0.81	0.81	0.80	0.80	0.80	0.79	0.79
$\lvert\eta\rvert$	0.96	0.95	0.95	0.95	0.96	0.96	0.96	0.97	0.98	0.98
Primary vertex	1.00	1.00	1.00	1.00	1.00	1.00	1.00	1.00	1.00	1.00
# Tracker hits (strips and pixels)	0.99	0.99	0.99	0.99	0.99	0.99	0.99	0.99	0.99	0.99
# Pixel hits	0.97	0.97	0.97	0.97	0.97	0.97	0.97	0.97	0.98	0.98
Valid fraction	0.96	0.97	0.97	0.97	0.97	0.97	0.97	0.97	0.97	0.97
# $\frac{\Delta E}{\Delta x}$ measurements	1.00	1.00	1.00	1.00	1.00	1.00	1.00	1.00	1.00	1.00
# $1/\beta$ measurements	0.87	0.88	0.89	0.90	0.90	0.89	0.89	0.88	0.88	0.87
Quality	1.00	1.00	1.00	1.00	1.00	1.00	1.00	1.00	1.00	1.00
χ^2/dof	1.00	1.00	1.00	1.00	1.00	1.00	1.00	1.00	1.00	1.00
p_T	0.63	0.83	0.92	0.95	0.97	0.99	1.00	1.00	1.00	1.00
I_h	1.00	1.00	1.00	1.00	1.00	1.00	1.00	1.00	1.00	1.00
$\sigma_{\langle 1/\beta \rangle}$	0.73	0.77	0.79	0.79	0.78	0.78	0.77	0.77	0.77	0.76
d_{xy}	1.00	1.00	1.00	1.00	1.00	1.00	1.00	1.00	1.00	1.00
$\sum_{\Delta R<0.3} p_T$	0.99	0.99	0.99	0.99	0.99	0.99	0.99	0.99	0.98	0.98
σ_{p_T}/p_T	1.00	1.00	1.00	1.00	1.00	0.99	0.99	0.99	0.98	0.98
d_z	1.00	1.00	1.00	1.00	1.00	1.00	1.00	1.00	1.00	1.00
$\langle 1/\beta \rangle$	0.74	0.91	0.95	0.97	0.98	0.99	0.99	0.99	1.00	1.00
Overall	0.22	0.38	0.45	0.47	0.48	0.48	0.48	0.48	0.47	0.46

Table C.13: Candidate efficiency of HSCPs with $Q = 5e$ and different masses for various offline selections at $\sqrt{s}$ =8 TeV.

Offline Selection	Mass (GeV)									
	100	200	300	400	500	600	700	800	900	1000
Global muon	0.75	0.79	0.78	0.76	0.75	0.74	0.73	0.72	0.71	0.70
$\lvert\eta\rvert$	0.97	0.97	0.96	0.96	0.97	0.97	0.97	0.97	0.98	0.98
Primary vertex	1.00	1.00	1.00	1.00	1.00	1.00	1.00	1.00	1.00	1.00
# Tracker hits (strips and pixels)	0.99	0.99	0.99	0.99	0.99	0.99	0.99	0.99	0.99	0.99
# Pixel hits	0.95	0.95	0.96	0.96	0.96	0.96	0.96	0.96	0.96	0.97
Valid fraction	0.96	0.96	0.96	0.97	0.97	0.97	0.97	0.97	0.97	0.97
# $\frac{\Delta E}{\Delta x}$ measurements	1.00	1.00	1.00	1.00	1.00	1.00	1.00	1.00	1.00	1.00
# $1/\beta$ measurements	0.79	0.80	0.82	0.84	0.84	0.83	0.83	0.83	0.82	0.81
Quality	1.00	1.00	1.00	1.00	1.00	1.00	1.00	1.00	1.00	1.00
χ^2/dof	1.00	1.00	1.00	1.00	1.00	1.00	1.00	1.00	1.00	1.00
p_T	0.55	0.77	0.86	0.91	0.94	0.97	0.98	0.99	1.00	1.00
I_h	1.00	1.00	1.00	1.00	1.00	1.00	1.00	1.00	1.00	1.00
$\sigma_{\langle 1/\beta \rangle}$	0.59	0.66	0.68	0.70	0.70	0.70	0.70	0.69	0.69	0.68
d_{xy}	1.00	1.00	1.00	1.00	1.00	1.00	1.00	1.00	1.00	1.00
$\sum_{\Delta R<0.3} p_T$	0.99	0.99	0.99	0.99	0.99	0.99	0.99	0.98	0.98	0.98
σ_{p_T}/p_T	1.00	1.00	1.00	1.00	1.00	1.00	1.00	0.99	0.99	0.99
d_z	1.00	1.00	1.00	1.00	1.00	1.00	1.00	1.00	1.00	1.00
$\langle 1/\beta \rangle$	0.66	0.88	0.94	0.96	0.98	0.98	0.99	0.99	0.99	0.99
Overall	0.11	0.25	0.31	0.34	0.36	0.36	0.36	0.36	0.35	0.34

Table C.14: Candidate efficiency of HSCPs with $Q = 6e$ and different masses for various offline selections at $\sqrt{s}$ =8 TeV.

Offline Selection	Mass (GeV)									
	100	200	300	400	500	600	700	800	900	1000
Global muon	0.74	0.76	0.74	0.71	0.69	0.67	0.66	0.64	0.62	0.62
$\lvert\eta\rvert$	0.96	0.97	0.97	0.97	0.97	0.97	0.98	0.98	0.98	0.98
Primary vertex	1.00	1.00	1.00	1.00	1.00	1.00	1.00	1.00	1.00	1.00
# Tracker hits (strips and pixels)	0.99	0.99	0.99	0.99	0.99	0.99	0.99	0.99	0.99	0.99
# Pixel hits	0.94	0.94	0.94	0.94	0.94	0.95	0.95	0.95	0.95	0.95
Valid fraction	0.96	0.96	0.96	0.96	0.96	0.97	0.96	0.97	0.96	0.96
# $\frac{\Delta E}{\Delta x}$ measurements	1.00	1.00	1.00	1.00	1.00	1.00	1.00	1.00	1.00	1.00
# $1/\beta$ measurements	0.71	0.71	0.75	0.78	0.78	0.78	0.78	0.76	0.76	0.76
Quality	1.00	1.00	1.00	1.00	1.00	1.00	1.00	1.00	1.00	1.00
χ^2/dof	1.00	1.00	1.00	1.00	1.00	1.00	1.00	1.00	1.00	1.00
p_T	0.40	0.65	0.78	0.85	0.89	0.94	0.96	0.98	0.99	1.00
I_h	1.00	1.00	1.00	1.00	1.00	1.00	1.00	1.00	1.00	1.00
$\sigma_{\langle 1/\beta \rangle}$	0.51	0.56	0.62	0.64	0.65	0.65	0.65	0.65	0.64	0.64
d_{xy}	1.00	1.00	1.00	1.00	1.00	1.00	1.00	1.00	1.00	1.00
$\sum_{\Delta R<0.3} p_T$	0.98	0.98	0.98	0.98	0.98	0.98	0.98	0.98	0.98	0.98
σ_{p_T}/p_T	1.00	1.00	1.00	1.00	1.00	1.00	1.00	1.00	1.00	0.99
d_z	1.00	1.00	1.00	1.00	1.00	1.00	1.00	1.00	1.00	1.00
$\langle 1/\beta \rangle$	0.71	0.85	0.93	0.95	0.97	0.98	0.98	0.99	0.99	0.99
Overall	0.06	0.14	0.21	0.24	0.26	0.27	0.27	0.26	0.26	0.25

Table C.15: Candidate efficiency of HSCPs with $Q = 7e$ and different masses for various offline selections at $\sqrt{s}$ =8 TeV.

Offline Selection	Mass (GeV)									
	100	200	300	400	500	600	700	800	900	1000
Global muon	0.65	0.61	0.62	0.61	0.61	0.59	0.57	0.55	0.53	0.51
$\lvert\eta\rvert$	0.96	0.98	0.98	0.98	0.98	0.98	0.98	0.98	0.98	0.98
Primary vertex	1.00	1.00	1.00	1.00	1.00	1.00	1.00	1.00	1.00	1.00
# Tracker hits (strips and pixels)	0.98	0.99	0.99	0.99	0.99	0.99	0.99	0.99	0.99	0.99
# Pixel hits	0.91	0.92	0.92	0.93	0.93	0.93	0.93	0.93	0.94	0.94
Valid fraction	0.95	0.96	0.96	0.96	0.97	0.96	0.97	0.96	0.97	0.97
# $\frac{\Delta E}{\Delta x}$ measurements	1.00	1.00	1.00	1.00	1.00	1.00	1.00	1.00	1.00	1.00
# $1/\beta$ measurements	0.64	0.62	0.67	0.72	0.72	0.73	0.72	0.72	0.71	0.70
Quality	1.00	1.00	1.00	1.00	1.00	1.00	1.00	1.00	1.00	1.00
χ^2/dof	1.00	1.00	1.00	1.00	1.00	1.00	1.00	1.00	1.00	1.00
p_T	0.30	0.63	0.75	0.80	0.85	0.89	0.93	0.96	0.98	0.99
I_h	1.00	1.00	1.00	1.00	1.00	1.00	1.00	1.00	1.00	1.00
$\sigma_{\langle 1/\beta \rangle}$	0.48	0.52	0.59	0.62	0.65	0.67	0.66	0.66	0.65	0.65
d_{xy}	1.00	1.00	1.00	1.00	1.00	1.00	1.00	1.00	1.00	1.00
$\sum_{\Delta R<0.3} p_T$	0.97	0.98	0.98	0.98	0.98	0.98	0.98	0.98	0.97	0.98
σ_{p_T}/p_T	1.00	1.00	1.00	1.00	1.00	1.00	1.00	1.00	1.00	1.00
d_z	1.00	1.00	1.00	1.00	1.00	1.00	1.00	1.00	1.00	1.00
$\langle 1/\beta \rangle$	0.68	0.85	0.91	0.96	0.97	0.98	0.98	0.98	0.99	0.99
Overall	0.03	0.09	0.14	0.18	0.20	0.21	0.21	0.21	0.20	0.19

Table C.16: Candidate efficiency of HSCPs with $Q = 8e$ and different masses for various offline selections at $\sqrt{s}$ =8 TeV.

Offline Selection	Mass (GeV)									
	100	200	300	400	500	600	700	800	900	1000
Global muon	0.52	0.53	0.54	0.52	0.52	0.50	0.47	0.45	0.42	0.41
$\lvert\eta\rvert$	0.96	0.97	0.98	0.98	0.98	0.98	0.98	0.98	0.98	0.98
Primary vertex	1.00	1.00	1.00	1.00	1.00	1.00	1.00	1.00	1.00	1.00
# Tracker hits (strips and pixels)	0.98	0.98	0.98	0.98	0.98	0.99	0.99	0.99	0.99	0.99
# Pixel hits	0.90	0.90	0.90	0.91	0.91	0.92	0.91	0.92	0.92	0.92
Valid fraction	0.94	0.95	0.95	0.96	0.96	0.96	0.96	0.96	0.96	0.96
# $\frac{\Delta E}{\Delta x}$ measurements	1.00	1.00	1.00	1.00	1.00	1.00	1.00	1.00	1.00	1.00
# $1/\beta$ measurements	0.62	0.62	0.66	0.67	0.70	0.70	0.71	0.68	0.68	0.68
Quality	1.00	1.00	1.00	1.00	1.00	1.00	1.00	1.00	1.00	1.00
χ^2/dof	1.00	1.00	1.00	1.00	1.00	1.00	1.00	1.00	1.00	1.00
p_T	0.21	0.41	0.60	0.69	0.76	0.82	0.87	0.93	0.96	0.98
I_h	0.99	1.00	0.99	1.00	1.00	1.00	1.00	1.00	1.00	1.00
$\sigma_{\langle 1/\beta \rangle}$	0.51	0.54	0.59	0.64	0.68	0.70	0.69	0.69	0.69	0.69
d_{xy}	1.00	1.00	1.00	1.00	1.00	1.00	1.00	1.00	1.00	1.00
$\sum_{\Delta R<0.3} p_T$	0.95	0.97	0.98	0.97	0.98	0.97	0.98	0.98	0.98	0.97
σ_{p_T}/p_T	1.00	1.00	1.00	1.00	1.00	1.00	1.00	1.00	1.00	1.00
d_z	1.00	1.00	1.00	1.00	1.00	1.00	1.00	1.00	1.00	1.00
$\langle 1/\beta \rangle$	0.74	0.84	0.91	0.96	0.97	0.98	0.99	0.99	0.98	0.99
Overall	0.02	0.05	0.09	0.12	0.15	0.16	0.16	0.16	0.16	0.15

APPENDIX D

INDIVIDUAL SYSTEMATIC UNCERTAINTIES

Systematic uncertainties due to various sources (Sec. 5.2) are shown for multiply charged HSCPs of $Q = 1$–$8e$ and mass of 100–1000 GeV.

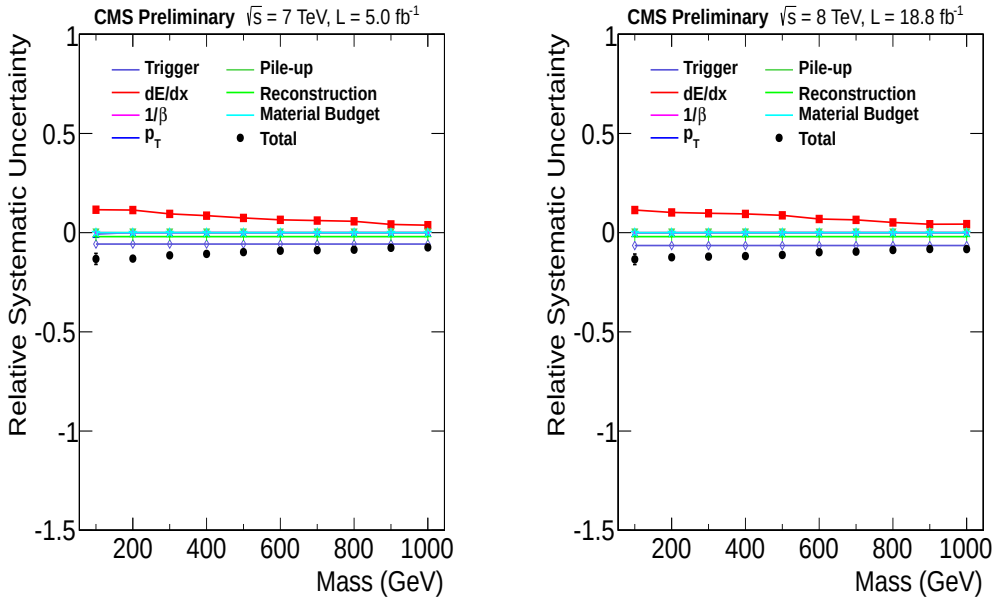

Figure D.1: Individual systematic uncertainties due to various sources and their total for multiply charged HSCPs with $Q = 1e$ for $\sqrt{s}$ =7 TeV (left) and $\sqrt{s} = 8$ TeV (right). Error bar on total uncertainty represents the statistical uncertainty on signal acceptance.

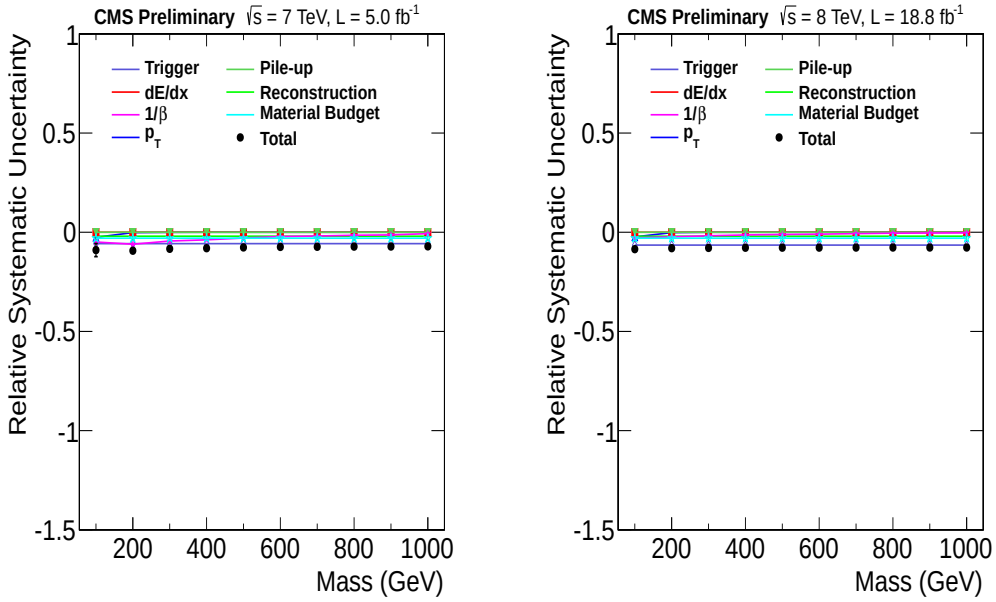

Figure D.2: Individual systematic uncertainties due to various sources and their total for multiply charged HSCPs with $Q = 2e$ for $\sqrt{s}$ =7 TeV (left) and $\sqrt{s} = 8$ TeV (right). Error bar on total uncertainty represents the statistical uncertainty on signal acceptance.

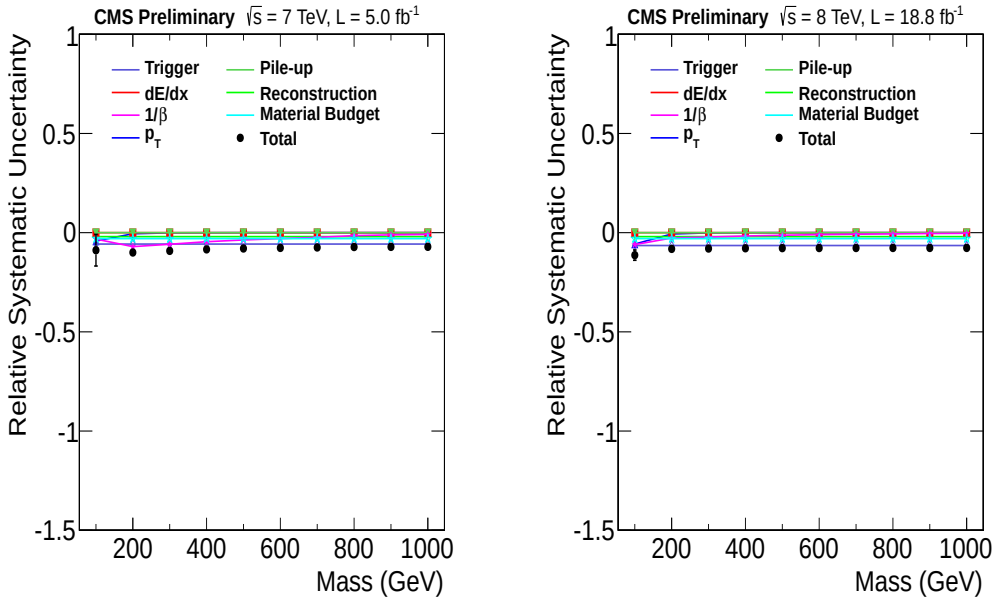

Figure D.3: Individual systematic uncertainties due to various sources and their total for multiply charged HSCPs with $Q = 3e$ for $\sqrt{s}$ =7 TeV (left) and $\sqrt{s} = 8$ TeV (right). Error bar on total uncertainty represents the statistical uncertainty on signal acceptance.

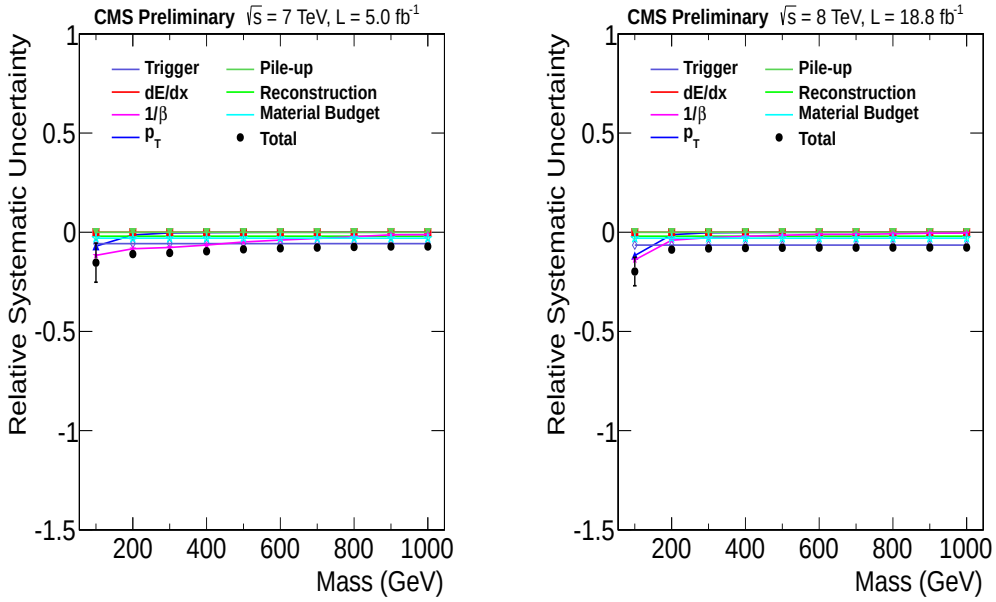

Figure D.4: Individual systematic uncertainties due to various sources and their total for multiply charged HSCPs with $Q = 4e$ for $\sqrt{s}$ =7 TeV (left) and $\sqrt{s} = 8$ TeV (right). Error bar on total uncertainty represents the statistical uncertainty on signal acceptance.

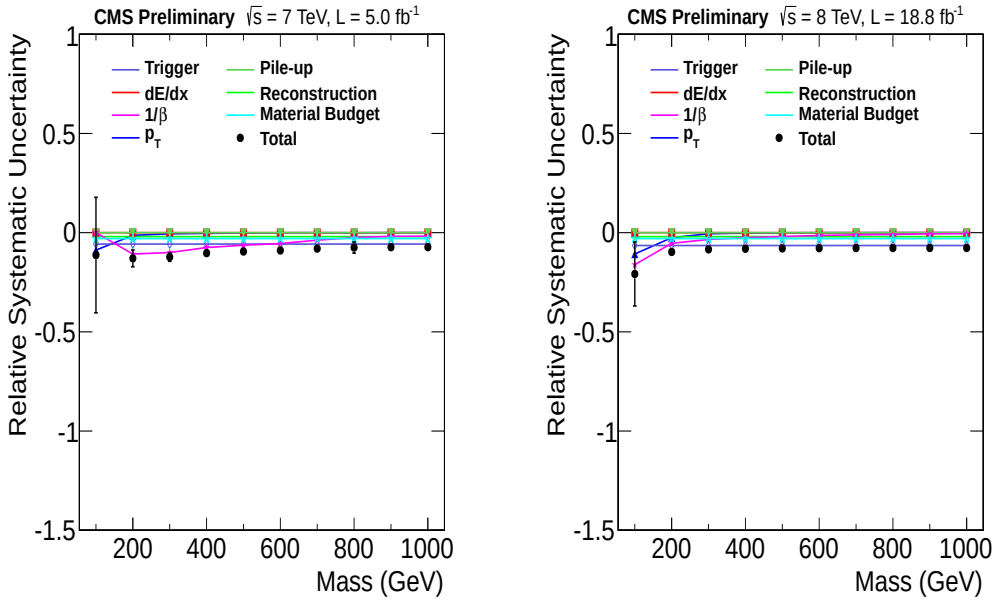

Figure D.5: Individual systematic uncertainties due to various sources and their total for multiply charged HSCPs with $Q = 5e$ for $\sqrt{s}$ =7 TeV (left) and $\sqrt{s} = 8$ TeV (right). Error bar on total uncertainty represents the statistical uncertainty on signal acceptance.

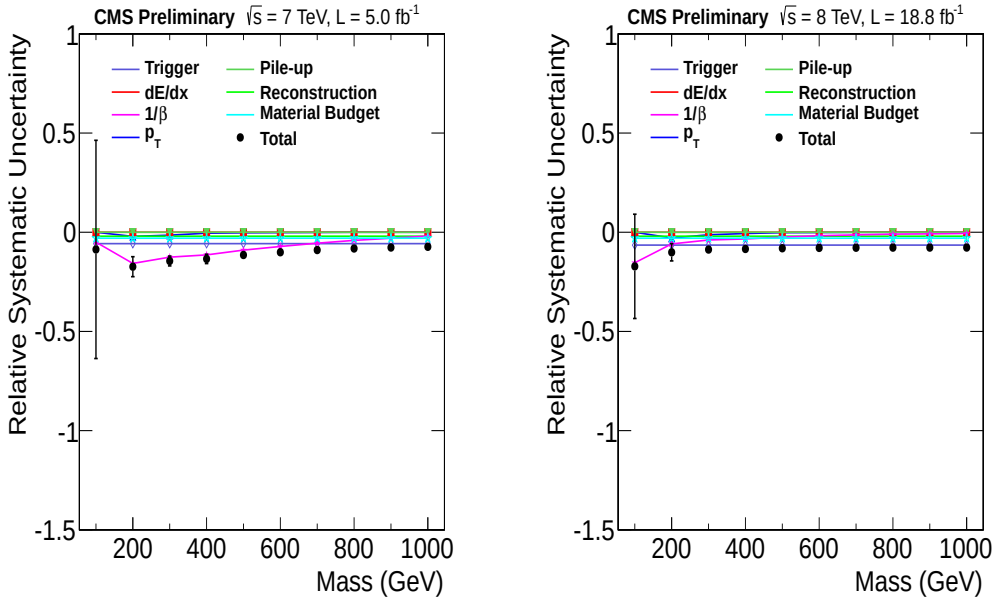

Figure D.6: Individual systematic uncertainties due to various sources and their total for multiply charged HSCPs with $Q = 6e$ for $\sqrt{s}$ =7 TeV (left) and $\sqrt{s} = 8$ TeV (right). Error bar on total uncertainty represents the statistical uncertainty on signal acceptance.

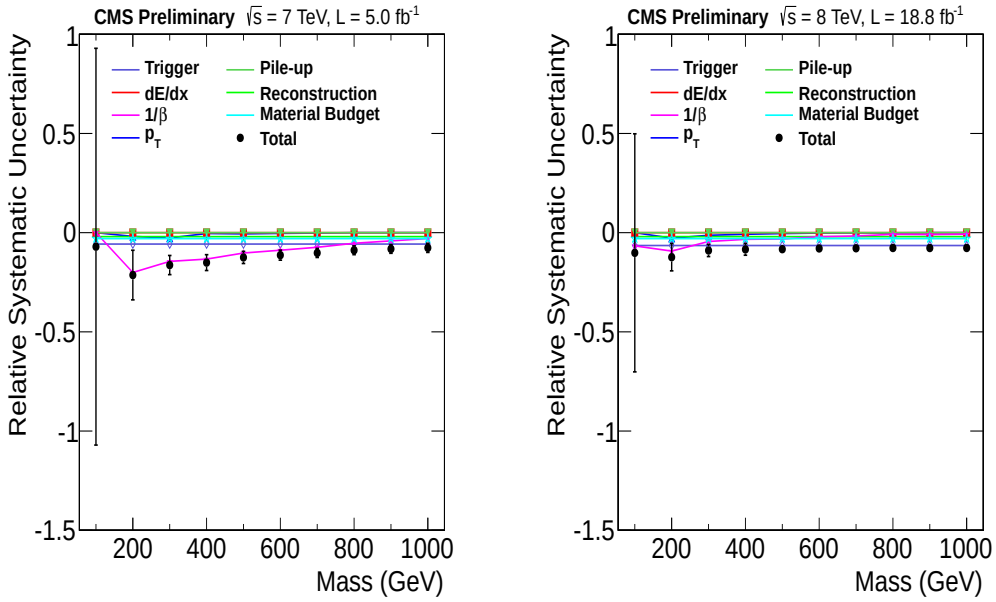

Figure D.7: Individual systematic uncertainties due to various sources and their total for multiply charged HSCPs with $Q = 7e$ for $\sqrt{s}$ =7 TeV (left) and $\sqrt{s} = 8$ TeV (right). Error bar on total uncertainty represents the statistical uncertainty on signal acceptance.

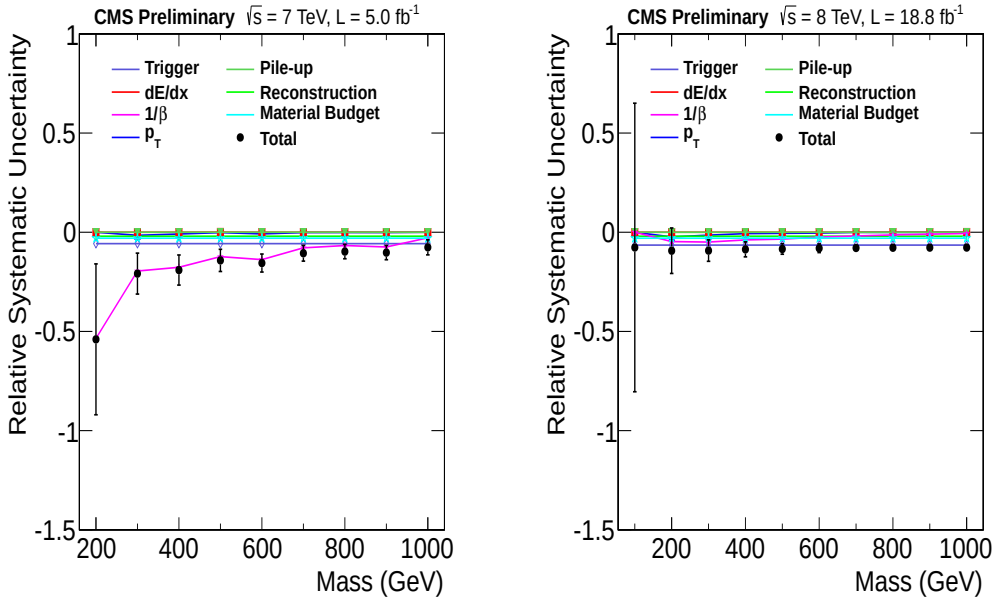

Figure D.8: Individual systematic uncertainties due to various sources and their total for multiply charged HSCPs with $Q = 8e$ for $\sqrt{s}$ =7 TeV (left) and $\sqrt{s} = 8$ TeV (right). Error bar on total uncertainty represents the statistical uncertainty on signal acceptance.

APPENDIX E

FULL RESULTS OF OPTIMIZATION

Complete results of optimization for multiply charged HSCPs with $Q = 1$–$8e$ and mass of 100–1000 GeV at $\sqrt{s}$ =7 and 8 TeV are listed here.

Table E.1: Results of optimization for multiply charged HSCPs with $Q = 1e$, and $2e$ for $\sqrt{s} = 7$ TeV showing optimized I_{as} and $1/\beta$ selections, signal acceptance, predicted numbers of background candidates, observed numbers of data candidates, and expected and observed cross section limits. The two quantities in the paranthesis next to signal acceptance are systematic and statistical uncertainties on signal acceptance respectively, expressed as a percentage of the signal acceptance.

Q (e)	Mass (GeV)	I_{as}	$1/\beta$	Acceptance	Prediction	Observation	σ (pb)	
							Exp.	Obs.
1	100	0.475	1.400	0.1476 (8%, 2.9%)	0.0024 ± 0.0007	0	0.0039	0.004
	200	0.500	1.400	0.2564 (8.4%, 2.2%)	0.0020 ± 0.0006	0	0.0023	0.0024
	300	0.500	1.425	0.3289 (7.1%, 1.9%)	0.0013 ± 0.0004	0	0.0018	0.0018
	400	0.525	1.450	0.3438 (7%, 1.9%)	0.0008 ± 0.0002	0	0.0017	0.0018
	500	0.525	1.450	0.3991 (7%, 1.6%)	0.0008 ± 0.0002	0	0.0015	0.0015
	600	0.525	1.450	0.4365 (7%, 1.1%)	0.0008 ± 0.0002	0	0.0013	0.0014
	700	0.525	1.450	0.4537 (6.9%, 1.1%)	0.0008 ± 0.0002	0	0.0013	0.0013
	800	0.525	1.450	0.4711 (6.8%, 1%)	0.0008 ± 0.0002	0	0.0012	0.0013
	900	0.525	1.450	0.4629 (6.8%, 0.98%)	0.0008 ± 0.0002	0	0.0013	0.0013
	1000	0.525	1.450	0.4563 (6.7%, 0.99%)	0.0008 ± 0.0002	0	0.0013	0.0013
2	100	0.525	1.200	0.1048 (9%, 3.3%)	0.1390 ± 0.0393	0	0.0055	0.0057
	200	0.525	1.250	0.3008 (8.9%, 1.9%)	0.0389 ± 0.0110	0	0.0019	0.002
	300	0.500	1.300	0.3885 (8.8%, 1.6%)	0.0136 ± 0.0038	0	0.0015	0.0016
	400	0.475	1.375	0.3753 (7.9%, 1.7%)	0.0037 ± 0.0010	0	0.0015	0.0017
	500	0.525	1.350	0.4498 (7.7%, 1.6%)	0.0045 ± 0.0013	0	0.0013	0.0013
	600	0.500	1.425	0.4139 (8%, 1.1%)	0.0013 ± 0.0004	0	0.0014	0.0015
	700	0.525	1.450	0.4126 (7.7%, 1.2%)	0.0008 ± 0.0002	0	0.0014	0.0015
	800	0.525	1.425	0.434 (7.5%, 1.6%)	0.0012 ± 0.0003	0	0.0013	0.0014
	900	0.525	1.425	0.4273 (7.5%, 1%)	0.0012 ± 0.0003	0	0.0013	0.0014
	1000	0.525	1.425	0.4157 (7.4%, 1%)	0.0012 ± 0.0003	0	0.0014	0.0015

Table E.2: Results of optimization for multiply charged HSCPs with $Q = 3e$, and $4e$ for $\sqrt{s} = 7$ TeV showing optimized I_{as} and $1/\beta$ selections, signal acceptance, predicted numbers of background candidates, observed numbers of data candidates, and expected and observed cross section limits. The two quantities in the paranthesis next to signal acceptance are systematic and statistical uncertainties on signal acceptance respectively, expressed as a percentage of the signal acceptance.

Q (e)	Mass (GeV)	I_{as}	$1/\beta$	Acceptance	Prediction	Observation	σ (pb)	
							Exp.	Obs.
3	100	0.525	1.175	0.02816 (10%, 7%)	0.2780 ± 0.0787	0	0.021	0.022
	200	0.525	1.250	0.1421 (9.3%, 1.9%)	0.0389 ± 0.0110	0	0.0039	0.0043
	300	0.525	1.275	0.2538 (9.7%, 1.6%)	0.0216 ± 0.0061	0	0.0023	0.0024
	400	0.500	1.300	0.3241 (9.1%, 0.93%)	0.0136 ± 0.0038	0	0.0018	0.0019
	500	0.475	1.300	0.3811 (8.4%, 0.96%)	0.0162 ± 0.0043	0	0.0015	0.0016
	600	0.525	1.350	0.3661 (8%, 0.92%)	0.0045 ± 0.0013	0	0.0016	0.0016
	700	0.525	1.350	0.3891 (8%, 1.2%)	0.0045 ± 0.0013	0	0.0015	0.0016
	800	0.525	1.425	0.3505 (7.7%, 1.7%)	0.0012 ± 0.0003	0	0.0017	0.0017
	900	0.525	1.425	0.3466 (7.6%, 1.2%)	0.0012 ± 0.0003	0	0.0017	0.0018
	1000	0.525	1.425	0.3438 (7.6%, 1.2%)	0.0012 ± 0.0003	0	0.0017	0.0018
4	100	0.500	1.100	0.0104 (18%, 4%)	2.7300 ± 0.7720	2	0.095	0.092
	200	0.525	1.225	0.05791 (11%, 1.7%)	0.0726 ± 0.0206	0	0.0098	0.011
	300	0.525	1.250	0.1328 (10%, 1.2%)	0.0389 ± 0.0110	0	0.0043	0.0045
	400	0.525	1.275	0.192 (10%, 0.88%)	0.0216 ± 0.0061	0	0.003	0.0033
	500	0.525	1.275	0.2496 (9.3%, 0.92%)	0.0216 ± 0.0061	0	0.0023	0.0025
	600	0.525	1.275	0.2845 (8.4%, 0.9%)	0.0216 ± 0.0061	0	0.002	0.0022
	700	0.525	1.275	0.2969 (8.2%, 1.5%)	0.0216 ± 0.0061	0	0.0019	0.002
	800	0.475	1.325	0.2777 (8.5%, 2.2%)	0.0095 ± 0.0026	0	0.0021	0.0022
	900	0.525	1.350	0.2661 (7.7%, 1.4%)	0.0045 ± 0.0013	0	0.0022	0.0022
	1000	0.500	1.375	0.2497 (7.7%, 1.5%)	0.0031 ± 0.0009	0	0.0023	0.0024

Table E.3: Results of optimization for multiply charged HSCPs with $Q = 5e$, and $6e$ for $\sqrt{s} = 7$ TeV showing optimized I_{as} and $1/\beta$ selections, signal acceptance, predicted numbers of background candidates, observed numbers of data candidates, and expected and observed cross section limits. The two quantities in the paranthesis next to signal acceptance are systematic and statistical uncertainties on signal acceptance respectively, expressed as a percentage of the signal acceptance.

Q (e)	Mass (GeV)	I_{as}	$1/\beta$	Acceptance	Prediction	Observation	σ (pb)	
							Exp.	Obs.
5	100	0.500	1.100	0.001745 (25%, 9.4%)	2.7300 ± 0.7720	2	0.59	0.56
	200	0.525	1.175	0.02349 (13%, 3.8%)	0.2780 ± 0.0787	0	0.025	0.026
	300	0.525	1.225	0.05786 (12%, 2.3%)	0.0726 ± 0.0206	0	0.0098	0.011
	400	0.525	1.250	0.09362 (12%, 1.3%)	0.0389 ± 0.0110	0	0.0061	0.0065
	500	0.525	1.250	0.1355 (10%, 1.4%)	0.0389 ± 0.0110	0	0.0042	0.0044
	600	0.525	1.275	0.1535 (9.9%, 2.1%)	0.0216 ± 0.0061	0	0.0037	0.0038
	700	0.475	1.300	0.1575 (8.9%, 2%)	0.0162 ± 0.0043	0	0.0036	0.0038
	800	0.525	1.300	0.1781 (9.4%, 3.1%)	0.0126 ± 0.0036	0	0.0032	0.0034
	900	0.525	1.275	0.1799 (8.1%, 1.8%)	0.0216 ± 0.0061	0	0.0032	0.0034
	1000	0.500	1.300	0.1635 (8%, 1.9%)	0.0136 ± 0.0038	0	0.0035	0.004
6	100	0.500	1.100	3.84×10^{-4} (24%, 13%)	2.7300 ± 0.7720	2	2.6	2.6
	200	0.525	1.150	0.005883 (16%, 3.8%)	0.5790 ± 0.1640	0	0.11	0.1
	300	0.525	1.200	0.02024 (14%, 2.5%)	0.1390 ± 0.0393	0	0.028	0.03
	400	0.525	1.250	0.03235 (16%, 2.8%)	0.0389 ± 0.0110	0	0.017	0.019
	500	0.525	1.250	0.05556 (14%, 2.2%)	0.0389 ± 0.0110	0	0.01	0.011
	600	0.525	1.250	0.07648 (12%, 1.8%)	0.0389 ± 0.0110	0	0.0074	0.0079
	700	0.525	1.275	0.08054 (11%, 1.7%)	0.0216 ± 0.0061	0	0.0071	0.0076
	800	0.525	1.300	0.08081 (11%, 1.7%)	0.0126 ± 0.0036	0	0.0072	0.008
	900	0.525	1.325	0.07714 (10%, 1.8%)	0.0074 ± 0.0021	0	0.0075	0.0077
	1000	0.525	1.325	0.07818 (9.3%, 1.8%)	0.0074 ± 0.0021	0	0.0073	0.0076

Table E.4: Results of optimization for multiply charged HSCPs with $Q = 7e$, and $8e$ for $\sqrt{s} = 7$ TeV showing optimized I_{as} and $1/\beta$ selections, signal acceptance, predicted numbers of background candidates, observed numbers of data candidates, and expected and observed cross section limits. The two quantities in the paranthesis next to signal acceptance are systematic and statistical uncertainties on signal acceptance respectively, expressed as a percentage of the signal acceptance.

Q (e)	Mass (GeV)	I_{as}	$1/\beta$	Acceptance	Prediction	Observation	σ (pb)	
							Exp.	Obs.
7	100	0.500	1.125	4.3×10^{-5} (47%, 37%)	1.2900 ± 0.3620	1	23	24
	200	0.500	1.100	0.002429 (29%, 5.8%)	2.7300 ± 0.7720	2	0.43	0.42
	300	0.525	1.175	0.00679 (17%, 4.3%)	0.2780 ± 0.0787	0	0.086	0.09
	400	0.500	1.200	0.01567 (15%, 4%)	0.1500 ± 0.0416	0	0.037	0.039
	500	0.525	1.225	0.02282 (15%, 3.3%)	0.0726 ± 0.0206	0	0.025	0.027
	600	0.500	1.275	0.02491 (17%, 3.1%)	0.0233 ± 0.0065	0	0.023	0.024
	700	0.525	1.300	0.02805 (13%, 3%)	0.0126 ± 0.0036	0	0.02	0.022
	800	0.525	1.325	0.02938 (13%, 2.9%)	0.0074 ± 0.0021	0	0.02	0.021
	900	0.525	1.325	0.03296 (13%, 2.7%)	0.0074 ± 0.0021	0	0.017	0.019
	1000	0.525	1.350	0.02956 (12%, 2.9%)	0.0045 ± 0.0013	0	0.019	0.021
8	100	0.500	1.100	3.5×10^{-5} (95%, 43%)	2.7300 ± 0.7720	2	49	45
	200	0.525	1.125	3.38×10^{-4} (23%, 17%)	1.1900 ± 0.3410	1	2.3	2.6
	300	0.525	1.150	0.002183 (19%, 7.9%)	0.5790 ± 0.1640	0	0.29	0.28
	400	0.525	1.175	0.005645 (18%, 6.8%)	0.2780 ± 0.0787	0	0.1	0.11
	500	0.525	1.225	0.007085 (20%, 6.1%)	0.0726 ± 0.0206	0	0.079	0.089
	600	0.525	1.250	0.008548 (22%, 5.5%)	0.0389 ± 0.0110	0	0.066	0.074
	700	0.525	1.275	0.0108 (16%, 5%)	0.0216 ± 0.0061	0	0.052	0.056
	800	0.525	1.300	0.01199 (18%, 4.7%)	0.0126 ± 0.0036	0	0.047	0.052
	900	0.500	1.325	0.01067 (15%, 4.9%)	0.0080 ± 0.0022	0	0.053	0.057
	1000	0.500	1.325	0.01221 (13%, 4.7%)	0.0080 ± 0.0022	0	0.046	0.05

Table E.5: Results of optimization for multiply charged HSCPs with $Q = 1e$, and $2e$ for $\sqrt{s} = 8$ TeV showing optimized I_{as} and $1/\beta$ selections, signal acceptance, predicted numbers of background candidates, observed numbers of data candidates, and expected and observed cross section limits. The two quantities in the paranthesis next to signal acceptance are systematic and statistical uncertainties on signal acceptance respectively, expressed as a percentage of the signal acceptance.

Q (e)	Mass (GeV)	I_{as}	$1/\beta$	Acceptance	Prediction	Observation	σ (pb)	
							Exp.	Obs.
1	100	0.475	1.400	0.1407 (9.6%, 2.7%)	0.0076 ± 0.0017	0	0.001	0.0012
	200	0.525	1.375	0.2309 (9.3%, 2.1%)	0.0065 ± 0.0015	0	6.6×10^{-4}	7.1×10^{-4}
	300	0.525	1.375	0.3114 (9.2%, 1.7%)	0.0065 ± 0.0015	0	5.0×10^{-4}	5.2×10^{-4}
	400	0.500	1.450	0.3296 (7.5%, 1.7%)	0.0029 ± 0.0007	0	4.7×10^{-4}	5.0×10^{-4}
	500	0.500	1.375	0.4184 (8.4%, 1.5%)	0.0081 ± 0.0018	0	3.6×10^{-4}	3.9×10^{-4}
	600	0.525	1.425	0.4195 (7.6%, 1.5%)	0.0033 ± 0.0008	0	3.7×10^{-4}	3.9×10^{-4}
	700	0.500	1.400	0.4453 (7.6%, 1.4%)	0.0055 ± 0.0012	0	3.4×10^{-4}	3.6×10^{-4}
	800	0.500	1.400	0.4404 (7.4%, 1.4%)	0.0055 ± 0.0012	0	3.5×10^{-4}	3.5×10^{-4}
	900	0.500	1.400	0.4198 (7.3%, 1.4%)	0.0055 ± 0.0012	0	3.6×10^{-4}	3.7×10^{-4}
	1000	0.500	1.400	0.4033 (7.4%, 1.5%)	0.0055 ± 0.0012	0	3.8×10^{-4}	3.9×10^{-4}
2	100	0.525	1.275	0.06808 (8.9%, 1.2%)	0.0584 ± 0.0132	0	0.0022	0.0023
	200	0.525	1.325	0.206 (7.9%, 0.69%)	0.0180 ± 0.0041	0	7.4×10^{-4}	7.9×10^{-4}
	300	0.525	1.325	0.3255 (7.9%, 0.54%)	0.0180 ± 0.0041	0	4.7×10^{-4}	4.8×10^{-4}
	400	0.500	1.350	0.3791 (7.8%, 0.5%)	0.0133 ± 0.0030	0	4.1×10^{-4}	4.2×10^{-4}
	500	0.500	1.325	0.4485 (7.8%, 0.45%)	0.0224 ± 0.0050	0	3.4×10^{-4}	3.5×10^{-4}
	600	0.500	1.375	0.4364 (7.8%, 0.45%)	0.0081 ± 0.0018	0	3.5×10^{-4}	3.7×10^{-4}
	700	0.500	1.375	0.4549 (7.7%, 0.44%)	0.0081 ± 0.0018	0	3.4×10^{-4}	3.6×10^{-4}
	800	0.525	1.400	0.4459 (7.7%, 0.46%)	0.0044 ± 0.0010	0	3.5×10^{-4}	3.7×10^{-4}
	900	0.525	1.400	0.4454 (7.7%, 0.44%)	0.0044 ± 0.0010	0	3.5×10^{-4}	3.7×10^{-4}
	1000	0.525	1.400	0.4336 (7.7%, 0.45%)	0.0044 ± 0.0010	0	3.6×10^{-4}	3.8×10^{-4}

Table E.6: Results of optimization for multiply charged HSCPs with $Q = 3e$, and $4e$ for $\sqrt{s} = 8$ TeV showing optimized I_{as} and $1/\beta$ selections, signal acceptance, predicted numbers of background candidates, observed numbers of data candidates, and expected and observed cross section limits. The two quantities in the paranthesis next to signal acceptance are systematic and statistical uncertainties on signal acceptance respectively, expressed as a percentage of the signal acceptance.

Q (e)	Mass (GeV)	I_{as}	$1/\beta$	Acceptance	Prediction	Observation	σ (pb)	
							Exp.	Obs.
3	100	0.525	1.175	0.02335 (12%, 2.2%)	0.8220 ± 0.1870	2	0.0075	0.013
	200	0.525	1.275	0.1244 (8.1%, 0.91%)	0.0584 ± 0.0132	0	0.0012	0.0013
	300	0.525	1.275	0.2406 (8%, 0.64%)	0.0584 ± 0.0132	0	6.3×10^{-4}	6.8×10^{-4}
	400	0.525	1.325	0.2868 (7.9%, 0.58%)	0.0180 ± 0.0041	0	5.4×10^{-4}	5.4×10^{-4}
	500	0.525	1.350	0.3275 (7.8%, 0.55%)	0.0107 ± 0.0024	0	4.7×10^{-4}	5.0×10^{-4}
	600	0.500	1.350	0.3658 (7.8%, 0.51%)	0.0133 ± 0.0030	0	4.2×10^{-4}	4.4×10^{-4}
	700	0.500	1.375	0.375 (7.8%, 0.5%)	0.0081 ± 0.0018	0	4.1×10^{-4}	4.3×10^{-4}
	800	0.500	1.375	0.389 (7.8%, 0.49%)	0.0081 ± 0.0018	0	3.9×10^{-4}	4.1×10^{-4}
	900	0.525	1.400	0.3768 (7.8%, 0.49%)	0.0044 ± 0.0010	0	4.1×10^{-4}	4.3×10^{-4}
	1000	0.525	1.400	0.3819 (7.7%, 0.49%)	0.0044 ± 0.0010	0	4.0×10^{-4}	4.3×10^{-4}
4	100	0.525	1.125	0.009946 (12%, 3.4%)	3.5400 ± 0.8050	3	0.029	0.029
	200	0.525	1.250	0.05377 (8.5%, 1.4%)	0.1100 ± 0.0250	0	0.0028	0.003
	300	0.525	1.275	0.1256 (8.1%, 0.92%)	0.0584 ± 0.0132	0	0.0012	0.0013
	400	0.525	1.300	0.1822 (8%, 0.76%)	0.0325 ± 0.0074	0	8.5×10^{-4}	8.8×10^{-4}
	500	0.525	1.325	0.2205 (7.9%, 0.68%)	0.0180 ± 0.0041	0	6.9×10^{-4}	7.3×10^{-4}
	600	0.525	1.325	0.2638 (7.8%, 0.62%)	0.0180 ± 0.0041	0	5.8×10^{-4}	5.9×10^{-4}
	700	0.525	1.325	0.2884 (7.8%, 0.59%)	0.0180 ± 0.0041	0	5.3×10^{-4}	5.4×10^{-4}
	800	0.525	1.325	0.3036 (7.8%, 0.57%)	0.0180 ± 0.0041	0	5.1×10^{-4}	5.1×10^{-4}
	900	0.500	1.375	0.283 (7.8%, 0.59%)	0.0081 ± 0.0018	0	5.4×10^{-4}	5.6×10^{-4}
	1000	0.500	1.375	0.2831 (7.8%, 0.59%)	0.0081 ± 0.0018	0	5.4×10^{-4}	5.6×10^{-4}

Table E.7: Results of optimization for multiply charged HSCPs with $Q = 5e$, and $6e$ for $\sqrt{s} = 8$ TeV showing optimized I_{as} and $1/\beta$ selections, signal acceptance, predicted numbers of background candidates, observed numbers of data candidates, and expected and observed cross section limits. The two quantities in the paranthesis next to signal acceptance are systematic and statistical uncertainties on signal acceptance respectively, expressed as a percentage of the signal acceptance.

Q (e)	Mass (GeV)	I_{as}	$1/\beta$	Acceptance	Prediction	Observation	σ (pb)	
							Exp.	Obs.
5	100	0.525	1.125	0.002168 (11%, 7.1%)	3.5400 ± 0.8050	3	0.13	0.13
	200	0.525	1.175	0.03205 (9.7%, 1.9%)	0.8220 ± 0.1870	2	0.0057	0.0095
	300	0.525	1.250	0.05928 (8.4%, 1.4%)	0.1100 ± 0.0250	0	0.0026	0.0027
	400	0.525	1.275	0.09979 (8.1%, 1.2%)	0.0584 ± 0.0132	0	0.0015	0.0016
	500	0.525	1.275	0.1461 (7.9%, 0.85%)	0.0584 ± 0.0132	0	0.001	0.0011
	600	0.525	1.325	0.1513 (8%, 0.85%)	0.0180 ± 0.0041	0	0.001	0.0011
	700	0.525	1.350	0.165 (7.9%, 0.8%)	0.0107 ± 0.0024	0	9.3×10^{-4}	0.00099
	800	0.525	1.325	0.1925 (7.8%, 0.74%)	0.0180 ± 0.0041	0	8.0×10^{-4}	8.5×10^{-4}
	900	0.525	1.325	0.1988 (7.8%, 0.73%)	0.0180 ± 0.0041	0	7.7×10^{-4}	8.2×10^{-4}
	1000	0.500	1.375	0.1798 (7.8%, 0.76%)	0.0081 ± 0.0018	0	8.6×10^{-4}	8.9×10^{-4}
6	100	0.525	1.125	7.48×10^{-4} (13%, 12%)	3.5400 ± 0.8050	3	0.38	0.39
	200	0.525	1.150	0.01265 (10%, 3.1%)	1.6900 ± 0.3830	2	0.018	0.022
	300	0.525	1.200	0.03422 (8.7%, 1.8%)	0.4140 ± 0.0938	1	0.0048	0.0071
	400	0.525	1.250	0.04918 (8.6%, 1.5%)	0.1100 ± 0.0250	0	0.003	0.0033
	500	0.525	1.275	0.07239 (8.1%, 1.3%)	0.0584 ± 0.0132	0	0.0021	0.0022
	600	0.525	1.300	0.08965 (8%, 1.1%)	0.0325 ± 0.0074	0	0.0017	0.0018
	700	0.525	1.325	0.1014 (8%, 1%)	0.0180 ± 0.0041	0	0.0015	0.0016
	800	0.525	1.325	0.1127 (7.8%, 0.99%)	0.0180 ± 0.0041	0	0.0014	0.0014
	900	0.525	1.350	0.1115 (7.8%, 1%)	0.0107 ± 0.0024	0	0.0014	0.0014
	1000	0.525	1.325	0.1231 (7.8%, 0.96%)	0.0180 ± 0.0041	0	0.0012	0.0013

Table E.8: Results of optimization for multiply charged HSCPs with $Q = 7e$, and $8e$ for $\sqrt{s} = 8$ TeV showing optimized I_{as} and $1/\beta$ selections, signal acceptance, predicted numbers of background candidates, observed numbers of data candidates, and expected and observed cross section limits. The two quantities in the paranthesis next to signal acceptance are systematic and statistical uncertainties on signal acceptance respectively, expressed as a percentage of the signal acceptance.

Q (e)	Mass (GeV)	I_{as}	$1/\beta$	Acceptance	Prediction	Observation	σ (pb)	
							Exp.	Obs.
7	100	0.525	1.125	1.92×10^{-4} (11%, 17%)	3.5400 ± 0.8050	3	1.5	1.5
	200	0.525	1.150	0.003969 (9.7%, 4.7%)	1.6900 ± 0.3830	2	0.056	0.069
	300	0.525	1.200	0.01336 (9%, 3.1%)	0.4140 ± 0.0938	1	0.012	0.018
	400	0.525	1.250	0.02289 (8.8%, 3.6%)	0.1100 ± 0.0250	0	0.0066	0.0069
	500	0.525	1.275	0.03617 (8.4%, 2.6%)	0.0584 ± 0.0132	0	0.0041	0.0044
	600	0.525	1.275	0.05667 (8%, 2.1%)	0.0584 ± 0.0132	0	0.0027	0.0029
	700	0.525	1.300	0.06403 (8%, 2%)	0.0325 ± 0.0074	0	0.0024	0.0026
	800	0.525	1.325	0.06907 (8%, 1.9%)	0.0180 ± 0.0041	0	0.0022	0.0024
	900	0.525	1.325	0.07377 (7.9%, 1.9%)	0.0180 ± 0.0041	0	0.0021	0.0022
	1000	0.525	1.350	0.06846 (8%, 2%)	0.0107 ± 0.0024	0	0.0022	0.0023
8	100	0.525	1.125	9.8×10^{-5} (27%, 24%)	3.5400 ± 0.8050	3	3.4	3.2
	200	0.525	1.125	0.002177 (10%, 6.1%)	3.5400 ± 0.8050	3	0.13	0.13
	300	0.525	1.175	0.007014 (10%, 4.6%)	0.8220 ± 0.1870	2	0.026	0.043
	400	0.525	1.200	0.01564 (8.6%, 3.8%)	0.4140 ± 0.0938	1	0.01	0.016
	500	0.525	1.225	0.02701 (8.7%, 2.9%)	0.2130 ± 0.0483	0	0.0057	0.0059
	600	0.525	1.275	0.03044 (8.3%, 2.7%)	0.0584 ± 0.0132	0	0.0049	0.0053
	700	0.525	1.275	0.03934 (8.2%, 2.4%)	0.0584 ± 0.0132	0	0.0038	0.004
	800	0.525	1.300	0.04436 (8.1%, 2.3%)	0.0325 ± 0.0074	0	0.0035	0.0038
	900	0.500	1.325	0.04377 (8%, 2.3%)	0.0224 ± 0.0050	0	0.0034	0.0037
	1000	0.525	1.325	0.04569 (7.9%, 2.2%)	0.0180 ± 0.0041	0	0.0033	0.0036

BIBLIOGRAPHY

[1] F. Englert and R. Brout. Broken symmetry and the mass of gauge vector mesons. *Phys. Rev. Lett.*, 13:321, 1964.

[2] P.W. Higgs. Broken symmetries, massless particles and gauge fields. *Phys. Lett.*, 12 (2):132, 1964.

[3] P.W. Higgs. Broken symmetries and the masses of gauge bosons. *Phys. Rev. Lett.*, 13: 508, 1964.

[4] G.S. Guralnik, C.R. Hagen, and T.W.B. Kibble. Global conservation laws and massless particles. *Phys. Rev. Lett.*, 13:585, 1964.

[5] P.W. Higgs. Spontaneous symmetry breakdown without massless bosons. *Phys. Rev.*, 145:1156, 1966.

[6] T.W.B. Kibble. Symmetry breaking in non-abelian gauge theories. *Phys. Rev.*, 155: 1554, 1967.

[7] S. Chatrchyan et al. Observation of a new boson at a mass of 125 GeV with the CMS experiment at the LHC. *Phys. Lett.*, B716:30, 2012.

[8] G. Aad et al. Observation of a new particle in the search for the standard model Higgs boson with the ATLAS detector at the LHC. *Phys. Lett.*, B716:1, 2012.

[9] ATLAS Collaboration. Combined coupling measurements of the Higgs-like boson with the ATLAS detector using up to 25 fb^{-1} of proton-proton collision data. Technical Report ATLAS-CONF-2013-034, CERN, Geneva, 2013.

[10] CMS Collaboration. Combination of standard model Higgs boson searches and measurements of the properties of the new boson with a mass near 125 GeV. Technical Report CMS-PAS-HIG-13-005, CERN, Geneva, 2013.

[11] ALEPH Collaboration, CDF Collaboration, DØ Collaboration, DELPHI Collaboration, L3 Collaboration, OPAL Collaboration, SLD Collaboration, LEP Electroweak Working Group, Tevatron Electroweak Working Group, SLD Electroweak and Heavy Flavour Groups. Precision electroweak measurements and constraints on the standard model. 2010. arXiv:hep-ex/1012.2367.

[12] M. Persic, P. Salucci, and F. Stel. The universal rotation curve of spiral galaxies - I. the dark matter connection. *Mon. Not. R. Astron. Soc.*, 281:27, 1996.

[13] A.G. Riess et al. Observational evidence from supernovae for an accelerating universe and a cosmological constant. *The Astronomical Journal*, 116:1009, 1998.

[14] E. Komatsu et al. Seven-year Wilkinson microwave anisotropy probe (WMAP) observations: cosmological interpretation. *The Astrophysical Journal Supplement Series*, 192:18, 2011.

[15] S.P. Martin. A supersymmetry primer. 1997. arXiv:hep-ph/9709356.

[16] S. Dawson. SUSY and such. *NATO ASI Series*, 365:33, 1997.

[17] G.F. Giudice and R. Rattazzi. Theories with gauge-mediated supersymmetry breaking. *Phys. Rept.*, 322:419, 1999.

[18] S. Ambrosanio and G.A. Blair. Measuring gauge-mediated supersymmetry breaking parameters at a 500 GeV e^+e^- linear collider. *Eur. Phys. J.*, C12:287, 2000.

[19] M. Fairbairn et al. Stable massive particles at colliders. *Phys. Rept.*, 438:1, 2007.

[20] A. Kusenko and M.E. Shaposhnikov. Supersymmetric Q-balls as dark matter. *Phys. Lett.*, B418:46, 1998.

[21] D. Fargion, M.Y. Khlopov, and C.A. Stephan. Dark matter with invisible light from heavy double charged leptons of almost-commutative geometry? *Class. Quantum Grav.*, 23:7305, 2006.

[22] B. Koch, M. Bleicher, and H. Stocker. Black holes at LHC? *J. Phys.*, G34:S535, 2007.

[23] A. Kusenko. Solitons in the supersymmetric extensions of the standard model. *Phys. Lett.*, B405:108, 1997.

[24] T.D. Lee and Y. Pang. Nontopological solitons. *Phys. Rept.*, 221(56):251, 1992.

[25] S. Coleman. Q-Balls. *Nucl. Phys.*, B262(2):263, 1985.

[26] K. Griest, E.W. Kolb, and A. Massarotti. Statistical fluctuations as the origin of nontopological solitons. *Phys. Rev.*, D40:3529, 1989.

[27] J.A. Frieman et al. Cosmic evolution of nontopological solitons. *Phys. Rev.*, D40:3241, 1989.

[28] K. Griest and E.W. Kolb. Solitosynthesis: cosmological evolution of nontopological solitons. *Phys. Rev.*, D40:3231, 1989.

[29] A. Kusenko. Phase transitions precipitated by solitosynthesis. *Phys. Lett.*, B406:26, 1997.

[30] A. Kusenko. Small Q balls. *Phys. Lett.*, B404:285, 1997.

[31] K.V.D. Dungen and W.D.V. Suijlekom. Particle physics from almost-commutative spacetimes. *Rev. Math. Phys.*, 24(09):1230004, 2012.

[32] C.A. Stephan. Almost-commutative geometries beyond the standard model. *J. Phys.*, A39:9657, 2006.

[33] N. Arkani-Hamed, S. Dimopoulos, and G. Dvali. The hierarchy problem and new dimensions at a millimeter. *Phys. Lett.*, B429:263, 1998.

[34] P.C. Argyres, S. Dimopoulos, and J. March-Russell. Black holes and submillimeter dimensions. *Phys. Lett.*, B441:96, 1998.

[35] J. Beringer et al. (Particle Data Group). Review of particle physics. *Phys. Rev.*, D86: 010001, 2012.

[36] G. Abbiendi et al. Search for stable and long-lived massive charged particles in e^+e^- collisions at $\sqrt{s} = 130$–209 GeV. *Phys. Lett.*, B572:8, 2003.

[37] G. Aad et al. Search for massive long-lived highly ionising particles with the ATLAS detector at the LHC. *Phys. Lett.*, B698:353, 2011.

[38] G. Aad et al. Search for long-lived, multi-charged particles in pp collisions at $\sqrt{s}$=7 TeV using the ATLAS detector. *Phys. Lett.*, B722:305, 2013.

[39] C. Lefèvre. The CERN accelerator complex. CERN-DI-0812015, 2008.

[40] L. Evans and P. Bryant. LHC machine. *JINST*, 3:S08001, 2008.

[41] G. Aad et al. The ATLAS experiment at the CERN Large Hadron Collider. *JINST*, 3:S08003, 2008.

[42] S. Chatrchyan et al. The CMS experiment at the CERN LHC. *JINST*, 3:S08004, 2008.

[43] K. Aamodt et al. The ALICE experiment at the CERN LHC. *JINST*, 3:S08002, 2008.

[44] A.A. Alves Jr. et al. The LHCb detector at the LHC. *JINST*, 3:S08005, 2008.

[45] CMS Collaboration. Public CMS luminosity information, 2013. https://twiki.cern.ch/twiki/bin/view/CMSPublic/LumiPublicResults.

[46] S. Boreham, M. Brice, P. Ginter, C. Marcelloni, M Hoch, and CMS Collaboration. Photos from the CMS photo book. CMS-PHO-GEN-2008-026, 2008.

[47] CMS Collaboration. Detector drawings. CMS-PHO-GEN-2012-002, 2012.

[48] CMS Collaboration. CMS tracker detector performance results, 2010. https://twiki.cern.ch/twiki/bin/view/CMSPublic/DPGResultsTRK.

[49] T. Sjostrand, S. Mrenna, and P. Skands. PYTHIA 6.4 physics and manual. *JHEP*, 2006(5):026, 2006.

[50] S. Chatrchyan et al. Search for heavy long-lived charged particles in pp collisions at $\sqrt{s} = 7$ TeV. *Phys. Lett.*, B713:408, 2012.

[51] S. Chatrchyan et al. Searches for long-lived charged particles in pp collisions at $\sqrt{s}$=7 and 8 TeV. *JHEP*, 2013(7):1, 2013.

[52] CMS Collaboration. Search for heavy stable charged particles. Technical Report CMS-PAS-EXO-11-022, CERN, Geneva, 2011.

[53] P. Langacker and G. Steigman. Requiem for a fractionally charged, massive particle. *Phys. Rev.*, D84:065040, 2011.

[54] J. Pumplin et al. New generation of parton distributions with uncertainties from global QCD analysis. *JHEP*, 2002(7):012, 2002.

[55] S. Agostinelli et al. GEANT4—a simulation toolkit. *Nucl. Instrum. Meth.*, A506:250, 2003.

[56] CMS Collaboration. Particle-flow event reconstruction in CMS and performance for jets, taus, and MET. Technical Report CMS-PAS-PFT-09-001, CERN, Geneva, 2009.

[57] CMS Collaboration. Performance of muon identification in pp collisions at $\sqrt{s}$ =7 TeV. Technical Report CMS-PAS-MUO-10-002, CERN, Geneva, 2010.

[58] CMS Collaboration. CMS luminosity based on pixel cluster counting - summer 2012 update. Technical Report CMS-PAS-LUM-12-001, CERN, Geneva, 2012.

[59] CMS Collaboration. Absolute calibration of the luminosity measurement at CMS: winter 2012 update. Technical Report CMS-PAS-SMP-12-008, CERN, Geneva, 2012.

[60] S. Chatrchyan et al. Performance of CMS muon reconstruction in pp collision events at $\sqrt{s}$ = 7 TeV. *JINST*, 7:P10002, 2012.

[61] S. Chatrchyan et al. Precise mapping of the magnetic Field in the CMS barrel yoke using cosmic rays. *JINST*, 5:T03021, 2010.

[62] CMS Collaboration. Measurement of tracking efficiency. Technical Report CMS-PAS-TRK-10-002, CERN, Geneva, 2010.

[63] CMS Collaboration. Search for multi-charged heavy stable charged particles. Technical Report CMS-PAS-EXO-11-090, CERN, Geneva, 2012.

[64] T. Junk. Confidence level computation for combining searches with small statistics. *Nucl. Instrum. Meth.*, A434:435, 1999.

[65] A.L. Read. Presentation of search results: The CL_s technique. *J. Phys.*, G28:2693, 2002.

[66] ATLAS Collaboration, CMS Collaboration. Procedure for the LHC Higgs boson search combination in summer 2011. Technical Report ATL-PHYS-PUB-2011-11, CMS-NOTE-2011-005, CERN, Geneva, 2011.

[67] W.T. Eadie et al. *Statistical methods in experimental physics*. North Holland, Amsterdam, 1971.

[68] F. James. *Statistical methods in experimental physics.* World Scientific, Singapore, 2006.

BIOGRAPHICAL SKETCH

The author was born and grew up in the city of Mumbai, India. He did his early education from South Indian Education Society (SIES) College, and University of Mumbai.